NSF Grants ATM-9321361 and ATM-9500108
National Science Foundation, and
NASA TRMM Grant NAG5-2692
National Aeronautics & Space Administration

DISSERTATION ON THE RELATIONSHIP BETWEEN PRECIPITATION AND LIGHTNING AS REVEALED BY MULTIPARAMETER RADAR OBSERVATIONS

by Lawrence D. Carey

Colorado State University

DEPARTMENT OF ATMOSPHERIC SCIENCE

PAPER NO. **699**

DISSERTATION

ON THE RELATIONSHIP BETWEEN PRECIPITATION AND LIGHTNING AS REVEALED BY MULTIPARAMETER RADAR OBSERVATIONS

Submitted by
Lawrence D. Carey
Department of Atmospheric Science

In partial fulfillment of the requirements for
the Degree of Doctor of Philosophy
Colorado State University
Fort Collins, Colorado
Spring 1999

COLORADO STATE UNIVERSITY

December 11, 1998

WE HEREBY RECOMMEND THAT THE DISSERTATION PREPARED UNDER OUR SUPERVISION BY LAWRENCE DAVID CAREY ENTITLED ON THE RELATIONSHIP BETWEEN PRECIPITATION AND LIGHTNING AS REVEALED BY MULTIPARAMETER RADAR OBSERVATIONS BE ACCEPTED AS FULFILLING IN PART REQUIREMENTS FOR THE DEGREE OF DOCTOR OF PHILOSOPHY.

Committee on Graduate Work

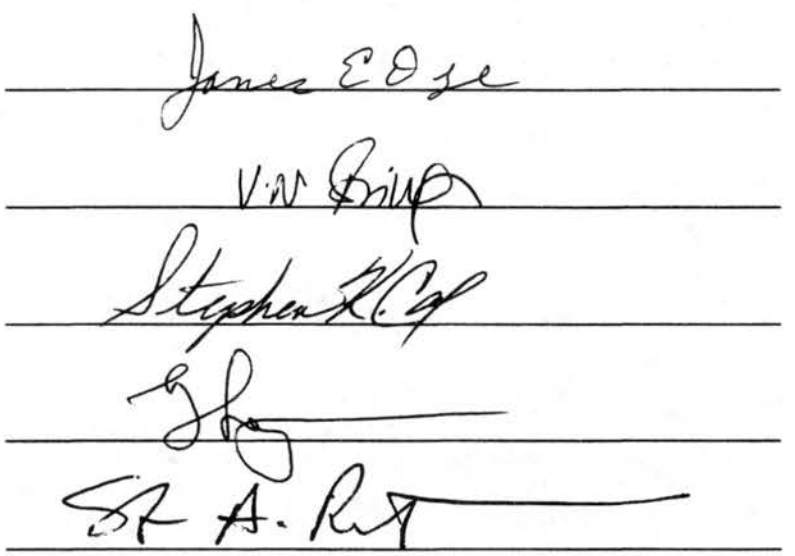

Adviser

Department Head

ABSTRACT OF DISSERTATION

ON THE RELATIONSHIP BETWEEN PRECIPITATION AND LIGHTNING AS REVEALED BY MULTIPARAMETER RADAR OBSERVATIONS

Part I.

Using data from the 11 cm, CSU-CHILL multiparameter radar, the simultaneous evolution of the radar inferred precipitation structure and electrical characteristics of a severe hailstorm is investigated. We compare the sub-storm point discharge current, intracloud (IC) lightning flash rate, cloud-to-ground (CG) lightning flash rate, ground strike location, and flash polarity to the progression of precipitation types and amounts. This study is unique in that it presents multiparameter radar observations of a thunderstorm complex which exhibited an extremely high IC-to-CG ratio (IC/CG, 20 - 70) and predominantly positive CG lightning (over 74%) after it became severe, producing large hail and weak tornadoes.

In particular, we investigate the reported relationship between large hail and positive CG lightning. Although a direct correlation is found between a rapid increase in IC/CG, the first positive CG lightning flashes, and the initial production of hail aloft, the temporal and spatial behavior of large hail and positive CG lightning appear to be anti-correlated, as broad peaks in the positive CG flash rate lag relative maxima in the fallout of large hail by up to thirty minutes. The majority of positive ground strikes were adjacent to the main precipitation core in a region of light rain and little or no hail at the surface. Aloft, radar data indicated that ice crystals were aligned vertically in a strong electric field. Corona point observations at the surface indicate that these regions adjacent to the convective core were characterized by net positive charge aloft. Possible mechanisms to explain these observations are discussed.

Part II.

A propagation correction algorithm utilizing the differential propagation phase (ϕ_{dp}) was developed and tested on C-band polarimetric radar observations of tropical convection obtained during the Maritime Continent Thunderstorm Experiment (MCTEX). An empirical procedure was refined to estimate the mean coefficient of proportionality, a (b), in the linear relationship between ϕ_{dp} and the horizontal (differential) attenuation throughout each radar volume. The empirical estimates of these coefficients were a factor of 1.5 to 2 times larger than predicted by prior scattering simulations. This discrepancy was attributed to the routine presence of large drops (e.g., $Z_{dr} \geq 3$ dB) within the tropical convection observed during MCTEX that were not included in prior theoretical studies.

Scattering simulations demonstrated that the coefficients a and b are nearly constant for small-to-moderate drops (e.g., $0.5 \leq Z_{dr} \leq 2$ dB) but actually increase with the differential reflectivity for drop size distributions characterized by $Z_{dr} > 2$ dB. As a result, the presence of large drops 1) bias the mean coefficients upward, and 2) increase the standard error associated with the mean empirical coefficients down range of convective cores which contain large drops. To reduce this error, we proposed and demonstrated a 'large drop correction' which utilizes enhanced coefficients a^* and b^* in large drop cores.

Validation of the propagation correction algorithm was accomplished with cumulative rain gauge data and internal consistency among the polarimetric variables. The bias and standard error of the cumulative radar rainfall estimator $R(Z_h)$ [$R(K_{dp},Z_{dr})$] were substantially reduced after the application of the attenuation [differential attenuation] correction procedure utilizing ϕ_{dp}. Similarly, scatterplots of uncorrected Z_h (Z_{dr}) versus K_{dp} substantially underestimated theoretical expectations. After application of the propagation correction algorithm, the bias present in observations of both $Z_h(K_{dp})$ and $Z_{dr}(K_{dp})$ were removed and the standard errors relative to scattering simulation results were significantly reduced.

In Part III of this study, the corrected polarimetric data set was then utilized to locate and roughly quantify regions of rain and precipitation sized-ice. This microphysical information provided valuable insight into the couplings between ice phase precipitation and storm electrification/lightning in tropical convection.

Part III.

One of the primary scientific objectives of the Maritime Continent Thunderstorm Experiment (MCTEX) was to study cloud electrification processes and to investigate the coupling between ice phase precipitation and lightning production in tropical island convection. To accomplish this goal, a C-band polarimetric radar (BMRC C-pol) was deployed in the tropics (11.6° S, 130.8° E) for the first time, accompanied by a suite of lightning measurements. Using observations of the propagation corrected horizontal reflectivity and differential reflectivity, along with specific differential phase, three-dimensional rain and ice mass were estimated during the entire life cycle of an electrically active tropical convective complex (known locally as Hector) over the Tiwi Islands on 28 November 1995. Hector's precipitation structure as inferred from these raw and derived radar fields was then compared in time and space to the measured surface electric field, cloud-to-ground and total lightning flash rates, and ground strike locations.

During Hector's developing stage, precipitating convective cells along two island sea-breezes were dominated by warm rain processes. No significant electric fields or lightning were associated with this stage of Hector, despite substantial rainfall rates. Aided by gust front forcing, the cumulus merger process resulted in larger, taller, and more intense convective complexes which were dominated by mixed phase ice processes. During the mature phase of Hector, lightning and the surface electric field were strongly correlated to the mixed phase ice mass and convective rainfall. Merged convective complexes produced 97% of the rainfall and mixed phase ice mass and 100% of the cloud-to-ground lightning. As Hector dissipated, the stratiform rain and area fractions increased as the cloud-to-ground lightning flash rate decreased significantly.

The multicell nature of Hector resulted in the continuous lofting of supercooled drops to the -20° C level in discrete updraft cores during both the early and mature phases. The freezing of these drops provided instantaneous precipitation sized ice particles which may have subsequently rimed and participated in thunderstorm electrification via the non-inductive charging mechanism.

ACKNOWLEDGMENTS

I thank my advisor Prof. Steven Rutledge for his support, expert guidance, and encouragement. I thank Prof. V. N. Bringi, Prof. Stephen Cox, Prof. Graeme Stephens, and Dr. Jim Dye for providing advice, guidance, and resources while serving on my graduate committee. I acknowledge Ms. Michelle Beckman, Mrs. Margi Cech, Mrs. Judy Gueswel, Mrs. Kristy Rouault, Mrs. Melissa Tucker, and Mrs. Jane Wilkins for their knowledgeable and friendly administrative support. I would like to recognize the many other people and organizations who have provided the data, software, technical assistance, and/or expert advice which were crucial to the successful completion of my dissertation. I especially thank the CSU-CHILL radar staff (Mr. Pat Kennedy, Mr. Dave Brunkow, Mr. Bob Bowie, and Mr. Ken Pattison), Dr. John Hubbert (CSU), Dr. John Beaver (CSU), Prof. V. Chandrasekar (CSU), Dr. Tom Keenan (BMRC), Dr. Peter May (BMRC), Mr. Ken Glasson (BMRC), the Lightning Research Group at NASA/MSFC (Dr. Rich Blakeslee, Mr. Jeff Bailey, Dr. William Koshak, Dr. Hugh Christian, and Dr. Steven Goodman), Dr. Dusan Zrnic' (NSSL), Dr. Earle Williams (MIT), Dr. Tsutomo Takahashi (Kyushu University), and Mr. Bob Rilling (NCAR/ATD).

All of the members of the Radar Meteorology Group at CSU over the past four years (including Dr. Walt Petersen, Dr. Terry Schuur, Mr. Paul Hein, Dr. Rob Cifelli, Dr. Tom Rickenbach, Dr. Charlotte Demott, Ms. Bethany Hobbs, Captain Rick Lucci, Mr. Jon Erdman, Mr. Tim Lang, Captain Christy Butler, Mr. Dave Ahijevych, Mr. Jesse Ryan, Ms. Cristina Kaufman, Captain Mike Gauthier, and Mr. Larry Belcher) have been an irreplaceable source of advice, knowledge, inspiration, encouragement, and friendship.

Part I of this research was supported by the NSF under grant ATM-9321361 and the CSU-CHILL cooperative agreement ATM-9500108. Parts II and III of this dissertation were supported by NASA under grant NAG 5-2692.

PREFACE

In recent years, a considerable body of scientific evidence has accumulated that indicates rebounding collisions between ice particles of dissimilar size in the presence of supercooled cloud liquid water are responsible for the separation of electric charge in thunderstorms. Laboratory experiments on charge separation during ice particle collisions, or the so-called non-inductive charging (NIC) mechanism (e.g., Takahashi, 1978; Jayaratne et al., 1983; Saunders et al., 1991 among others), have yielded results consistent with large-scale observations of thunderstorm electrical structure and lightning production (e.g., Williams, 1989).

Concurrent with these developments in atmospheric electricity, significant advances have occurred in the discrimination of hydrometeor types and in the estimation of precipitation rates in mixed-phase environments using multiparameter radar techniques as summarized in Doviak and Zrnic′ (1993). In particular, linear dual-polarization radars (such as the CSU-CHILL or BMRC C-pol radars) provide additional information which yield estimates of important hydrometeor characteristics such as particle size, shape, spatial orientation, and thermodynamic phase. This information has been used for the identification of mixed-phase hydrometeors (e.g., Zrnic′ et al., 1993), the detection of hail and the estimation of its size (e.g., Bringi et al., 1986; Aydin et al., 1990; Balakrishnan and Zrnic′, 1990a), estimation of rain and hail rates in mixed-phase precipitation (e.g., Sachidananda and Zrnic′, 1987; Balakrishnan and Zrnic′, 1990b), and the discrimination of ice forms (e.g., Zrnic′ et al., 1993).

Since collisions between graupel (or hail) and ice crystals in the presence of supercooled cloud water is hypothesized to generate charge in thunderstorms, and since multiparameter radar techniques offer significant promise in distinguishing precipitation sized ice from raindrops and in providing a gross estimate of ice mass, multiparameter

radar provides an ideal remote sensing platform for the study of cloud microphysics and precipitation processes relevant to storm electrification and lightning. The additional benefit of studying cloud microphysical processes with multiparameter radar is that a *full storm volume* sample can be obtained in minutes. By contrast, in-situ microphysical sampling by aircraft typically is limited by altitude restrictions and the inability to penetrate intense convection (e.g., reflectivity > 40 - 50 dBZ) in both midlatitude and particularly tropical cumulonimbus.

As a result, *the scientific objectives of our research over the last six years have been 1) to develop and/or refine techniques to infer bulk-hydrometeor types and to estimate precipitation amounts at two precipitation radar wavelengths (S- and C-band) and 2) to apply these techniques in a variety of storm types (e.g., ordinary Colorado thunderstorms, severe High Plains hailstorms, and deep tropical island convection) to better understand the temporal and spatial relationship between precipitation and lightning and therefore to gain additional insights into thunderstorm charging mechanisms.*

In my M.S. thesis, we utilized known techniques at S-band to study the correlation between precipitation ice and lightning in non-severe, Colorado thunderstorms (Carey, 1994; Carey and Rutledge, 1996). The first efforts of this Ph.D. dissertation were to refine these techniques at S-band to study severe High Plains hailstorms which exhibit an anomalous signature in the percentage of positive polarity cloud-to-ground lightning flashes (Carey and Rutledge, 1998; Part I of the dissertation). The emphasis in this research was the refinement of published polarimetric radar techniques at S-band and, to a greater extent, the application of these methods to the better understanding and documentation of positive CG producing severe hailstorms.

Following the study of severe hailstorm electrification, our research efforts focused on the development of C-band polarimetric radar techniques to correct propagation effects (Part II of the dissertation) and estimate precipitation types and amounts, and the application of these new methods to the better understanding of the role of ice (and frozen drops in particular) in the electrification of tropical island convection observed during the Maritime Continent Thunderstorm Experiment (MCTEX, Part III of the dissertation).

To my wife, Shawna, whose support, encouragement, friendship, and love have sustained me through six years of graduate school and have motivated my mind and nourished my soul for a wonderful fourteen years.

TABLE OF CONTENTS

LIST OF TABLES

Part I

Part II

Part III

LIST OF FIGURES

Part I

Part II

Part III

PART I, ELECTRICAL AND S-BAND MULTIPARAMETER RADAR OBSERVATIONS OF A SEVERE HAILSTORM

CHAPTER 1
INTRODUCTION

More than 90% of cloud-to-ground (CG) lightning in warm-season thunderstorms are of negative polarity (Fuquay, 1982; Orville et al., 1987; Reap and MacGorman, 1989; Orville, 1994; Orville and Silver, 1997). As a result, the number of negative CG lightning flashes typically dominates the number of positive CG flashes at any given stage and location in an ordinary (i.e. non-severe), summertime thunderstorm. Exceptions to this situation have been noted in a few scenarios during the warm-season. 1) The dissipating phase (i.e., vertical motions characterized by precipitation filled downdrafts only) of some ordinary thunderstorms can be dominated by positive CG flashes, although the flash density is usually small (e.g., Fuquay, 1982); 2) The trailing stratiform region of mesoscale convective systems (MCS's) (e.g., Rutledge and MacGorman, 1988; Rutledge et al., 1990; Engholm et al. 1990; Stolzenburg, 1990) and the anvil region of some severe storms (Rust et al., 1981a,b) are dominated by positive CG lightning while the deep convective regions of these storms are still characterized by predominantly negative CG lightning. The positive CG flashes in these storms occur over a large area during the course of several hours such that the positive CG flash density is typically low (< 0.01 km^{-2} h^{-1}, Stolzenburg, 1994); 3) Although cloud-to-ground lightning activity during the *mature* phase (i.e., characterized by the presence of an active updraft and precipitation filled downdraft; Houze 1993) of non-severe thunderstorms is typically dominated by negative flashes, growing observational evidence suggests that severe thunderstorms which produce large hail (diameter $\geq$ 2 cm) and sometimes tornadoes are often characterized by a predominance of positive CG lightning for extended periods of time ($\geq$ 30 minutes) during the mature phase (e.g., Rust et. al, 1985; Reap and MacGorman, 1989; Branick and Doswell, 1992; Curran and Rust, 1992; Seimon, 1993; MacGorman and Burgess, 1994; Stolzenburg, 1994). In these severe thunderstorms, the positive CG

lightning flashes are clustered in time and space in or near convective regions similar to negative CG flashes in ordinary storms and have comparable flash densities.

There are currently few detailed case studies of the co-evolving precipitation structure and lightning behavior in severe convection. MacGorman (1993) reviewed earlier studies which suggested that many severe storms are characterized by enhanced intracloud (IC) lightning flash rates and high percentages of positive CG lightning discharges. More recently, Branick and Doswell (1992) and Curran and Rust (1992) both investigated the occurrence of dominant positive CG lightning activity in low-precipitation (LP) supercells which produced large hail and tornadoes. Seimon (1993) analyzed visual and radar observations of a tornadic F5 supercell which produced primarily positive cloud-to-ground lightning during the development phase and which exhibited a reversal in dominant CG polarity from positive to negative at the time of tornado touchdown. MacGorman and Burgess (1994) and Stolzenburg (1994) have surveyed a large number of cases (15 and 24 respectively) of predominantly positive CG lightning producing storms with lightning mapping networks, storm reports, and limited radar data. These studies have confirmed an intriguing and robust one-way correlation between high positive CG flash densities and severe weather. Although not all severe storms produce predominant positive CG lightning, *the majority of storms which are characterized by high positive CG flash densities (in excess of negative CG flash densities) during the mature phase are associated with severe weather such as large hail and tornadoes.*

However, the above studies have demonstrated that there is also significant variability in the kinematic, microphysical, and electrical attributes of these storms. As suggested by MacGorman and Burgess (1994), "...the next obvious step in studying positive ground flashes in severe storms is to examine relationships with storm evolution more completely." Therefore, the purpose of this paper is to present detailed observations of the co-evolving precipitation structure, surface electric field, and lightning activity associated with a severe hailstorm occurring in eastern Colorado on 7 June 1995. Over three hours of CSU-CHILL multiparameter radar (S-band, 11 cm) observations with high temporal resolution ($\leq$ 6 minutes) and at close range ($\leq$ 60 km) are analyzed in the context of the IC lightning flash rate inferred from a flat plate antenna, CG lightning properties

such as flash rate, polarity, and ground strike location measured by the NLDN, and the sub-storm point discharge current (proxy for surface electric field) measured beneath the severe hailstorm with a mobile corona point sensor. The location of these instruments relative to the CSU-CHILL radar can be found in Fig. 1.1. During this three hour period, the storm produced over 74% positive CG lightning (a total of 184 positive flashes) with a peak positive CG flash rate of 7 per minute and a peak percentage of positive lighting of 100% when considering 6 minute averaging periods. In addition, the intracloud lightning flash rate peaked near one per second and the IC/CG exceeded 20. At the same time, the storm produced multiple tornadoes and large hail up to 5 cm in diameter as verified by chase vans working with the CSU-CHILL radar (Hubbert et al., 1998). Multiparameter radar measurables collected by the CSU-CHILL radar allowed inferences regarding hydrometeor types (such as large hail) and precipitation amounts (both rain and hail rates) to be made.

As a result, we are able to investigate the reported association of positive ground flashes and enhanced intracloud lightning flash rates to the occurrence of severe weather such as large hail using unique multiparameter radar analyses of the three-dimensional precipitation structure. In Chapter 2, we briefly review the data collected and analysis methods used in this study. (More details of multiparameter radar techniques can be found in Appendix A and references given therein). In Chapter 3, we present electrical and radar observations of the severe hailstorm. In Sec. 3.1, we discuss the meteorological conditions leading up to the development of a severe storm complex along the Front Range of Colorado. Next, we review the storm evolution using reflectivity data and storm reports in Sec. 3.2. In Sec. 3.3, we present detailed multiparameter radar analyses exploring the temporal and spatial relationship between large hail production, positive CG lightning, the intracloud flash rate, and the surface electric field in an isolated supercell. We then investigate the correlation between large hail, precipitation (rain and hail) rates, and lightning in the entire severe hailstorm complex which resulted from the merging of two supercell storms (Sec. 3.4). In Sec. 3.5, we show the characteristic evolution of the three-dimensional precipitation structure in the vicinity of an intense positive CG lightning cluster. Subsequently in Sec. 4.1, we summarize our observational results and compare

and contrast them to past findings. Lastly, we speculate on the plausibility of a few potential hypotheses put forward to explain the dominance of positive CG lightning in Sec. 4.2.

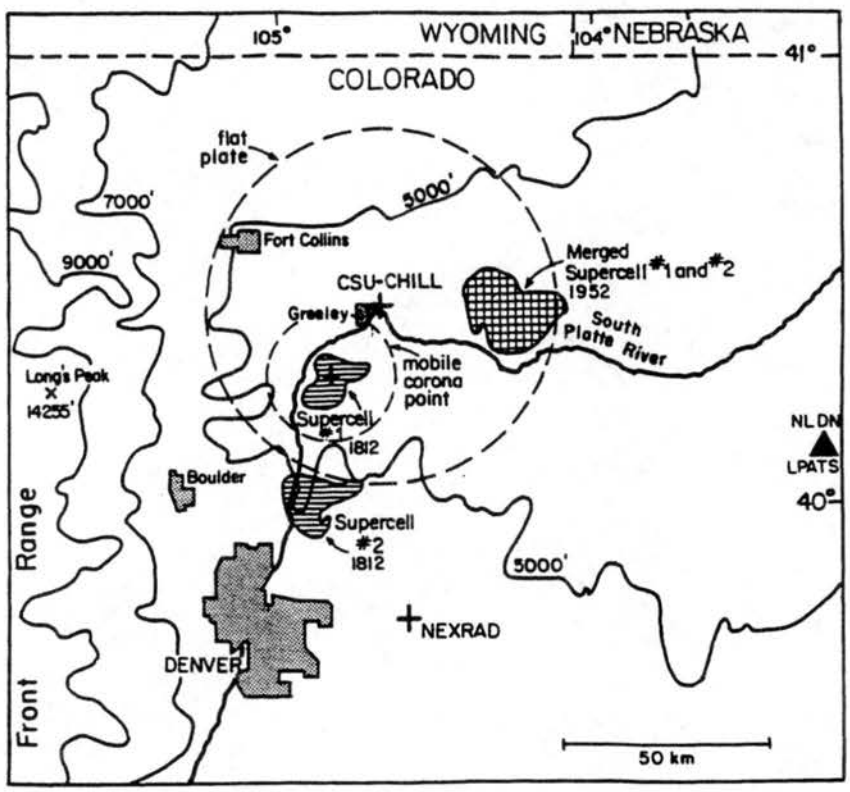

Figure 1.1. Depiction of the observational network used in this study. Locations of the 11 cm, dual-polarized CSU-CHILL and Denver WSR-88D radars are indicated. The position of the mobile corona point sensor is shown about 19 km to the southwest of the CSU-CHILL radar. The maximum operating range of the flat plate antenna (located at the CSU-CHILL radar) and the corona point sensor (located about 19 km to the southwest of the CSU-CHILL radar) are depicted by dashed rings of 40 km and 15 km respectively. The location of the closest NLDN (National Lightning Detection Network) LPATS (Lightning Position and Tracking System) station is depicted by a triangle. Hatched areas represent regions of storm echo exceeding 55 dBZ at 1812 and 1952 MDT.

CHAPTER 2

MEASUREMENTS AND ANALYSIS METHODS

Storm precipitation structure was inferred from measurements made by the linearly, dual-polarized CSU-CHILL radar which operates at S-band (2.725 GHz or 11 cm). The radar was recently upgraded with a new antenna and the implementation of a dual-transmit and dual-receive system to improve isolation between the vertical and horizontal channels, allowing accurate estimation of the linear depolarization ratio (Mueller et al., 1995). For the storm under study, a PPI (Plan Position Indicator) sector scanning strategy was employed. Azimuthal spacing provided a slight over-sample with 0.8° while spacing in the elevation angle was variable but software controlled to maintain better than 1 km resolution at 60 km in range. An attempt was made to compromise between satisfactory horizontal and vertical spatial coverage and sufficient temporal resolution. Sector volume times were typically four to six minutes in length and covered the entire extent of the radar echo (at least down to 10 dBZ). However, when the hailstorm approached within 25 km of the radar, it was necessary to sacrifice spatial coverage to maintain acceptable volume times appropriate for deep convection ($\leq$ 6 minutes). In this situation, the CSU-CHILL radar maintained horizontal coverage focused on reflectivity cores ($>$ 30 dBZ) and obtained as much vertical coverage as possible in the allotted time. As a result of these occasional scanning deficiencies imposed by the storm location relative to the radar, reflectivity data from the Denver WSR-88D radar was utilized when necessary to supplement analysis of precipitation structure.

The measured multiparameter radar observables include the horizontal reflectivity (Z_h), differential reflectivity (Z_{dr}), linear depolarization ratio (LDR), differential phase (Ψ_{dp}), and the correlation coefficient at zero-lag (ρ_{hv}). One important variable, the specific differential phase (K_{dp}), was estimated by first isolating the propagation differential phase

(ϕ_{dp}) from Ψ_{dp} by a filtering method (e.g., Hubbert et al., 1993, Hubbert and Bringi, 1995) and then differentiating ϕ_{dp} with range. For complete definitions of the multiparameter radar variables used in this study, we refer the reader to several comprehensive reviews of dual-polarimetric radar measurables (e.g., Rogers, 1984; Bringi and Hendry, 1990; Doviak and Zrnic', 1993). As discussed in these reviews, multiparameter radar variables provide information on the size, shape, orientation, and thermodynamic phase of hydrometeors in a bulk sense. When used concurrently, these measurables can often be used to categorize the predominant, bulk precipitation type in a radar resolution volume (Jameson, 1985a; Jameson and Johnson, 1990; Doviak and Zrnic', 1993). For example, it is possible to use the above variables to distinguish large ($\geq$ 2 cm) hail from other hydrometeor types (Balakrishnan and Zrnic', 1990a; Zrnic' et al., 1993). The technique of bulk hydrometeor identification has been used by various authors to compare the evolution of precipitation structure, especially ice, to that of lightning and storm electric fields (e.g., Carey and Rutledge, 1996; Jameson et al., 1996; Ramachandran et al., 1996; French et al., 1996). In this study, we optimize the above method to distinguish between vertically oriented ice, rain, small hail, large hail, and mixed-phase precipitation (rain mixed with small or large hail). In addition, we have utilized the above variables to calculate both rain and hail rates as discussed in Balakrishnan and Zrnic', (1990b). For more specific details on how the radar data was processed and analyzed to identify hydrometeor types and estimate precipitation rates, see Appendix A.

The three-dimensional precipitation structure inferred from multiparameter radar data is placed in the context of storm electricity and lightning data which was obtained from three sources: a flat plate antenna located at the CSU-CHILL radar, a mobile corona point sensor which was located about 19 km southwest of the radar for this event, and the National Lightning Detection Network (NLDN). The placement of these instruments relative to the CSU-CHILL and Denver WSR-88D radars and their range of operation are depicted in Fig. 1.1.

The flat plate antenna (e.g., Uman, 1987), or "field change meter," was used to measure the electrostatic field change from both intracloud and cloud-to-ground lightning within about 40 km of the CSU-CHILL radar and was therefore used to obtain the total

lightning flash rate. An estimate of the intracloud lightning flash rate was obtained by subtracting the NLDN inferred CG lightning flash rate within 40 km of the CSU-CHILL radar from the flat plate antenna estimated total lightning flash rate. Details regarding the field change meter used in this study and the processing and analysis of the data for lightning flashes can be found in Carey and Rutledge (1996).

The polarity and strength of the point discharge current was measured with a mobile corona point sensor. The instrument consisted of a conducting rod with a pointed tip which was mounted on a portable instrument tower approximately 5 m AGL and fed into an A-to-D converter sampling at 1 Hz via an operational amplifier. This corona point measured the small currents (microamperes) which flowed from elevated points in response to the net electrostatic field caused by regions of charge within approximately 15 km. As a result, corona current was used to provide a measure of the polarity and relative strength of the near surface electrostatic field due to the net charge within the storm aloft. The gradual and continuous changes (order of a minute) in the corona current were associated with changes in the charge structure aloft due to charge generation and/or advection. Sudden discontinuities (order of a second) in the corona current were associated with changes in the electrostatic field associated with a lightning flash (either IC or CG). More details on corona point sensors and their applications can be found in Engholm et al. (1990) and Carey and Rutledge (1996).

Cloud-to-ground lightning data including LLP (Lightning Location and Protection) signal strength, polarity, and ground strike location were obtained from the National Lightning Detection Network (NLDN) owned and operated by Geomet Data Services (GDS). The LLP signal strength values were converted to peak current (kA), I_{peak}, using the estimate found in Orville (1991),

$$I_{peak} = 0.19 \bullet I_{LLP} + 2.3 \quad [kA]. \tag{2.1}$$

The NLDN was recently upgraded (Cummins et al., 1995 and 1998) and now employs a new hybrid lightning location methodology combining time-of-arrival and direction finding techniques (see Holle and López, 1993 for a review of both techniques). Two of the primary objectives of the NLDN upgrade were to 1) improve location accuracy and 2) improve detection efficiency, especially for low peak current events (down to 5 kA). As a

result, Cummins et al. (1998) reported an improvement in location accuracy by a factor of 4 to 8, resulting in an average accuracy of 0.5 km, and an estimated flash detection efficiency of 80 to 90%.

One unexpected result from the recent upgrade of the NLDN is the inclusion of a previously undetected population of small positive discharges. Following changes to sensitivity and wave form discrimination criteria in the NLDN sensors, the percentage of positive flashes has approximately doubled beginning late summer, 1995 (K. Cummins, private communication, 1996). These newly detected events are low current (5 to 15 kA estimated peak current) discharges which exhibit flash multiplicities that appear identical to those for larger positive flashes. At the time of this writing, it is not known if these events are long vertical cloud discharges (since they can be detected at distances of up to 500 km and thus falsely detected as positive ground flashes) or if they are a population of previously undetected positive cloud-to-ground discharges. By analyzing and comparing NLDN, flat plate antenna, and corona point sensor data, we demonstrate in Appendix B that the positive cloud-to-ground discharges detected from the storm complex under study are probably *not* a part of this new subset of potentially false positive CG detections.

CHAPTER 3
OBSERVATIONS

3.1. Meteorological Conditions

The meteorological conditions of 7 June 1995 along the Front Range of northeastern Colorado (CO) closely resembled those described by Doswell (1980) for High Plains severe thunderstorms. The key ingredients were 1) a quasi-stationary front south of the area through northern New Mexico and the Oklahoma and Texas panhandles, 2) steadily increasing surface dewpoint temperatures in excess of 45° F (7.2° C) with maximum values reaching 53° F (11.7° C) associated with upslope flow which veered from northeasterly to southeasterly during the day at 2 to 5 m s^{-1}, and 3) strong southwesterly flow at 500 mb in excess of 20 m s^{-1} with weak temperature and vorticity advection associated with a closed low in the Great Basin. At 300 mb, a jet streak rotated through central CO, placing the area of interest in the right exit region which is often a synoptically unfavorable location (i.e., subsident). However, diffluent flow was present at this level which is dynamically favorable for thunderstorm development. Typically, severe weather occurs on several days in succession associated with these relatively benign synoptic conditions (Doswell, 1980). It is interesting to note that severe thunderstorms had occurred on the previous day (6 June 1995) and were therefore expected on 7 June as well.

Thermodynamic conditions along the Front Range also strongly suggested the possibility of severe weather. A late morning sounding at 1114 MDT (or 1714 UTC; UTC = MDT + 6 h) taken by NCAR (National Center for Atmospheric Research) near Denver, CO (within 20 km of where storms became severe shortly after 1700 MDT) is shown in Fig. 3.1. The freezing level is located at 2.4 km AGL (4.0 km MSL or 616 mb). The sounding is characterized by an adiabatic environment from the surface to a capping frontal inversion at 680 mb with a relatively dry layer at the surface and a relatively moist

layer from about 750 mb to the bottom of the inversion. Above the inversion, the environment was conditionally stable up to 400 mb with the tropopause located at 210 mb and exhibited a deep, mid-level dry layer centered on 500 mb. Due to the presence of this capping inversion, there was substantial Convective Inhibition (CIN) of -725 J kg^{-1}. This cap prevented deep convection prior to 1600 MDT. During the day there was significant moistening in the boundary layer due to the upslope flow. In order to more accurately represent the pre-convective environment which was about five hours following the actual rawinsonde release, the sounding was modified to account for 1) moistening of the surface dewpoint to a maximum of 11.7° C, 2) warming of the surface temperature to a maximum of 22° C, 3) assuming a deep mixed layer up to the Convective Condensation Level (CCL) at about 715 mb, and 4) eliminating the frontal inversion to allow the available convective energy to be explosively released.

Realizing that these assumptions merely allow an estimate of the *maximum* potential energy in the atmosphere, we obtain a Convective Available Potential Energy (CAPE) of 2268 J kg^{-1}. Winds veered with height from southeasterly to southwesterly and were characterized by moderate shear (20 m s^{-1}) in the lowest 6 km of the troposphere. Combining these shear and buoyancy estimates, the modified sounding yields a bulk Richardson number of 11.3 which is suggestive of supercell development (Weisman and Klemp, 1982; 1984). Considering the favorable synoptic conditions, moderate-to-high CAPE, and moderate shear, the atmosphere was primed for severe thunderstorms capable of producing large hail, damaging winds, and tornadoes.

3.2. Storm Evolution: Reflectivity and Storm Reports

In order to provide an overview of storm evolution in the vicinity of the CSU-CHILL radar during a four hour period, we present a series of two-dimensional (2-D) maximum horizontal reflectivity composites at half-hour temporal resolution in Figs. 3.2a-i. We chose this approach over a horizontal cut at some arbitrary level because it provides the best overall summary of storm evolution. The 2-D maximum Z_h composites were derived from Denver WSR-88D reflectivity data by determining the maximum Z_h in a vertical column at every (x, y) location depicted. The Denver WSR-88D radar was used for this

purpose instead of the CSU-CHILL because it provides the best overall horizontal and vertical storm coverage with repeating 360° sector volumes from a vantage point well south of the storm complex (cf. Fig. 3.2). In comparison, the CSU-CHILL was sometimes forced to compromise its scanning in the horizontal and vertical due to the proximity of the storm (see Figs. 3.2d-g). Surface observations from the public (Storm Data, 1995) and two chase vans working with the CSU-CHILL radar will be set in the context of the storm evolution as seen in these maximum reflectivity composites.

Because of the strong post frontal inversion discussed in Sec. 3.1, convection was suppressed along the Front Range until after 1600 MDT. Between 1600 and 1645 MDT, several non-severe thunderstorm cells developed just north of Denver approximately 60 km to the southwest of the CSU-CHILL, with their echoes topping out at about 9-10 km AGL. As can be seen in the 1700 MDT Denver sounding in Fig. 3.1, the steering level flow was out of the SSW at about 10 m s^{-1}. As a result, most cells moved generally toward the NNE prior to 1700 MDT. A depiction of these early (1644 MDT) conditions is given in Fig. 3.2a. Note that peak reflectivities are still generally below 55 dBZ. The largest and most intense cell at this time was centered at about x = -25 km and y = -45 km relative to the CSU-CHILL. From 1644 MDT to 1713 MDT, this particular cell (now centered on x = -15 km and y = -35 km as seen in Fig. 3.2b) began to develop explosively in the vertical, exhibited early signs of a supercell including a weak echo region and forward overhang, and began to move toward the northeast which is about 14° to the right of the mean shear vector which was directed toward the NNE. This cell which will be called supercell #1 throughout the rest of the paper was just beginning to move within range of the CSU-CHILL flat plate as can be seen in Fig. 3.2b. Another strong cell of interest which will be referred to as supercell #2 was over northwest Denver by 1713 MDT (x = -37 km, y = -67 km) and began to grow rapidly and exhibit similar signatures of severe supercells.

By 1748 MDT, both supercell #1 and #2 possessed clearly defined mesocyclones as seen in CSU-CHILL radial velocity data (not shown), bounded weak echo regions (BWER), forward overhangs, and intense (> 65 dBZ) reflectivities as seen in Fig. 3.2c. At this time, supercell #1 was in a sparsely populated region of Weld County (centered on x =

-12 km and y = -23 km) but well within the range of both flat plate and the mobile corona point sensor. As a result, the early development of hail within supercell #1 relative to its electrical characteristics is the subject of the next section. Although no hail was reported by the public for supercell #1 by 1748 MDT, it is clear from reflectivity data that hail was very probable. This will be explored more with multiparameter radar data in the following sections. On the other hand, supercell #2 exhibited a large area of greater than 65 dBZ reflectivities around x = -30 km and y = -47 km over a heavily populated area in the suburbs north of Denver. During this time, there were two public reports of large hail (1.5-1.75 inches or 3.8-4.4 cm). From 1748 MDT to 1812 MDT, supercell #1 moved very little (Fig. 3.2d) as it produced copious amounts of large hail and a tornado on its right (southern) flank. Public reports of 1 inch hail (2.5 cm) during this period are supported by reports of hail up to 2 inches (5.0 cm) in diameter from two chase vans (one of which contained the mobile corona point sensor as depicted in Fig. 1.1 and Fig. 3.2d). The other chase van which was outfitted to collect hail and measure rain rates in order to compare to the CSU-CHILL multiparameter radar data (Hubbert et al., 1998) collected several bags of large hail from about 1806 MDT to 1812 MDT. Interestingly, supercell #2 which was located just outside the flat plate's 40 km operational range by 1812 MDT continued to move toward the northeast at about 5 m s^{-1}.

In order to characterize the vertical structure of supercell #1 near this time (1812 MDT), we present a vertical cross-section of CSU-CHILL reflectivity oriented from east-to-west along y = -20.5 km taken from 1808-1812 MDT (Fig. 3.3). The dashed line in Fig. 3.2d delineates the plane of the cross-section. In this vertical cross section, there are several familiar supercell features including a bounded weak echo region (BWER) centered on x = -6 km and $4 < z < 5.5$ km, a forward overhang at x = -4 km and $4 < z < 7$ km, and an impressive hail cascade (Browning and Foote, 1976) with peak reflectivities near 70 dBZ. To investigate this hail cascade further, we present profiles of the CSU-CHILL multiparameter variables Z_{dr} and ρ_{hv} in Fig. 3.4a and LDR and K_{dp} in Fig. 3.4b through the hail cascade marked by the path of "X's" in the vertical cross-section (Fig. 3.3). Above the melting level (2.4 km AGL), Z_h is greater than 60 dBZ, Z_{dr} is slightly negative (-0.2 to -0.4 dB), ρ_{hv} is high (0.97 to 0.98), K_{dp} is less than 0.5° km^{-1}, and LDR is

greater than -26 dB. According to the bulk hydrometeor identification method outlined in Appendix A (Table A.1), these multiparameter variables indicate the presence of hail. Of course, this is not surprising given the conceptual models of hail growth in supercell thunderstorms (e.g., Browning and Foote, 1976). Below the melting level, the multiparameter variables are consistent with the presence of large hail with K_{dp} near zero, LDR enhanced to greater than -15 dB, ρ_{hv} down to 0.88, strongly negative Z_{dr} (-1 dB), and high reflectivity (> 60 dBZ). Coincidentally, one of the CSU-CHILL chase vans collected hailstones up to 5 cm in diameter within 2 km of the base of the marked hail cascade (Hubbert et al., 1998). The combination of ground truth data (although limited) and the consistency between multiparameter radar inferred areas of hail and conceptual models, provides support for the method of bulk hydrometeor identification outlined in Table A.1 (at least for large hail).

Over the next half hour, observations from the corona point van included large hail and later (after 1820 MDT) a prodigious amount of small hail mixed with heavy rain which resulted in flooded farm fields. The large hail and heavy rain produced over $33 million dollars of damage in several small towns and surrounding fields in Weld County to the southwest of the CSU-CHILL radar (Storm Data, 1995). There were four public reports of large hail (2-5 cm) and one tornado report between 1812 MDT and 1847 MDT for the two supercells depicted in Fig. 3.2e which were beginning to merge into one large thunderstorm complex as supercell #2 caught up with supercell #1 from the south. By 1916 MDT, the two supercell storms were completely merged at mid- to upper-levels and could be distinguished only by two reflectivity maximum (> 65 dBZ) near the surface that are evident in the maximum reflectivity composite in Fig. 3.2f (supercell #1: x = 8 km, y = -4 km; supercell #2: x = 12 km, y = -20 km). This merged hailstorm complex was moving almost due east by this time. During the period from 1847 MDT to 1916 MDT, there were three more public reports of large hail (2.5-4.4 cm) and a tornado near Kersey, CO (x = 2.2 km and y = -9.6 km). This tornado which was evident in the CSU-CHILL radial velocity data as a tornado vortex signature (TVS; Lucci, 1996) appeared to occur along a shear zone in a descending hail curtain adjacent to the storm updraft. Lucci (1996) analyzed and compared the kinematic structure of the hailstorm complex during this

period to the occurrence of positive CG lightning. Note that a third cell began to form by 1916 MDT on the right flank (southwest side) of the merged supercell #1 and #2.

From 1916 MDT to 1946 MDT, the merged complex continued to move toward the ENE, producing large hail and a weak tornado in Weld county to the ESE of the radar. Notice that the reflectivity maximum (> 65 dBZ) originally associated with supercell #1 at 1916 MDT (Fig. 3.2f: x = 8 km, y = -4 km) has fallen out of the storm by 1946 MDT as seen in Fig. 3.2g. As will be demonstrated in Sec. 3.5 below, the fallout of large hail in this area around 1929-1940 MDT was followed by an intense positive CG lightning cluster (grouping of 20 ground strike locations in a 10 km x 10 km area, centered on x = 22 km and y = 15 km, during an 18 minute period). Interestingly, this positive CG cluster which occurred from about 1940 to 2001 MDT was followed closely by a public report of two tornadoes at 2004 MDT only 10 km to the SSE of the positive CG cluster.

As the storm complex continued to move toward the ENE from 2015-2044 MDT (Figs. 3.2h,i), it took on the characteristics of a short, severe multicell squall line with new cells developing on the right (southwestern) flank. Occasional reports of large hail continued during this period. After 2044 MDT, the storm continued its eastward march and eventually moved out of range for quality CSU-CHILL multiparameter radar analyses (best at ranges of ≤ 60 km). With the storm evolution described in general for this four hour period, it is now possible to analyze in detail the relationships between radar derived precipitation structure and electrical behavior for this anomalous hailstorm.

3.3. Electrical Characteristics Associated with Hail Development in a Supercell

Before tackling the association between hail development and electrical characteristics for the complex storm evolution of the two merging supercells discussed in the previous section, we first investigate these relationships for supercell #1 alone from its genesis at about 1620 MDT up to its merger (of the 55 dBZ reflectivity contours) with supercell #2 around 1855 MDT (e.g., Figs. 3.2e,f). The reasons behind this analysis choice are two fold: 1) any correlation between electrical characteristics and precipitation development will be more evident when analyzing a single supercell, and 2) simultaneous corona point sensor data and flat plate antenna data were available for supercell #1 as it approached the

CSU-CHILL from the southeast while supercell #2 was still out of range (e.g., Figs. 3.2c-d) and therefore not affecting the corona point or flat plate measurements.

The evolution of intracloud and cloud-to-ground lightning for supercell #1 is shown in Fig. 3.5. An estimate of the IC flash rate is only available while supercell #1 was fully within range of the flat plate antenna and while supercell #2 was still out of range (1730-1810 MDT, e.g. Figs. 3.2b-d). Note that this particular cell produced exclusively negative CG lightning in its early, non-severe phase. The reflectivity structure in Fig. 3.2a at 1644 MDT just follows this maxima in the negative CG flash rate from 1630-1645 MDT. Interestingly, as this cell began to develop rapidly in the vertical, it produced *no* NLDN detectable CG lightning. This dearth in CG lightning lasted for just over one hour (1645-1750 MDT) as the cell evolved from an ordinary thunderstorm to a severe supercell. Based on flat plate measurements, we know that the storm was indeed electrified because it was producing IC flashes at a rate of 2.6 - 4.4 flashes min^{-1} from 1730-1750 MDT (Fig. 3.5). When the cell finally produced CG lightning again at 1750 MDT, the polarity switched to primarily positive and the number of IC flashes began to increase dramatically as can be seen in Fig. 3.5. Supercell #1 continued to produce primarily positive CG lightning (87%) for the rest of its lifecycle (1750-1900 MDT) until it merged with supercell #2. (As shown in the next section, the merged storm also produced mostly positive CG lightning flashes). A broad peak in the positive CG flash rate for supercell #1 began at 1835 MDT and continued until the merger process commenced at 1900 MDT. This peak positive flash rate was actually fairly low (1.2 flashes min^{-1}) compared to typical negative CG flash rates in ordinary storms.

In Fig. 3.6, the precipitation history at the surface for the same time period covered by Fig. 3.5 is given. In particular, the evolution of the rain and hail mass fluxes and the peak hail rate calculated from K_{dp} and Z_h (as outlined in Appendix A) is depicted for supercell #1 from 1620 MDT to 1900 MDT. First, note that a peak in the rain mass flux and peak hail rate occurred during and just following the peak in the negative CG flash rate from 1635 MDT to 1645 MDT. Most ordinary thunderstorms exhibit a similar correlation between the rain mass flux, hail rate, and negative CG flash rate (e.g., Carey and Rutledge, 1996) as seen in this non-severe precursor phase of supercell #1. As the storm began to

transition from an ordinary, isolated cell to a supercell, the rain and hail mass fluxes rebounded and then continued to increase by an order of magnitude over the next hour *despite* the fact that there were no detected CG lightning flashes. Relative maxima in the peak hail rate and hail mass flux are coincident with a relative maximum in the IC flash rate at 1735 MDT as the quasi-steady supercell underwent a pulse in growth. Next, when the positive CG lightning began and the IC flash rate rapidly increased at 1750 MDT, the rain mass flux was steady at peak values (around 3 - 4 $\times$ 10^6 kg s^{-1}) and the hail mass flux began a broad maximum (around 3 $\times$ 10^5 kg s^{-1}) which lasted until 1830 MDT during the collapse of a high reflectivity convective core (see Figs. 3.7 and 3.10). The hail rate increased with the IC flash rate and both reached a maximum value around 1810 MDT of 35.5 mm h^{-1} and 16.6 flashes min^{-1}. Of course, the IC flash rate for supercell #1 may have continued to increase since the total flash rate for supercell #1 and #2 combined eventually reached a maximum near 55 flashes min^{-1} around 1850 MDT (see Fig. 3.11a). As shown in Fig. 3.6, the peak hail rate began to decrease after 1810 MDT and the hail mass flux also declined significantly after 1830 MDT. At the same time, the positive CG flash rate was at its maximum for supercell #1 as seen in Fig. 3.5. So, the hail rate and positive CG flash rate appear anti-correlated in the later half of this lifecycle. This temporal pattern seems to suggest that enhancement of the IC lightning flash rate and the initial production of positive CG lightning was associated with an intense pulse in cell development. However, the broad peak in the positive CG flash rate appears to occur during a peak in the rain mass flux and just after a peak in the hail mass flux at the surface associated with the collapse of this pulsing cell.

To explore this idea further, a time-height cross section of hail echo volume[1] (km^3) from 1740 MDT to 1855 MDT is depicted in Fig. 3.7. Essentially, this plot tracks the hail volume aloft at each vertical level above the freezing level using criteria 6 from Table A.1. Fig. 3.7 also shows the evolution of the associated surface area of the large hail swath at the surface (using category 3 and 4 from Table A.1 at the lowest grid level z = 0.5 km

[1] The hail echo volume at each vertical level is calculated by multiplying the number (N) of grid points at each given grid level which satisfy criteria 6 (Table A.1) by the volume of an individual grid point (i.e., N • surface area • vertical depth = N • 0.125 km^3).

AGL). First, it is important to notice the temporal consistency between the amount of hail production aloft and the surface area of large hail reaching the ground. Hail aloft inferred from multiparameter radar first appears between -10° and 0° C at 1745 MDT followed by the first large hail falling to the ground at 1750 MDT. Between 1745 and 1805 MDT, there is a surge in the amount of hail being produced aloft, accompanied by a rapid increase in the descent of large hail to the surface. The hail production aloft peaks around 1805 MDT at all levels in the mixed phase zone (0 to -40° C) with peak values of 10 - 12 km^3 (between 0 and -14° C). Peak hail production aloft is quickly followed by a peak in the surface area coverage of large hail of 18.2 km^2 by 1810 MDT associated with the collapsing convective cell. As expected, the amount of large hail at the surface then begins to decrease from 1810 MDT to 1835 MDT as the quantity of hail above the freezing level begins to decrease and descend in altitude. This storm wide evolution of large hail is also consistent with surface reports compiled from two chase vans that were directly in the path of the supercell (see Sec. 3.2).

Comparing the trends in the IC and CG lightning given in Fig. 3.5 to those of hail in Fig. 3.7, we find that the initial occurrence of large hail aloft precedes the first positive CG lightning flash by less than five minutes. The rapid increase in the IC flash rate from 1750 to 1810 MDT is coincident with the accelerated growth of hail in the entire mixed phase region and then the subsequent descent of large hail to the surface during cell collapse. Interestingly, the broad maxima in the positive CG flash rate which occurs between 1835 and 1900 MDT appears to be associated with a broad *minima* in both the amount of hail production aloft and the amount of large hail at the surface. Essentially, most of the large hail has already fallen out of the storm when the positive CG lightning begins its broad maximum during cell collapse. Although the first occurrence of positive CG lightning is associated with the initial production of large hail aloft, the temporal trends in the amount of large hail and positive CG lightning appear to be *anti-correlated*. However, both phenomena do appear to be indirectly related via the process of *convective cell collapse*.

With an understanding of the temporal relationship between large hail and positive CG lightning for supercell #1, we now turn our attention to the spatial relationship between the two phenomenon. To explore this spatial correlation, a representation of the

multiparameter radar inferred hail swath and the overlaid CG lightning ground strike locations is given in Fig. 3.8. Areas of small hail (criteria 1 and 2, Table A.1) and large hail (criteria 3 and 4, Table A.1) are depicted regardless of whether they are mixed with rain. Note the two small circles representing the chase vans at the following (x, y) coordinates: (-10.5 km, -15.8 km) and (-13 km, -22 km). Both vans were in the multiparameter radar inferred large hail swath and both vans reported hail from 2 - 5 cm in diameter. As can be seen in Fig. 3.8, the positive flash ground strike locations tended to lie outside regions of hail, especially large hail. The large majority (73%) of the flashes occurred downstream of the hail shaft, toward the northeast. This area is dominated by light to moderate rain rates (< 60 mm h^{-1}) and is beneath the downshear anvil adjacent to the main precipitation shaft. In summary, the temporal and spatial behavior of large hail and positive CG lightning for supercell #1 appear to be *anti-correlated*.

Next, we investigate the gross electrostatic structure of supercell #1 as revealed by ground based (5 m AGL) corona point measurements. In order to obtain measurements directly beneath the supercell thunderstorm, a mobile corona point sensor was placed in the direct path of the oncoming storm (reference Figs. 1.1 and 3.2 for the location relative to the storm). Point discharge measurements were obtained during a very opportune time (1748 MDT to 1848 MDT) to study trends in the surface electric field associated with hail production, enhanced IC flash rates, and a predominance of positive CG lightning. In Fig. 3.9, the dark trace is a plot of the 1 Hz point discharge current and the lighter trace is a smoothed version of the current (33 point moving filter). From the 1 Hz data, a copious amount of lightning transients can be seen, especially from 900 seconds (1803 MDT) and onward, which is consistent with the rapid increase in the flat plate measured total flash rate (e.g., Fig. 3.5). The transients are directed both upward (suggesting net negative charge aloft neutralized) and downward (suggesting net positive charge aloft neutralized). However, the strongest transients which saturated the data logger between 2400 and 3000 seconds (1828-1838 MDT) are downward directed. The smoothed corona point current gives an idea of the relative strength and polarity of the net electrostatic field aloft. There appears to be four phases in the trend of the smoothed current. From 0 to 600 seconds (1748-1758 MDT), the corona current was positive (0-2 μA) which suggests a net fair

field aloft of moderate magnitude (i.e., that is net positive charge aloft). In the second phase (600-1200 seconds or 1758-1808 MDT), the negative point discharge current varied between 0 and -2 μA indicating a net foul field aloft of moderate magnitude (i.e., that is net negative charge aloft). During the third phase from 1200 to 2100 seconds (1808-1823 MDT), the current was very weakly negative, suggesting a negligible net foul field aloft (probably near the minimum E-field threshold for the on-set of corona current around ±1 kV m^{-1}). The fourth and final phase was characterized by moderately strong positive corona current (over 3 μA) from 1823 MDT to about 1845 MDT (2100-3300 seconds) suggesting a net fair field aloft of moderate magnitude. The corona current values in all but the third phase are of similar magnitude to those beneath non-severe thunderstorms (e.g., Carey and Rutledge, 1996; Williams et al., 1989a,b).

To place these point discharge measurements in the context of storm precipitation structure, a time-height cross-section of reflectivity (color shaded) and LDR (contoured) directly above the corona point sensor is shown in Fig. 3.10 for the same times as the corona point data. As can be inferred from the values of Z_h and LDR, small hail (sometimes mixed with heavy rain) fell at the corona point site from about 1808 to 1810 MDT and then from 1825 to 1834 MDT. From about 1810 to 1825 MDT, large hail (sometimes mixed with heavy rain) came down over the sensor. These radar inferred precipitation types are well supported by notes taken in the field. The time-height cross-section suggests that a combination of advection and discrete growth or dissipation occurred over the corona point. Two tilted hail shafts passed over the radar: 1) 1755-1810 MDT which produced mostly small hail and rain and, 2) 1810-1825 MDT which produced large hail. It is possible to discern that the cores were tilted toward the northeast (downshear) because the reflectivity and LDR cores are slanted with height with maximum reflectivity values occurring at higher altitudes first in time.

Comparing the corona point data (Fig. 3.9) and radar time-height cross-section (Fig. 3.10), one can deduce that the arrival of the first tilted (i.e., in the downshear direction) precipitation shaft with large reflectivities aloft (i.e., the forward overhang as seen in Fig. 3.3) was associated with a net fair field at the surface indicating positive charge aloft. When the main precipitation shaft containing small hail and rain was overhead (around

1803 MDT), the corona point current indicates net foul field aloft (negative charge). When the second surge in reflectivity and LDR occurred associated with an increase in the amount of large hail overhead (likely through a combination of production and advection), the E-field aloft appears to be weakly foul. Finally, as the supercell moves slowly toward the ENE and the large hail falls out of the collapsing convective core, the field reverses polarity to fair values (i.e., net positive charge aloft) associated with the passage of the reflectivity gradient region beneath the initial portion of the upshear anvil.

With the analyses of supercell #1 complete, we now attempt to demonstrate that the temporal and spatial relationships established between electrical behavior and precipitation structure are actually valid for the entire severe storm complex observed on the afternoon of 7 June 1995.

3.4. Electrical Characteristics Associated with a Severe Hail Storm Complex

In the section above, we demonstrated that for an isolated supercell 1) the IC lightning flash rate is enhanced during vigorous storm development, 2) the positive CG lightning also begins during an intense pulse in storm development, and 3) the positive CG flash rate peaks long after most large hail has fallen out of the storm, just after a peak in the hail mass flux (associated primarily with *small*, D < 2 cm, hail), and during a broad peak in the rain mass flux associated with cell collapse. This behavior results in a strong anti-correlation in time and space between positive cloud-to-ground lightning and large hail for supercell #1. We now wish to determine if these relationships are valid for the entire history of this severe hailstorm complex (including supercell #2 and the merged supercell #1 and #2 at later times). First, we present (Fig. 3.11a) the entire lightning history of the 7 June 95 severe hailstorm complex from 1731 MDT to 2050 MDT while it was within about 60 km of the CSU-CHILL radar. The negative and positive CG lightning flash rate, the IC lightning flash rate, and the IC/CG ratio is included for all cells shown in Figs 3.2a-i.

The positive CG flash rate has two broad maxima from 1836 to 1905 MDT and 1946 to 2009 MDT. There are also two secondary maxima in the positive CG flash rate at 2026 and 2038 MDT. The first broad maxima is associated primarily with supercell #1 but also

has a contribution from supercell #2, especially before 1830 MDT. The highest positive CG flash rate (six minute average) is 2.7 min^{-1}, occurs in the second maxima at 1946 MDT, and is associated with the storm complex which results from the merger between supercell #1 and #2. Although the positive CG flash rate exceeds the negative CG flash rate during the entire 3.3 hour period, the percentage of negative ground flashes increases towards the end of the period (i.e., after 2015 MDT) as the storm begins to take on the characteristics of a severe, multicell squall line.

Before 1748 MDT when both supercell #1 and supercell #2 were in the developing phase, the ground strike polarity was predominantly negative. In addition, the IC flash rate for the cells within range was relatively small (< 5 min^{-1}) and hence the IC/CG ratio had values between 5 and 10 which are just slightly larger then those measured for typical warm season thunderstorms (e.g., Prentice and Mackerras, 1977; Price and Rind, 1993). When both supercell #1 and #2 began to explosively develop around 1748 MDT, the predominant polarity for both storms switched to positive and the IC/CG ratio immediately ramped up to values greater than 20 as the IC flash rate increased from 5 min^{-1} at 1748 MDT to 55 min^{-1} by 1847 MDT when the flat plate became saturated by heavy rain.

For comparison with the lightning data, Fig. 3.11b depicts the evolution of the surface coverage of large hail (km^2), and the rain and hail mass fluxes for all cells. A comparison of Figs. 3.11a,b reveals that all of the positive CG lightning flash rate maxima are associated with rapid increases and subsequent peaks in both the rain and hail mass fluxes associated with collapsing cells. Associated with these descending echo cores, there were two broad maxima in the descent of large hail to the surface from 1806 to 1830 MDT and from 1905 to 1928 MDT. In addition, there were two small relative maxima at 2003 and 2021 respectively. By closely comparing the trend of the positive CG lightning (Fig. 3.11a) and that of large hail in Fig. 3.11b, it is apparent that the two phenomena are anti-correlated in time (correlation coefficient = -0.23). The two broad maxima in the surface coverage of large hail are followed by two extended peaks in the positive CG flash rate. These relationships are summarized in Table 3.1. Detailed analyses of the multiparameter

radar data reveals that very few (< 5%) positive CG ground strike locations coincide with large hail at the surface (cf. Fig. 3.8).

Table 3.1. Temporal relationships between large hail and positive CG lightning maxima.

Large Hail Maxima	Positive CG Lightning Maxima
1. 1806 - 1830 MDT	1. 1836 - 1905 MDT
2. 1905 - 1928 MDT	2. 1946 - 2009 MDT
3. 2003 MDT	3. 2027 MDT
4. 2021 MDT	4. 2038 MDT

To further investigate the spatial relationship between positive CG lightning and storm structure, we present frequency and cumulative percentage histograms of 1) rain and hail rates which occurred at each of the 184 positive CG ground strike locations (R, H), and 2) *maximum* rain and hail rate which occurred within 10 km of all the positive ground strokes (R_{max}, H_{max}). The rain (R) and maximum rain (R_{max}) rates are depicted in Fig. 3.12a while the hail (H) and maximum hail (H_{max}) rates are depicted in Fig. 3.12b. Considering the widespread nature of heavy rain and hail which each separately had a peak surface area coverage of about 200 km^2 in this storm complex, the results are quite striking.

As can be seen in Fig. 3.12a, the majority (54%) of positive cloud-to-ground flashes were situated in regions of light rain ($\leq$ 20 mm h^{-1}) while 28% of flashes occurred in moderate rain (20 - 60 mm h^{-1}), and only 18% in heavy rain ($\geq$ 60 mm h^{-1}). By comparison, only 34% of negative cloud-to-ground lightning occurred in light rain during the same period while 46% were collocated with regions of moderate rain (not shown). The distribution for the peak rain rate within 10 km is very flat with relative maxima at 10, 100, 130, 150, and 180 mm h^{-1}, suggesting that many positive ground strokes are within a convective scale distance (10 km) of a sometimes intense precipitation shaft.

Similar analyses were accomplished for both hail rates (H) at the ground strike location and maximum hail rates (H_{max}) within 10 km of the positive ground strike and similar results as above were obtained as shown in Fig. 3.12b. Only a surprising 14% of positive CG flashes struck ground in precipitation with significant hail rates (i.e., $\geq$ 2 mm h^{-1}). On the other hand, the rather flat histogram for the maximum hail rate demonstrates that a majority (58%) of the positive CG flashes occurred within a convective scale

distance from a hail shaft. Approximately 29% of the time, the hail shaft is quite intense with hail rates in excess of 20 mm h^{-1}.

Having demonstrated that the patterns of behavior revealed in Sec. 3.3 for an isolated supercell storm appear to apply to the storm complex as a whole, we now show that an individual cell within the multicell severe hailstorm that resulted from the merging of two supercell storms (see Sec. 3.2) also exhibited similar relationships between precipitation and lightning.

3.5. An Intense Positive Cloud-to-Ground Lightning Cluster

Observations of an intense positive CG cluster associated with a streak of large hail embedded within a larger hail swath are given in Figs. 3.13a,b. This cluster occurred from 1943 MDT to 2001 MDT during the period of peak positive CG flash rates for the entire storm history (c.f., Fig. 3.11a). During this 18 minute period, the average positive (negative) CG flash rate was about 1.5 (0.2) min^{-1}. The positive CG peak current ranged widely from 14 kA to 103 kA with a mean value of 38 kA. Inspection of the horizontal cross-section of reflectivity (shaded) and K_{dp} derived rain rate (contoured, Fig. 3.13a) reveals that the majority of positive CG flashes struck ground adjacent to and on the left flank of the heavy precipitation (and maximum reflectivity) core centered at x = 25 km and y = 4 km. It is interesting to note that 54% of the positive flashes and 25% of the negative flashes come to ground in light rain but within 10 km of heavy precipitation, consistent with the results given in Fig. 3.12a. Notice the bipole pattern in the ground strike locations with negative CG flashes coincident with the heaviest rain and the center of the positive CG cluster occurring about 8 km to the NNW in light to moderate rain.

The vertical cross-section of Z_h and K_{dp} (Fig. 3.13b) through the positive CG cluster at x = 28 km depicted in Fig. 3.13a provides a revealing perspective of storm structure relative to CG ground strike locations. First, notice the tilt of the reflectivity contours with altitude away from the main precipitation shaft at y = 4 km. The core tilts toward the north by 4 to 10 km between the -30° C to -40° C level (6.5 to 7.7 km AGL). Also, note that the positive CG cluster occurs directly beneath this tilted core (see y = 8 - 18 km). A similar phenomena is occurring on the opposite end for the complex around y = -7 km.

Observations of K_{dp} and Z_h clearly indicate that the negative polarity CG lightning is occurring in the heaviest rain while the positive CG flashes are occurring along the edge of the heaviest precipitation and beneath the tilting core aloft similar to the findings of Rust et al. (1981a,b). Even more dramatic are the negative values of K_{dp} found at the -40° C level at the tops of the tilted precipitation echoes (see y = 8 - 15 km and y = -8 km).

These specific differential phase shifts of up to -0.6° km^{-1} are consistent with the orientation of ice crystals in a strong electric field such that a significant component of the major axis is in the vertical, as per the findings of Caylor and Chandrasekar (1996). (See Appendix A for more details). These negative values of K_{dp} persisted for at least 15 minutes from 1943 to 1958 MDT (period of highest positive CG flash rate) in an irregularly shaped disk with an area of about 50 km^2 almost directly above the positive CG cluster. Furthermore, the surface area of the positive CG cluster was only slightly larger than the area of the negative K_{dp} region aloft.

The temporal trend of the CG lightning and precipitation field for the northern most convective cell depicted in the cross-sections of Figs. 3.13a,b at 1952 MDT (centered on x = 28 km and y = 5 km) is given in Fig. 3.14. The evolution of the positive and negative CG lightning flash rate is compared to the amount of rain, small hail, and large hail at the surface and the amount of vertically oriented[2] ice crystals aloft. A pattern is revealed that actually repeats itself several times over in the severe hailstorms of 7 June 1995. First, note that the positive CG flash rate is increasing from 1938 - 1957 MDT while the negative CG flash rate is already decreasing toward zero. Next, the maximum number of negative CG flashes immediately follows the peak in large hail and is coincident with the maxima in rain rate and small hail at the surface, consistent with the findings of Carey and Rutledge (1996) for non-severe thunderstorms. The correlation between negative CG lightning and the area average rain rate is very high ($\rho = 0.93$). The maximum number of positive CG flashes lags the peak in large hail by 24 minutes, small hail by 19 minutes, and a pulse in heavy rain centered at x = 25 km and y = 4 km (Fig. 3.13a) by about 5 minutes.

[2] By "vertically oriented," we strictly mean that the component of the major axis in the vertical must exceed 50%. See Appendix A for more details.

Apparently, positive CG lightning is one of the final acts of a severe convective cell undergoing dissipation and eventual collapse.

In Fig. 3.15, a time-height cross-section of hail echo volume (similar to Fig. 3.7) for this convective cell is compared to a trace of the positive CG lightning flash rate. From this depiction, it is obvious that the positive CG flash rate rapidly increases *following* the rapid growth and subsequent descent of hail in a collapsing convective core. By analyzing the behavior of this individual hail swath and positive CG cluster, the anti-correlation between large hail and positive CG lightning is much more significant (ρ = -0.85). A similar temporal anti-correlation between small hail and positive CG lightning exists as well (Fig. 3.14). Lastly, note that the trend in the amount of vertically aligned ice crystals aloft closely follows the trend in the positive CG lightning (ρ = 0.75) as seen in Fig. 3.14. The quantity of vertically oriented ice aloft peaks just 5 minutes prior to the peak in the positive CG flash rate. Correlation coefficients between the CG lightning and the precipitation amounts are summarized in Table 3.2.

Table 3.2. Correlation coefficients between precipitation and CG lightning.

CG type	*Large Hail*	*Small Hail*	*Rain*	*Vertical Ice Crystal*
+ CG	**-0.85**	**-0.86**	0.17	**0.75**
- CG	-0.44	0.32	**0.93**	0.61

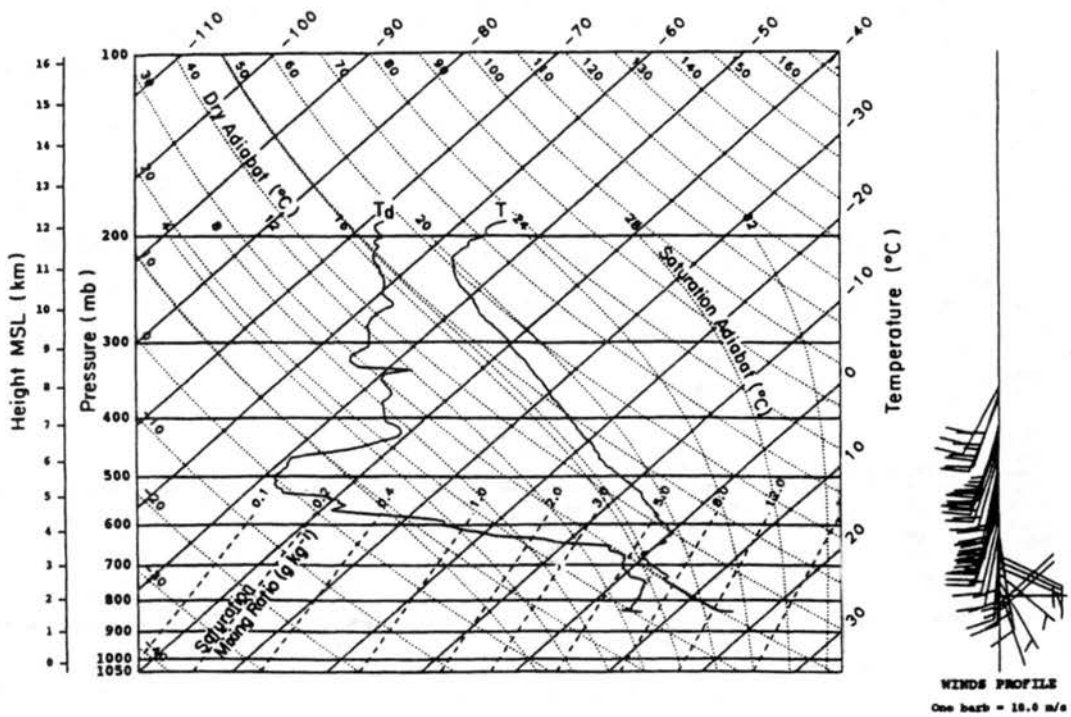

Figure 3.1. Skew T-Log P plot of Denver, Colorado radiosonde data from 1114 MDT (1714 UTC) on 7 June 1995. Both temperature and dewpoint temperature are given in degrees Celsius. Wind data, which terminated at 360 mb, is given in m s^{-1} (1 barb = 10 m s^{-1}).

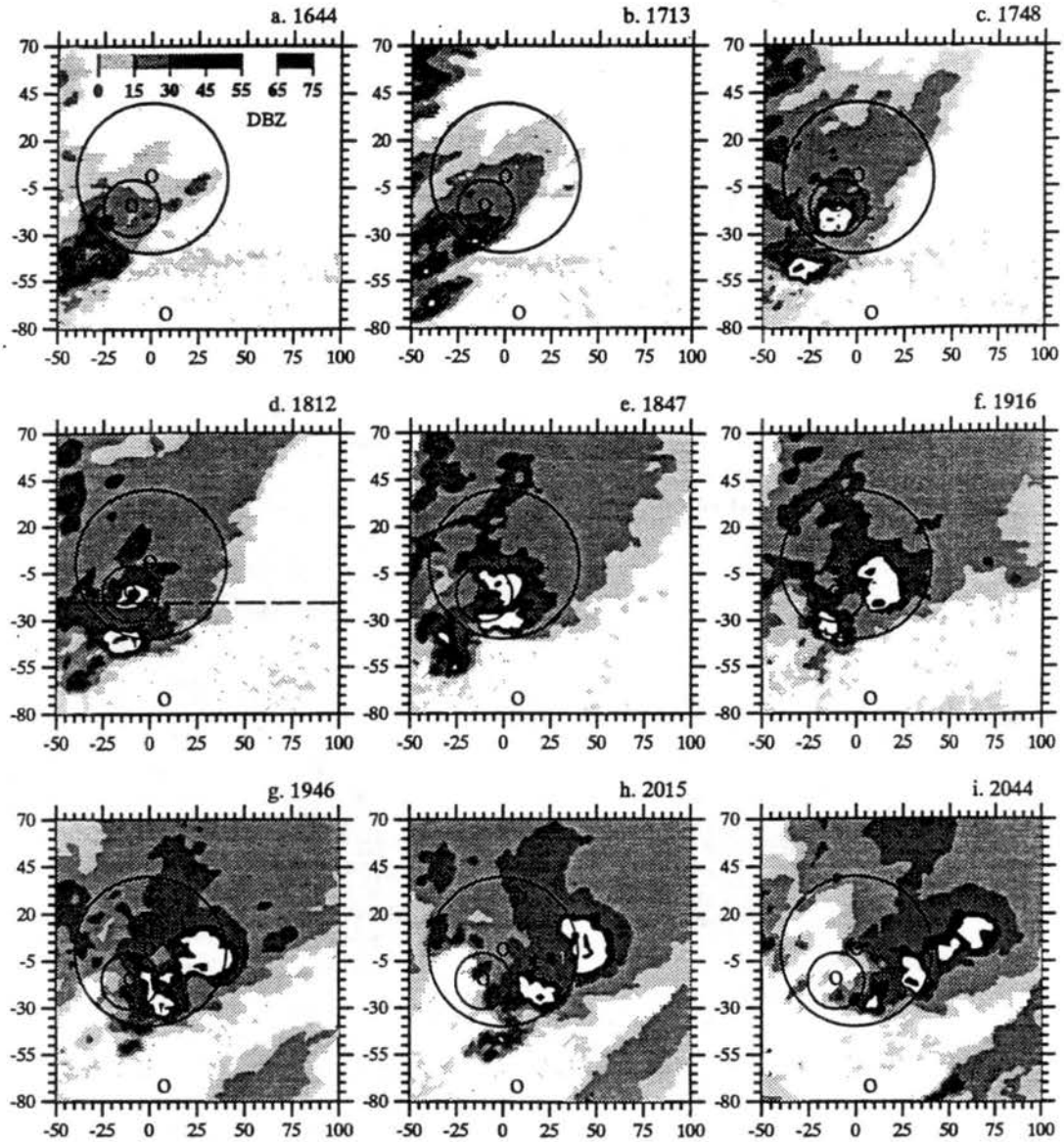

Figure 3.2. Two dimensional maximum reflectivity composite computed from Denver WSR-88D radar data. The horizontal (vertical) axis represents east-west (north-south) distance in km from the CSU-CHILL radar at (0,0). The location of the CSU-CHILL radar, Denver WSR-88D radar (7.8, -73.2), and the mobile corona point sensor (-10.6, -15.8) are marked by a '**O**'. The large ring centered on the CSU-CHILL radar represents the 40 km maximum range of the flat plate antenna. The 15 km circle centered on the corona point sensor indicates its operational range. Results at (a) 1644 (all times MDT). (b) 1713. (c) 1748. (d) 1812 (dashed line at y = -20.5 km represents the plane of the vertical cross-section in Fig. 3.3. (e) 1847. (f) 1916. (g) 1946. (h) 2015. (i) 2044. The reflectivity key for all parts (a) - (i) is located in part (a).

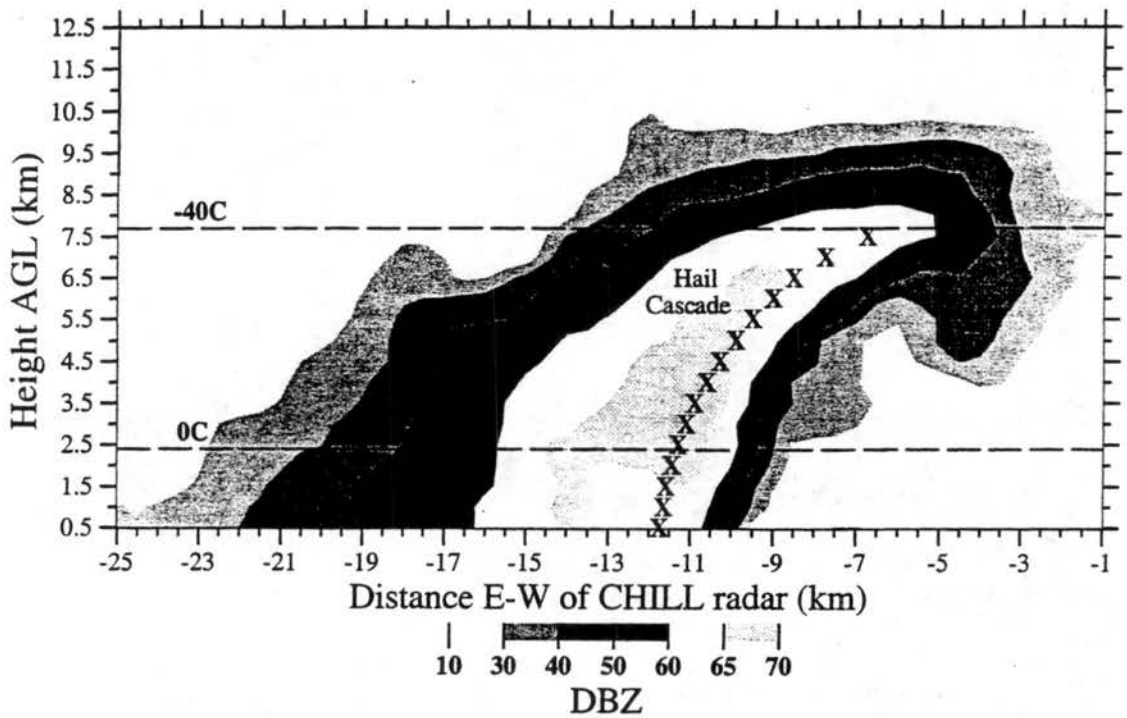

Figure 3.3. East-west vertical cross-section of CSU-CHILL horizontal reflectivity (dBZ) at y = -20.5 km (see Fig. 3.2d). Note the forward overhang and bounded weak-echo region (BWER) from x =-7 km to x = -3 km. The path of the hail cascade which is analyzed in Figs. 3.4a,b is marked by X's.

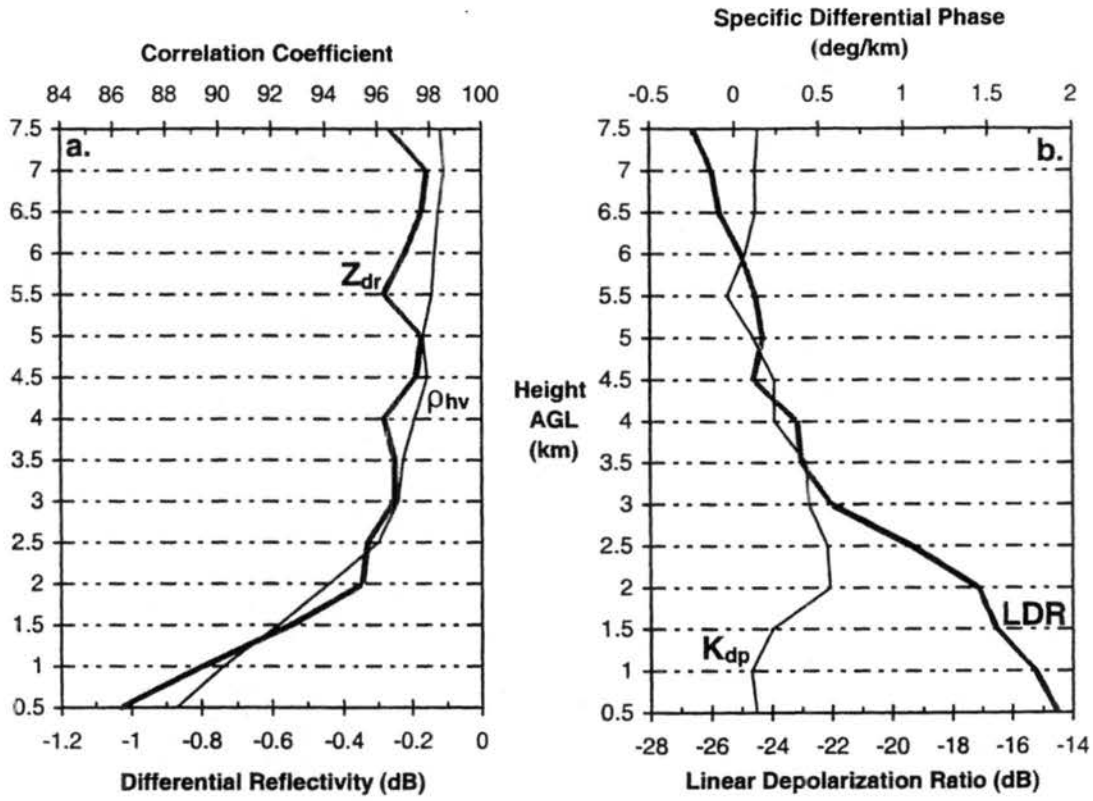

Figure 3.4. Vertical profile of CSU-CHILL multiparameter radar variables through the hail cascade depicted in Fig. 3.3. The melting level is at 2.4 km AGL. (a) The correlation coefficient (ρ_{hv}) and differential reflectivity (Z_{dr}, dB). (b) The specific differential phase (K_{dp}, ° km^{-1}) and linear depolarization ratio (LDR, dB).

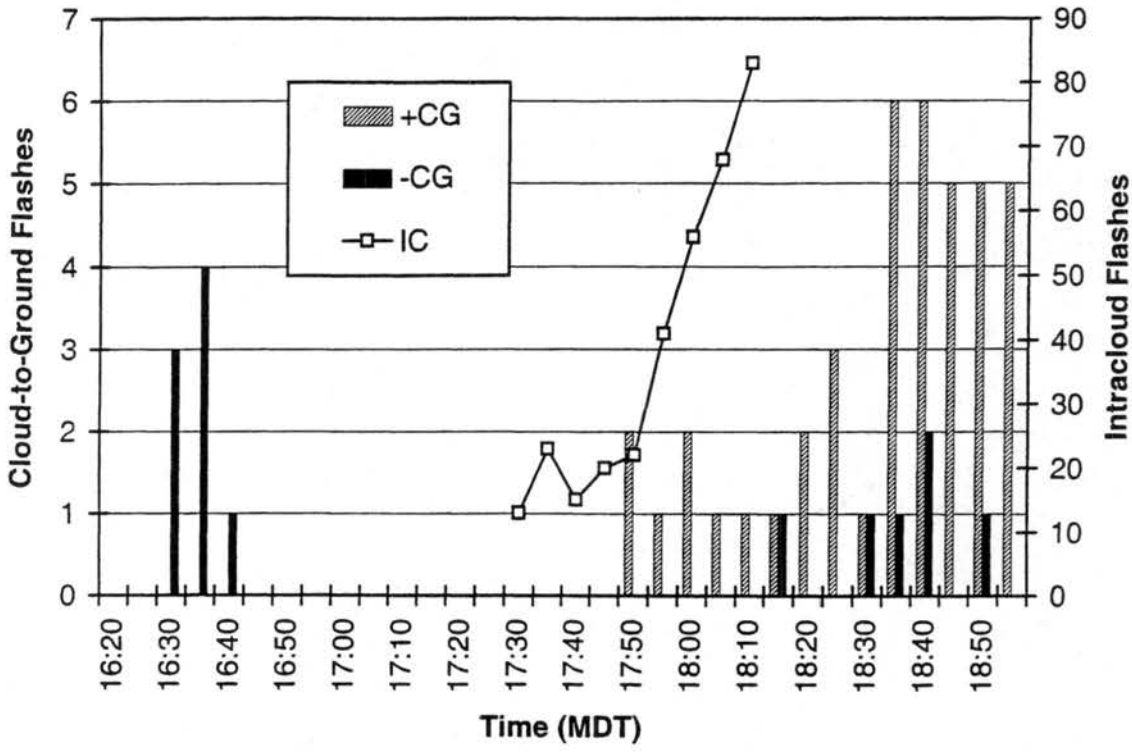

Figure 3.5. Evolution of the number of intracloud (IC), positive cloud-to-ground (+ CG), and negative cloud-to-ground (- CG) lightning per five minute period for supercell #1 from 1620 - 1900 MDT. An estimate of the IC lightning flash rate was only available from 1730 - 1815 MDT (see text for explanation).

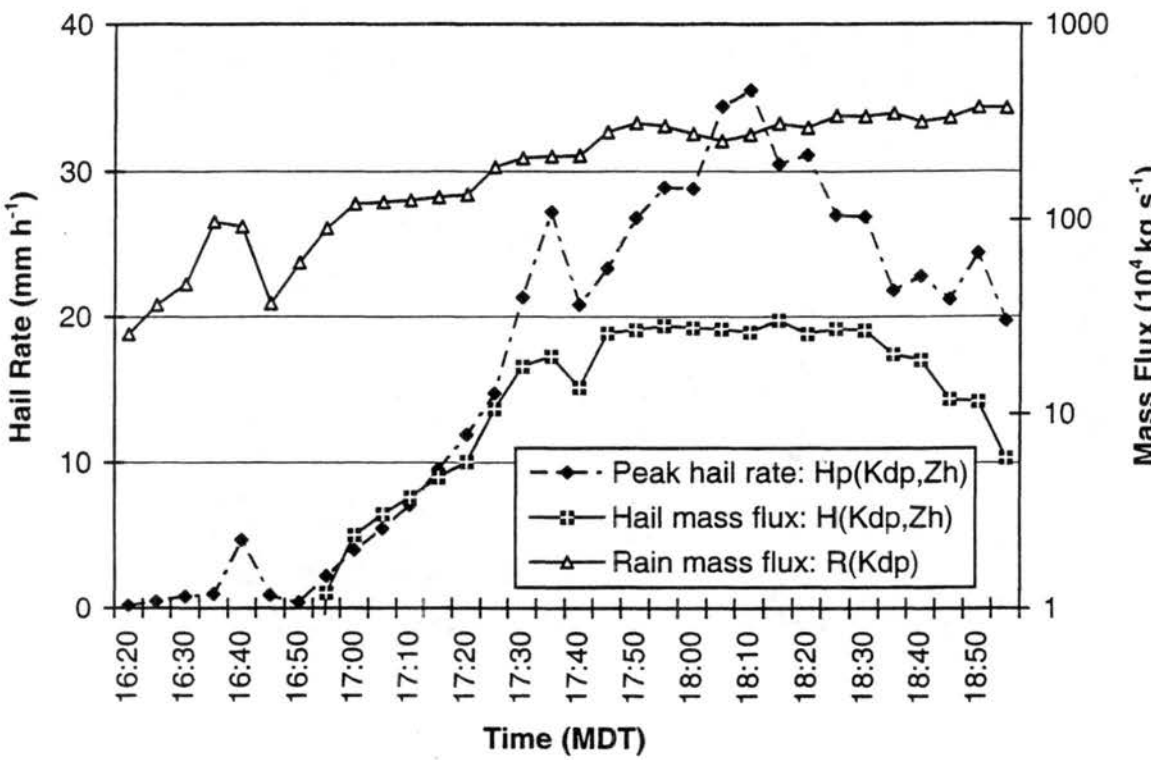

Figure 3.6. Temporal trend of the peak hail rate, in mm h^{-1}, and the hail and rain mass fluxes with units of 10^4 kg s^{-1} for supercell #1 from 1620 - 1900 MDT.

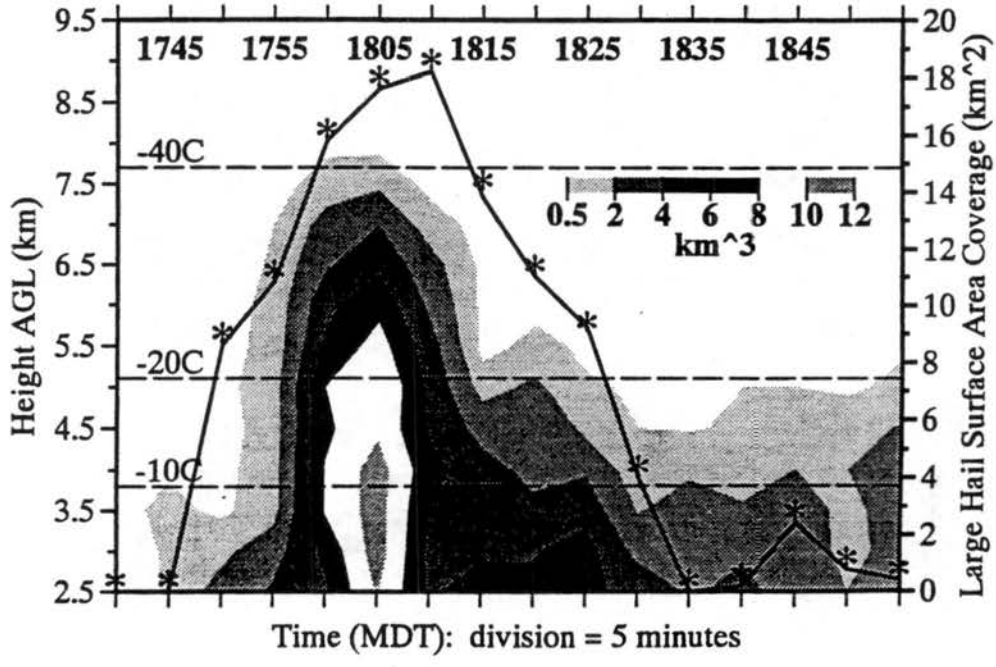

Figure 3.7. Time-height cross-section of the multiparameter radar inferred hail echo volume (shaded; km^3) above the freezing level at each vertical level in supercell #1 from 1740-1900 MDT. Superimposed on the time-height cross-section is the temporal evolution of the areal extent of the hailswath at the ground caused by the descent of *large* hail (solid line with '*' marks; km^2) during the same time period.

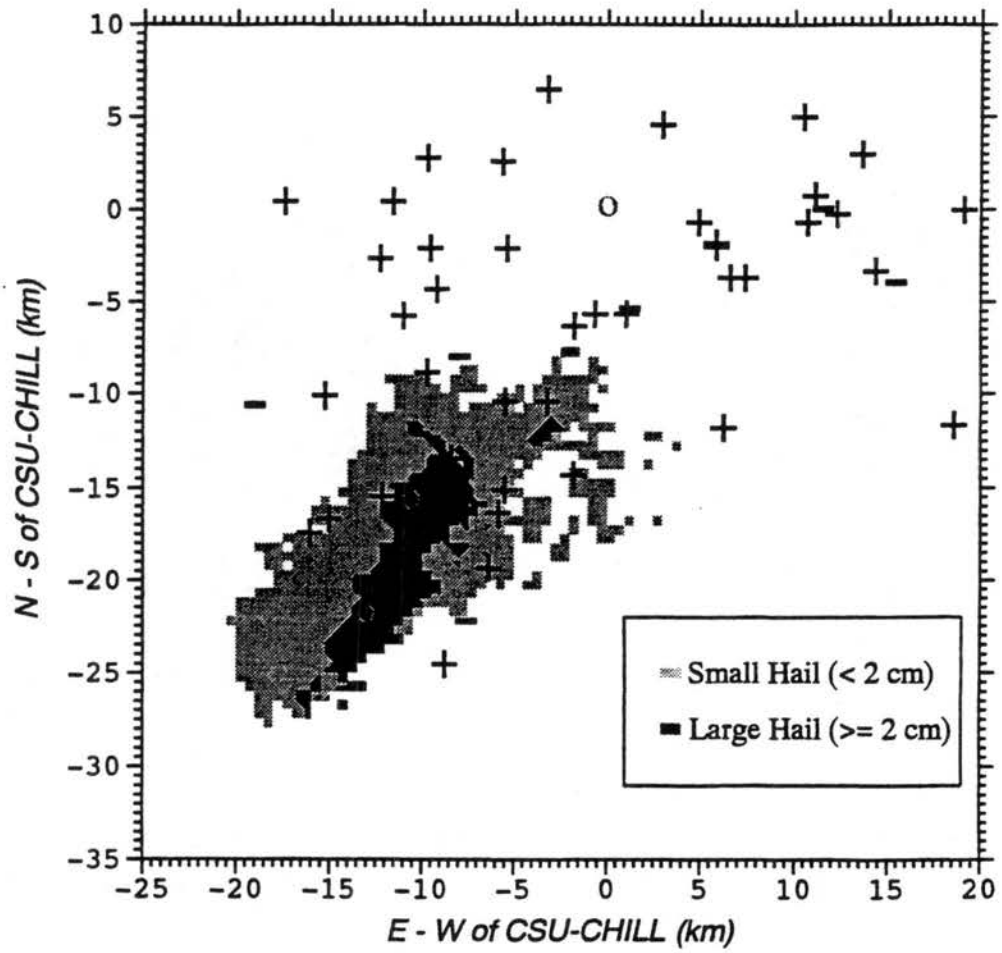

Figure 3.8. Depiction of the multiparameter radar inferred hail swath (both small, < 2 cm, and large, ≥ 2 cm, hail) from 1740 - 1900 MDT for supercell #1. Lightning ground strike locations are overlaid on the hail swath (+: positive polarity, and -: negative polarity). Location of the CSU-CHILL radar (0,0), hail chase van (-13, -22), and mobile corona point van (-10.6, -15.8) are marked by **O**'s. Note that both vans are within the large hail streak embedded in the center of the hail swath.

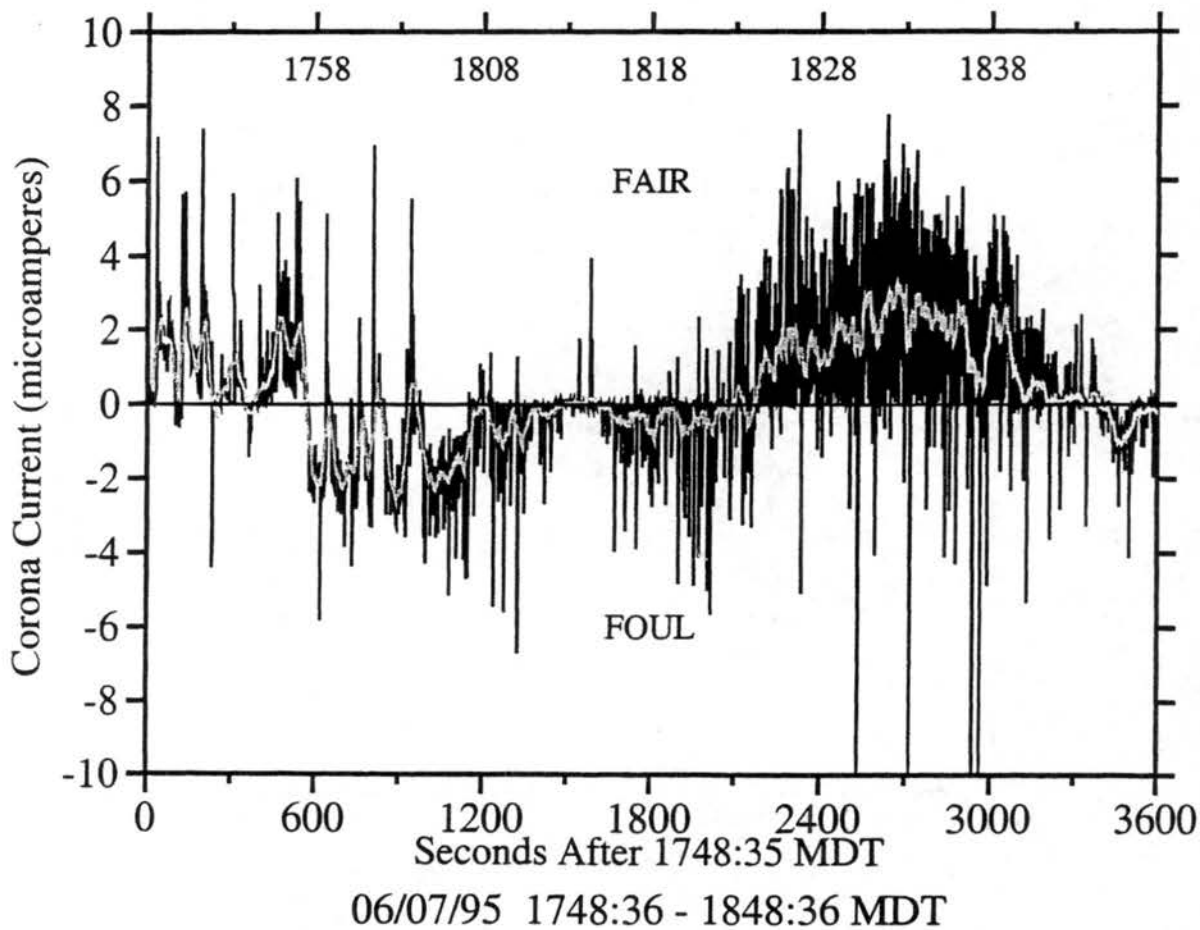

Figure 3.9. Evolution of the corona current (μA) beneath supercell #1 from 1748 - 1848 MDT. The dark trace depicts the 1 Hz corona point current and the light trace is a smoothed (33 point running mean filter) version of the corona point current. Each horizontal division represents five minutes. Negative corona current indicates a foul field (or net negative charge aloft) and positive corona current indicates a fair field (or net positive charge aloft).

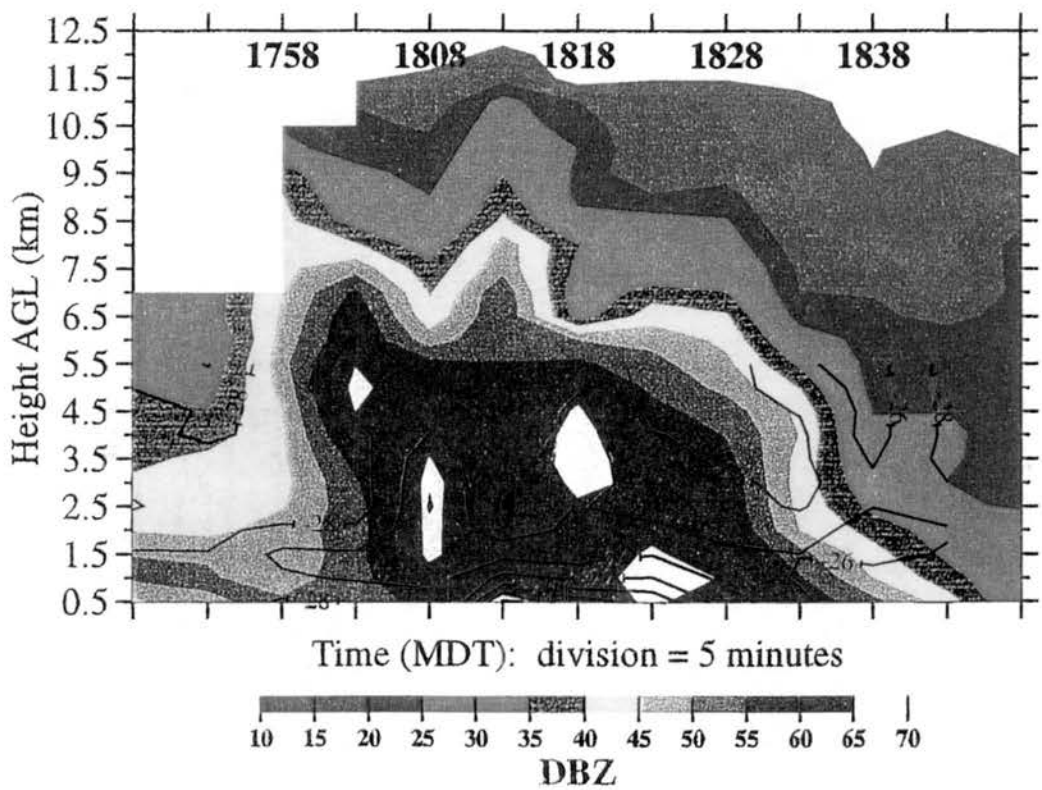

Figure 3.10. Time-height cross-section of reflectivity (color shaded, dBZ) and the linear depolarization ratio (contoured every 2 dB starting at -28 dB) for supercell #1 directly above the mobile corona point sensor from 1748 - 1848 MDT. Each horizontal division represents five minutes and can be directly compared to the corona point current shown in Fig. 3.9.

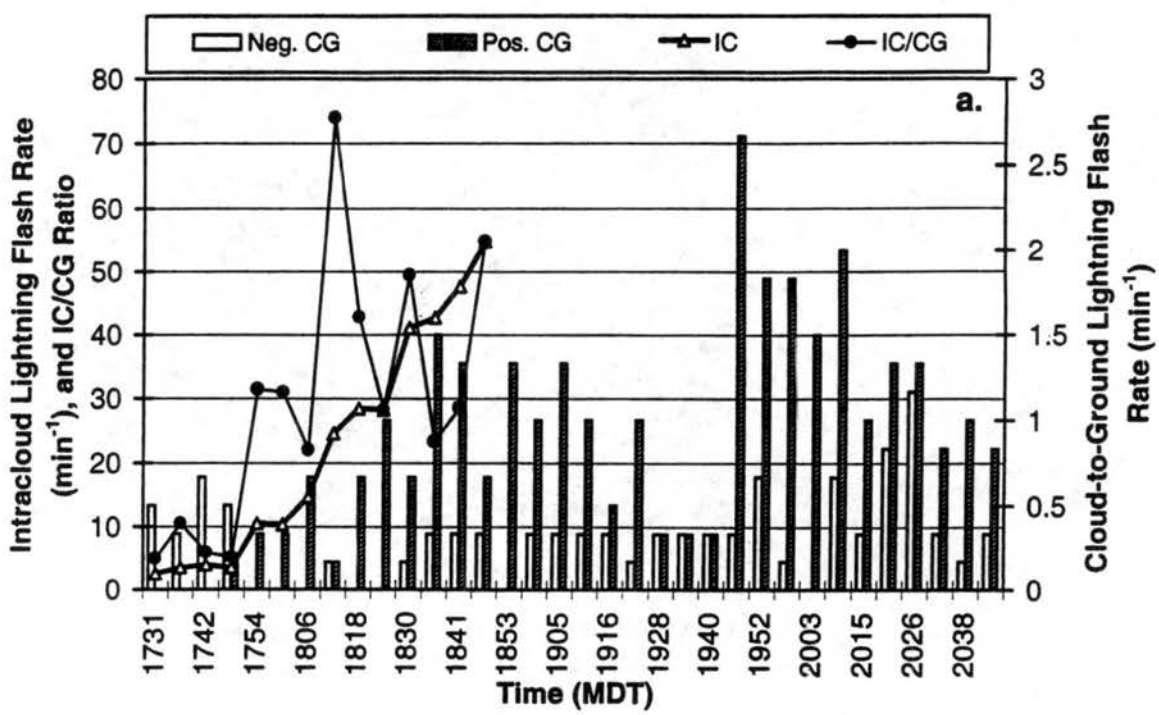

Figure 3.11. Temporal evolution of the lightning and precipitation rates in the 7 June 1995 storm complex depicted in Figs. 3.2a-i from 1731 - 2050 MDT.. (a) negative and positive cloud-to-ground (CG) flash rate (# min^{-1}), intracloud lightning flash rate (# min^{-1}), and IC/CG ratio.

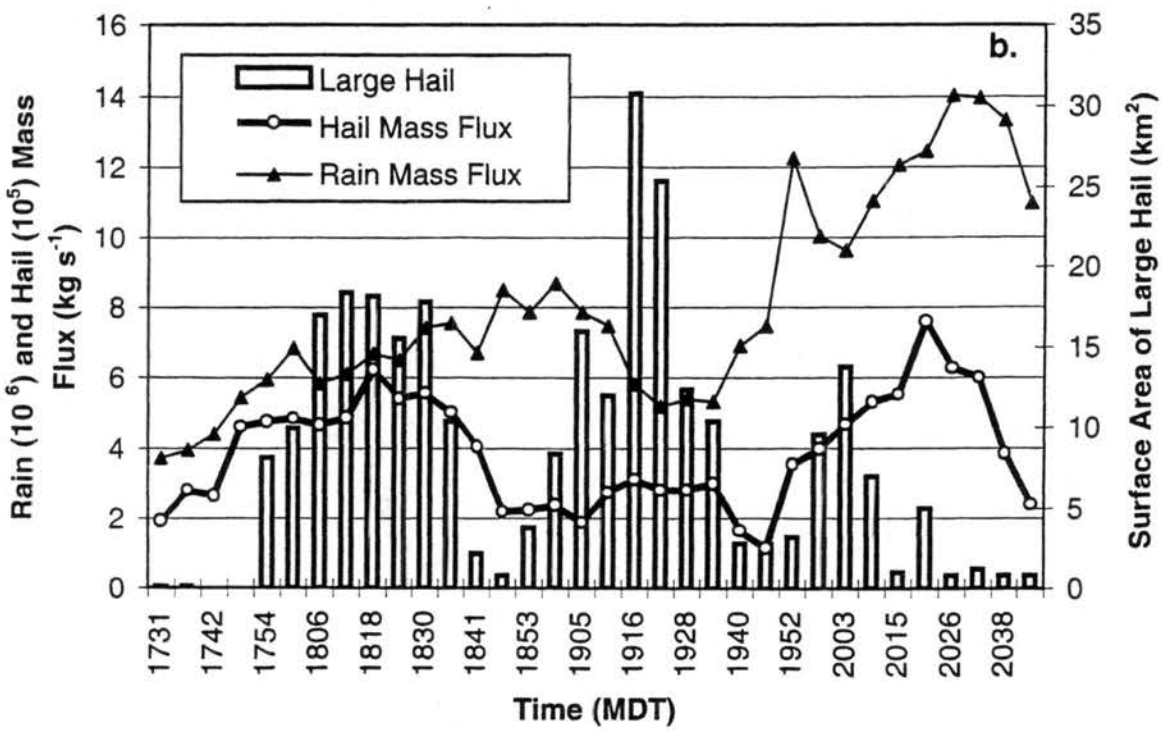

Figure 3.11. (b) as in (a) but rain mass flux (10^6 kg s^{-1}), hail mass flux (10^5 kg s^{-1}), and the surface coverage of large hail (km^2).

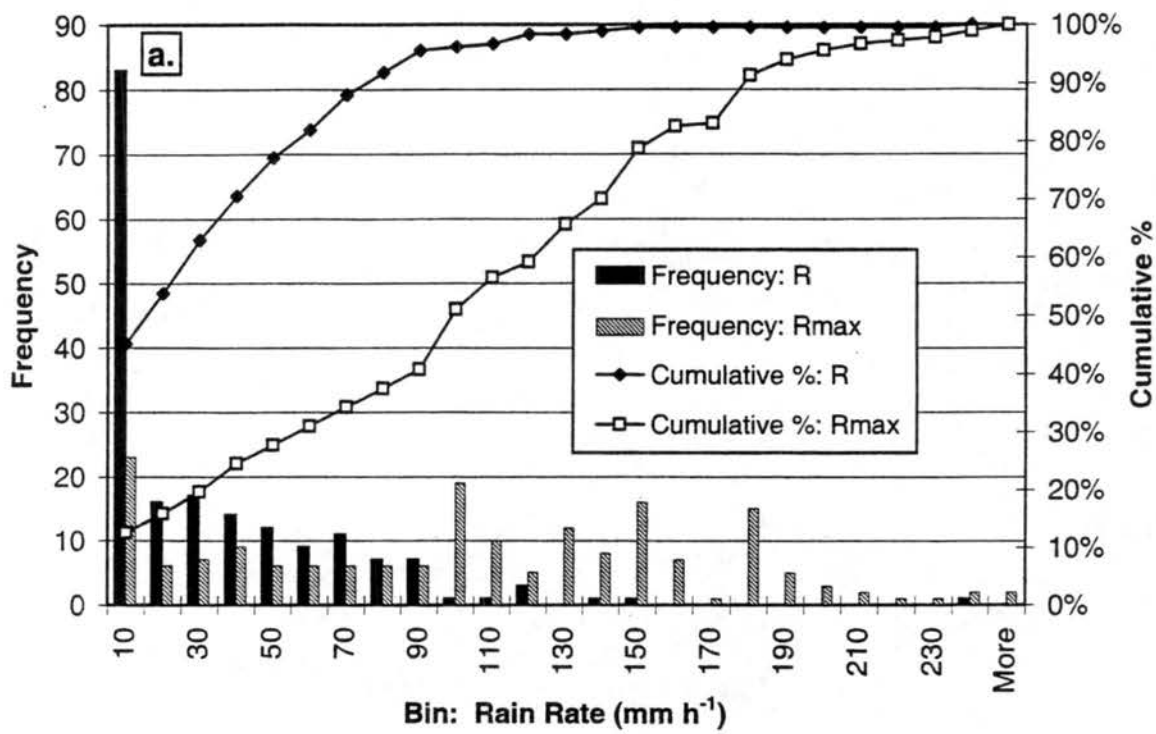

Figure 3.12. Frequency and cumulative percentage histograms of the precipitation rate ($mm\,h^{-1}$) occurring at all positive ground strike locations (sample size is 184 positive CG's) and of the *maximum* precipitation rate within 10 km of each positive ground strike location from 1748 to 2048 MDT. (a) Rain rate (R) and maximum rain rate (R_{max}).

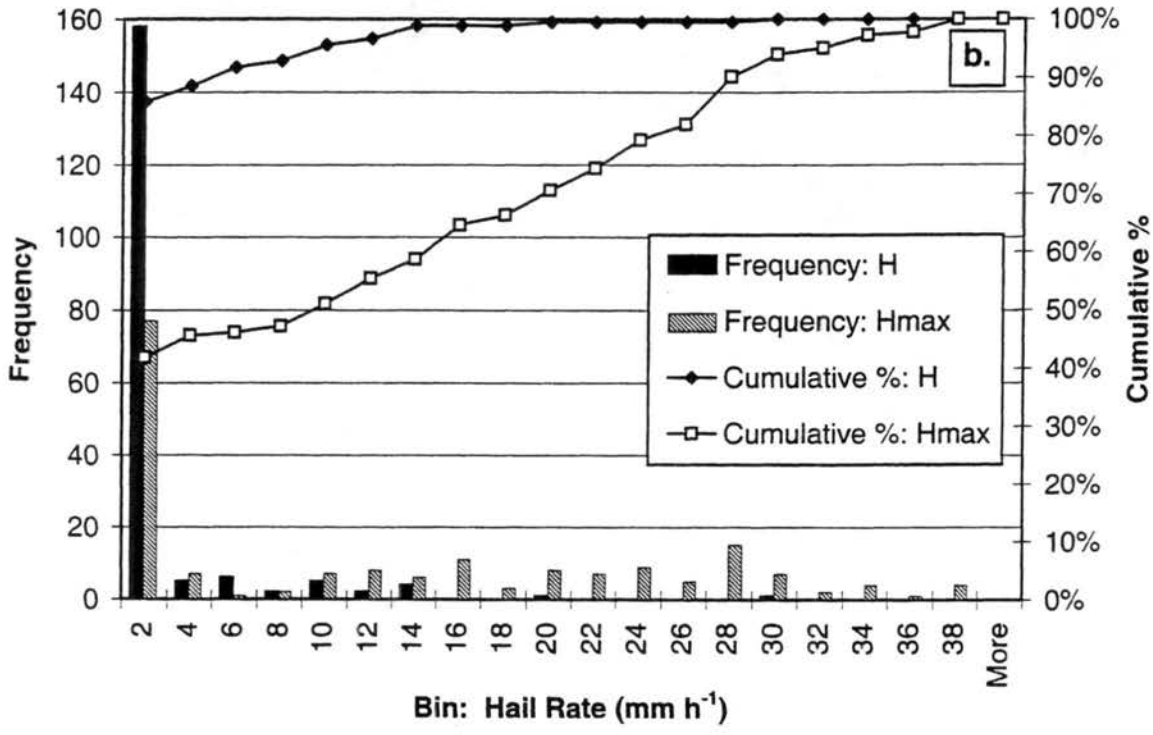

Figure 3.12. (b) as in (a) but hail rate (H) and maximum hail rate (H_{max}).

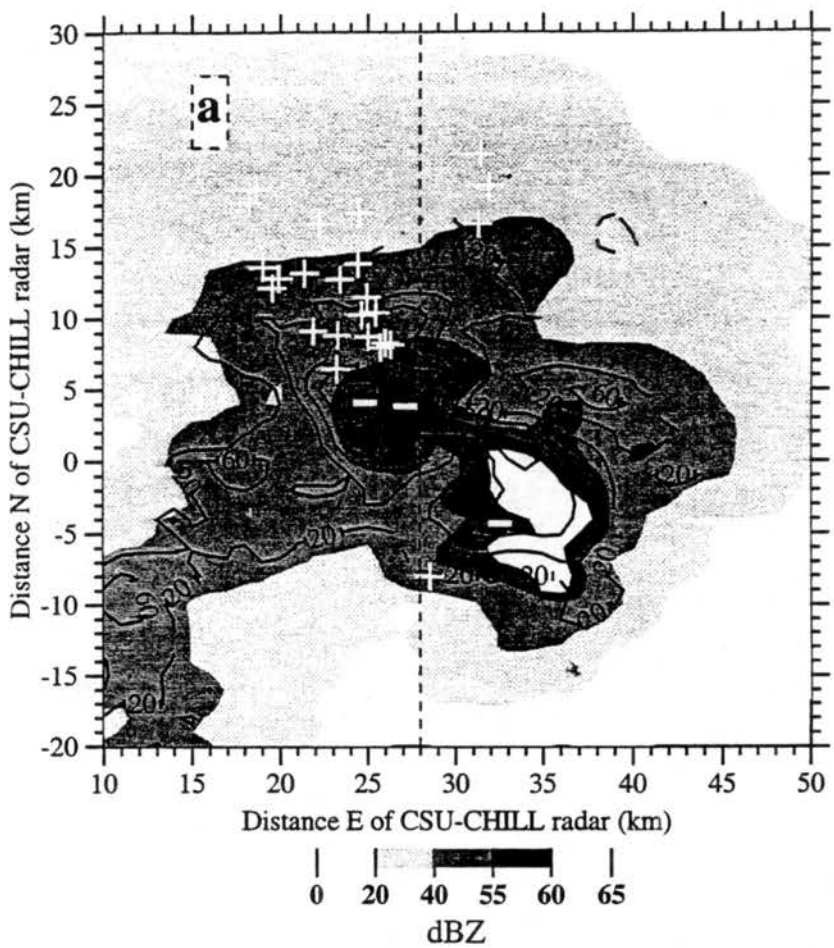

Figure 3.13. Observations of an intense positive CG cluster which occurred around 1952 MDT. (a) Horizontal cross-section at 0.5 km AGL of shaded reflectivity, K_{dp} derived rain rates contoured every 20 mm h^{-1}, and CG ground strike locations and polarities for an 18 minute period centered on 1952 MDT. CG positions were advection corrected.

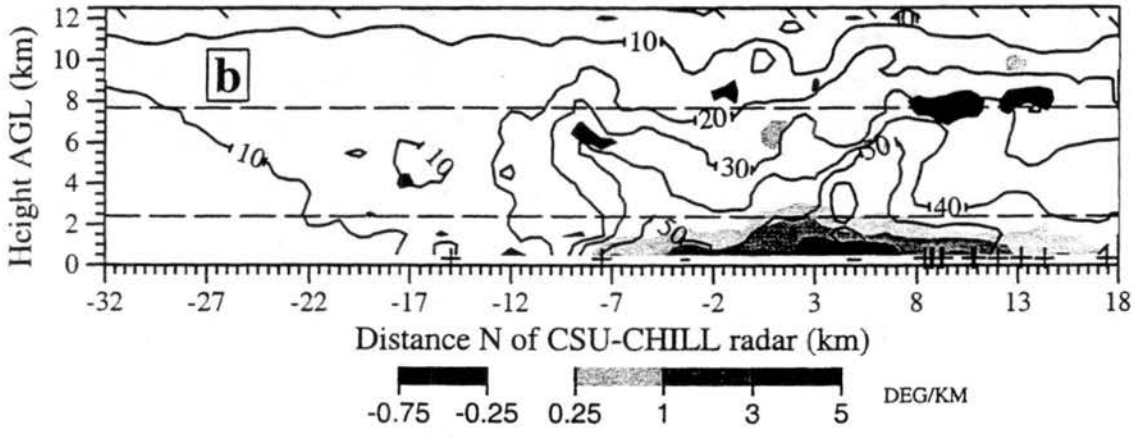

Figure 3.13. (b) as in (a) except a north-south vertical cross-section of contoured reflectivity (every 10 dBZ) and shaded specific differential phase, (° km^{-1}), through x = 28 km (see dashed line in part a). The T = 0 C and -40 C levels are indicated by dashed lines. Polarities and ground strike locations of CG flashes within 5 km either side of the depicted N-S oriented vertical plane are shown beneath the echo.

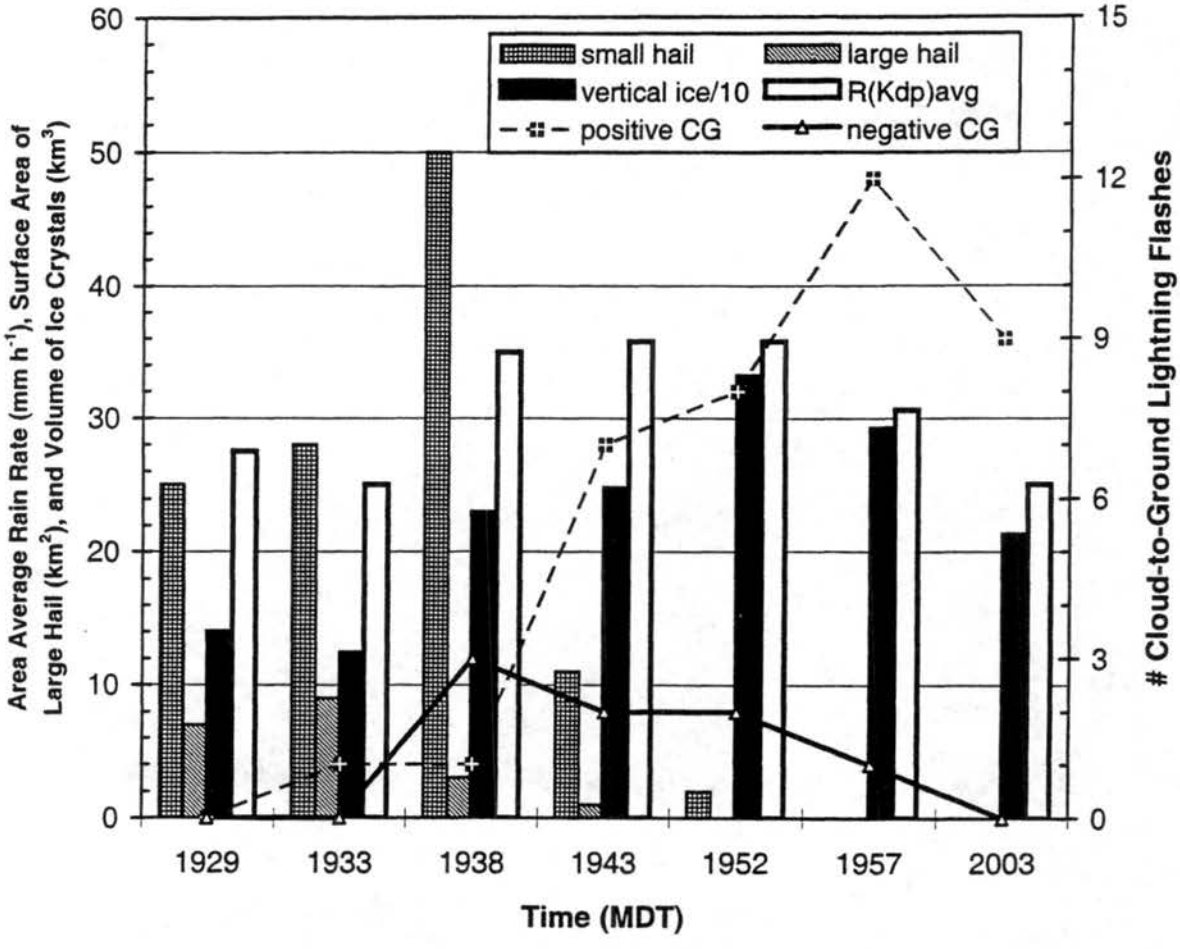

Figure 3.14. Evolution of the surface coverage of small hail and large hail (km^2), the area averaged rain rate based on K_{dp} (mm h^{-1}), the volume of vertically aligned ice aloft (km^3 / 10), and the number of positive and negative cloud-to-ground (CG) lightning flashes from 1929 - 2003 MDT for the northern most convective cell centered on x = 28 km and y = 5 km in Figs 3.13a,b. The hail echo volume aloft for this same cell is presented in Fig. 3.15.

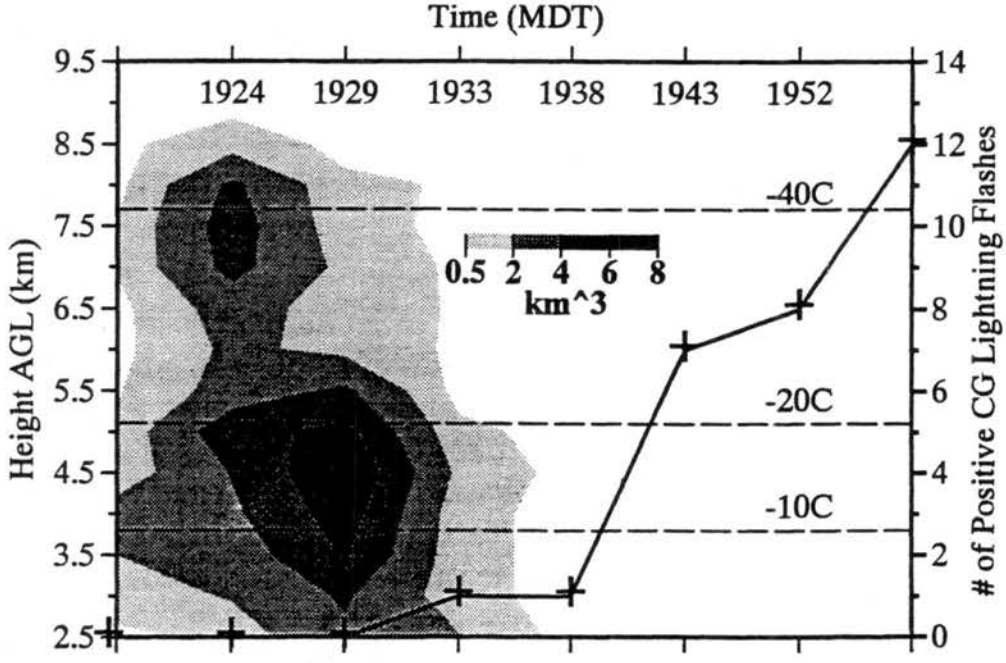

Figure 3.15. Time-height cross-section of the multiparameter radar inferred hail echo volume (shaded; km^3) aloft for the same convective cell analyzed for surface precipitation rates in Fig. 3.14. The hail echo volume for this cell is presented above the freezing level at each vertical level from 1919 - 1957 MDT. Superimposed on the time-height cross-section is the number of positive cloud-to-ground lightning flashes (solid line with '+' marks) during each five minute period associated with the collapse of this hail shaft. The positive CG lightning data is repeated from Fig. 3.14 for the purpose of comparison.

CHAPTER 4
SUMMARY AND CONCLUSIONS

4.1 Electrical and Precipitation Characteristics of a Severe Hailstorm

Our analyses of a severe hailstorm complex have revealed some interesting relationships between the multiparameter radar inferred precipitation structure, lightning, and the surface electric field. The following points summarize the key findings of this study:

1) This severe hailstorm was characterized by an unusually large intracloud flash rate (up to 55 flashes per minute) and an enhanced IC/CG ratio (> 20). This is similar to a tornadic storm studied by MacGorman et al. (1989) and the early sferic studies reviewed by MacGorman (1993) in which the intracloud flash rate increases while cloud-to-ground lightning activity is usually decreasing or steady during the severe stage of storms. As suggested by MacGorman et al. (1989), intense updrafts in severe storms could enhance IC flash rates to the detriment of CG flashes by carrying negative charge to higher altitudes and for longer periods of time compared to ordinary thunderstorms (i.e., elevated dipole hypothesis).

2) Measurements of the sub-storm discharge current (i.e., a useful proxy for the surface electric field) suggest that the storm was dominated by net negative charge aloft during the passage of a high reflectivity core containing heavy rain and hail. There appeared to be an inverse relationship between the strength of the net foul field (i.e., negative charge) aloft and hail size. As multiparameter radar inferred hail size aloft increased (confirmed by surface reports), the magnitude of the net foul field aloft decreased. Surface observations also suggest that there was net positive charge aloft (i.e., fair field) as both the downshear anvil and the reflectivity gradient region beneath the initial portion of the upshear anvil passed overhead. The strongest fair field was associated with the collapse of a hail shaft

to the northeast as the reflectivity gradient region beneath the initial portion of the upshear anvil passed overhead.

Since a non-negligible amount of precipitation sized ice particles occurs in the intervening region between the corona point and the non-precipitation sized ice particles in the forward anvil, it is somewhat ambiguous as to whether the precipitation sized ice particles (roughly corresponding to $Z_h > 25$ dBZ) in the reflectivity gradient region on the upshear side of the main precipitation core or the non-precipitating ice above this region carry predominantly positive charge. Clearly, additional in-situ particle charge and electric field measurements in this region are required to definitively answer this question.

3) Similar to recent studies by MacGorman and Burgess (1994) and Stolzenburg (1994), this severe hailstorm complex produced a predominance (74%) of positive polarity cloud-to-ground lightning. The six minute averaged peak positive CG flash rate was 2.7 min^{-1} and the peak positive CG flash density was approximately 0.1 km^{-2} h^{-1}. These values are comparable in magnitude but on the low side of the typical range in values for peak negative CG flash rates and densities in non-severe storms (Stolzenburg, 1990).

4) This severe hailstorm complex produced predominately positive CG lightning despite complex changes in storm morphology (including supercell, multicell, and squall-line structures; see Sec. 3.2). During *all* of these different phases, positive ground strikes dominated. This is in contrast to earlier studies (Branick and Doswell, 1992; Curran and Rust, 1992) which suggested that the predominance of positive CG lightning could be a unique signature of low-precipitation supercells. As shown in this study and in MacGorman and Burgess (1994), this is not the case. Predominant positive CG lightning during the mature phase can occur in a wide variety of storm types, including classic supercell and multicell storms. Apparently, the common characteristic of most storms dominated by positive ground discharges is *storm severity* (e.g., the presence of large hail and possibly tornadoes).

5) In MacGorman and Burgess (1994) and Stolzenburg (1994), a loose correlation between large hail occurrence and positive ground discharges was suggested using surface hail reports. Detailed analysis of multiparameter data in this case revealed that positive CG lightning and large hail are *anti-correlated* in time. The peak in the amount of large

hail reaching the surface typically occurs 20 - 35 minutes *prior* to broad maxima in the positive CG ground flash rate. If this relationship holds for most severe hailstorms, then it has important implications for the nowcasting of severe weather using CG lightning data.

6) Analysis of multiparameter radar data also revealed that the majority of positive CG lightning struck ground in regions of light rain with little or no hail. In general, the positive ground strike locations appeared to avoid regions of active hail fall. This is similar to the findings of Changnon (1992) who found that lightning generally struck ground to the left or right flank of hailstreaks in his study of lightning in Illinois hailstorms. Since these storms occurred in a different geographical region and likely under different meteorological settings, we are unable to generalize the results regarding hailswaths and positive CG lightning.

7) Maxima in the positive CG lightning flash rate tended to occur during and just after the collapse of high reflectivity convective cores containing hail and heavy rain. Typically, large hail falls out of the collapsing cores first. As the cell continues to collapse, the rain and hail mass flux (associated primarily with *small* hail) near the surface rapidly increases. Coincident in time with this rapid increase in the surface mass flux, clusters of positive CG lightning typically occur. This behavior is similar to the findings of Seimon (1993) who studied an F5-tornado producing supercell in Illinois. In this storm, the peak positive CG flash rate occurred during a major downburst which resulted from the descent of an exceptionally large elevated reflectivity core.

8) Observations of persistent negative K_{dp} shifts near the top of a tilted convective core may suggest the presence of oriented ice crystals in a strong electric field (Caylor and Chandrasekar, 1996) almost directly above the region where an intense positive CG cluster occurred. Weinheimer and Few (1987) calculated that columnar ice crystals with major dimensions between 200 μm and 1 mm would be aligned vertically in a vertically directed electric field of about 100 kV m^{-1}. Recent research by Marshall et al. (1995) suggests that lightning may occur whenever the electric field exceeds the breakeven field. For the altitudes at which the negative K_{dp} signatures occurred (5.5 - 8.5 km AGL or 7 - 10 km MSL), the breakeven field ranges from 61 to 88 kV m^{-1}. Since the E-field required to orient the ice crystals in the near vertical is on the order of the breakeven field at these

altitudes, one could speculate that the positive ground discharges located almost directly below emanated from this region of moderate reflectivity near storm top. This observation is consistent with the findings of Rust et al. (1981a,b) who showed that positive CG flashes emanated from high in the storm (up to 15 km) and did not occur in the precipitation core of a severe storm. Of course, further observations such as in-situ electric field measurements, visual observations, or lightning flash mapping (2-D or 3-D) using acoustic, electric field change, interferometry, or VHF time-of-arrival (TOA) techniques would be necessary to substantiate this claim.

4.2 Positive Cloud-to-Ground Lightning in Severe Storms: Hypotheses

Although these observations of one severe storm provide insufficient grounds upon which to judge various hypotheses for explaining a high fraction of positive CG lightning flashes, we feel that a few speculative comments are warranted. Current hypotheses for explaining the occurrence of high positive CG flash densities in mature thunderstorms typically fall into one of two categories: 1) the tilted-dipole, and 2) the enhanced lower positive charge (sometimes called an inverted dipole).

A tilted-dipole is a normal polarity dipole (positive over negative; Wilson, 1920) in which the positive charge carried on ice crystals is tilted downshear by storm relative winds from the precipitation shaft which carries negative charge, thus resulting in an electrical dipole tilted with respect to the vertical. As the positive charge center moves outward from directly above the negative charge center, it is no longer shielded from the earth's surface by the negative charge center. This charge arrangement could then facilitate the occurrence of positive flashes to ground. MacGorman and Nielsen (1991) and Branick and Doswell (1992) both suggested this mechanism for explaining the occurrence of positive CG lightning flashes in supercells. Some limited evidence for this mechanism can be found in our observations. For example, a majority of positive ground discharges tended to occur in light rain with little or no hail on the downshear side of a tilted precipitation shaft (see Figs. 3.8; 3.12a,b; and 3.13a,b). However, not all positive CG flashes exhibited this behavior. Some positive ground strokes occurred on the upshear side and a small percentage were found in heavy precipitation (see Fig. 3.13a). In

addition, the tilted dipole hypothesis fails to elucidate why there are so few negative cloud-to-ground lightning flashes (e.g., see Table B.1). If the dipole is merely tilted, one would *not* expect there to be a preference for positive ground discharges since the negative charge center is still assumedly closer to ground.

MacGorman and Nielsen (1991) and Williams et al. (1991) independently proposed that the occurrence of positive ground flashes in severe hailstorm could be the result of an enhanced region of significant positive charge at low levels in thunderstorms. Observations of a lower positive charge in some thunderstorms were first reported by Simpson and Scrase (1937). Jayaratne et al. (1983) first proposed that this lower positive center could be the result of the non-inductive charging mechanism (NIC; e.g., Takahashi, 1978; Jayaratne et al., 1983; Saunders et al. 1991). Williams (1989) later supported this hypothesis with a critical review of thunderstorm scale observations. Under certain circumstances, graupel or hail particles can obtain positive charge and ice crystals acquire negative charge during a rebounding collision in the presence of supercooled cloud liquid water. The gravitational separation of these particles could result in a lower positive charge. This "charge reversal" process is the opposite of what is normally hypothesized to occur under "typical" conditions in which the graupel particle obtains negative charge and the ice crystal acquires positive charge. Charge reversal occurs at temperatures warmer than some threshold between about -10° C and -20° C (depending on liquid water content) or at some very high liquid water content, regardless of temperature.

Williams et al. (1991) point out that most hailstones with diameters of 1 cm or larger would experience wet growth at high liquid water contents for which positive charging of the precipitation particle might occur. Based on the laboratory results of Takahashi (1978), Williams et al. (1991) and Williams (1995) suggest that the prevalence of wet growth conditions for riming hail may explain the presence of positive CG clusters in severe thunderstorms. However, the laboratory experiments of non-inductive ice-ice collision charging by Saunders and Brooks (1992) suggest that charging of the rimer (i.e., simulated hailstone) becomes negligible during wet growth conditions. The details of this controversy and their implications are further discussed in Saunders (1993 and 1995) and Williams and Zhang (1993) and Williams (1995).

Based on their hypothesis, Williams et al. (1991) suggest that "new emphasis be placed on developing polarization-diversity radar techniques for identifying the growth regime of graupel particles." Our study represents the first polarimetric radar investigation of this question. Using enhanced values of the linear depolarization ratio (see Appendix A and Table A.1), we have demonstrated that the peak occurrence of likely regions of large hail in wet growth preceded the peak positive CG lightning flash rate by 20 - 35 minutes. Given the temporal and spatial anti-correlation between large hail and positive CG lightning, it does not seem likely that the non-inductive charging of hail during wet growth and collisions with ice crystals was the source for positive ground strokes in this storm. As such, our polarimetric radar observations support the laboratory results of Saunders and Brooks (1992) and are inconsistent with the hypothesis put forward in Williams et al. (1991) for explaining the occurrence of positive CG lightning clusters beneath vigorous hailstorms.

On the other hand, it is interesting to note that the majority of the positive CG lightning tends to occur during convective cell descent when the rain and hail mass flux are rapidly increasing at the surface. It is possible that the descent of a large number of graupel particles in a weak updraft below the so-called "charge reversal level" (e.g., Jayaratne et al., 1983) to warmer temperatures (0° C to -15° C) causes the graupel to charge positively and form an enhanced and descending positive charge layer. This enhanced lower positive charge center could easily explain the preference for positive polarity ground discharges over negative CG lightning flashes. A similar hypothesis was suggested by MacGorman and Burgess (1994). Potential evidence against this hypothesis is that the majority of positive CG flashes occurred in light rain, avoiding the areas of heaviest precipitation. In addition, the corona point sensor data suggest that the storm was typically characterized by negative charge aloft as the convective cores passed overhead and by positive charge when an anvil region was above the instrument (reference Figs. 3.9 and 3.10, 1748 - 1833 MDT). The only exception to this behavior was the fair field measured by the corona point sensor as precipitation sized ice passed overhead in the high reflectivity gradient region beneath the initial portion of the upshear anvil (reference Figs. 3.9 and 3.10, 1823 - 1833 MDT). This result suggests the need for *in-situ*

measurements in this region to determine whether ice crystals in the upshear anvil or the intervening precipitation in the reflectivity gradient region carry the predominately positive charge.

The separation of charge as air bubbles burst at the surfaces of a large number of melting, millimeter sized graupel or small hail particles could be an alternative (or additional) source of the hypothesized enhanced lower positive charge center (Dinger and Gunn, 1946; Drake, 1968). According to the laboratory experiments of Drake (1968), strong convection currents developed in the melt water of millimeter (1 - 5 mm) sized ice particles. Bubbles released from the ice during melting were swept up by the currents and rapidly transferred to the surface where they burst. The bursting of these bubbles in melt water was accompanied by a significant separation of electric charge, leaving the melt water surrounding the ice positively charged. It is interesting to note that the peak positive CG lightning flash rates occurred almost simultaneously with rapid increases in the rain mass flux (e.g., Figs. 3.6, 3.11, and 3.14), associated with the melting of large numbers of millimeter sized graupel and hail particles as confirmed by multiparameter radar data (not shown). Also, surface and multiparameter radar observations suggest that moderate-to-heavy rain and pea sized hail were falling over the corona point sensor associated with cell collapse when the peak positive electric field was recorded at the surface around 1833 MDT (Fig. 3.10). These observations are generally consistent with the generation of an enhanced, lower positive charge center through the Drake (1968) melting mechanism.

Based on our limited observations, we can only speculate on the possibility of a third mechanism. Since peaks in the positive CG flash rate appear to be coincident with the collapse of intense precipitation cores, perhaps it is the *unshielding* of a large reservoir of upper level positive charge by the action of rapid precipitation echo descent which results in a favorable electrostatic condition for positive CG lightning. Once much of the heaviest precipitation and associated charge has fallen out of a convective cell, the upper level positive charge typically resident on ice crystals would no longer be shielded from ground by the lower negative charge typically resident on precipitation particles. The longevity and intensity of severe storms might allow an extremely large reservoir of positive charge

to be accumulated aloft. Assuming that the enhanced amount of precipitation mass descending to the surface carries significant negative charge, this mechanism could also explain the predominance of positive over negative CG lightning flashes. We speculate that the precipitation current (J_p) in some severe storms may be augmented to the point of reducing the electrical requirement for other current sinks such as the lightning current (J_l) associated with negative ground discharges.

This "precipitation unshielding" hypothesis is broadly consistent with all of our observations: 1) positive CG lightning is associated with the descent of an intense convective echo, 2) large hail falls out of the storm ten's of minutes before the peak in positive CG lightning, 3) the rain and hail mass flux (associated with mostly *small* hail) is either rapidly increasing or experiencing maxima during the peak in positive CG lightning activity, 3) many of the positive ground strokes occur in light rain and little or no hail, 4) the corona point data suggest that the gross electrostatic structure of the storm could be characterized by a normal polarity dipole (negative charge aloft as the convective cores passed by and positive charge aloft as either an anvil passed overhead or after the descent of a convective core, and 5) radar observations suggest that ice crystals aloft were oriented in the near-vertical by a strong electric field on the order of the breakeven field in a large and persistent region which was almost directly above a positive CG lightning cluster.

Clearly, more case studies of positive CG producing severe storms are required before any definitive statement can be made regarding causal mechanisms. In particular, more polarimetric radar studies would be useful since they can remotely probe cloud precipitation in all regions of these severe storms. Of course, the most powerful approach would be to study several of these storms using a host of observational techniques in concert, including 1) polarimetric radar observations set in the context of the three dimensional wind field obtained by dual-Doppler synthesis, 2) in-situ (e.g., aircraft) microphysical, electric field, and particle charge measurements, and 3) a detailed lightning observational network (NLDN, flat plate antennas, surface field mills, and 3-D lightning mapper using interferometry or VHF TOA techniques).

Future studies of the unique electrical aspects of severe storms will benefit both the atmospheric electricity community by giving us a better understanding of thunderstorm electrification mechanisms and the operational forecasting community by further exploring the potential of lightning data in the identification and nowcasting of severe weather (e.g., Knapp, 1994).

APPENDICES

Appendix A. Multiparameter Radar Analysis Method

Using the gridded polarimetric radar observables (Z_h, Z_{dr}, K_{dp}, ρ_{hv}, and LDR), it is possible to estimate first the predominant precipitation type and then the amount at each grid point in the storm. In this study of a severe hailstorm, we are particularly interested in two objectives: 1) determine the bulk hydrometeor type with emphasis given to the identification of small (< 2 cm) and large (≥ 2 cm) hail, and 2) calculate rain and hail rates near the surface throughout the storm.

Jameson (1985a) was one of the first investigators to suggest that polarimetric radar measurements could provide a possible framework for precipitation identification. In particular, he discussed the discrimination of liquid from solid hydrometeors and discrimination among solid hydrometeors. More recently, Doviak and Zrnic´ (1993) proposed a multiparameter radar decision process that partitions the five-dimensional space of Z_h, Z_{dr}, K_{dp}, ρ_{hv}, and LDR so that each category uniquely corresponds to a distinct hydrometeor type. This method of bulk hydrometeor identification is based on both modeling and observational studies. For detailed reviews of these studies and a general discussion of the technique, see Jameson and Johnson (1990) or Doviak and Zrnic´ (1993).

These techniques have been applied in a variety of case studies. For example, the method was used successfully in a severe hailstorm by Zrnic´ et al. (1993) to identify various hydrometeor types including large hail, small hail, rain, mixed phase precipitation (e.g., rain and hail mixture), graupel, and ice crystals. Höller et al. (1994) employed C-band polarimetric observations of LDR and Z_{dr} to identify rain, graupel, hail, and mixed phase precipitation in the investigation of a hybrid-type hailstorm. Carey and Rutledge (1996) utilized bulk hydrometeor identification (without LDR) to differentiate between

rain and graupel in a multicell storm in CO in order to correlate the evolution of the multiparameter radar inferred graupel volume to that of lightning and storm electric fields. Jameson et al. (1996), Ramachandran et al. (1996), and French et al. (1996) used multiparameter radar observations including Z_h, Z_{dr}, and LDR of isolated Florida thunderstorms during the CaPE (Convective and Precipitation/Electrification) project to demonstrate that initial electrification was coincident with the freezing of supercooled raindrops above the -7° C level. In this study, we utilize similar methods to track the production of hail, especially large hail, in a positive CG producing storm in order to assess the temporal and spatial relationship between the two phenomenon.

A summary of the bulk hydrometeor method utilized in this study is shown in Table A.1. The range of each multiparameter radar observable is an adaptation of the proposed values found in Table 8.1 of Doviak and Zrnic´ (1993). A few minor adjustments in these ranges were made in order to 1) account for the effect of imperfect measurements, 2) incorporate more recent modeling and observational results, and 3) maximize agreement between surface reports of precipitation type and size from the public (Storm Data, 1995) and two storm chase vans as summarized in Sec. 3.2. The primary goal of the analysis below the melting level (2.4 km AGL, cf. Fig. 3.1) was to locate regions of both small and large hail (categories 1 and 3 in Table A.1), regardless of whether the hailstones were mixed with rain as they often are (categories 2 and 4).

Table A.1. Bulk-hydrometeor identification using multiparameter radar data.

Hydrometeor Type	Z_h *(dBZ)*	Z_{dr} *(dB)*	*LDR (dB)*	K_{dp} *(° km^{-1})*	ρ_{hv}
T ≥ 0° C					
1. Small hail (D < 2 cm)	≥ 50	≤ 0.5	< -18	< 0.5	> 0.96
2. Small hail and rain	≥ 50	< 1.0	-27 to -20	≥ 0.5	≤ 0.98
3. Large hail (D > 2 cm)	≥ 55	≤ 0.5	≥ -18	< 0.5	≤ 0.96
4. Large hail and rain	≥ 55	< 1.0	≥ -20	≥ 0.5	≤ 0.96
5. Rain	< 60	> 0.5	≤ -27	≥ 0.5	≥ 0.97
T < 0° C					
6. Hail (D > 1 cm)	≥ 55	< 0.5	> -26	< 0.5	> 0.97
T ≤ -20 C					
7. Vertically Oriented Ice Crystals	< 40	not used	not used	< -0.25	not used

An elevated value of K_{dp} is the best indication of rain since it is linearly proportional to the mass-weighted mean axis ratio, as discussed in Jameson (1985b). Typically, $K_{dp} \geq 0.5°$ km^{-1} suggests the presence of significant rain ($R > 22$ mm h^{-1}, see Eqn. A.3 in Table A.2). Note that Z_{dr} can be an unreliable measure of the presence of rain in mixed phase precipitation if hail dominates the reflectivity. Differentiating mixed phase precipitation from pure rain depends largely on the magnitudes of LDR and ρ_{hv}. Assuming K_{dp} suggests the presence of rain, the probability of hail being present increases with decreasing Z_{dr}, decreasing ρ_{hv}, and increasing values of LDR (Bringi et al., 1986; Aydin and Zhao, 1990; Balakrishnan and Zrnic′, 1990a; Zrnic′ et al., 1993; Kennedy et al. 1997). Similarly, the determination of hail size (small vs. large) also falls largely on the values of LDR and ρ_{hv}. Increasing values of LDR and decreasing values of ρ_{hv} are associated with increasing probability of the presence of large hail (Bringi et al., 1986; Aydin and Zhao, 1990; Balakrishnan and Zrnic′, 1990a; Zrnic′ et al., 1993; Kennedy et al., 1997). The presence of large hail is often associated with the occurrence of negative Z_{dr} (Balakrishnan and Zrnic′, 1990a). However, since this is not *always* the case (e.g., tumbling or spherical hailstone between 2 and 4 cm in diameter), it is not required.

Above the freezing level, our intention is to locate probable locations of hail (category 6 in Table A.1) which are often associated with an enhanced value of LDR (Bringi et al., 1986) due to hail's increasing oblateness with size (Knight, 1986), tendency to tumble (Knight and Knight, 1970), and high density or dielectric factor (especially if it is experiencing wet growth). The chosen threshold for LDR (> -26 dB) is based on 1) available modeling studies (e.g., Bringi et al., 1986; Aydin and Zhao, 1990), 2) the general agreement between analyzed areas of LDR > -26 dB with regions of hail growth in conceptual models of supercell thunderstorms (e.g., hail cascade along the edge of the weak echo region in Browning and Foote, 1976; reference Figs. 3.3 and 3.4a,b), and 3) consistency between the temporal and spatial trends in the identification of hail above and below the melting level (see Fig. 3.7). Of course, it is possible that a few nearly spherical hailstones with no surface irregularities could be characterized by LDR ≤ -26 dB. We therefore suggest that our estimates of hail volume aloft represent a *lower bound* since no

other hydrometeor type in areas of uncorrupted data could be characterized by the ranges of multiparameter variables listed in Table A.1.

The final hydrometeor category of interest in Table A.1 is that of vertically oriented ice crystals (category 7). Caylor and Chandrasekar (1996) demonstrated that negative values of K_{dp} aloft (7 to 11 km MSL) are associated with vertically oriented ice crystals in a strong electric field. By "vertically oriented," we strictly mean that the component of the major axis in the vertical exceeds 50%. In fact, an ice crystals only needs to exhibit orientation of the major axis more than 45° from the horizontal polarization plane (which is parallel to the ground for an elevation angle of 0°) to result in a negative value of K_{dp}. The closer the orientation angle is to 90° from the horizontal polarization plane; the higher K_{dp} will be for a fixed concentration of ice crystals (Caylor and Chandrasekar, 1996). For a fixed orientation angle, K_{dp} will increase with increasing numbers of ice crystals. Vivekanandan et al. (1994) demonstrated that K_{dp} scales with the N_o parameter of an assumed exponential distribution for ice crystals. Similar observations of oriented ice crystals in circular polarization radar data were first found by Hendry and McCormick (1976) and have been investigated more recently by Metcalf (1995,1997) and Krehbiel et al. (1996). Weinheimer and Few (1987) calculated that columnar ice crystals with major dimensions between 200 μm and 1 mm would be aligned with a vertical electric field of about 100 kV m^{-1}. In this study, "vertically" oriented ice crystals are associated with spatially coherent areas of Kdp < -0.25 km in order to differentiate from noise (Bringi et al., 1996) and Z_h < 40 dBZ in order to differentiate from vertically oriented hail (Doviak and Zrnic', 1993) at temperature less than -20° C (altitudes > 5.1 km AGL or 6.6 km MSL). Small conical graupel oriented in the vertical with reflectivities less than 40 dBZ will typically not have a sufficiently large dielectric constant (due to reduced ice density) or oblateness to cause measurable K_{dp}.

With regions of rain, hail, and mixed phase precipitation identified, the next analysis step was to utilize the available multiparameter radar data to calculate the rain and hail rate at each grid point near the surface (0.5 km AGL) using Eqns. A.1 - A.4 summarized in Table A.2. Light rain (≤ 20 mm h^{-1}) is still measured best with a simple R-Z_h relationship (Eqn. A.1), as discussed in Chandrasekar and Bringi (1988). Chandrasekar et

al. (1990) demonstrated that precipitation estimators using a combination of Z_h and Z_{dr} (Eqn. A.2) provide superior estimates at intermediate rain rates (20 - 60 mm h^{-1}) and that equations based on K_{dp} (Eqn. A.3) perform best in heavy rain ($\geq$ 60 mm h^{-1}). In order to avoid the possibility of hail contamination in $R(Z_h, Z_{dr})$, Z_{dr} was corrected when the ice fraction exceeded 10% using the Z_h, Z_{dp} method of Golestani et al. (1989). The difference reflectivity, or Z_{dp}, is defined as $Z_{dp} = 10 \log (\mathbf{Z_h} - \mathbf{Z_v})$ [dB]. The relationship between Z_{dp} and Z_h for rain is linear (Golestani et al., 1989). As a result, it is possible to estimate the fractional contribution of ice to the measured reflectivity by calculating the reflectivity deviation from the Z_h, Z_{dp} line. Using the Z_h/Z_{dp} line derived in Carey and Rutledge (1996) (their Eqn. 5) from data in a Colorado thunderstorm, the ice fraction was calculated at each grid point. If the ice fraction of the total reflectivity exceeded 10%, it was subtracted from Z_h and then Z_{dr} was re-calculated before estimating the rain rate, $R(Z_h, Z_{dr})$, thus minimizing contamination from hail.

Table A.2. Equations for multiparameter radar-based rain and hail rates (mm h^{-1}).

Light Rain: $1 \leq R(Z_h) \leq 20$ mm h^{-1}
$\mathbf{Z_h} = 486 \bullet R(\mathbf{Z_h})^{1.37}$ (A.1)
Moderate Rain: $20 < R(Z_h) < 60$ mm h^{-1}
$R(\mathbf{Z_h}, Z_{dr}) = 6.84 \bullet 10^{[\,0.1 \bullet (Z_h - 30 - 4.86 \bullet Z_{dr})\,]}$ (A.2)
Heavy Rain: $R(K_{dp}) \geq 60$ mm h^{-1}
$R(K_{dp}) = 40.683 \bullet (K_{dp})^{0.866}$ (A.3)
Hail: $H(K_{dp}, \mathbf{Z_{hail}})$ mm h^{-1}
$H(K_{dp}, \mathbf{Z_{hail}}) = \dfrac{88.0}{\exp\left[\left(5.38 \times 10^{-6}\, \mathbf{Z_{hail}} \left\{K_{dp}\right\}^{-0.297}\right)\right]}$ (A.4)
A1. Jones, 1955; A2 and A3. Sachidananda and Zrnic', 1987; A4. Balakrishnan and Zrnic', 1990b.

Balakrishnan and Zrnic' (1990b) demonstrated that the hail rate could be calculated by using K_{dp} and Z_h to separate the hail contribution to the reflectivity factor, $\mathbf{Z_{hail}} = \mathbf{Z_h} - \mathbf{Z_{rain}}(K_{dp})$ [mm^6 m^{-3}]. The reflectivity from rain is estimated by combining the K_{dp}, R

relationship in Eqn. A.3 and Z_h, R relationship in Eqn. A.1 to obtain $\mathbf{Z_{rain}}(K_{dp}) = 77899 (K_{dp})^{1.186}$. According to Balakrishnan and Zrnic' (1990b), the value of Z_{hail} will possess sufficient precision to use if it is within 7 dB of Z_{rain}. If this constraint was met, then the hail rate in mm h^{-1} (liquid equivalent) was calculated by substituting $\mathbf{Z_{hail}}$ into Eqn. (A.4) which is based on the Cheng and English (1983) hail size distribution. Otherwise, it was assumed that the hail rate was negligible. Since there are several assumptions which must be made in order to estimate the hail rate (e.g., a Z_h-R relationship; a hail size distribution; spherical or tumbling hail), there could be occasional point-to-point uncertainties in the hail estimate as conditions vary from our assumptions. However, the analyses in this study depend more on storm wide spatial and temporal trends rather than point-to-point estimates of precipitation rate. Therefore, we interpret our results with confidence.

Appendix B. Cloud-to-Ground Lightning Statistics and Assessment of the Validity of Positive Ground Flashes

To demonstrate that the positive cloud-to-ground lightning flashes analyzed in this study are probably *not* part of a subset of newly detected discharges by the NLDN which may or may not be positive CG lightning, we first analyze cloud-to-ground lightning statistics. Negative CG lightning data is included for reference. In Fig. B.1, we present frequency and cumulative percentage histograms of peak current (kA) for all cloud-to-ground flashes produced by the severe hailstorm complex under study. The statistics associated with these peak currents are given in Table B.1. Negative CG lightning flashes have a median peak current of -14.4 kA with values in a rather tight range from -5.3 kA down to -45.2 kA. Interestingly, about 80% of all negative ground flashes are characterized by peak currents less than 20 kA. In contrast, positive CG peak currents have a median value of 32.7 kA and range from a minimum of 13.7 kA to a maximum of 110.6 kA. As seen in Fig. B.1, approximately 73% of the positive CG peak currents are between 20 kA and 50 kA. About 20% of the flashes occur in a long tail from 50 kA up to 120 kA with the remaining flashes (7%) occurring between 10 kA and 20 kA.

Table B.1. Cloud-to-Ground Lightning Statistics.

Statistic	*Positive cloud-to-ground lightning*	*Negative cloud-to-ground lightning*
Count	184 (74.5 %)	63 (25.5 %)
Mean (kA)	38.9	-14.4
Median (kA)	32.7	-12.9
Standard Deviation (kA)	18.1	7.4
Minimum (kA)	13.7	-45.2
Maximum (kA)	110.6	-5.3

As discussed in Chapter 2, the NLDN underwent changes in sensitivity and discrimination criteria between the 1994 and 1995 warm season (Cummins et al., 1995) which resulted in the inclusion of a previously undetected population of small amplitude positive discharges. At this time, it is unclear whether these event are long vertical cloud discharges or a new population of previously undetected positive cloud-to-ground flashes. However, recent research suggests that these newly detected events exhibit low currents from 5 kA to 15 kA (K. Cummins, private communication, 1996). As can be clearly seen from the histogram in Fig. B.1, the overwhelming majority of flashes in this storm are *not* part of this newly identified population. As a matter of fact, only 3 out of 184 (1.6%) positive CG flashes under study for this severe hailstorm have peak return stroke currents of under 15 kA.

In order to pursue this matter further, we have analyzed available corona point sensor data and flat plate data. Although it is not generally possible to unequivocally differentiate IC flashes from positive CG flashes with the data from either of these devices alone (e.g., Beasley, 1985), it is possible to demonstrate that all available data is *consistent* with the NLDN identification of positive CG lightning. We obtained approximately 1.3 hours (1730 - 1850 MDT) of quality flat plate data while the severe hailstorm complex was within range (40 km). During this period, there were 40 NLDN identified positive CG flashes within 40 km of the flat plate which was located at the CSU-CHILL (see Fig. 1.1 and Fig. 3.2). Although the storm complex was in range for a longer period of time, the flat plate data was later (after 1850 MDT) contaminated by heavy rain which eventually saturated the system's electronics.

Our procedure was to analyze the flat plate waveform for all NLDN detected positive CG flashes within 5 km to 25 km of the CSU-CHILL. We chose to limit the range to outside of 5 km in order to minimize the chance for IC flashes being mistakenly identified

as positive CG flashes (Brook et al., 1989). We also chose to restrict the range to be within 25 km so that the waveform recorded by our flat plate would have sufficient amplitude to be above the noise level of the instrument (the detection efficiency drops rapidly for ranges greater than 35 km). These range requirements decreased our sample of NLDN detected positive CG lightning flashes to thirty with peak currents ranging from 15.6 kA to 85 kA. All 30 of the analyzed waveforms had a large amplitude, initially upward going (positive deflection) electrostatic field change. A positive deflection represents a positive electric field change and, in our convention adapted from Brook et al. (1989), represents a positive stroke. Typically, this upward going deflection was followed by a downward going (negative deflection) ionospheric reflection. For about 30% of the analyzed flashes, the subsequent downward going ionospheric reflection was evident but barely discernible. A typical example representing the other 70% of the waveforms which had more obviously classic positive CG lightning characteristics is shown in Fig. B.2. This flash occurred at approximately 1839:13 MDT and was detected by the NLDN with a peak current of 30.8 kA (close to the median positive CG flash in Table B.1) at about 11.7 km due south of the CSU-CHILL radar. As in most of the 30 positive CG flashes, the initial upward going deflection temporarily saturated the flat plate electronics since the instrument was set at the second highest gain setting during the analysis period.

By comparing the corona point data shown in Fig. 3.9 to seventeen NLDN detected positive CG flashes located within 10 km of the mobile corona point sensor located to the southwest of the CHILL (see Fig. 1.1 and Fig. 3.2) from 1748 MDT to 1859 MDT, we were able to further support the NLDN polarity identification. All seventeen of the NLDN identified positive CG flashes within 10 km of the corona point were characterized by large amplitude, downward directed transients which started and recovered to "fair" weather (positive) field as the storm was overhead. Two of the strongest downward transients associated with positive cloud-to-ground lightning are located between 2400 and 3000 seconds in Fig. 3.9. These transients occurred while the corona point measurements indicate net positive charge aloft. The fact that the transients were downward directed and the current then recovered within seconds to positive values suggests that net positive charge aloft was neutralized, as in a positive CG lightning flash.

Of course, it also possible that an IC lightning flash could generate a similar transient (notice the other two strong downward deflections between 2000 and 3000 seconds in Fig. 3.9 that were not detected by the NLDN as positive CG lightning flashes). However, the strong support for the NLDN positive CG identifications comes from the consistent pattern of downward directed transients for *all* 17 NLDN detected positive CG flashes within 10 km of the corona point sensor.

Based on the above analyses, we feel that most if not all of the 184 positive CG lightning flashes detected by the NLDN in this severe hailstorm complex were correctly identified because 1) 98.4% of the positive CG flashes have peak currents above the suspected range of 5-15 kA, 2) all available flat plate waveforms associated with the NLDN positive CG lightning flashes within 5 km to 25 km of the CSU-CHILL were similar and consistent with known positive CG waveform at a distance, and 3) all NLDN positive CG flashes within 10 km of the mobile corona point were accompanied by transients in the point discharge current which suggest net positive charge being neutralized aloft.

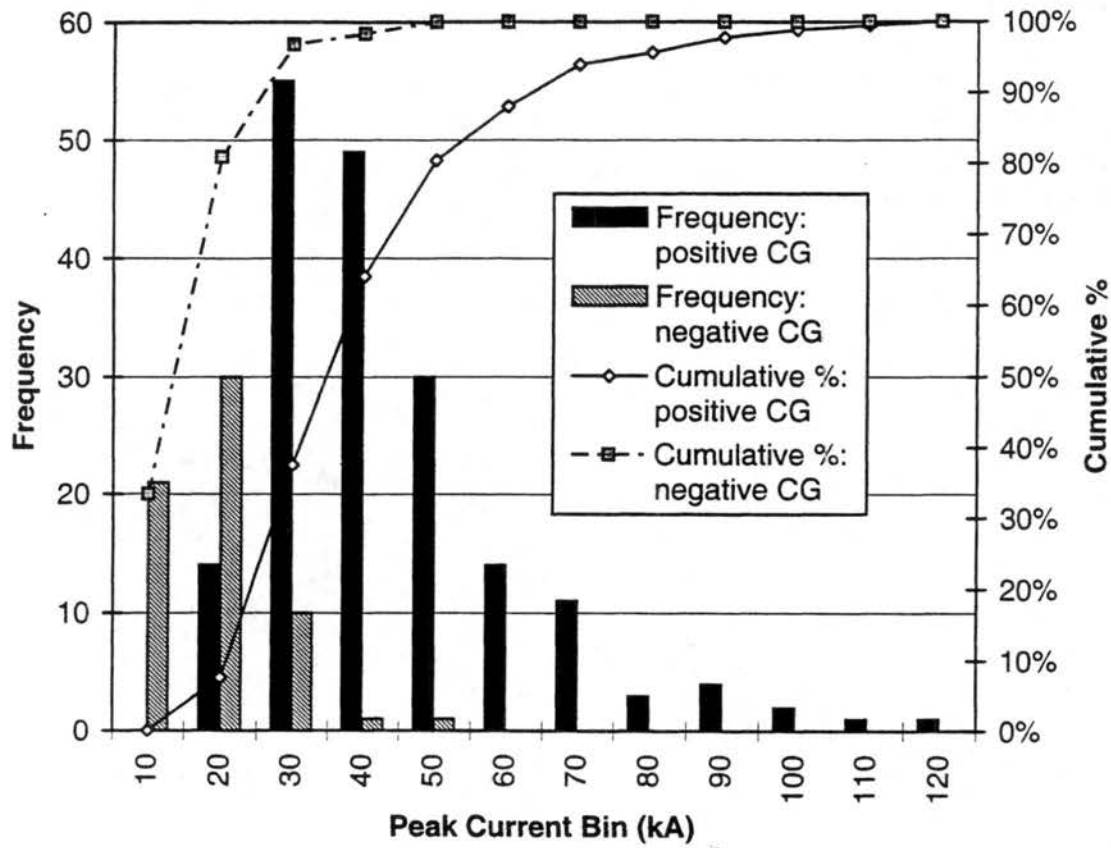

Figure B.1. Frequency and cumulative percentage histograms of the positive and negative CG peak currents (kA) for all ground flashes under study.

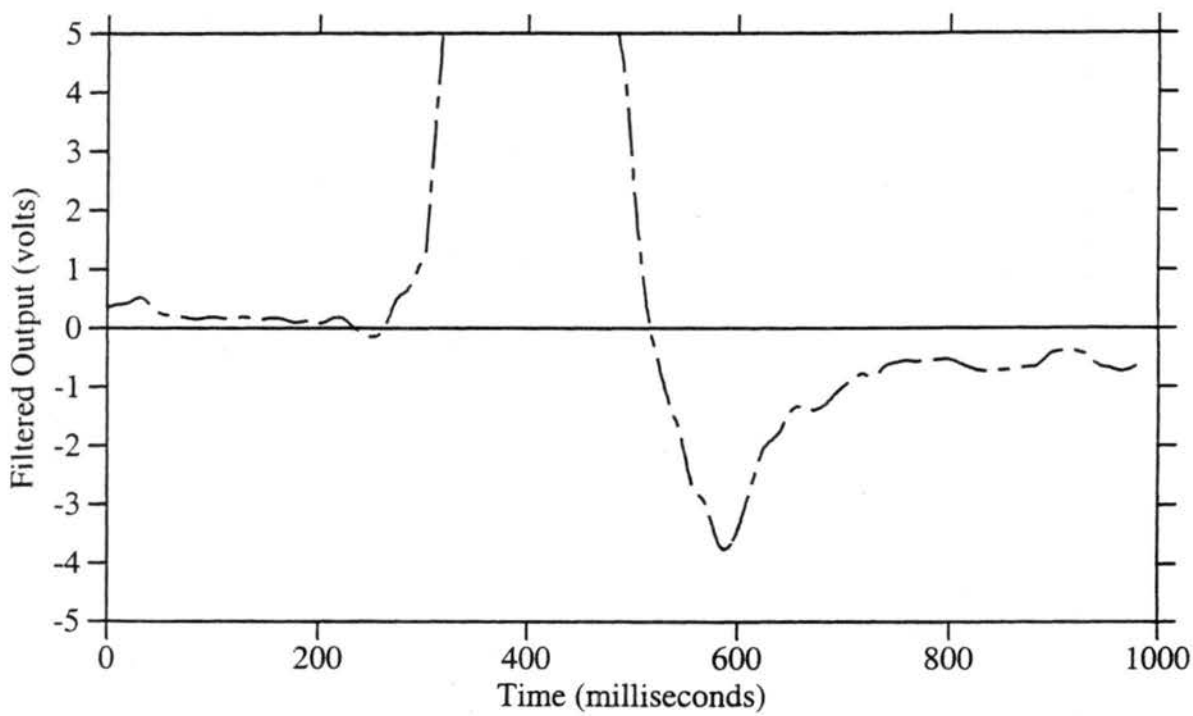

Figure B.2. Filtered output of the flat plate antenna at 1839:13 MDT (0039:13 UTC) on 7 June 1995, corresponding to an NLDN identified positive CG lightning flash with a peak current of 30.8 kA.

REFERENCES

Aydin, K., Y. Zhao, and T. A. Seliga, 1990: A differential reflectivity radar hail measurement technique: Observations during the Denver hailstorm of 13 June 1984. *J. Atmos. Oceanic Technol.*, **7**, 104-113.

——, Y. Zhao, 1990: A computational study of polarimetric radar observables in hail. *IEEE Trans. on GeoSci. and Remote Sensing,* **28**, 412-422.

Balakrishnan, N., and D. S. Zrnic′, 1990a: Use of polarization to characterize and discriminate large hail. *J. Atmos. Sci.*, **47**, 1525 - 1540.

——., and D. S. Zrnic′, 1990b: Estimation of rain and hail rates in mixed-phase precipitation. *J. Atmos. Sci.*, **47**, 565-583.

Beasley, W., 1985: Positive cloud-to-ground lightning observations, *J. Geophys. Res.*, **90**, 6131-6138.

Branick, M. L., and C. A. Doswell III, 1992: An observation of the relationship between supercell structure and lightning ground strike polarity. *Wea. Forecasting,* **7**, 143-149.

Bringi, V. N., J. Vivekanandan, and J. D. Tuttle, 1986: Multiparameter radar measurements in Colorado convective storms. Part II: Hail detection studies, *J. Atmos. Sci.*, **43**, 2564-2577.

——, A. Hendry, 1990: Technology of polarization diversity radars for meteorology. in *Radar in Meteorology: Battan Memorial and 40th Anniversary Radar Meteorology Conference,* ed. David Atlas, Amer. Meteor. Soc., Boston, MA.

——, L. Liu, P. C. Kennedy, V. Chandrasekar, and S. A. Rutledge, 1996: Dual Multiparameter radar observations of intense convective storms: The 24 June 1992 case study. *Meteorol. Atmos. Phys.*, **59**, 3-32.

Brook, M., R. W. Henderson, and R. B. Pyle, 1989: Positive lightning strokes to ground. *J. Geophys. Res.*, **94**, 13,295-13,303.

Browning, K. A., and G. B. Foote, 1976: Airflow and hail growth in supercell storms and some implications for hail suppression. *Quart. J. Roy. Meteor. Soc.*, **102,** 499-533.

Carey, L. D., and S. A. Rutledge, 1996: A multiparameter radar case study of the microphysical and kinematic evolution of a lightning producing storm. *Meteorol. Atmos. Phys.*, **59**, 33-64.

Caylor, I. J., and V. Chandrasekar, 1996: Time-varying ice crystal orientation in thunderstorms observed with multiparameter radar. *IEEE Trans. on Geosciences and Remote Sensing,* **34**, 847-858.

Chandrasekar, V., and V. N. Bringi, 1988: Error structure of multiparameter radar and surface measurements of rainfall. Part 1: Differential reflectivity, *J. Atmos. Oceanic Technol.*, **5**, 783-795.

——., ——, N. Balakrishnan, and D. S. Zrnic', 1990: Error structure of multiparameter radar and surface measurements of rainfall. Part III: Specific differential phase. *J. Atmos. Oceanic Technol.*, **7**, 621-629.

Changnon, S. A., 1992 Temporal and spatial relations between hail and lightning. *J. Appl. Meteor.*, **31**, 587-604.

Cheng, L., and M. English, 1983: A relationship between hailstone concentration and size. *J. Atmos. Sci.*, **40**, 204-213.

Cummins, K. L., E. A. Bardo, W. L. Hiscox, R. B. Pyle, and A. E. Pifer, NLDN95: 1995 A combined technology upgrade of the U.S. national network. *Presented at the Intl. Aerospace & Ground Conference on Lightning and Static Electricity,* Williamsburg, VA, September 1995.

——, M. J. Murphy, E. A. Bardo, W. L. Hiscox, R. B. Pyle, and A. E. Pifer, 1998: A combined TOA/MDF technology upgrade of the U.S. national lightning detection network. *J. Geophys. Res.*, **103**, 9035-9044.

Curran, E. B., and W. D. Rust, 1992: Positive ground flashes produced by low-precipitation thunderstorms in Oklahoma on 26 April 1984. *Mon. Wea. Rev.*, **120**, 544-553.

Dinger, J. E., and R. Gunn, 1946: Electrical effects associated with a change of state of water. *Terr. Mag. and Atmos. Elec.*, **51**, 477 - 494.

Doswell, C. A. III, 1980: Synoptic-scale environments associated with high plains severe thunderstorms, *Bull. Amer. Soc., 61*, 1388-1400.

Doviak, R. J., and D. S. Zrnic', 1993: *Doppler Radar and Weather Observations.* 2nd Ed., 562 pp., Academic Press, San Diego, CA.

Drake, J. C., 1968: Electrification accompanying the melting of ice particles. *Q. J. R. Meteorol. Soc.*, **94**, 176 - 191.

Engholm, C. D., E. R. Williams, and R. M. Dole, 1990: Meteorological and electrical conditions associated with positive cloud-to-ground lightning. *Mon. Wea. Rev.*, **118**, 470-487.

French, J. R., J. H. Helsdon, A. G. Detwiler, and P. L. Smith, 1996: Microphysical and electrical evolution of a Florida thunderstorm, 1, observations. *J. Geophys. Res.*, **101**, 18,961-18,978.

Fuquay, D. M., 1982: Positive cloud-to-ground lightning in summer thunderstorms. *J. Geophys. Res.*, **87**, 7131-7140.

Golestani, Y., V. Chandrasekar, and V. N. Bringi, 1989: Intercomparison of multiparameter radar measurements. *Proc. 24th Conf. Radar Meteorology,* Tallahassee, FL, pp. 309-314, Amer. Meteorol. Soc., Boston, Mass.

Hendry, A., and G. C. McCormick, 1976: Radar observations of the alignment of precipitation particles by electrostatic fields in thunderstorms. *J. Geophys, Res.*, **81**, 5353-5357.

Holle, R. L., and R. E. Lopez, 1993: Overview of real-time lightning detection systems and their meteorological uses. NOAA Technical Memorandum, National Severe Storms Laboratory, Norman, OK, ERL NSSL-102, 68 pp.

Höller, H., V. N. Bringi, J. Hubbert, M. Hagen, and P. F. Meischner, 1994: Life cycle and precipitation formation in a hybrid-type hailstorm revealed by polarimetric and Doppler radar measurements. *J. Atmos. Sci.*, **51**, 2500-2522.

Houze, R. A., Jr., 1993: *Cloud Dynamics*, 573 pp., Academic Press, San Diego, CA.

Hubbert, J., V. Chandrasekar, V. N. Bringi, P. Meischner, 1993: Processing and interpretation of coherent dual-polarized radar measurements. *J. Atmos. Oceanic Technol.*, **10,** 155-164.

——, and V. N. Bringi, 1995: An iterative filtering technique for the analysis of copolar differential phase and dual-frequency radar measurements. *J. Atmos. Oceanic Technol.*, **12**, 643-648.

——, V. N. Bringi, L. D. Carey, S. Bolen, 1998: CSU-CHILL polarimetric radar measurements from a severe hailstorm in eastern Colorado. *J. Appl. Meteor.*, **37**, 749-775.

Jameson, A. R., 1985a: Deducing the microphysical character of precipitation from multiple-parameter radar polarization measurements. *J. Climate and Appl. Meteor.*, **24**, 1037-1047.

——, 1985b: Microphysical interpretation of multiparameter radar measurements in rain. Part III: interpretation and measurement of propagation differential phase shift between orthogonal linear polarizations. *J. Atmos. Sci,* **42,** 607-614.

——, and D. B. Johnson, 1990: Cloud microphysics and radar, in *Radar in Meteorology: Battan Memorial and 40th Anniversary Radar Meteorology Conference,* ed. David Atlas, Amer. Meteor. Soc., Boston, MA.

——, M. J. Murphy, and E. P. Krider, 1996: Multiple-Parameter radar observations of isolated Florida thunderstorms during the onset of electrification. *J. Appl. Meteor.*, **35**, 343-354.

Jayaratne, E. R., C. P. R. Saunders, and J. Hallet, 1983: Laboratory studies of the charging of soft hail during ice crystal interactions. *Q. J. R. Meteorol. Soc.*, **109**, 609-630.

Jones, D. M. A., 1955: 3 cm and 10 cm wavelength radiation backscatter from rain. *Proc. Fifth Wea. Radar Conf.*, Amer. Meteor. Soc., Boston, MA, 281-285.

Knapp, D. I., 1994: Using cloud-to-ground lightning data to identify tornadic thunderstorm signatures and nowcast severe weather. *National. Weather Digest,* **19**, 35-42.

Kennedy, P. C., S. A. Rutledge, and V. N. Bringi, 1997: Hail precursor signatures observed in multiparameter radar data. Preprints, *28th Conf. on Radar Meteorology*, September 7-12, 1997, Austin, TX, Amer. Meteorol. Soc., Boston, Mass.

Knight, C. A., and N. C. Knight, 1970: The falling behavior of hailstones. *J. Atmos. Sci.*, **27**, 672-681.

Knight, N. C., 1986: Hailstone shape factor and its relation to radar interpretation of hail. *J. Clim. and Appl. Meteorol.*, **25**, 1956-1958.

Krehbiel, P. T. Chen, S. McCrary, W. Rison, G. Gray, and M. Brook, 1996: The use of dual channel circular-polarization radar observations for remotely sensing storm electrification. *Meteorol. Atmos. Phys.*, **59**, 65-82.

Lucci, R. M., 1996: Doppler radar investigation of tornadic and lightning producing storms in northeast Colorado. *M. S. Thesis, Atmos. Science Paper 612,* Colorado State University, 151 pp., 1996.

MacGorman, D. R., D. W. Burgess, V. Mazur, W. D. Rust, W. L. Taylor, and B. C. Johnson, 1989: Lightning rates relative to tornadic storm evolution on 22 May 1981. *J. Atmos. Sci.*, **46**, 221-250.

——, and K. E. Nielsen, 1991: Cloud-to-ground lightning in a tornadic storm on 8 May 1986. *Mon. Wea. Rev.*, **119**, 1557-1574.

——, 1993: Lightning in tornadic storms: A review, in *The Tornado: Its Structure, Dynamics, Prediction, and Hazards,* pp. 173-182, Amer. Geophys. Union Monograph 79.

——, and D. W. Burgess, 1994: Positive cloud-to-ground lightning in tornadic storms and hailstorms. *Mon. Wea. Rev.*, **122**, 1671-1697.

Metcalf, J. I., 1995: Radar observations of changing orientations of hydrometeors in thunderstorms. *J. Appl. Meteor.*, **34**, 757-772.

——, 1997: Temporal and spatial variations of hydrometeor orientations in thunderstorms. *J. Appl. Meteor.*, **36**, 315 - 321.

Marshall, T. C., M. P. McCarthy, and W. D. Rust, 1995: Electric field magnitudes and lightning initiation in thunderstorms. *J. Geophys. Res.*, **100**, 7097-7104.

Mueller, E. A., S. A. Rutledge, V. N. Bringi, D. Brunkow, P. C. Kennedy, K. Pattison, R. Bowie, and V. Chandrasekar, 1995: CSU-CHILL radar upgrades, in *Preprints, 27th Conf. Radar Meteor., Vail, CO,* pp. 703-706, Amer. Meteorol. Soc., Boston, Mass

Orville, R. E., R. A. Weisman, R. B. Pyle, R. W. Henderson, and R. E. Orville, Jr., 1987: Cloud-to-ground lightning flash characteristics from June 1984 through May 1985. *J. Geophys. Res.*, **92**, 5640-5644.

——, 1991: Calibration of a magnetic direction finding network using measured triggered lightning return stroke peak currents. *J. Geophys. Res.*, **96**, 17,135-17,142.

——, 1994: Cloud-to-ground lightning flash characteristics in the contiguous United States: 1989-1991. *J. Geophys. Res.*, **99**, 10,833-10,841.

——, and A. C. Silver, 1997: Lightning ground flash density in the contiguous United States: 1992-1995. *Mon. Wea. Rev.*, **125**, 631-638.

Prentice, S. A., and D. Mackerras, 1977: The ratio of cloud to cloud-to-ground lightning flashes in thunderstorms. *J. Appl. Meteor.*, **16**, 545-550.

Price, C., and D. Rind, 1993: What determines the cloud-to-ground lightning fraction in thunderstorms? *Geophys. Res. Letters.*, **20**, 463-466.

Ramachandran, R., A. Detwiler, J. Helsdon Jr., P. L. Smith, and V. N. Bringi, 1996: Precipitation development and electrification in Florida thunderstorm cells during Convection and Precipitation/Electrification Project. *J. Geophys. Res.*, **101**, 1599-1620.

Reap, R. M., and D. R. MacGorman, 1989: Cloud-to-ground lightning: Climatological characteristics and relationships to model fields, radar observations, and severe local storms. *Mon. Wea. Rev.*, **117**, 518-535.

Rogers, R. R., 1984: A review of multiparameter radar observations of precipitation. *Radio Science*, **19**, 23 - 36.

Rust, W. D., W. L. Taylor, D. R. MacGorman, and R. T. Arnold, 1981a: Research on electrical properties of severe thunderstorms on the Great Plains. *Bull. Amer. Meteor. Soc.*, **62**, 1286-1293.

——, D. R. MacGorman, and R. T. Arnold, 1981b: Positive cloud-to-ground lightning flashes in severe storms. *Geophys. Res. Lett.*, **8**, 791-794.

——, D. R. MacGorman, and S. J. Goodman, 1985: Unusual positive cloud-to-ground lightning in Oklahoma storms on 13 May 1983, in *Preprints, 14th Conf. on Severe Local Storms, Indianapolis, IN*, Amer. Meteor. Soc., 372-375.

Rutledge, S. A., and D. R. MacGorman, 1988: Cloud-to-ground lightning activity in the 10-11 June 1985 mesoscale convective system observed during the Oklahoma-Kansas PRE-STORM Project. *Mon. Wea. Rev.*, **116**, 1393-1408.

——, C. Lu, and D. R. MacGorman, 1990: Positive cloud-to-ground lightning in mesoscale convective systems. *J. Atmos. Sci.*, **47**, 2085-2100.

Sachidananda, M., and D. S. Zrnić, 1987: Rain rate estimates from differential polarization measurements. *J. Atmos. Oceanic. Tech.*, **4**, 588-598.

Saunders, C. P. R., W. D. Keith and R. P. Mitzeva, 1991: The effect of liquid water on thunderstorm charging. *J. Geophys. Res.*, **96**, 11007-11017.

——, and I. M. Brooks, 1992: The effects of high liquid water content on thunderstorm charging. *J. Geophys. Res.*, **97**, 14671-14676.

——, 1993: Reply. *J. Geophys. Res.*, **98**, 10,823-10,825.

——, 1995: Reply. *J. Geophys. Res.*, **100**, 1507-1510.

Seimon, A., 1993: Anomalous cloud-to-ground lightning in an F5 tornado-producing supercell thunderstorm on 28 August 1990. *Bull. Amer. Meteor. Soc.*, **74**, 189-203.

Simpson, G. C., and F. J. Scrase, 1937: The distribution of electricity in thunderclouds. *Proc. R. Soc. London, Ser. A*, **161**, 309-352.

Stolzenburg, M., 1990: Characteristics of the bipolar pattern of lightning locations observed in 1988 thunderstorms. *Bull. Amer. Meteor. Soc.*, **71**, 1331-1338.

——, 1994: Observations of high ground flash densities of positive lightning in summertime thunderstorms. *Mon. Wea. Rev.*, **122**, 1740-1750.

Takahashi, T., 1978: Riming electrification as a charge generation mechanism in thunderstorms. *J. Atmos. Sci.*, **35**, 1536-1548.

Uman, M. A., 1987: *The Lightning Discharge*, 377 pp., Academic Press, Orlando, FL.

Vivekanandan, J., V. N. Bringi, M. Hagen, and P. Meischner, 1994: Polarimetric radar studies of atmospheric ice particles. *IEEE Trans. on Geoscience and Remote Sensing*, **32**, 1-10.

Weinheimer, A. J., and A. A. Few, 1987: The electric field alignment of ice particles in thunderstorms. *J. Geophys. Res,* **92**, 14,833-14,844.

Weisman, M. L., and J. B. Klemp, 1982: The dependence of numerically simulated convective storms on vertical wind shear and buoyancy. *Mon. Wea. Rev.,* **110**, 504-520.

——, and ——, 1984: The structure and classification of numerically simulated convective storms in directionally varying wind shears. *Mon. Wea. Rev.,* **112**, 2479-2498.

Williams, E. R., 1989: The tripole structure of thunderstorms. *J. Geophys. Res.*, **94**, 13,151-13,167.

——, M. E. Weber and R. E. Orville, 1989a: The relationship between lightning type and convective state of thunderclouds. *J. Geophys. Res.,* **94**, 13,213-13,220.

——, M. E. Weber and C. D. Engholm, 1989b: Electrical characteristics of microburst-producing storms in Denver, *Proc. 24th Conf. Radar Meteorology, Tallahassee, FL*, pp. 89-92, Amer. Meteor. Soc., Boston, Mass.

——, R. Zhang, and J. Rydock, 1991: Mixed phase microphysics and cloud electrification. *J. Atmos. Sci.,* **48**, 2195-2203.

——, and ——, 1993: Comment on "The effect of liquid water on thunderstorm charging" by C. P. R. Saunders et al.. *J. Geophys. Res.,* **98**, 10,819-10,821.

——, 1995: Comment on "Thunderstorm electrification laboratory experiments and charging mechanisms," by C. P. R. Saunders. *J. Geophys. Res.,* **100**, 1503-1505.

Wilson, C. T. R., 1920: Investigations on lightning discharges and on the electric field of thunderstorms. *Philos. Trans.* A, **221**, 73-115.

Zrnić, D. S., V. N. Bringi, N. Balakrishnan, K. Aydin, V. Chandrasekar and J. Hubbert, 1993: Polarimetric measurements in a severe hailstorm. *Mon. Wea. Rev.,* **121**, 2223-2238.

PART II, C-BAND POLARIMETRIC RADAR STUDIES OF TROPICAL ISLAND CONVECTION: CORRECTING PROPAGATION EFFECTS IN THE PRESENCE OF LARGE RAINDROPS USING DIFFERENTIAL PROPAGATION PHASE

CHAPTER 1
INTRODUCTION

Before meteorological interpretation (e.g., bulk hydrometeor identification) or quantitative analysis (e.g., rainfall rate estimation) of C-band (e.g., 5.625 GHz or 5.3 cm for this study) radar measurements can be accomplished, propagation effects must be identified and corrected in order to obtain meaningful results. The need to correct higher frequency (e.g., C-band) radar reflectivity for attenuation effects has long been recognized (Ryde, 1946; Atlas and Banks, 1951; Hitschfeld and Bordan, 1954; Gunn and East, 1954). There are many examples in the scientific literature of severe attenuation effects at C-band which render the radar reflectivity data nearly useless for quantitative and even qualitative interpretation (e.g., Johnson and Brandes, 1987; Shepherd et al., 1995).

Before the advent of polarization diverse radars, a reliable empirical estimate of attenuation was elusive. Hitschfeld and Bordan (1954) demonstrated that an indirect estimate of the specific attenuation, A, can be obtained from empirical Z-R (reflectivity versus rain rate) and A-R (attenuation vs. rain rate) relationships. In their technique, the correction for attenuation at the n_{th} gate is accomplished using the reflectivity measurements made at all preceding $(n\text{-}1)$ gates, beginning with the gate closest to the radar. Hitschfeld and Bordan (1954) concluded that even a small error in the radar power calibration could cause a large error in the corrected reflectivity. Indeed, this error, which accumulates as the correction is successively carried out in range, is liable to be more serious than the original error caused by attenuation, rendering reflectivity-based attenuation correction futile (e.g., Hitschfeld and Bordan, 1954; Johnson and Brandes, 1987). Using a similar attenuation estimation scheme, Hildebrand (1978) also found that radar calibration accuracy is a limiting factor for reliable attenuation correction at C-band.

With the development of polarization diverse radars (e.g., Bringi and Hendry, 1990), a better estimate of attenuation is possible than with reflectivity alone (e.g., Aydin et al., 1989; Bringi et al., 1990; Gorgucci et al., 1998). In addition, polarimetric radar data such as the differential reflectivity (Z_{dr}) and the specific differential phase (K_{dp}) in combination with the horizontal reflectivity (Z_h) can provide remotely sensed microphysical information on the size, shape, thermodynamic phase, and orientation of hydrometeors (e.g., Jameson and Johnson, 1990; Doviak and Zrnic', 1993) and improved rainfall estimation (e.g., Zrnic' and Ryzhkov, 1997). At attenuating microwave frequencies such as C-band however, the horizontal reflectivity must be corrected for the effects of the horizontal attenuation (α_h, dB) through a rain medium before qualitative or quantitative analyses can begin. In addition, the differential reflectivity, which is defined as the decibel difference of reflectivities at horizontal and vertical polarizations ($Z_{dr} = Z_h - Z_v$, dB; Seliga and Bringi, 1976), must be corrected for the differential attenuation ($\alpha_{hv} = \alpha_h - \alpha_v$, dB) where α_v (dB) is the attenuation at vertical polarization through a rain medium.

1.1. Background material on polarimetric radar attenuation correction schemes

Aydin et al. (1989) derived an empirical relationship to estimate A_h (specific horizontal attenuation) from Z_h and Z_{dr} and developed an attenuation estimation algorithm for C-band data. The empirical relationship relating attenuation to Z_h and Z_{dr} is less sensitive to variations in the drop size distribution (DSD) than past relationships relying on Z_h alone (Aydin et al., 1989). This approach has recently been modified, extended to include a correction for α_{hv}, and tested at C-band by Gorgucci et al. (1996; 1998). Except for the empirical relationship relating α_h (or α_{hv}) to the radar measurements, attenuation (or differential attenuation) correction schemes utilizing Z_h and Z_{dr} are similar in procedure to the original proposal by Hitschfeld and Bordan (1954) and therefore suffer from some of the same sensitivities. For example, these algorithms use radar measurands at all (n-1) radar gates that are adversely affected by propagation effects themselves (e.g., Z_h and Z_{dr}) in order to estimate the attenuation or differential attenuation at the n_{th} gate. As first noted by Aydin et al. (1989) and later by Gorgucci et al. (1996; 1998), these propagation

correction methods are therefore very sensitive to biases, including calibration errors, in the measurements of Z_h and Z_{dr}.

Holt (1988) and Bringi et al. (1990) proposed an alternative approach to correct Z_h (Z_{dr}) for the deleterious effects of α_h (α_{hv}) which utilizes an estimate of the differential propagation phase (ϕ_{dp}) through the rain medium. The differential propagation phase represents the difference in the phase shift between horizontally and vertically polarized waves as they propagate through a rain medium (e.g., Oguchi, 1983). Holt (1988) and Bringi et al. (1990) demonstrated that α_{hv} and ϕ_{dp} are approximately linearly related at precipitation radar frequencies (3 - 10 GHz). In addition, Bringi et al. (1990) showed that the relationship between α_h and ϕ_{dp} is also approximately linear at these frequencies. This method for estimating the attenuation and differential attenuation using the differential propagation phase has two distinct advantages over the power-based methods discussed above. The differential propagation phase is 1) unaffected by attenuation as long as the returned power is above the noise power and 2) independent of radar calibration errors (e.g., Zrnic' and Ryzhkov, 1996).

The accuracy of the correction procedure depends on 1) variability in the drop size distribution (Bringi et al., 1990; Jameson, 1991a; Keenan et al., 1998a), 2) deviations from the assumed temperature (Jameson, 1992; Aydin and Giridhar, 1992), 3) departures from the postulated drop shape vs. size relationship (Keenan et al., 1998a) 4) non-zero values of the backscatter differential phase (δ) between horizontal and vertical polarizations (Jameson and Mueller, 1985; Aydin and Giridhar, 1992), and 5) errors in the estimation of ϕ_{dp} due to measurement fluctuations (Bringi et al., 1990). These sensitivities limit the physical distance (or accumulated propagation phase shift) over which the correction can be applied successfully (Bringi et al., 1990; Jameson, 1991a; Jameson, 1992).

Based on scattering simulations, Bringi et al. (1990) estimated the correction accuracy for horizontal attenuation and differential attenuation to be within 30% and 35% respectively of the mean at C-band. This implies that the horizontal reflectivity and differential reflectivity could be estimated to within acceptable error limits, of 1 dB and 0.3 dB respectively, if $\phi_{dp} \leq 60°$. Jameson (1991a) clearly demonstrated the sensitivity of the

method to variations in the DSD. Jameson (1991a) concluded that the specific differential phase (K_{dp}) could be used to extend the range over which useful measurements of Z_h and Z_{dr} can be obtained at C-band. However, due to residual errors in the method, Jameson (1991a) also concluded that the corrected Z_h and Z_{dr} are more suitable for qualitative microphysical applications than quantitative rainfall estimation, except at short penetration ranges (e.g., < 40 km) or in light rain. Since attenuation is dominated by temperature sensitive molecular absorption at C-band for typical drop sizes whereas differential phase shift is not strongly dependent on temperature, the relationship between ϕ_{dp} and α_h (or α_{hv}) is therefore a sensitive function of temperature (Jameson, 1992). As shown in Jameson (1992), the amount of attenuation or differential attenuation for a fixed value of differential propagation phase increases for decreasing temperature. Jameson (1992) demonstrated that the standard error for estimating α_h and α_{hv} based on ϕ_{dp} increases significantly at 5 GHz if temperature effects are neglected. As noted in Jameson (1992), accurate estimates of precipitation temperature would be difficult to achieve, particularly since a wide range of temperatures occur in a typical radar echo volume. As a result, it may be difficult to reduce this error source in practice.

Using disdrometer measurements of raindrop size distributions from Boulder, CO, Aydin and Giridhar (1992) developed power law equations for estimating the specific horizontal attenuation (A_h) and the specific differential attenuation (A_{hv}) from K_{dp} at C-band. They also noted significant sensitivity to raindrop temperature. They emphasized the need to separate the backscatter differential phase (δ) from the measured, total differential phase (Φ_{dp}) before calculating K_{dp} (from ϕ_{dp}) since δ can be significant at C-band (e.g., Hubbert et al., 1993; Hubbert and Bringi, 1995). Using disdrometer measurements of DSDs collected over the Tiwi Islands during the Maritime Continent Thunderstorm Experiment (MCTEX; Keenan et al., 1994; 1996), Keenan et al. (1998a) conducted a sensitivity analyses of C-band polarimetric variables in tropical rainfall. In this study, Keenan et al. (1998a) showed that the K_{dp}-based estimation of attenuation and differential attenuation is sensitive to the assumed drop size versus drop shape relationship and to the presence of large drops at C-band. Their study demonstrates that the application of an incorrect raindrop axial ratio versus equivolume drop diameter

relationship can result in a significant bias in $A_h(K_{dp})$ and $A_{hv}(K_{dp})$. In addition, Keenan et al. (1998a) concluded that the occurrence of large drops as manifested by an increased maximum drop diameter (D_{max}) and/or median volume drop diameter (D_0) leads to a significant enhancement in the attenuation and differential attenuation at C-band. As a result, large drops can cause significant local increases of attenuation (or differential attenuation) over very short paths, thereby increasing the standard error of the A_h and A_{hv} estimates using K_{dp}.

1.2. Motivation and purpose

Many of the primary scientific objectives of MCTEX (Keenan et al., 1994) require accurate correction of propagation effects in the Bureau of Meteorology Research Centre (BMRC) C-band polarimetric radar (C-pol; Keenan et al., 1998b) observations of tropical island convection. These objectives include convective initiation and lifecyle studies (Carbone et al., 1999; Wilson et al., 1999), the improvement of ground based rainfall algorithms at C-band (May et al., 1998; Keenan et al., 1998a), the quantification of microphysical processes and hydrometeor distributions (Part III of this study; Keenan et al., 1998a), and the investigation of cloud electrification mechanisms and the relationship between lightning and precipitation (Part III of this study).

Despite the sensitivities and potential sources of error reviewed in Sec. 1.1, the attenuation correction method utilizing the specific differential phase has been applied by several investigators to both simulated and actual Z_h and Z_{dr} radar data measured at C-band (Scarchilli et al., 1993; Tan et al., 1995; Gorgucci et al., 1998; Keenan et al., 1998b; May et al., 1998) and S-band (Torlaschi and Holt, 1993; Ryzhkov and Zrnic', 1994, 1995a, and 1996a,b; Tan et al., 1995; Ryzhkov et al., 1997; Smyth and Illingworth, 1998) with some success. In several of the above studies, quantitative improvements in the estimated rain rate using propagation corrected Z_h and/or Z_{dr} were achieved (e.g., Ryzhkov and Zrnic', 1995a; Ryzhkov et al., 1997; Gorgucci et al., 1998; May et al., 1998; Smyth and Illingworth, 1998). Given the calibration sensitivities of the power-based attenuation correction algorithms discussed above and based on the initial successes of the

above studies, we chose to utilize the phased-based propagation correction scheme in our C-band polarimetric radar studies of tropical island convection during MCTEX.

Initially, we had intended to use published relationships for $A_h(K_{dp})$ and $A_{hv}(K_{dp})$ for correcting Z_h and Z_{dr} respectively. However, it quickly became apparent that such a choice was not a simple matter and required knowledge regarding the DSD, temperature, and drop shape versus size relationship on temporal and spatial scales that were not available. Figs. 1.1a,b depict a sample of the range of $A_h(K_{dp})$ and $A_{hv}(K_{dp})$ relationships available in the literature for C-band. For a given value of the specific differential phase, there is *at least a factor of two* variability in the estimate of A_h (Fig. 1.1a) and A_{hv} (Fig. 1.1b). As discussed in Sec. 1.1, this variability (and hence potential error) in the estimates of attenuation and differential attenuation is the result of varying temperatures, DSDs, and drop shape relationships utilized in the scattering simulation studies from which these equations were obtained.

As a result, we adapted an *empirical* correction method utilizing the slope of the linear relationship between the observed differential propagation phase (ϕ_{dp}) and the propagation affected Z_h (Z_{dr}) to estimate "correction factors" which are then used to estimate α_h (α_{hv}) throughout the radar echo volume. This empirical procedure was first proposed by Ryzhkov and Zrnic' (1994) for S-band radar observations. The correction scheme was further refined in Ryzhkov and Zrnic' (1995a) and applied in several S-band polarimetric radar studies of mid-latitude convection (Ryzhkov and Zrnic', 1995a, 1996a,b; Ryzhkov et al., 1997). This method has the advantage of determining the mean linear relationship between ϕ_{dp} and α_h (or α_{hv}) first proposed by Holt (1988) and Bringi et al. (1990) for a particular convective complex without *a priori* knowledge of the appropriate temperature, DSD, or drop shape versus size relationship. As will be demonstrated, this property of the empirical approach eliminates any potential bias and likely mitigates the resultant error in the correction procedure that might have occurred if inappropriate attenuation relationships from Figs. 1.1a,b had been chosen instead. In this study, we adapt, improve, and validate the empirical method proposed by Ryzhkov and Zrnic' (1995a) at S-band for use at C-band in the tropics. An alternate empirical procedure to estimate α_{hv} ray-by-ray

at S-band using the negative Z_{dr} in light precipitation behind the attenuation region was proposed recently by Smyth and Illingworth (1998).

The value of α_h (or α_{hv}) for a given ϕ_{dp} increases with both D_0 and D_{max} for a gamma drop size distribution (Holt, 1988; Jameson, 1991a; Ryzhkov and Zrnic', 1994; Smyth and Illingworth, 1998; Keenan et al., 1998a). Therefore, the error associated with using a single relationship between ϕ_{dp} and α_h (or α_{hv}) in the correction procedure becomes larger as both D_0 and D_{max} increase above the mean. This "large drop" effect is particularly important at C-band (Keenan et al., 1998a). As a result, we have extended the Ryzhkov and Zrnic' (1994, 1995a) empirical method to include a simple, "large drop correction" which extends the conditions over which a useful correction can be applied for the qualitative interpretation of C-band Z_h and Z_{dr} observations.

In Chapter 2, we formalize (Secs. 2.1 and 2.2) and demonstrate (Sec. 2.3) a phase-based empirical attenuation correction algorithm for C-band polarimetric radar observations of tropical convection. The theoretical basis for the technique is reviewed in Sec. 2.1. In Sec. 2.2, the empirical propagation correction procedure is specified. Using C-pol radar observations from MCTEX, results from the correction algorithm are reviewed and compared to theoretical expectations (Sec. 2.3). In Chapter 3 (Sec. 3.1), we demonstrate the enhanced propagation effects caused by large drops in tropical convection suggested earlier by the C-band polarimetric sensitivity studies of Keenan et al. (1998a). We propose a simple adjustment to the empirical attenuation correction method to account for the potential presence of large raindrops in tropical convection and present a preliminary demonstration of the technique (Sec. 3.2). Independent evaluations of the propagation correction algorithm using rain gauge data from the Tiwi Islands and internal consistency among the polarimetric radar observables are implemented in Chapter 4 (Secs. 4.1 and 4.2 respectively). Finally, we summarize and conclude in Chapter 5. Armed with these corrections for propagation effects, we then use C-band multiparameter radar data in Part III to investigate the role of ice processes in cloud electrification and lightning production in this tropical convection.

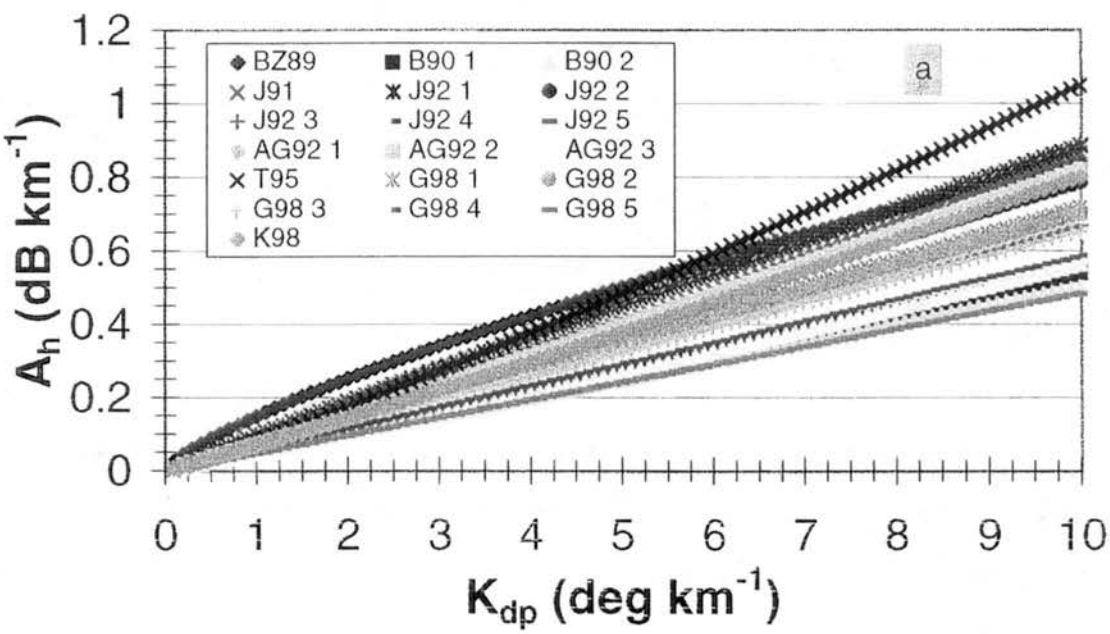

Figure 1.1. Relationship between attenuation and differential phase from available data in the literature. Plot of (a) the specific horizontal attenuation (A_h, dB km^{-1}) versus the specific differential phase (K_{dp}, deg km^{-1}). Equations were taken from published scattering simulations which utilized various drop size distributions and temperatures. BZ89 = Balakrishnan and Zrnic' (1989); B90 = Bringi et al. (1990) 1: Ulbrich (1983) DSD, 2: disdrometer DSD; J91 = Jameson (1991); J92 = Jameson (1992) 1: T = 0° C, 2: T = 10° C, 3: T = 20° C, 4: T = 30° C, 5: mean T = 0 - 30° C; AG92 = Aydin and Giridhar (1992) 1: T = 10 °C, 2: T = 0° C, 3: T = 10° C; T95 = Tan et al. (1995); G98 = Gorgucci et al. (1998) 1: T = 0.5° C, 2: T = 2° C, 3: T = 5° C, 4: T = 10° C, 5: T = 20° C; K98 = Keenan et al. (1998).

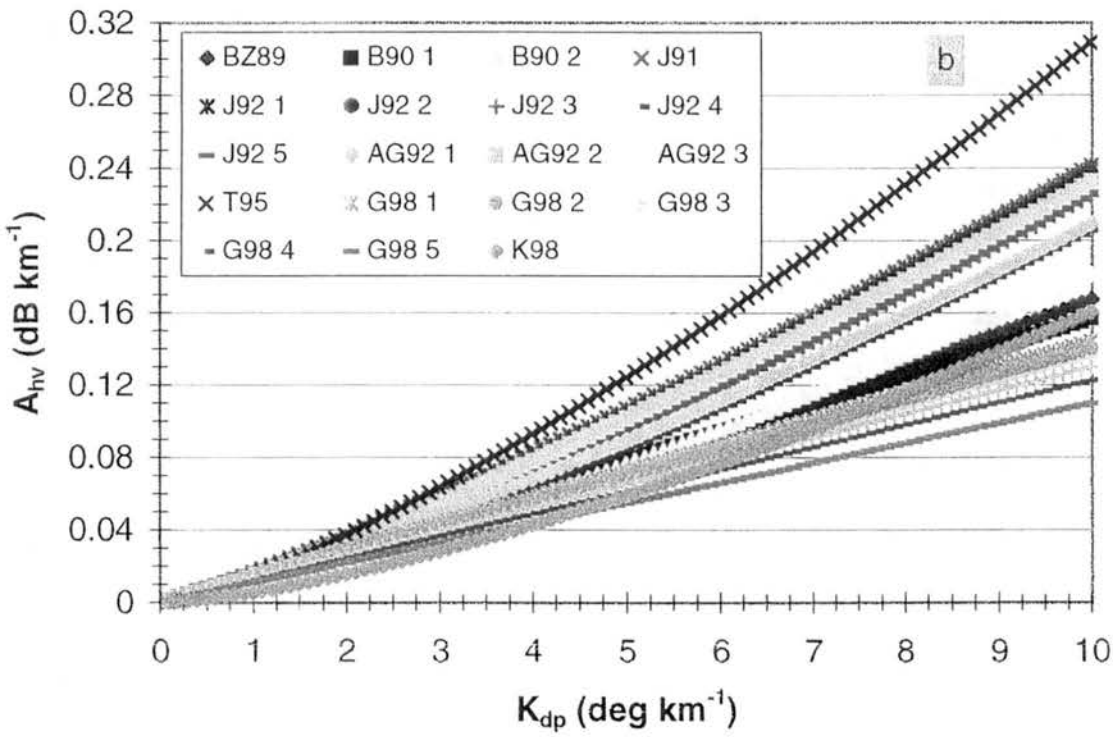

Figure 1.1. (b) as in (a) except the specific differential attenuation (A_{hv}, dB km^{-1}) versus the specific differential phase (K_{dp}, deg km^{-1}).

CHAPTER 2

MEAN EMPIRICAL CORRECTION USING DIFFERENTIAL PROPAGATION PHASE

2.1. Polarization radar data and theoretical basis

During MCTEX, observations of tropical rainfall over the Tiwi Islands (Bathurst and Melville Islands which are centered at about 11.6° S and 130.8° E ; cf. Fig. 1.1 in Part III of this study) were obtained with the BMRC C-band (5.3 cm) dual-polarimetric radar (C-pol; Keenan et al., 1998b) from 13 November to 10 December 1995. In this study, we focus on results from an intense and heavy raining tropical convective complex on 28 November 1995. An examination of the complete life-cycle of the horizontal and vertical structure of this storm as observed by the C-pol radar can be found in Part III of this study. We supplement these data with additional observations of tropical rainfall on 23 and 27 November 1995.

For C-pol radar specifications and definitions of all observed quantities, see Keenan et al. (1998b). We will review herein those definitions required for development of the empirical attenuation correction scheme which utilizes the differential propagation phase. The theoretical basis for attenuation correction schemes using the differential propagation phase (ϕ_{dp}) derives from the finding that specific attenuation (A_h) and specific differential attenuation (A_{hv}) are approximately linearly proportional to the specific differential phase (K_{dp}) at precipitation radar wavelengths (e.g., Bringi et al., 1990).

$$A_h \approx a \bullet K_{dp} \tag{2.1}$$

$$A_{hv} \approx b \bullet K_{dp} \tag{2.2}$$

Bringi et al. (1990) and more recently Gorgucci et al. (1998) derived the coefficients of proportionality (a and b) in a rain medium for C-band using scattering simulations of gamma drop size distributions (DSD) specified by Ulbrich (1983). Other investigators

(e.g., Jameson, 1991a and 1992; Aydin and Giridhar, 1992; Keenan et al., 1998) have derived power-law relationships for $A_h(K_{dp})$ and $A_{hv}(K_{dp})$ at C-band because they provide a better fit (as judged by the correlation coefficient) for broad DSDs. The exponent in these relationships is typically close to unity (1.0 to 1.3). In Chapter 3 (Sec. 3.1), we demonstrate with scattering simulations that Eqns. 2.1 and 2.2 are very accurate when the DSD is partitioned by the median volume diameter (D_0) or the differential reflectivity (Z_{dr}). Eqns. 2.1 and 2.2 imply the assumption of a single mean D_0 throughout the correction echo volume. Hence, the nomenclature of a "mean empirical correction." Analysis of C-pol radar data in Appendix D suggest that the majority of attenuation effects in tropical rainfall are caused by a propagation medium that is characterized by $0.5 \leq Z_{dr} \leq 1.5$ dB, and hence a relatively narrow range of D_0 (e.g., approximately 1 to 2 mm). For the above reasons and for methodological simplicity, a linear approximation for $A_h(K_{dp})$ and $A_{hv}(K_{dp})$ is justified. In those instances when Z_{dr} and hence D_0 are significantly larger than mean conditions, a "big drop correction" must be applied since propagation effects are enhanced in large drops (Keenan et al., 1998a), as discussed further in Chapter 3.

By definition, the two-way horizontal attenuation (α_h) and the two-way differential propagation phase (ϕ_{dp}) can be expressed as

$$\alpha_h = 2 \int_{r_1}^{r_2} A_h(r)\,dr \tag{2.3}$$

$$\phi_{dp} = 2 \int_{r_1}^{r_2} K_{dp}(r)\,dr \tag{2.4}$$

By combining Eqns. 2.1, 2.3, and 2.4, we find that $\alpha_h = a \bullet \phi_{dp}$. This result is then substituted into the definition for the intrinsic horizontal reflectivity[1] unmodified by propagation effects to obtain

$$Z_h = Z_h^{\text{int}} - \alpha_h = Z_h^{\text{int}} - a \bullet \phi_{dp}, \tag{2.5}$$

[1] The intrinsic reflectivity, Z^{int}, is the reflectivity caused solely by the scattering properties of the hydrometeors in a radar resolution volume.

where Z_h is the *measured* horizontal reflectivity. Taking the derivative of Eqn. 2.5 with respect to ϕ_{dp}, we obtain the following result (when using finite difference notation):

$$a = \frac{\Delta Z_h^{\text{int}}}{\Delta \phi_{dp}} - \frac{\Delta Z_h}{\Delta \phi_{dp}} \tag{2.6}$$

If the *intrinsic* variation of horizontal reflectivity with ϕ_{dp} can be neglected, then the correction factor '*a*' is obtained empirically by analyzing the slope of the trend of the observed Z_h with respect to ϕ_{dp}.

$$a \approx -\frac{\Delta Z_h}{\Delta \phi_{dp}} \tag{2.7}$$

The two-way differential attenuation (α_{hv}) defined as

$$\alpha_{hv} = 2 \int_{r_1}^{r_2} A_{hv}(r)\, dr \tag{2.8}$$

can be combined in a similar fashion with Eqns. 2.2 and 2.4 to obtain the correction coefficient '*b*' from actual radar data using the slope of the trend of Z_{dr} with ϕ_{dp}, neglecting the *intrinsic* variation of Z_{dr} with ϕ_{dp}.

$$b \approx -\frac{\Delta Z_{dr}}{\Delta \phi_{dp}} \tag{2.9}$$

As shown in the next section, the linear slopes in Eqn. 2.7 and 2.9 are determined using least squares regression on observed data. If the regression sample is of sufficient size (N $\geq$ 200), represents a range of ϕ_{dp} values ($\phi_{dp}(\max) \geq 15°$ at a minimum with best results occurring for $\phi_{dp}(\max) \geq 60°$), and is restricted to a hydrometeor type with a limited range of intrinsic Z_h and Z_{dr}, then the intrinsic variation (e.g., first term on RHS of Eqn. 2.6) contributes only to the scatter of the regression and does not bias the estimate of the slope.

Using these empirically derived correction factors, the propagation corrected horizontal reflectivity and differential reflectivity can be obtained from

$$Z_h^{cor} = Z_h + a \bullet \phi_{dp} \tag{2.10}$$

$$Z_{dr}^{cor} = Z_{dr} + b \bullet \phi_{dp}, \tag{2.11}$$

where Z_h and Z_{dr} are the *observed* quantities.

2.2. Method

Before analysis can begin, regions of spurious polarimetric radar data must be carefully identified and removed. The data processing and quality control procedures for this study are detailed in Appendix A. The mean attenuation correction procedure described in this section[2] can be applied to polarimetric radar data in either Cartesian gridded format or spherical radar coordinates. Since many atmospheric scientists are accustomed to working with gridded data, the ability to perform this phased-based procedure with ease on Cartesian radar data is an additional advantage over the traditional power-based correction algorithms which typically require a ray-by-ray approach. Details regarding the interpolation of radar data on to Cartesian grids can be found in Appendix A.

Although the correction method suggested by the theory presented in Sec. 2.1 above is simple in principle, implementation of the technique with real radar data requires careful consideration of the assumptions made in the derivation of Eqns. 2.7 and 2.9. First, a linear dual-polarimetric radar such as C-pol measures the total differential phase (Φ_{dp}; Jameson and Mueller, 1985)

$$\Phi_{dp} = \delta + \phi_{dp} + \phi_0 \tag{2.12}$$

which must be separated into the backscatter differential phase (δ), the differential propagation phase (ϕ_{dp}), and the system offset phase (ϕ_0). The system offset phase is a known engineering quantity and can be simply subtracted from the phase measurement. At C-band, the backscatter differential phase associated with Mie resonance can be significant, depending on the value of the maximum drop diameter (e.g., Bringi et al., 1990, 1991; Aydin and Giridhar, 1992; Hubbert et al., 1993; Keenan et al., 1998a). Scarchilli et al. (1993) applied an iterative attenuation correction procedure at C-band which solves for δ as a function of Z_{dr} using a 3rd-order polynomial fit. However, Aydin

[2] The procedure described in Chapter 3 which corrects for the enhanced propagation effects caused by large raindrops is accomplished on a ray-by-ray basis in spherical radar coordinates.

and Giridhar (1992) demonstrated that the parameterization of δ is a very sensitive function of the DSD parameters, especially the assumed maximum drop diameter. Therefore, we applied a filtering procedure to remove the contribution of δ to Φ_{dp} and thereby isolate ϕ_{dp} (e.g., Balakrishnan and Zrnic', 1990; Hubbert et al., 1993; Hubbert and Bringi, 1995). More details regarding this procedure and the estimation of K_{dp} and its accuracy can be found in Appendix A.

Second, we utilized all available multiparameter variables to minimize the intrinsic variation in the Z_h and Z_{dr} samples before determining the correction coefficients in Eqns. 2.7 and 2.9. The goal is to develop a procedure which isolates a particular class of hydrometeors for which the intrinsic (i.e., non-propagation) variations in Z_h and Z_{dr} are mitigated. In other words, the procedure should minimize the scatter about the slope of Z_h (Z_{dr}) versus ϕ_{dp} (i.e., the first term on the right hand side of Eqn. 2.6) such that the effects of attenuation (differential attenuation) are clearly represented (i.e., the second term on the right hand side of Eqn. 2.6). As shown later in Sec. 2.3, failure to minimize the intrinsic scatter of Z_h (Z_{dr}) about ϕ_{dp} can result in a significantly biased estimate of $a = A_h/K_{dp}$ ($b = A_{hv}/K_{dp}$). This goal must be balanced with the requirement to obtain a statistically significant (i.e., sufficiently large) sample of Z_h (Z_{dr}) observations from which a meaningful regression line between Z_h (Z_{dr}) and ϕ_{dp} can be fit. As will be demonstrated below, small sample sizes or samples for which the maximum ϕ_{dp} is below some threshold can also seriously compromise the inferred correction coefficients a and b. Assuming that the scatter of Z_h (Z_{dr}) about ϕ_{dp} is effectively minimized and that the sample size is sufficiently large, the method is not overly sensitive to the particular class of hydrometeors that is isolated. This insensitivity is demonstrated using sensitivity studies in Appendix C.

We utilized specific intervals of K_{dp}, δ, and the correlation coefficient at zero-lag between horizontally and vertically polarized electromagnetic waves (ρ_{hv}) in order to isolate a hydrometeor type which is characterized by a limited range of Z_h and Z_{dr}. Ryzhkov and Zrnic' (1995a) used S-band radar data characterized by a narrow interval of K_{dp} between 1 and 2° km^{-1}. In order to choose appropriate ranges for C-band observations of K_{dp}, δ, and ρ_{hv} in tropical convection, we simulated radar observables (Z_h,

Z_{dr}, K_{dp}, δ, and ρ_{hv}) utilizing DSD data measured with a disdrometer during MCTEX (Keenan et al., 1998a) as input to the T-matrix scattering model (Barber and Yeh, 1975). The reader is referred to Appendix B for specific details and assumptions of the scattering simulations in this study.

From these scattering simulations, we present plots of Z_h and Z_{dr} versus K_{dp} in Figs. 2.1a and 2.1b respectively. As in other scattering simulations of rain at C-band (e.g., Aydin and Giridhar, 1992; Keenan et al., 1998a), Z_h is a logarithmic function of K_{dp}. Note that the range of possible values of Z_h for 1° km^{-1} intervals of K_{dp} is much larger at the low end of K_{dp}. This is especially true if we partition the scatterplot in Fig. 2.1a using ρ_{hv} and δ. The solid (open) squares in Figs. 2.1a,b are characterized by $\rho_{hv} > 0.97$ and $\delta < 1°$ ($\rho_{hv} \leq 0.97$ and $\delta \geq 1°$). As shown in Aydin and Giridhar (1992) and Keenan et al. (1998a), DSD's distinguished by lowered values of ρ_{hv} and large δ have large values of the median volume diameter (D_0) and hence large Z_{dr}. As shown in Fig. 2.1b, the open (solid) squares are characterized by a mean Z_{dr} of 4 dB (0.7 dB) with a range of 2.5 to 5.4 dB (0.2 to 2.6 dB). Essentially, it is possible to separate DSD's containing large drops from those which do not. By removing those DSD's characterized by lowered ρ_{hv} and significant δ (i.e., removing DSD's with large D_0), the scatter of Z_h for a given interval of K_{dp} is significantly reduced. Using this restricted sample, the range of Z_h for $0.5 \leq K_{dp} \leq 1.5°$ km^{-1} is 36 - 46 dBZ. In comparison, Z_h ranges from 42 to 48 dBZ for K_{dp} between 1 and 2° km^{-1}. In general, the range of Z_h values for a given K_{dp} interval decreases with increasing K_{dp}. Similarly, the range of Z_{dr} values which have been restricted by $\rho_{hv} > 0.97$ and $\delta < 1°$ also decreases with increasing K_{dp} (Fig. 2.1b).

Therefore, the use of a 1° km^{-1} interval of K_{dp} above $K_{dp} = 2°$ km^{-1} would minimize the scatter of Z_h and Z_{dr} about ϕ_{dp}. However, the need to minimize the intrinsic scatter must be balanced by the need for a sufficiently large sample to obtain a representative slope described by Eqns. 2.7 and 2.9. Using Eqn. E.2, these values of K_{dp} would correspond to rain rates in excess of 40 mm h^{-1}. Our experience indicates that there are often insufficient grid points characterized by these high rain rates to obtain a good regression. In general, the K_{dp} interval utilized by Ryzhkov and Zrnic' (1995a) at S-band of 1 to 2° km^{-1} is

typically a good compromise at C-band as well. Inspection of Figs. 2.1a,b suggest that most values of Z_h (Z_{dr}) should be between 41 and 45 dBZ (0.75 and 1.5 dB). Of course, there are other possibilities. Due to the rapid change of Z_h with K_{dp} for $K_{dp} < 1°$ km^{-1}, it is important to reduce the size of the K_{dp} interval if small values of K_{dp} are utilized. For samples characterized by higher rain rates, we recommend a larger K_{dp} interval in order to increase the sample size. Some of these options are explored in a sensitivity test of the method in Appendix C.

When applying this procedure to actual radar data, one must account for the performance of the radar in determining the actual ρ_{hv} and δ thresholds. Based on the performance of the C-pol radar (Keenan et al., 1998b) and a detailed inspection of the data, we chose to restrict the regression using $\rho_{hv} > 0.95$, $| \delta | < 5°$, and $1 \leq K_{dp} \leq 2°$ km^{-1} at grid levels between 0.5 and 2.0 km AGL (above ground level). The effect of varying the regression sample by changing the K_{dp}, ρ_{hv}, δ, and altitude thresholds was explored in a series of sixteen sensitivity tests as summarized in Appendix C. As shown in Appendix C, the above polarimetric and height thresholds (Test 1) provided the most reliable and statistically superior (i.e., low standard error, high coefficient of correlation, and large sample size) least squares fit to the data. Using these thresholds, regression samples for Z_h and Z_{dr} versus ϕ_{dp} are shown in Figs. 2.2a,b respectively for 0416 UTC (all times UTC herein after) on 28 November 1998.

In both Figs. 2.2a,b, there is an unmistakably decreasing trend of Z_h and Z_{dr} with ϕ_{dp} due to the effects of horizontal and differential attenuation respectively. The slope of Z_h (Z_{dr}) versus ϕ_{dp} for the unrestricted sample (N = 1099) is -0.071 dB deg^{-1} (-0.0199 dB deg^{-1}). There is significant scatter of Z_h (4.4 dB) and Z_{dr} (0.5 dB) about a least squares fit to the data. This scatter is generally consistent with the simulated data presented in Figs. 2.1a,b. In addition, there are obvious outliers from the linear fits. For example, the low values of Z_h (< 32 dBZ) at relatively low ϕ_{dp} (< 20°) in Fig. 2.2a are inconsistent with the theoretical expectations (c.f., Fig. 2.1a) for Z_h at these ranges of K_{dp}. Enhanced attenuation due to the presence of large raindrops may have caused the presence of these outliers (see Chapter 3). However, it is also possible that errors in the estimated K_{dp} due

to partial beam filling (Ryzhkov and Zrnic', 1998a) resulted in the erroneous inclusion of these data points into the regression sample. In Fig. 2.2b, there are also obvious outliers from the general decreasing trend of Z_{dr} with ϕ_{dp} (e.g., $Z_{dr} < 0.5$ dB and $Z_{dr} > 2.5$ dB for $\phi_{dp} < 15°$). The presence of outliers such as these can seriously bias the inferred correction coefficient.

The final step in determining the correction coefficients '*a*' and '*b*' is to eliminate outliers from the linear assumption implicit in the derivation of Eqns. 2.7 and 2.9. Based on the example above and the findings from prior scattering studies reviewed in Chapter 1 (Sec. 1.1), outliers in plots of Z_h and Z_{dr} versus ϕ_{dp} can be the result of 1) variations in precipitation temperature (Jameson, 1992), 2) variations in the DSD of the propagation medium (Jameson, 1991a), 3) failure to minimize the intrinsic scattering properties of hydrometeors within the regression sample using the above thresholds, 4) the approximate nature of the linear assumption given in Eqns. 2.1 and 2.2 (Jameson, 1991a), and 5) errors in the actual data. In order to avoid biasing the mean correction coefficients for each radar volume, these outliers must be removed using simple statistics.

We utilized the standard error of the estimate (S) of Z_h (Z_{dr}) on ϕ_{dp} from a least squares regression line to restrict the sample. We began by removing data outside of $2 \bullet S$ from the regression line if $\rho < 0.9$.[3] We continued to restrict the sample incrementally by $0.2 \bullet S$ until $\rho \geq 0.9$ or the data was restricted to within S of the original regression line. Once the restricted sample was obtained, we recalculated the best fit slope to the data using least squares regression. An example of the restricted data sets from 0416 and their associated regression lines are presented in Figs. 2.2a,b for Z_h vs. ϕ_{dp} and Z_{dr} vs. ϕ_{dp} respectively.

Frequently, the slope resulting from the least squares fit to the restricted sample is somewhat different than the original slope. This was the case for Z_h vs. ϕ_{dp} at 0416 as shown in Fig. 2.2a. The final slope of -0.081 dB deg^{-1} is 14% lower than the original slope of Z_h vs. ϕ_{dp}. When a good slope could be determined, the final slope Z_h/ϕ_{dp} differed

[3] The coefficient of correlation (ρ) of a least squares regression line should not be confused with ρ_{hv}, which is the correlation coefficient at zero-lag between horizontally and vertically polarized backscattered electromagnetic radiation measured by the radar.

by no more than 18% from the initial, unrestricted slope. The mean change in Z_h/ϕ_{dp} due to restricting the sample was 9%. Sometimes outliers did not bias the least squares fit and the regression slope did not change significantly after restricting the sample, as for Z_{dr} vs ϕ_{dp} in Fig. 2.2b. For the entire data set, retrieved slopes of Z_{dr}/ϕ_{dp} changed by up to 16% with a mean change of 5%. Once the final regression slopes are determined as in Figs. 2.2a-b, the correction coefficients *a* and *b* in Eqns. 2.7 and 2.9 are simply the negative of these two respective slopes. Restricting the regression sample minimized the potential bias in the correction coefficients and was therefore a necessary step. However, the relatively small (< 20 %) statistical variation in the coefficients *a* and *b* compared to the potential factor of two or more natural variability (cf Figs. 1.1a,b) suggests that the above method is sound and reliable. Further investigations into the regression procedure and its performance can be found in Appendix C.

In order to eliminate significant errors in the propagation corrected Z_h and Z_{dr}, it is important to assess the representativeness of each *a* and *b*. The y-intercepts from the restricted data sets in Figs. 2.2a,b should be representative of the propagation-free, intrinsic value of Z_h and Z_{dr} respectively. The y-intercept for Z_h (Z_{dr}) is approximately 42 dBZ (1.3 dB) which is generally consistent with the median value of the scattering simulation results in Fig. 2.1a (2.1b) for $1 \leq K_{dp} \leq 2°$ km^{-1}. Before utilizing the correction coefficients, we required the coefficient of correlation (ρ), the number of data points in the final regression sample (N), the standard error (*S*), and the maximum observed ϕ_{dp} to meet the following thresholds: $\rho^2 \geq 0.25$ for *a* ($\rho^2 \geq 0.6$ for *b*), $N \geq 200$, $S \leq 5.5$ dB for *a* ($S \leq 0.55$ dB for *b*), and $\phi_{dp}(max) \geq 15°$. If all of these conditions were met, then the inferred *a* and *b* were used. Otherwise, alternate correction coefficients were determined. If possible, we utilized an interpolation of *a* and *b* from adjacent times. As a last resort, we used the median of all successfully determined correction coefficients.

Once correction coefficients *a* and *b* were identified for each radar volume, the correction was applied to Z_h (Z_{dr}) at each radar gate (or Cartesian grid point) as specified in Eqn. 2.10 (2.11). A summary of this propagation correction procedure in the form of a flow-chart can be found in Steps 1 - 4 in Fig. 2.3. This portion of the algorithm is referred to as the "mean correction" because it is equivalent to assuming a single, mean D_0 for the

radar volume. This will be demonstrated in Chapter 3 (Sec. 3.1). Occasionally, the presence of convective cores containing raindrops which are significantly larger than mean conditions in the radar volume (e.g., $D_0 > 2.5$ mm or $Zdr \geq 3$ dB) necessitate an extension of this method to account for the enhanced propagation effects in large drop cores (Keenan et al., 1998a). The extension to the mean correction (steps 5 - 6 in Fig. 2.3) will be explored in Chapter 3. First, results from the mean correction are reviewed.

2.3. Results

Horizontal cross-sections of pre-corrected Z_h and Z_{dr} at 2 km associated with Figs. 2.2a,b are presented in Figs. 2.4a,b respectively. We chose data from 0416 on 28 November 1995 because the convection was mature, widespread, and intense. By this time, precipitation had merged on the mesoscale (reference Part III of this study). Intense convective cores were embedded throughout the mesoscale convective system. Even prior to propagation correction, peak reflectivities and differential reflectivities in these cores ranged from 50 to 55 dBZ and 2.5 to 4 dB respectively.

Typically, the effects of attenuation on Z_h are not readily apparent at C-band via visual inspection (Fig. 2.4a). However, differential attenuation visibly decreases the differential reflectivity in range (Fig. 2.4b). Large areas of negative Z_{dr}, sometimes as low as -2 dB, are apparent on the backside of the convection down range from the radar. Note that the lowest values of Z_{dr} on the back edge of the convection are not necessarily furthest from the radar nor are they always behind the largest precipitation echo path. Typically, the greatest propagation effects discernible in Z_{dr} are down range from intense convective cores characterized by large values of reflectivity ($Z_h > 50$ dBZ) and differential reflectivity ($Z_{dr} > 2$ dB), suggesting the presence of large raindrops. These "large drop cores" create readily apparent range "shadows" of lowered Z_{dr} relative to their immediate surroundings. One example of a shadow in Z_{dr} down range of an intense convective core is highlighted in Figs. 2.4b, 3.5a, and 3.6a.

A horizontal cross-section at 2 km of differential propagation phase for 0416 UTC is shown in Fig. 2.5. Comparison of Figs. 2.4b and 2.5 further demonstrates the anti-correlation between ϕ_{dp} and Z_{dr}. As shown earlier in Fig. 2.2b, increasing values of ϕ_{dp} are

generally associated with decreasing Z_{dr} as a result of differential attenuation. Maximum ϕ_{dp} exceeds 120° at this time. Interestingly, this peak occurs less than 50 km in range from the radar. During 28 November 1995, the maximum ϕ_{dp} exceeded 200° several times.

As shown in Chapter 2 (Sec. 2.1), the differential propagation phase is linearly proportional to both the path integrated horizontal and differential attenuation where *a* and *b* respectively are the constants of proportionality. By multiplying ϕ_{dp} by a = 0.081 and b = 0.0196 (as determined in Figs. 2.2a,b), estimates of α_h and α_{hv} were obtained (Fig. 2.5). Maximum estimates of α_h and α_{hv} at 2 km exceed 9 dB and 2 dB respectively. Approximately 26 % of the echo is characterized by significant attenuation (α_h > 1 dB) and differential attenuation (α_{hv} > 0.25 dB). Five percent of the precipitation echo experienced severe propagation effects (e.g., defined here as α_h > 4 dB and α_{hv} > 1 dB).

Using the above estimates of propagation effects at 0416 UTC, the corrected Z_h and Z_{dr} were calculated according to Eqns. 2.10 and 2.11 (Figs. 2.6a,b respectively). As expected, a comparison of Figs. 2.4a,b to Figs. 2.6a,b respectively reveals significant differences between observed Z_h/Z_{dr} and propagation corrected Z_h/Z_{dr} in regions of significant ϕ_{dp} (Fig. 2.5). Most notable is the elimination of most negative values of Z_{dr} in Fig. 2.6b. Another striking difference is the increased area of precipitation echo characterized by Z_{dr} > 1 dB, particularly in the north-to-south oriented complex centered on x = 75 km and in the cells located 20 - 50 km to the north-northeast of the radar (Fig. 2.6b). Similarly, the precipitation echo characterized by Z_h > 40 dBZ also has been substantially enhanced (Fig. 2.6a) in these convective complexes.

To examine the effects of the correction algorithm in three dimensions at 0416 UTC, CFAD's (Contoured Frequency by Altitude Diagrams; Yuter and Houze, 1995) of the pre- and post-corrected Z_h and Z_{dr} are presented in Figs. 2.7a and 2.7b respectively. As expected, the correction algorithm primarily affects the lower half of the precipitation echo (< 9 km). Below the melting level (5 km), the 1% contour in the Z_h CFAD (Fig. 2.7a) is shifted approximately 2 dB higher. In other words, 1% of the pre-corrected (post-corrected) echo at a given level is characterized by reflectivities in excess of 44 - 46 dBZ (46 - 48 dBZ). Inspection of Fig. 2.7b shows that most of the anomalously negative (<

-0.5 dB) Z_{dr} present in the original observations were removed by the mean empirical correction procedure. In the pre-corrected data, 1% of the Z_{dr} values below the melting level are less than -1 dB. In the propagation corrected data set, less than 0.1% of the data is characterized by $Z_{dr} < -1$ dB and the 1% line, on the negative side, ranges from -0.25 to -0.5 dB below the melting level. In addition, the correction algorithm shifted the mode of Z_{dr} higher by 0.5 dB at heights below 7 km AGL. For example, the greater than 10% frequency space for the pre-corrected Z_{dr} data at 0.5 km AGL ranges from -0.25 to 0.75 dB. After the correction procedure, the greater than 10% frequency contour for Z_{dr} near the surface brackets the space from 0.25 to 1.25 dB. Similar shifts in the mode occurred at all heights below the melting level.

The procedure summarized in Steps 1 - 4 of Fig. 2.3 was applied to 51 polarimetric radar volumes occurring between 0206 and 0802 UTC on 28 November 1995. Of the 51 polarimetric radar volumes, 61% yielded reliable correction coefficients. Most of the reliable estimates of *a* and *b* were obtained during the mature stage (0330 - 0630) of the tropical convection when there were ample propagation effects and widespread convection. During the developing and decaying stage, there were often too few samples with significant attenuation to obtain good regression slopes. For these times, alternate correction coefficients were determined as described above. We chose this approach, as opposed to not correcting the data, because significant propagation effects (α_h = 1 dB and α_{hv} = 0.25 dB) can occur for just 10° to 15° of differential propagation phase which almost always occurred in at least one range ray somewhere over the islands. Fortunately, when propagation effects became larger and more widespread, the method always yielded a useable estimate of *a* and *b*.

Histograms of the inferred correction coefficients *a* and *b* for 28 November are shown in Figs. 2.8a and 2.8b respectively. The estimated values of *a* range from 0.057 to 0.11 dB deg^{-1}. The mean and median of *a* are both 0.089 dB deg^{-1}. Most inferred values of *a* range from 0.08 to 0.10 dB deg^{-1}. Retrieved values of *b* range from 0.012 to 0.030 dB deg^{-1}. The mean and median *b* are 0.018 and 0.017 dB deg^{-1} respectively. A majority of estimated values of *b* range from 0.014 to 0.022 dB deg^{-1}. Statistics for the correction coefficients, *a* and *b*, for 28 November are summarized in Tables 2.1 and 2.2 respectively.

Table 2.1. Summary of statistics for C-band correction coefficient $a = A_h/K_{dp}$ (dB deg^{-1}) from MCTEX 28 Nov 95; MCTEX 23, 27, and 28 Nov 95 combined; and a literature survey.

a (dB deg^{-1}) statistics	*28 Nov 95*	*23, 27, 28 Nov 95*	*literature**	*literature* 10 < T < 25 °C*
Mean	0.0885	0.0932	0.0688	0.0591
Standard Error	0.0025	0.0031	0.0032	0.0033
Standard Deviation	0.0137	0.0229	0.0153	0.0115
Median	0.0890	0.0901	0.0681	0.0551
Minimum	0.0568	0.0557	0.0426	0.0426
Maximum	0.1113	0.1493	0.1011	0.0789
Count	31	55	23	12

* The literature statistics were derived from the relationships presented in Fig. 1.1a. When necessary, power-based equations were linearized for comparison using a curve fitting procedure.

Table 2.2. Summary of statistics for C-band correction coefficient $b = A_{hv}/K_{dp}$ (dB deg^{-1}) from MCTEX 28 Nov 95; MCTEX 23, 27, and 28 Nov 95 combined; and a literature survey.

b (dB deg^{-1}) statistics	*28 Nov 95*	*23, 27, 28 Nov 95*	*literature**	*literature* 10 < T < 25 °C*
Mean	0.01819	0.02010	0.01785	0.01617
Standard Error	0.00072	0.00057	0.00105	0.00127
Standard Deviation	0.00403	0.00435	0.00458	0.00381
Median	0.01720	0.01996	0.01680	0.01570
Minimum	0.0119	0.01190	0.01100	0.01100
Maximum	0.0299	0.03154	0.02810	0.02210
Count	31	59	19	9

* The literature statistics were derived from the relationships presented in Fig. 1.1b. When necessary, power-based equations were linearized for comparison using a curve fitting procedure.

For reference, we have supplemented these statistics with results from two other days during MCTEX (23 and 27 November). Statistics for the three combined days are presented in Tables 2.1 and 2.2. Note that the 3-day mean and median values for *a* and *b* are very similar to those for 28 November (i.e., vary by less than 15%) and the overall ranges of the correction coefficients are comparable. The stability in the MCTEX correction coefficient statistics presented in Tables 2.1 and 2.2 suggest that the method is reliable and that the propagation characteristics (e.g., DSD, temperature, drop shape versus size) vary within a similar range from day-to-day in tropical island convection.

For comparison, statistics for a and b obtained from scattering simulations in the published literature (cf Figs. 1.1a,b) are also include in Tables 2.1 and 2.2 respectively. These simulations represent a range of temperatures and drop size distributions. Inspection of Tables 2.1 and 2.2 demonstrates that these theoretical values of a and b have a similar range as those determined empirically from MCTEX observations. The mean and median of the literature values of a are 25% - 30% lower than those determined from MCTEX data. Similarly, the literature simulations of b are about 5 - 15 % lower than the empirically determined values in the mean. Given the range of conditions simulated in the literature statistics, it is perhaps surprising that the theoretical and empirical methods obtain reasonably similar estimates of the propagation correction coefficients.

However, closer inspection of the literature scattering simulations suggests more significant discrepancies between theory and empirical results. If we limit literature results to those temperatures which are most representative of the conditions from 0.5 to 2.0 km on 28 November (10° C to 25° C based on an atmospheric sounding at 02 UTC), then the literature mean values are reduced to a = 0.059 dB deg^{-1} and b = 0.0162 dB deg^{-1} (Table 2.1). Note that the maximum values for the coefficients a and b obtained from the literature survey for $10° \leq T \leq 25°$ C are much closer to the *mean* empirical results from MCTEX. In some studies such as Bringi et al. (1990) and Gorgucci et al. (1998), the disagreements with our empirical results are even more serious, particularly for b. In these two studies which utilize similar assumptions regarding the drop size distribution, the simulated values of a (b) range from 0.050 to 0.059 dB deg^{-1} (0.0110 to 0.0157 dB deg^{-1}) for the range of temperatures given above. These values are a factor of 1.6 to 1.9 smaller than the 3-day empirical means for the coefficients a and b from MCTEX.

Similar discrepancies between theoretically and experimentally derived estimates of $a = A_h/K_{dp}$ and $b = A_{hv}/K_{dp}$ at S-band were reported recently by Ryzhkov and Zrnic' (1994, 1995a) and Smyth and Illingworth (1998). Both studies suggest that their higher experimentally inferred values of a and b were the result of large, oblate raindrops (e.g., $D_0 > 2.5$ mm or $Z_{dr} \geq 2.5$ dB) which were present in their observations but not accounted for in prior theoretical simulations (e.g., Bringi et al., 1990). Both Ryzhkov and Zrnic' (1994, 1995a) and Smyth and Illingworth (1998) demonstrate that the coefficients a and b

at S-band increase significantly as a function of D_0, particularly for $D_0 > 2.5$ mm. As a result, they suggest that simulations which do not include these large drops tend to underestimate the correction coefficients a and b under certain microphysical circumstances. As discussed in the next section, we have found a similar dependency of the correction coefficients a and b on drop size at C-band when DSD's including $Z_{dr} > 2$ dB are considered.

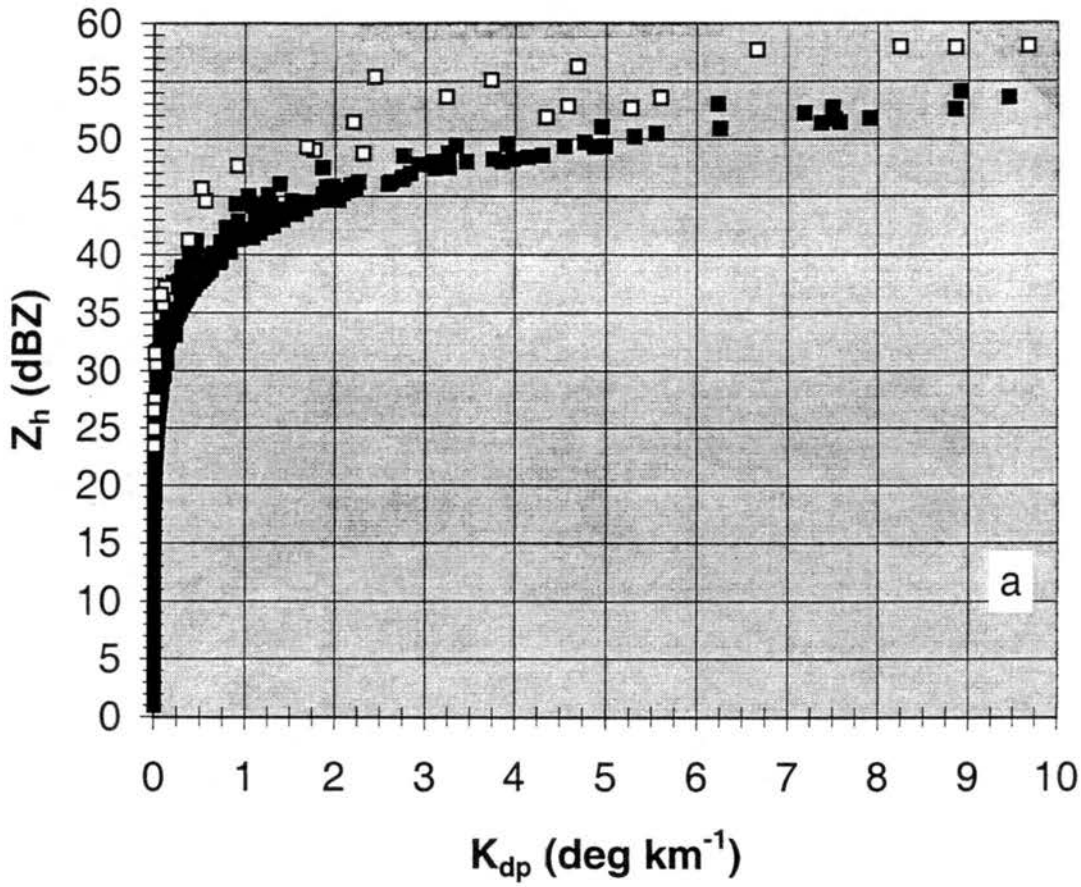

Figure 2.1. Plots of the (a) horizontal reflectivity (Z_h, dBZ) versus the specific differential phase (K_{dp}, deg km^{-1}) as taken from scattering simulations. Solid squares (open squares) are drop size distributions characterized by $\rho_{hv} > 0.97$ and $|\delta| < 1°$ ($\rho_{hv} \leq 0.97$ and $|\delta| \geq 1°$). Details regarding scattering simulations are described in Appendix B.

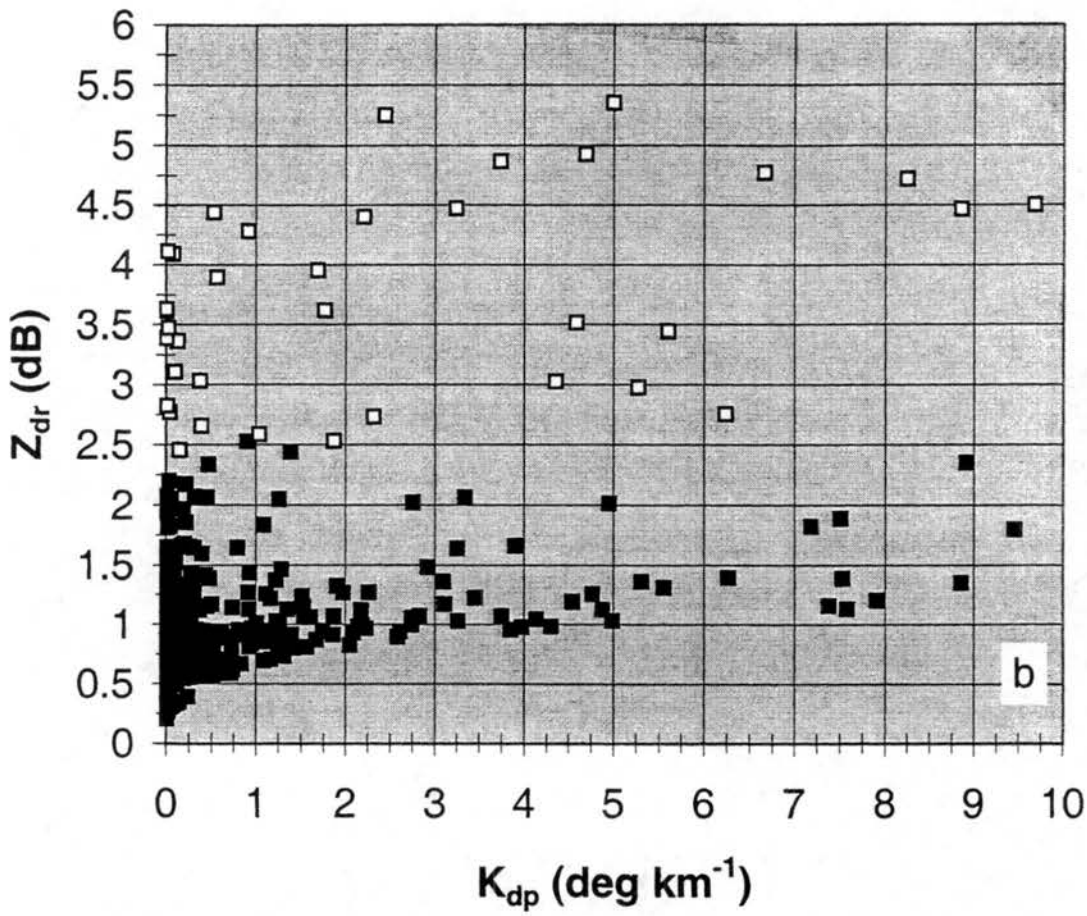

Figure 2.1. (b) as in (a) except differential reflectivity (Z_{dr}, dB) versus the specific differential phase (K_{dp}, deg km^{-1}).

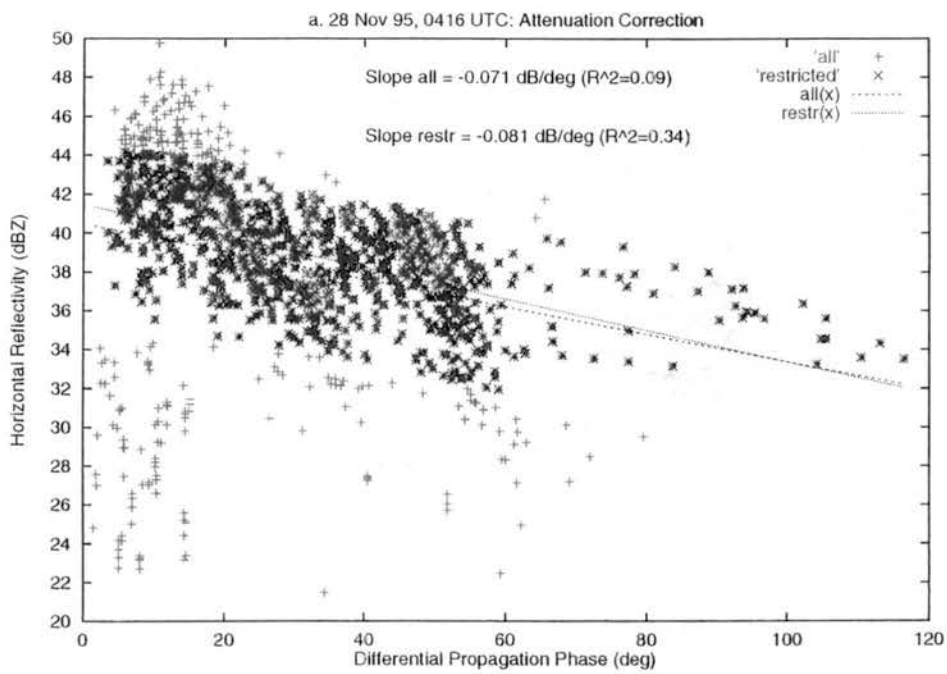

Figure 2.2. Least squares linear regression results for (a) the horizontal reflectivity (Z_h, dBZ) versus the differential propagation phase (ϕ_{dp}, deg) taken from 0416 UTC on 28 November 1995. The original data sample (+) originated from 0.5 to 2 km and met the following polarimetric radar criteria: $1 < K_{dp} < 2°$ km^{-1} , $\rho_{hv} > 0.95$, and $|\delta| < 5°$. The sample was further restricted by the standard error of the least squares estimate (X). Least square regression slopes for both samples are shown (original sample: short dash; restricted sample: dot).

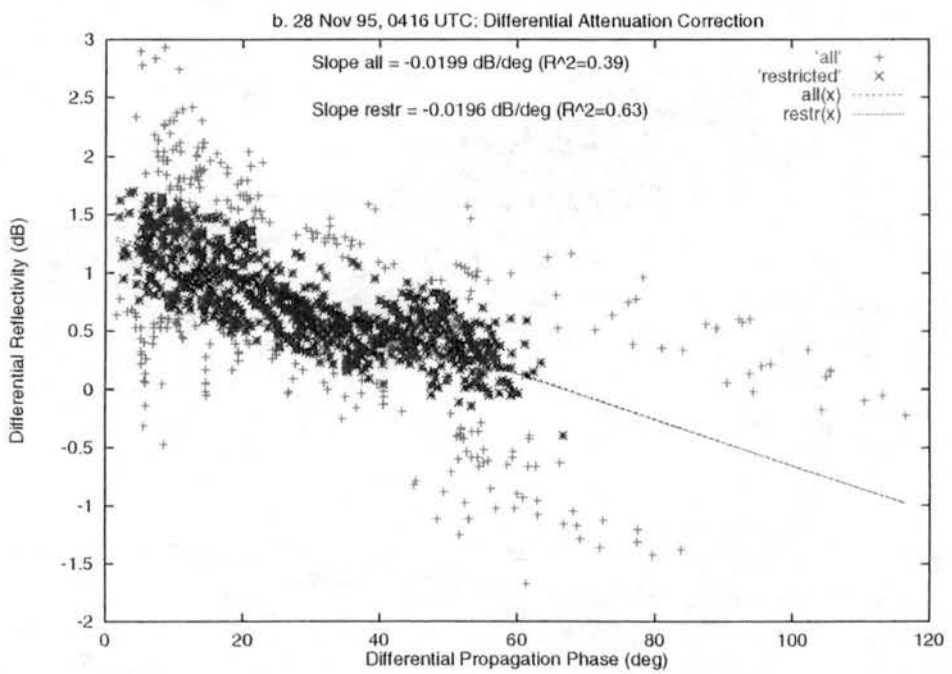

Figure 2.2. (b) as in (a) except the differential reflectivity (Z_{dr}, dB) versus the differential propagation phase (ϕ_{dp}, deg).

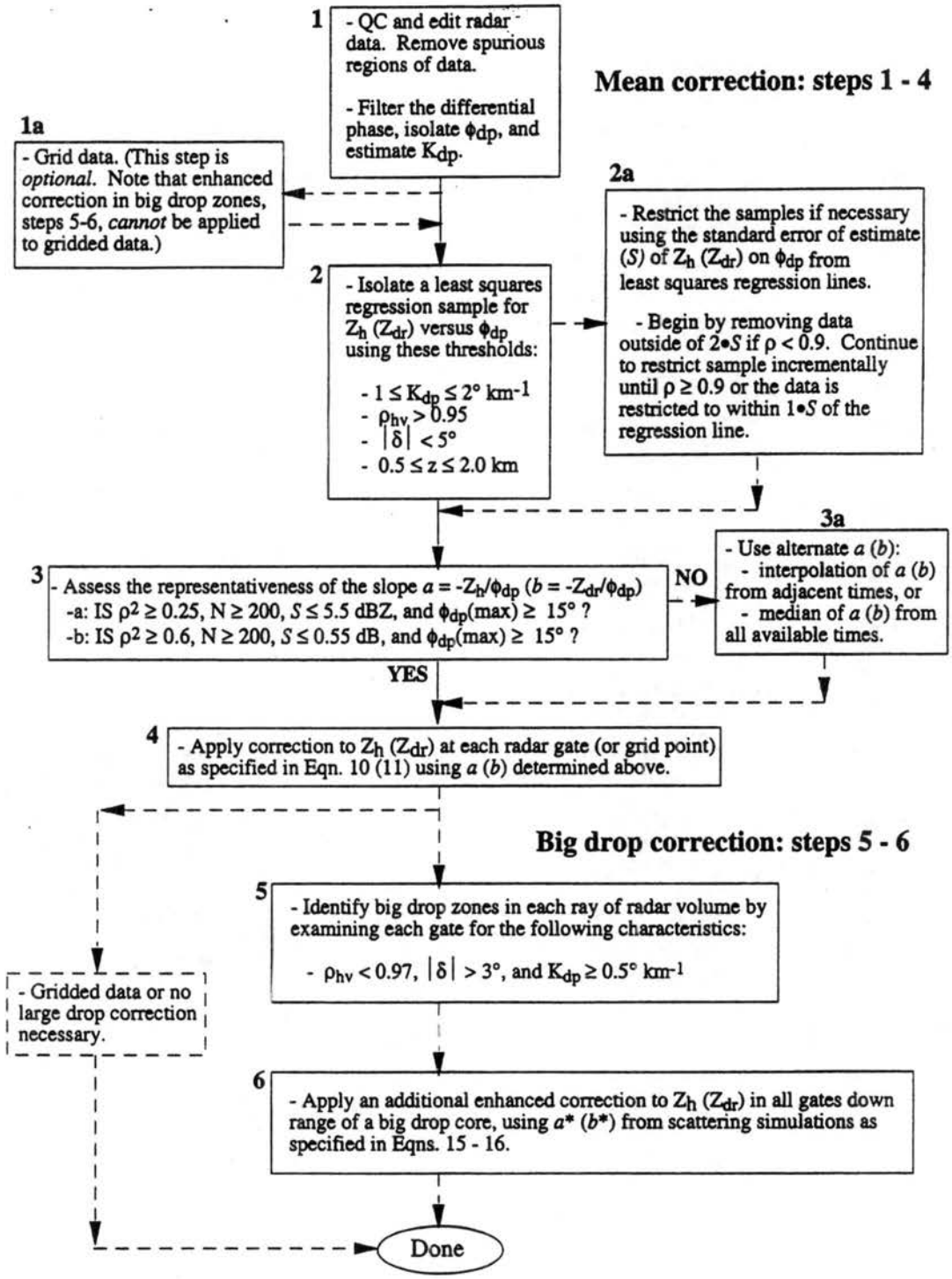

Figure 2.3. Flow chart summary of the propagation correction algorithm. Steps 1 - 4 summarize the mean empirical correction procedure (Chapter 2) and steps 5 - 6 encapsulate the big drop correction described in Chapter 3.

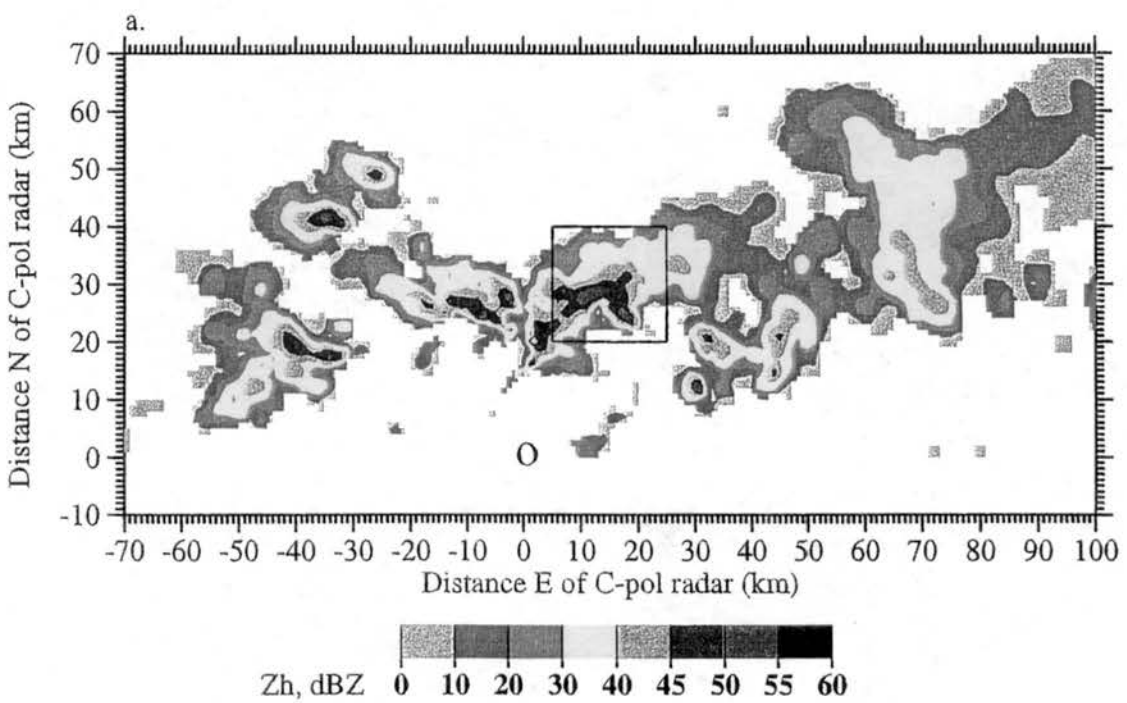

Figure 2.4. Horizontal cross-section of (a) the horizontal reflectivity (Z_h, dBZ, shaded) at 2 km AGL from 0416 UTC on 28 November 1995 *before* propagation correction. The position of the C-pol radar is indicated. The box indicates the area covered by Figs. 3.5a-c.

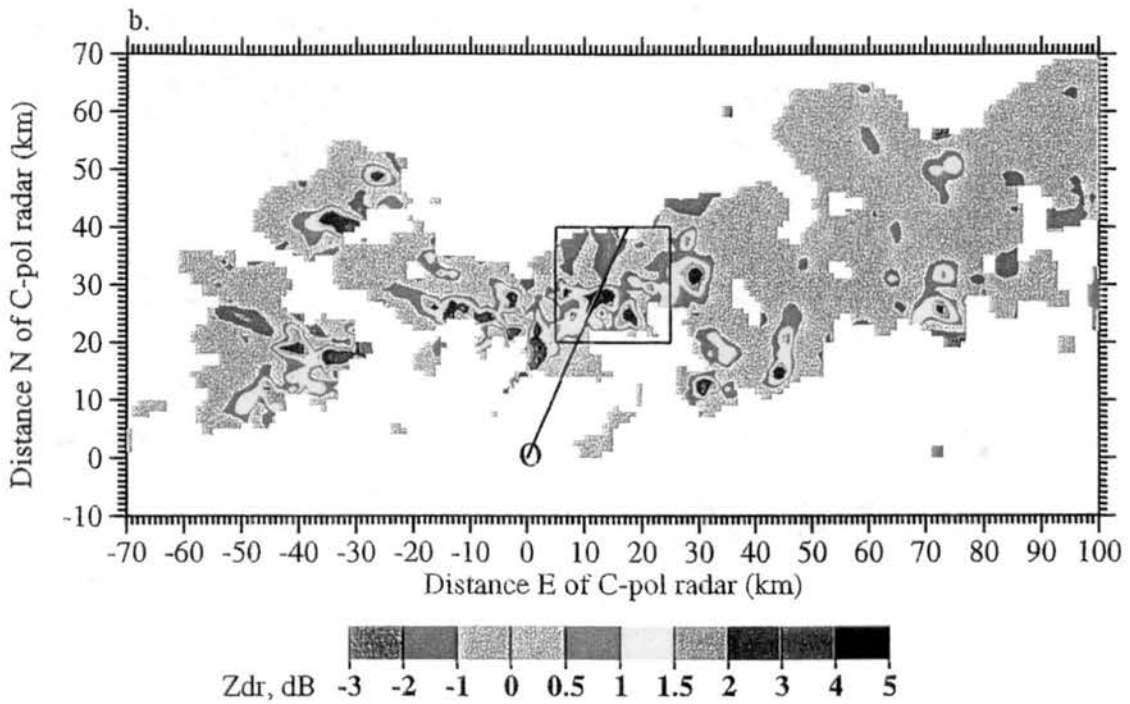

Figure 2.4. (b) as in (a) except the differential reflectivity (Z_{dr}, dB, shaded). The line highlights the range ray analyzed in Figs. 3.6a-c.

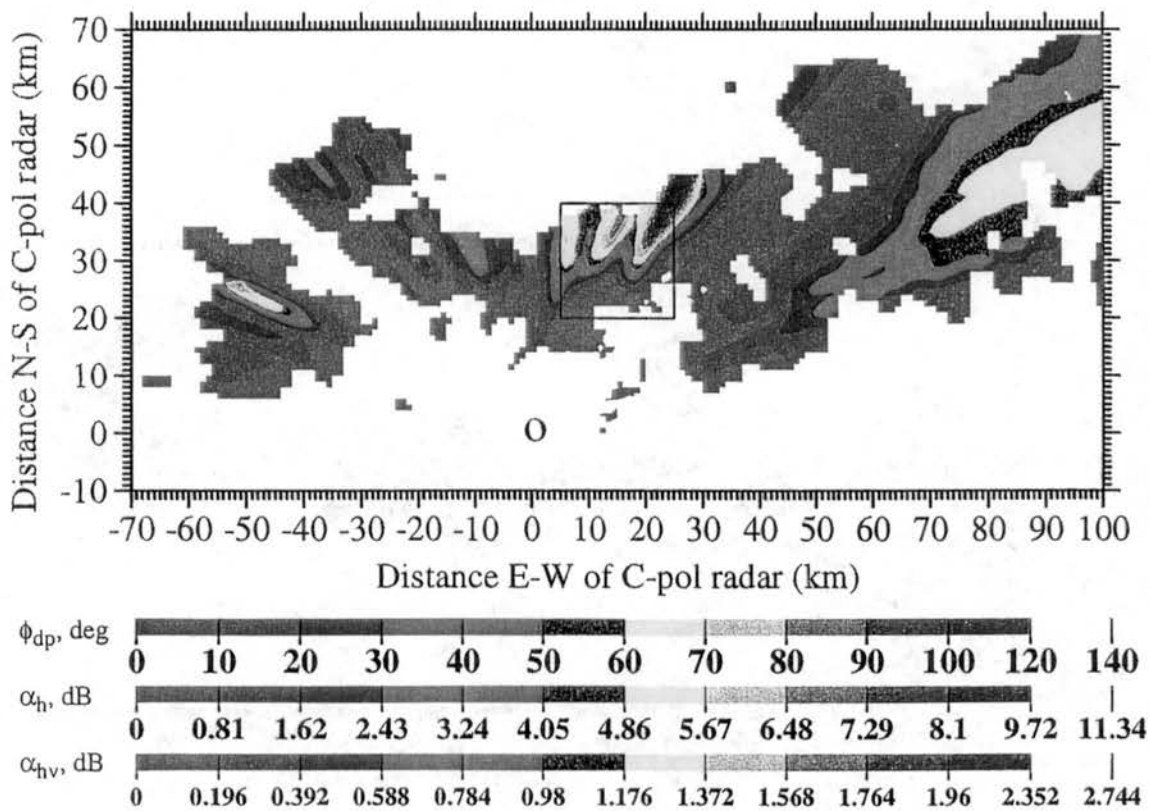

Figure 2.5. Horizontal cross-section of the differential propagation phase (ϕ_{dp}, deg, top shade scale), estimated horizontal attenuation (α_h, dB, middle shade scale), and estimated differential attenuation (α_{hv}, dB, bottom shade scale) at 2 km AGL from 0416 UTC on 28 November 1995. The box indicates the area covered by Figs. 3.5a-c.

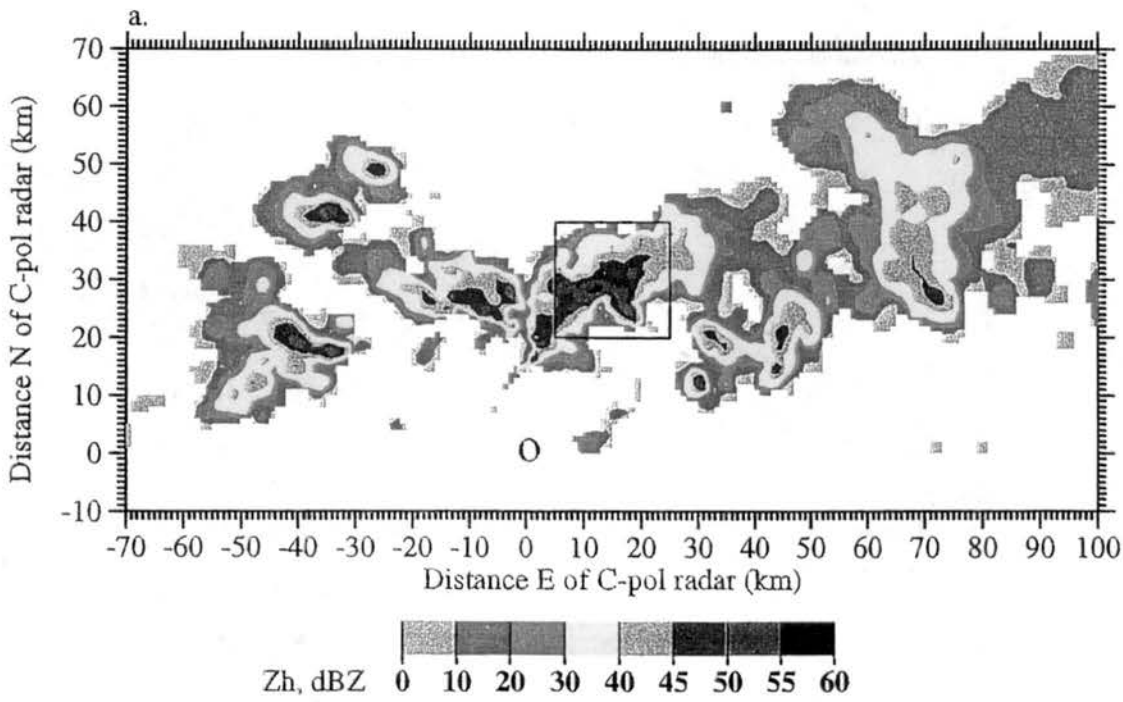

Figure 2.6. As in Fig. 2.4 except *after* the mean propagation correction procedure summarized in steps 1 - 4 of Fig. 2.3. (a) horizontal reflectivity (Z_h, dBZ, shaded).

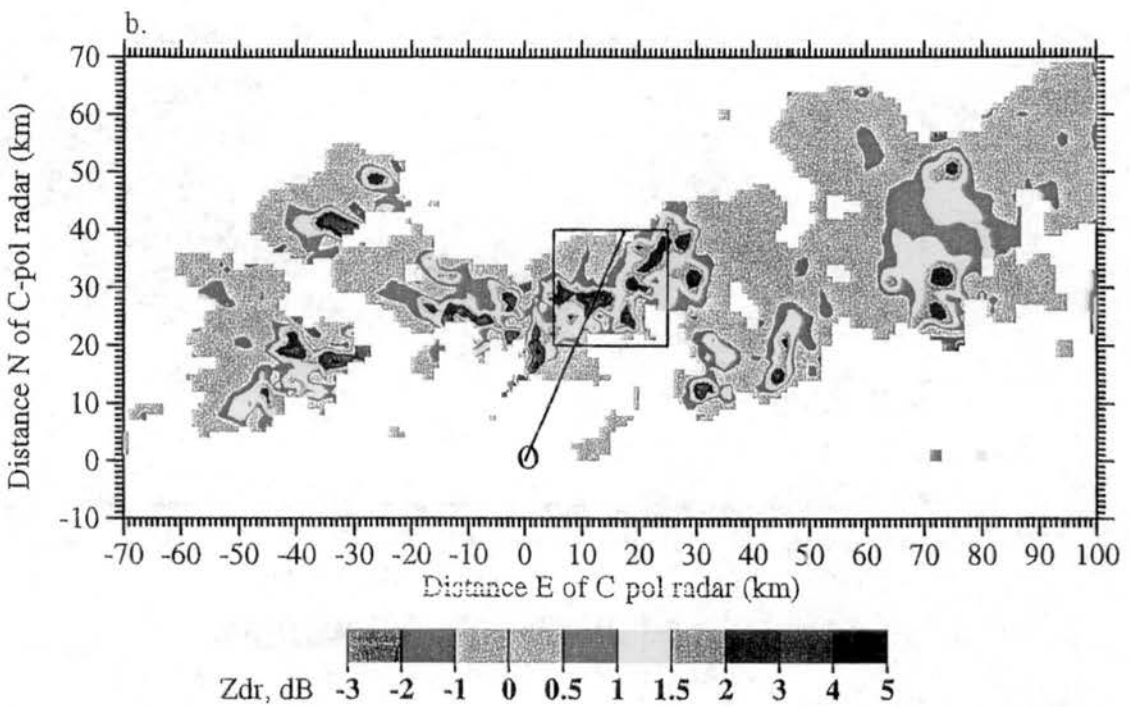

Figure 2.6. (b) as in (a) except differential reflectivity (Z_{dr}, dB, shaded).

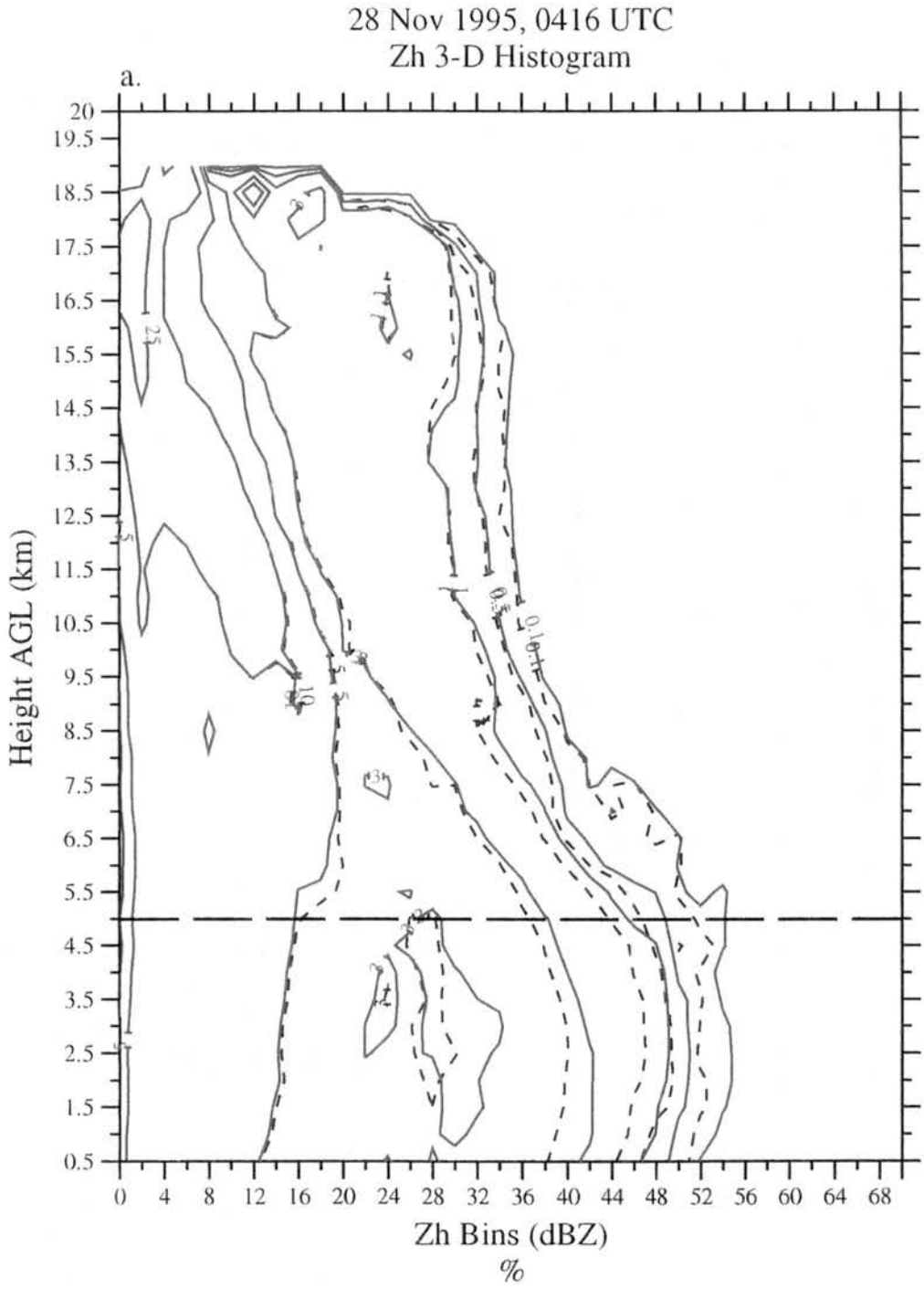

Figure 2.7. A Contour Frequency (%) by Altitude Diagram (CFAD) of the (a) horizontal reflectivity both before and after propagation correction at 0416 UTC on 28 November 1995. Before mean propagation correction: dashed line. After mean propagation correction: solid line.

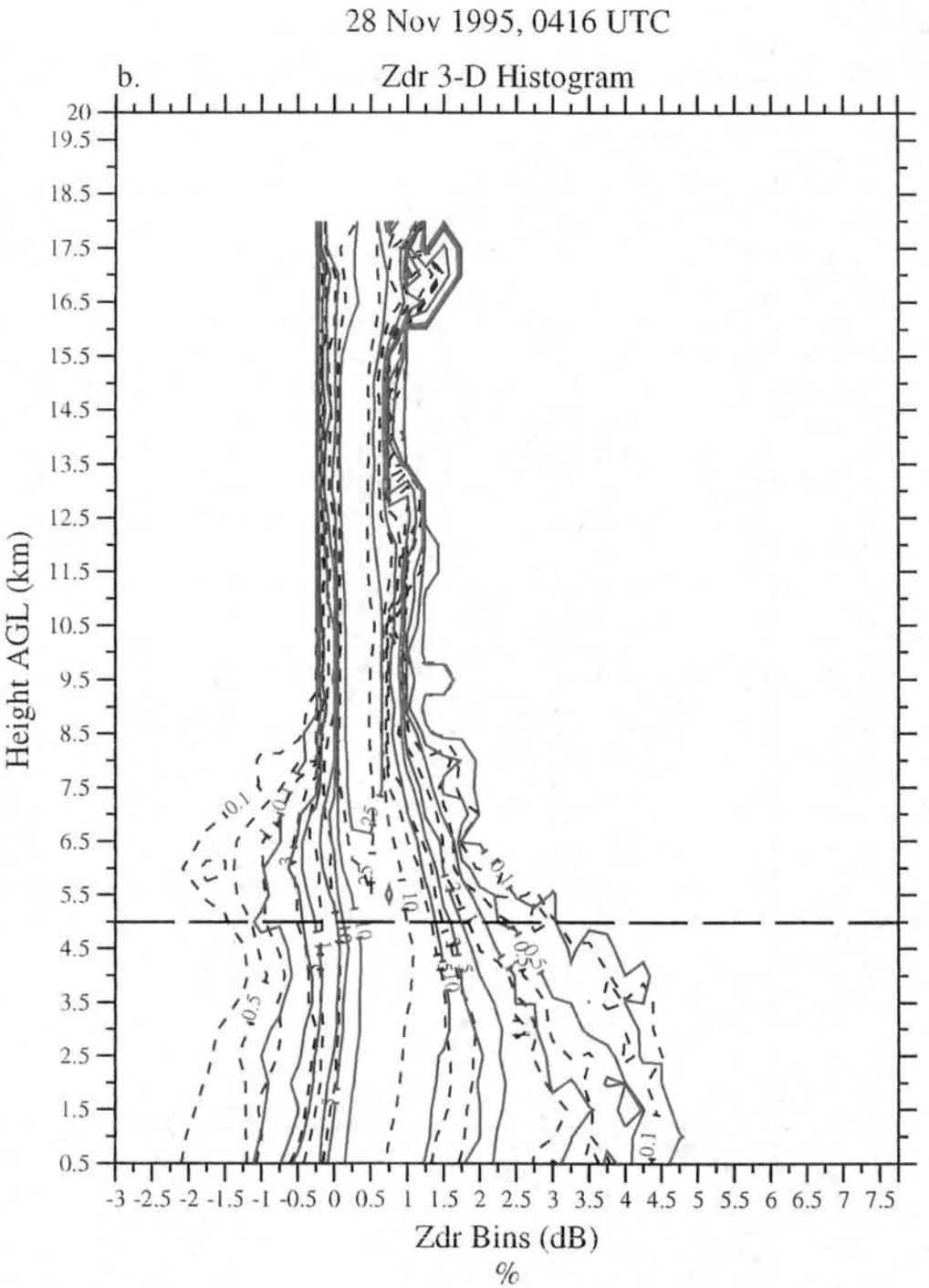

Figure 2.7. (b) as in (a) except differential reflectivity.

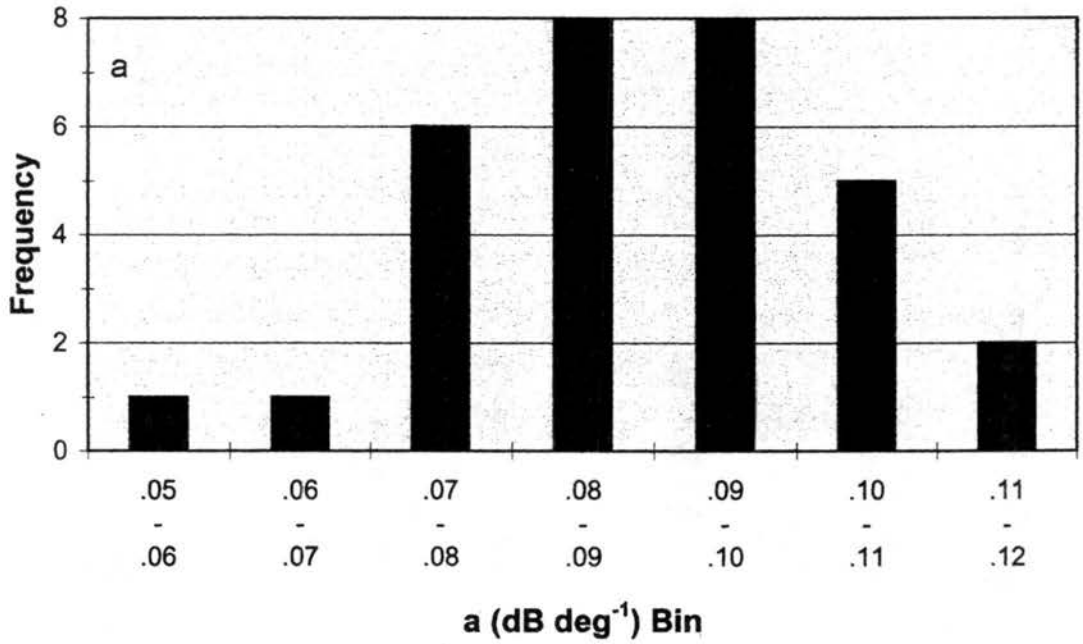

Figure 2.8. Histogram of the correction coefficient (a) a (dB deg^{-1}) derived from the least squares regression technique applied to C-pol radar data from 0206 to 0802 UTC on 28 November 1995.

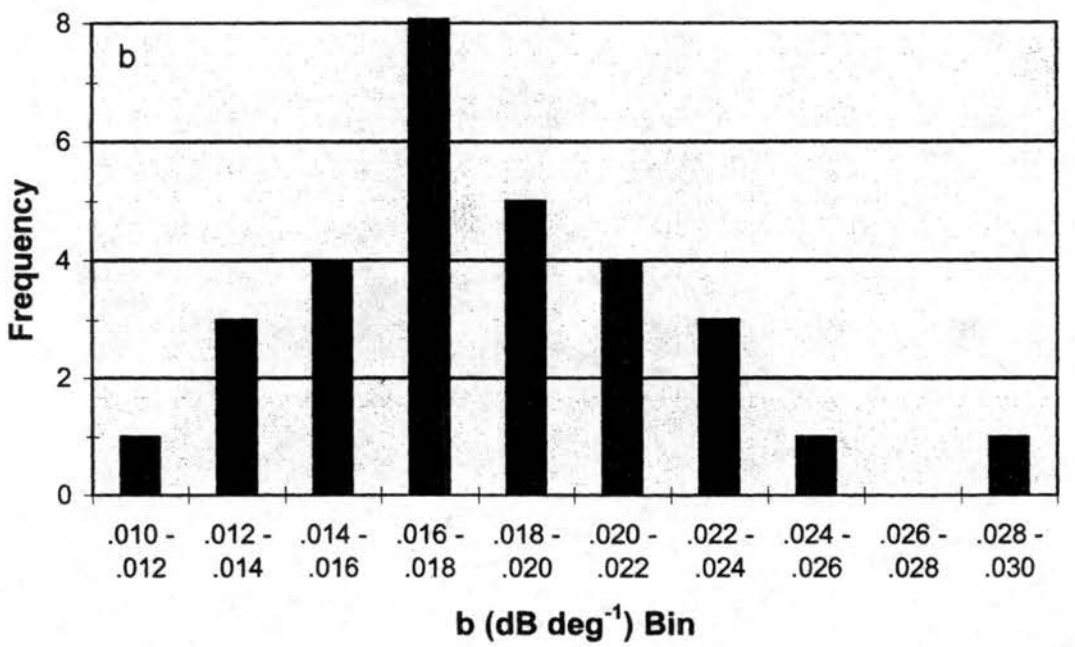

Figure 2.8. (b) as in (a) except correction coefficient b (dB deg^{-1}).

CHAPTER 3

LARGE DROP CORRECTION: A PIECE-WISE LINEAR APPROACH

3.1. Method

The presence of large raindrops (e.g., Z_{dr} > 2.5 - 3 dB) in tropical convection complicates the correction of propagation effects at C-band because the correction coefficients $a = A_h/K_{dp}$ and $b = A_{hv}/K_{dp}$ are an increasing function of Z_{dr}, particularly for Z_{dr} > 2 dB, as shown with scattering simulations in Fig. 3.1. For very large Z_{dr} (e.g., 4 dB), the correction coefficient a (b) can be a factor of two (four) times larger than the coefficient for small-to-moderate Z_{dr} (e.g., 0.5 - 2 dB). The correction coefficients a and b do not vary significantly at these small-to-moderate values of Z_{dr} and the linear assumptions given by Eqns. 2.1 and 2.2 respectively are quite accurate as shown in Figs. 3.2a,b. Fortunately, a large majority of the propagation medium in this study was comprised of drops characterized by $0.5 < Z_{dr} < 2$ dB (cf Fig. D.2 in Appendix D). As a result, the underlying assumptions of the mean empirical correction method (i.e., Eqns. 2.1 and 2.2) presented in Chapter 2 are sound in the mean, and the standard error of the method for most regions of the storm should fall within the bounds determined by Bringi et al. (1990) and Jameson (1991a, 1992).

When drops with differential reflectivity larger than about 2 dB are considered, the relationship between A_h (A_{hv}) and K_{dp} is better represented by a family of lines in which the slope rapidly increases with Z_{dr} [Fig. 3.2a (b)]. So, even if the bias in the correction coefficients a and b is mitigated using the empirical method described in Chapter 2, the standard error within and down range of any big drop region could be significantly larger than predicted by Bringi et al. (1990) since their simulations were truncated at D_0 = 2.5 mm. As demonstrated in Appendix D, large drop (Z_{dr} > 3 dB or D_0 > 2.5 mm) precipitation cores occurred frequently enough during MCTEX to require an extension to the mean empirical correction method in order to reduce the standard error.

Obviously, a reliable procedure must be identified to locate large drop zones where enhanced attenuation and differential attenuation can occur. Since differential reflectivity is potentially lowered by differential attenuation, it is not, by itself, a reliable indicator of large drops before correction. At C-band, large drop zones can be identified by Mie resonance effects in ρ_{hv} and δ (Bringi et al, 1990, 1991; Aydin and Giridhar, 1992; Keenan et al., 1998a). As shown with MCTEX scattering simulations (Fig. 3.3), ρ_{hv} decreases and δ increases significantly with increasing Z_{dr} above 2 dB. For large $Z_{dr} > 3$ dB, these Mie resonance signatures were detectable by the C-pol radar (Keenan et al., 1998a,b). After consideration of radar performance and a detailed inspection of the C-pol data, we first identified large drop zones by "dips" in ρ_{hv} below 0.97. Since the exact value of δ is a function of maximum drop size (Aydin and Giridhar, 1992) and is estimated as a residual from a filtering process (e.g., Hubbert and Bringi, 1995), we chose to search for a single perturbation of $|\delta|$ above C-pol's phase noise level of 3° (Keenan et al., 1998b) within the region identified by the ρ_{hv} dip. In order to avoid mistaking echoes with low signal-to-noise level as large drops, we also required $K_{dp} > 0.5°$ km^{-1} within the ρ_{hv} dip. If all three of these conditions were met, then the region was declared a large drop zone.

We utilized enhanced correction factors a^* and b^* in those regions defined as 'big drop zones'. Ideally, a family of correction coefficients which increase in value as Z_{dr} increases from 2 to 5 dB would be utilized (e.g., Figs 3.2a,b). However, it was not possible to partition reliably the large drop zones in this manner with C-pol observations because Z_{dr} is affected by differential attenuation and ρ_{hv} and δ cannot be measured with sufficient precision to accomplish this partitioning (Keenan et al., 1998b). Therefore, we opted for a simple, first-order correction in big drop zones which utilized a single set of enhanced correction coefficients a^* and b^*. Based on comparisons of the scattering simulations (cf. Fig. 3.1, 3.2ab, Appendix B) with the mean empirical coefficients a and b (cf. Figs. 2.8a,b), we chose $a^* = 0.13$ dB deg^{-1} and $b^* = 0.05$ dB deg^{-1} which are the mean values of the simulated correction factors for which $\rho_{hv} < 0.97$, $|\delta| > 3°$, and $3 < Z_{dr} < 5$ dB.

The use of enhanced correction coefficients in large drop zones requires minor modifications to the theoretical basis provided in Chapter 2 (Sec. 2.1). In this instance, a piece-wise linear correction approach is utilized. The mean empirical correction factors based on the linear assumption in Eqns. 2.1 and 2.2 are utilized everywhere except in the large drop cores where different slopes are used. We begin by modifying the expression for path integrated horizontal attenuation as a function of range, $\alpha_h(r)$, to include the piece-wise linear approximation

$$\alpha_h(r) = 2\int_0^r a(r')K_{dp}(r')dr' \tag{3.1}$$

which for the simple case shown in Fig. 3.4 of a single 'big drop' core occurring from r_1 to r_2 up-range (i.e., closer to the radar) from the range gate of interest (r) is,

$$\alpha_h(r) = 2a\int_0^{r_1} K_{dp}(r')dr' + 2a^*\int_{r_1}^{r_2} K_{dp}(r')dr' + 2a\int_{r_2}^{r} K_{dp}(r')dr'. \tag{3.2}$$

By combining Eqns. 2.4 and 3.2 and substituting the result into Eqn. 2.5, an expression for the intrinsic or propagation corrected horizontal reflectivity at range r is obtained from

$$Z_h^{cor}(r) = Z_h(r) + a\bullet\phi_{dp}(r) + (a^* - a)\bullet\left[\phi_{dp}(r_2) - \phi_{dp}(r_1)\right] \tag{3.3}$$

where Z_h is the observed horizontal reflectivity, ϕ_{dp} is the differential propagation phase, a is the mean empirical correction factor obtained from the procedure described in Chapter 2 (Secs. 2.2-2.3), and a^* is the enhanced correction coefficient. Given the scenario in Fig. 3.4, a similar approach can be used to derive an expression for the propagation corrected differential reflectivity

$$Z_{dr}^{cor}(r) = Z_{dr}(r) + b\bullet\phi_{dp}(r) + (b^* - b)\bullet\left[\phi_{dp}(r_2) - \phi_{dp}(r_1)\right] \tag{3.4}$$

where Z_{dr} is the observed differential reflectivity, b is the mean empirical correction factor obtained from the procedure described in Chapter 2 (Secs. 2.2-2.3), and b^* is the enhanced correction coefficient. The above derivation can be easily extended to include any number of big drop cores in a given range ray. The complete propagation correction technique utilized in this study, including the big drop correction (steps 5 - 6), is summarized in flowchart form in Fig. 2.3.

3.2. Results

To demonstrate the enhanced correction procedure in large drop zones, we focus on a region of intense convection at 0416 UTC highlighted by the box in Figs. 2.4a-b, 2.5, and 2.6a-b. An enlarged view of the horizontal and differential reflectivity in this boxed region is presented in Figs 3.5a (pre-corrected, corresponding to Figs. 2.4a-b), 3.5b (mean correction, corresponding to Figs. 2.6a-b), and 3.5c (enhanced correction). In Fig. 3.5a, notice the wedge of negative differential reflectivities (centered on x = 14 km and y = 35 km) down range from a core (centered on x = 13 km and y = 28 km) of large, pre-corrected reflectivity (> 50 dBZ) and differential reflectivity (2 - 4 dB). This is a clear example of a big drop precipitation core causing a "shadow" in Z_{dr} down range from the radar due to severe differential attenuation.

Based on a visual inspection of Fig. 3.5b, the mean empirical procedure outlined in Chapter 2 does a reasonably good job correcting the Z_h and Z_{dr}. However, notice the continued presence of the wedge-shaped shadow of lowered Z_{dr} (0 - 0.5 dB; centered on x = 14 km and y = 34 km) relative to its surroundings (0.5 - 1.5 dB) down range of the big drop core. Typical differential reflectivities in rain for Z_h > 40 dBZ are 1 - 1.5 dB with values as low as 0.5 dB and high as 2.5 dB (e.g., Bringi et al., 1991; Aydin and Giridhar, 1992; Keenan et al., 1998a). The existence of a large area of Z_{dr} < 0.5 dB for Z_h > 40 dBZ (centered x = 14 km and y = 33 km) in Fig. 3.5b is a clear indicator that some propagation effects remain in Z_{dr} (and therefore probably Z_h too) following the mean correction. The fact that this region exists in a wedge shape down range from a region of very large Z_h (> 55 dBZ) and Z_{dr} (> 3 dB) which was shown above to cause enhanced propagation effects, provides further evidence for the need of an enhanced, 'big drop' correction.

To demonstrate how the big drop correction is applied, range plots passing through a large drop core (Figs. 3.5a,b,c) of Z_h and ρ_{hv}, Z_{dr} (and ρ_{hv} repeated), and the various phase measurements (Φ_{dp}, ϕ_{dp}, K_{dp}, and δ) are presented in Figs. 3.6a,b,c respectively. Using the procedure described above, the big drop zone in the range plots of Figs. 3.6a-c is located at a range of 27.5 km to 34 km. Throughout the big drop zone, $|\delta|$ exceeds the threshold

of 3° several times (Fig. 3.6c), ρ_{hv} is below 0.97 (Fig. 3.6a), and K_{dp} ranges from 0.5 to 5° km^{-1} (Fig. 3.6c). Note that even prior to correction, the range plots pass through two distinct maxima in Z_h (> 50 dBZ) and Z_{dr} (> 3 dB) within the defined large drop core. The overall minimum in ρ_{hv} is collocated with both the maximum Z_h (pre- and post-corrected, Fig. 3.6a) and the maximum Z_{dr} (post-corrected, Fig. 3.6b). The combined polarimetric radar signature of large post-corrected Z_h (50 - 60 dBZ) and Z_{dr} (2.5 - 4.5 dB), a minima in ρ_{hv} of 0.88, a maximum $|\delta|$ of 8°, and a peak K_{dp} just under 5° km^{-1} is convincing evidence of a large drop core (e.g., Bringi et al., 1990; Aydin and Giridhar, 1992; Keenan et al., 1998a).

Clearly, there are severe propagation effects visually evident in raw Z_{dr} as evidenced by the -2 dB value at R = 40 km in Fig. 3.6b. Despite a range of K_{dp} between 1.5 and 4° km^{-1}, the mean corrected Z_{dr} between a range of 33 km and 40 km ranges from -0.5 to 0 dB. Results from scattering simulations (Fig. 2.1b) suggest that the minimum Z_{dr} for the above range of K_{dp} is no less than 0.75 dB. This discrepancy is additional evidence that the mean propagation correction coefficients are insufficient in large drop zones. The enhanced correction procedure results in a final range of Z_{dr} from 0.7 to 1.4 dB at R = 33 to 40 km (Fig. 3.6b). These values of final, enhanced corrected Z_{dr} and estimated K_{dp} are consistent with theoretical expectations (Fig. 2.1b).

Inspection of Figs. 3.6a,b reveal that the maximum A_h and A_{hv} within the large drop core reaches 0.64 dB km^{-1} and 0.25 dB km^{-1} respectively. The final path integrated attenuation (α_h, Fig. 3.6a) and differential attenuation (α_{hv}, Fig. 3.6b) down range of the big drop zone at R = 40 km are 9.3 dB and 2.9 dB respectively. The enhanced, big drop correction added 1.9 dB to α_h and 1.1 dB to α_{hv}. After applying the complete propagation correction algorithm, the maximum values of Z_h and Z_{dr} at R = 32 km (Figs., 3.6a,b) are 60 dBZ and 4.8 dB respectively. While large, equivalent and larger values of Z_h and Z_{dr} were observed in the raw C-pol radar data during MCTEX (Keenan et al., 1998b).

The final, enhanced propagation corrected Z_h and Z_{dr} in the boxed region of Figs. 2.6a,b are shown in Fig. 3.5c. The wedge of anomalously low Z_{dr} in moderate reflectivity down range of the big drop core is no longer present. The enhanced correction increased Z_{dr} (Z_h) in some areas by 0.25 - 1 dB (0.5 - 2 dB) relative to the mean correction. The

Z_h/Z_{dr} pairs in Fig. 3.5c are much more consistent with scattering simulation results (Bringi et al., 1991; Aydin and Giridhar, 1992; Keenan et al., 1998) than the uncorrected or mean corrected data. Validation of the complete propagation correction method using cumulative rain gauge data and internal consistency between polarimetric radar observables will be pursued further in Chapter 4.

After applying the complete propagation correction procedure (Steps 1 - 6) to all polarimetric radar volumes on 28 Nov 95, approximately 25% of all range gates containing precipitation echo experienced a significant attenuation correction ($\alpha_h \geq 1$ dB). Similarly, the differential reflectivity was significantly increased ($\alpha_{hv} \geq 0.25$ dB) about 22% of the time. In about 7% (6%) of the precipitation echo during 28 Nov 95, there were massive propagation corrections to Z_h (Z_{dr}) defined as $\alpha_h \geq 5$ dB ($\alpha_{hv} \geq 1$ dB). Clearly, propagation effects at C-band in the tropics are significant and must be corrected before using the data either qualitatively or quantitatively. This premise will be tested further in the next section.

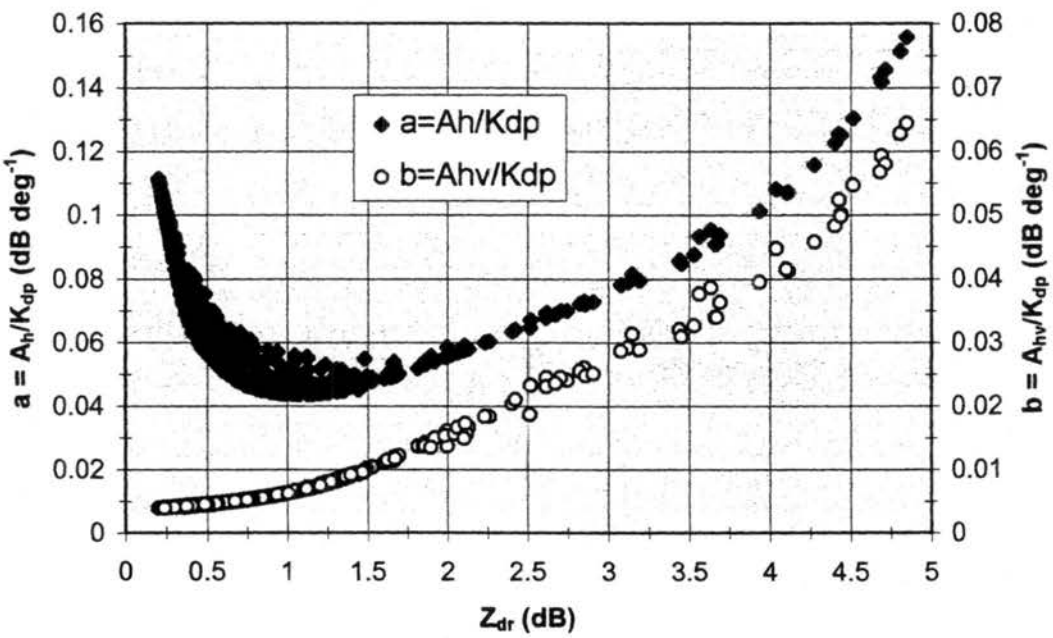

Figure 3.1. A plot of the coefficients a (dB deg^{-1}) and b (dB deg^{-1}) versus Z_{dr} (dB) as derived from scattering simulations described in Appendix B.

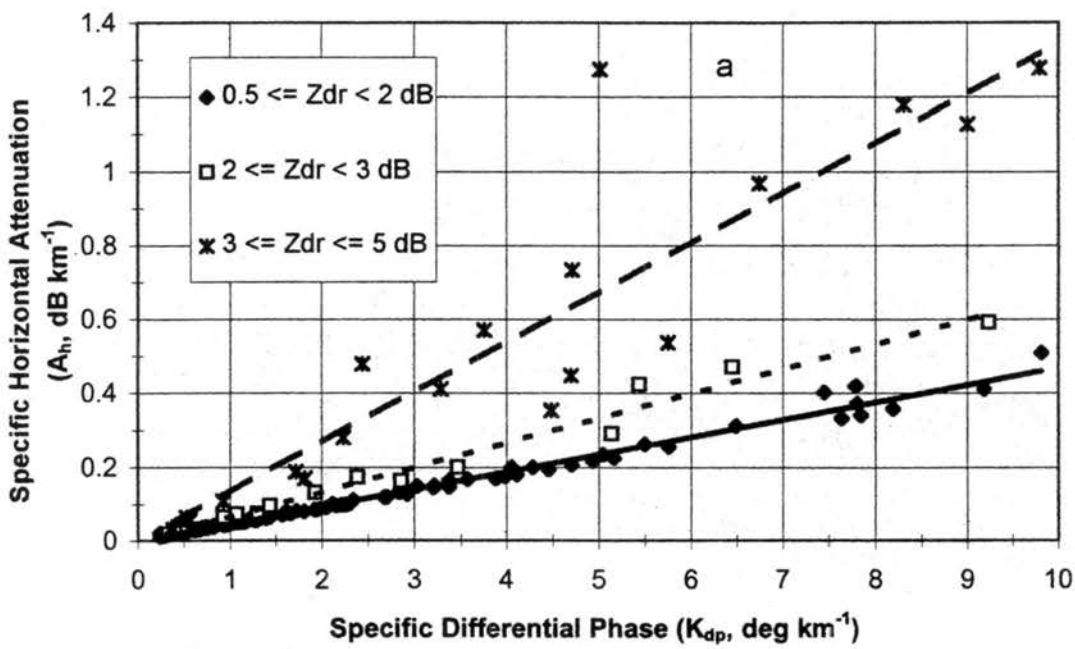

Figure 3.2. Scatterplot of the (a) specific horizontal attenuation (A_h, dB km^{-1}) versus the specific differential phase (K_{dp}, deg km^{-1}) as derived from scattering simulations described in Appendix B. The scatterplots are partitioned by the differential reflectivity into three samples as shown. The least squares linear regression line for each group of data partitioned by Z_{dr} is shown. The slope of each line is equivalent to the coefficient *a* for each data group.

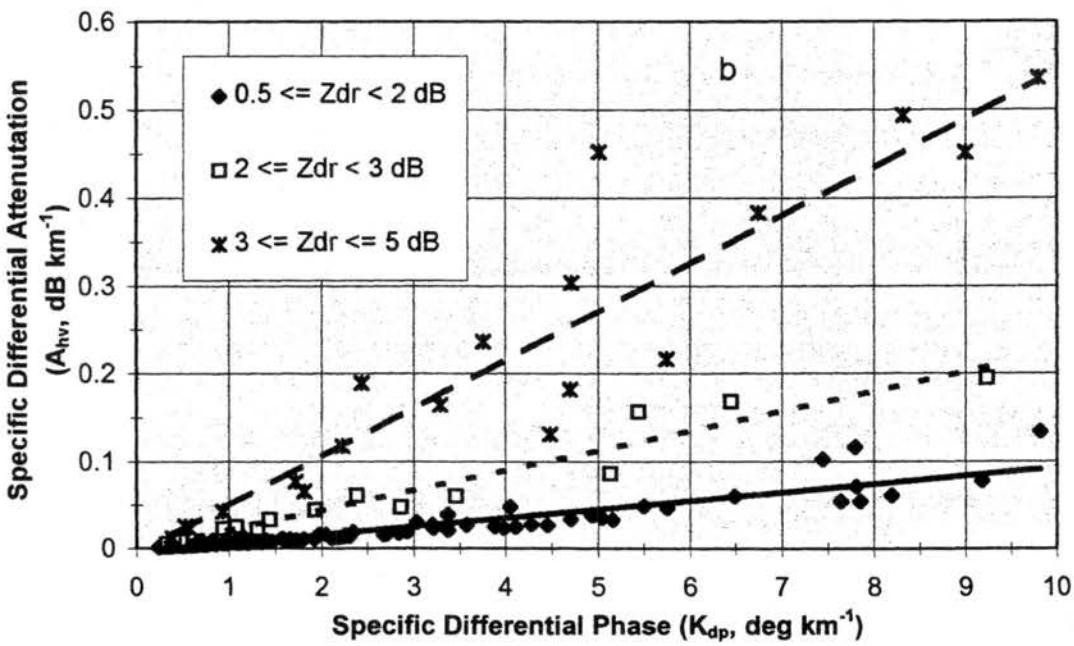

Figure 3.2. (b) as in (a) except specific differential attenuation (A_{hv}, dB km^{-1}) versus the specific differential phase (K_{dp}, deg km^{-1}). The slope of each line is equivalent to the coefficient *b* for each data group.

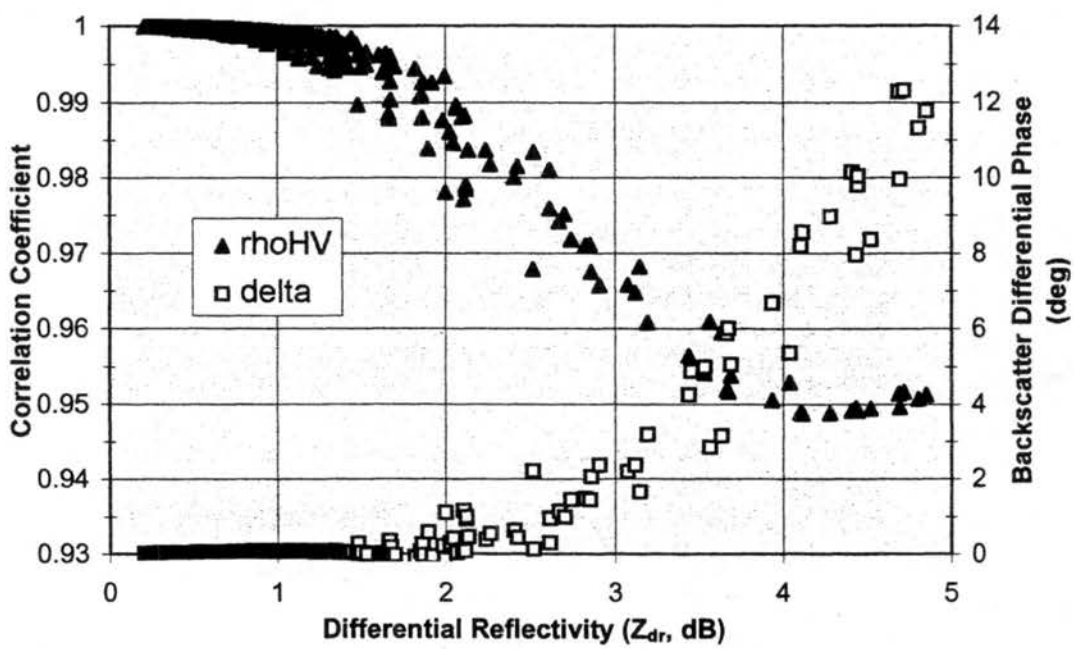

Figure 3.3. Scatterplots of the correlation coefficient (ρ_{hv}) and the backscatter differential phase (δ, deg) versus the differential reflectivity (Z_{dr}, dB) as derived from the scattering simulations described in Appendix B.

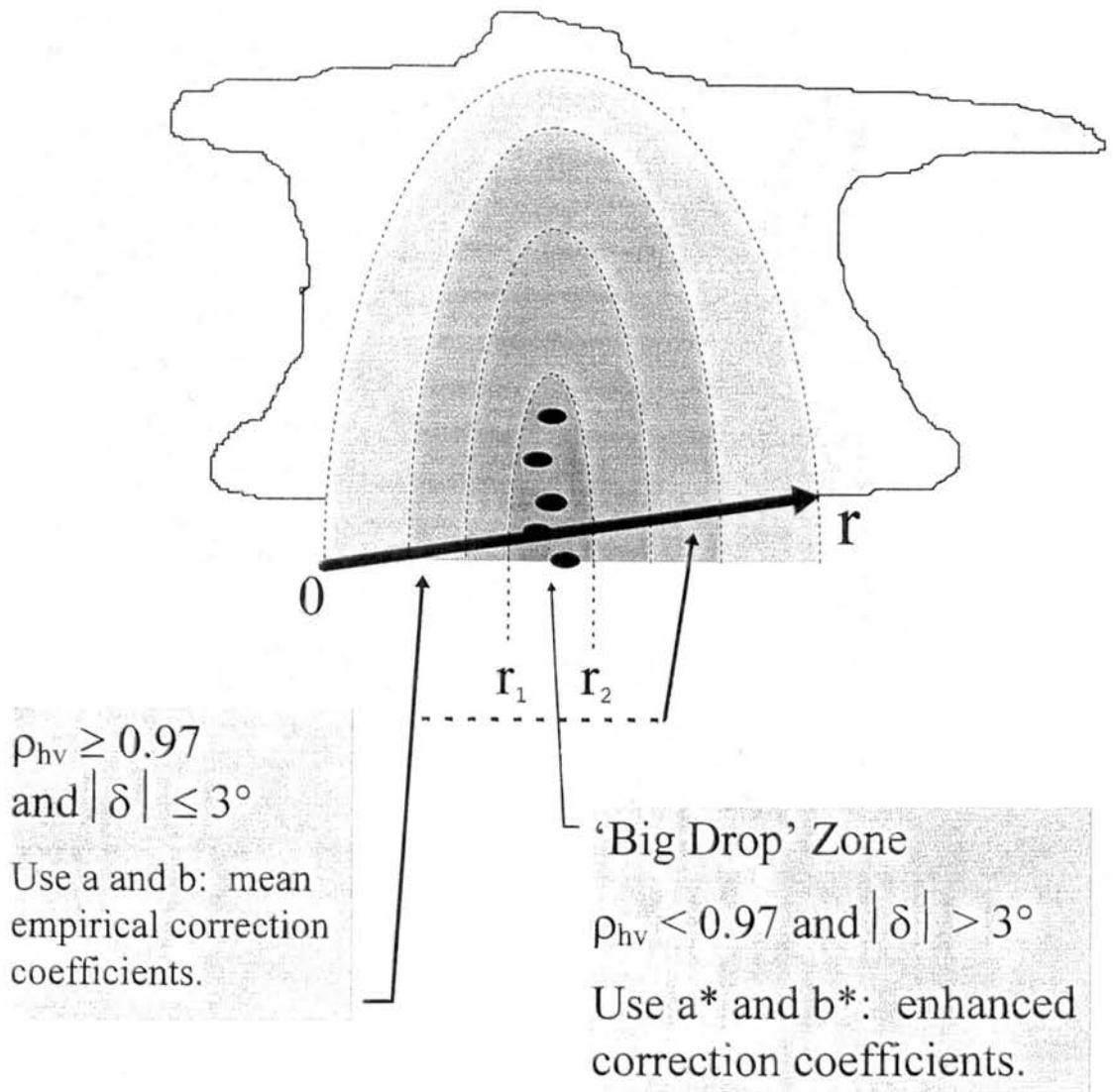

Figure 3.4. Illustration of a range ray passing through a single big drop zone at ranges r_1 to r_2. See text for accompanying details.

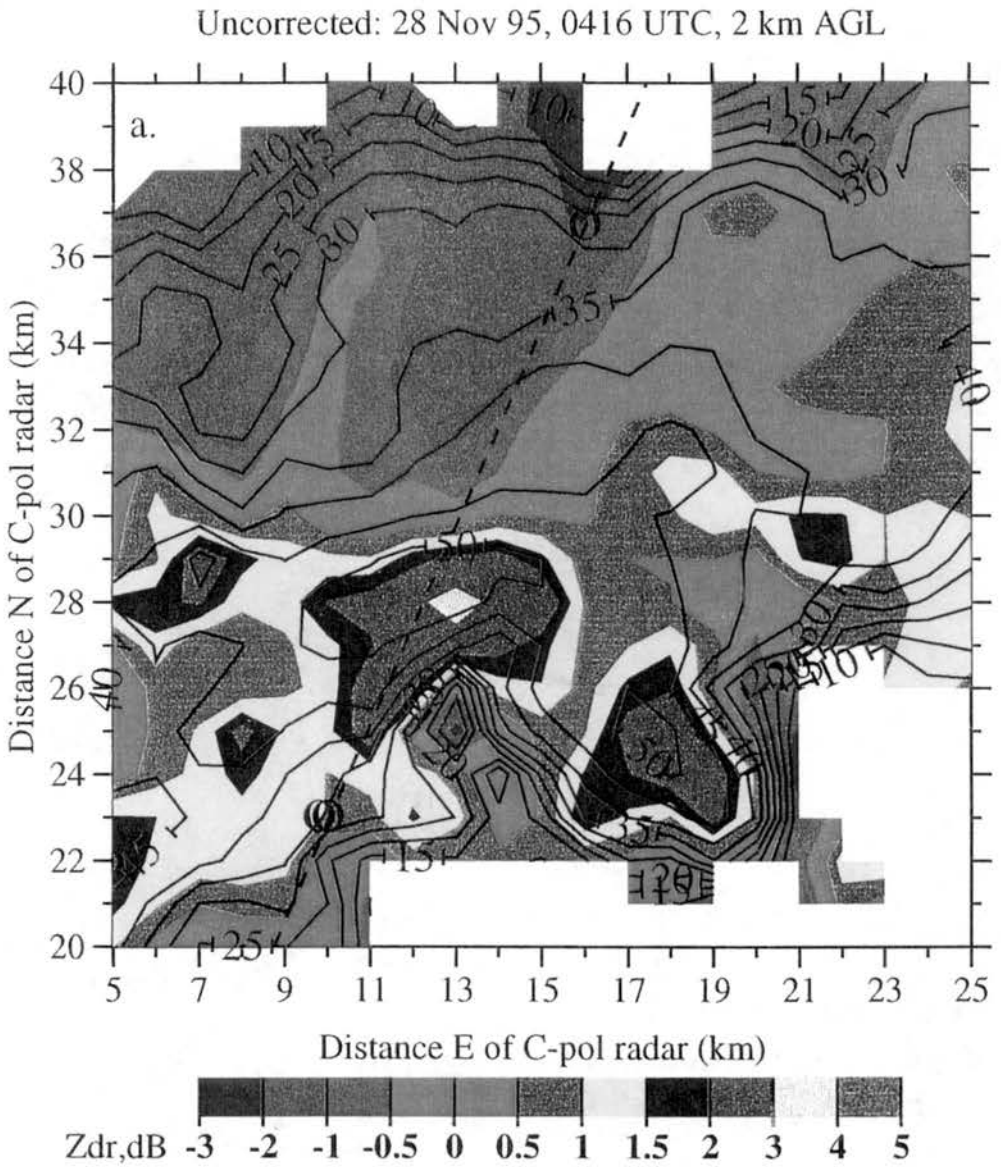

Figure 3.5. Horizontal cross-section of the differential reflectivity (Z_{dr}, shaded in dB as shown) and horizontal reflectivity (Z_h, contoured every 5 dBZ starting at 10 dBZ) at 2 km AGL from 0416 UTC on 28 November 1995 (a) before any propagation correction. The dashed line indicates the azimuth analyzed in Figs. 3.6a-c. Marks (**O**) along the dashed line approximate the range coverage of Figs. 3.6a-c. This horizontal cross-section zooms-in on the boxed area highlighted in Fig. 2.4.

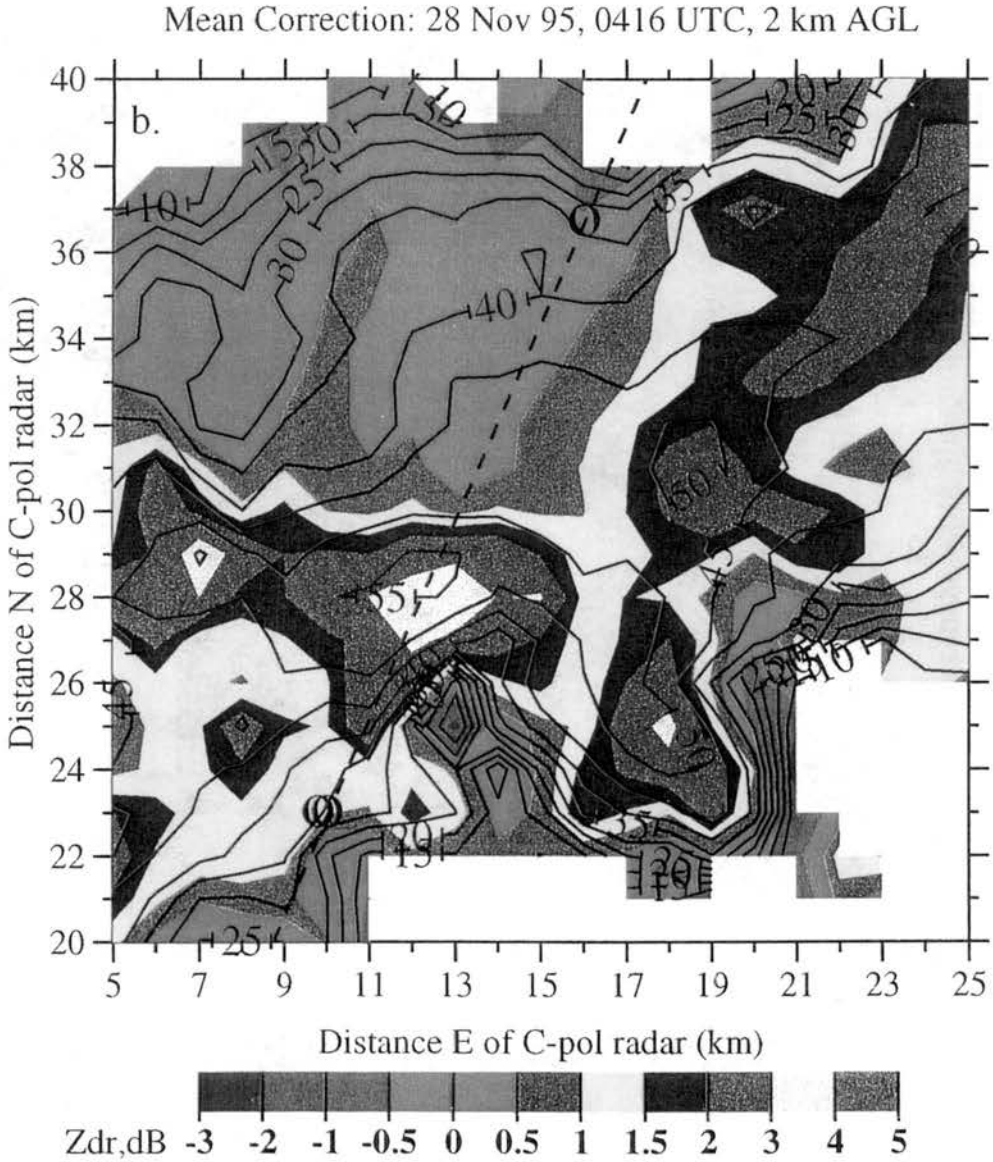

Figure 3.5. (b) as in (a) except after the mean propagation correction (steps 1 - 4 in Fig. 2.3).

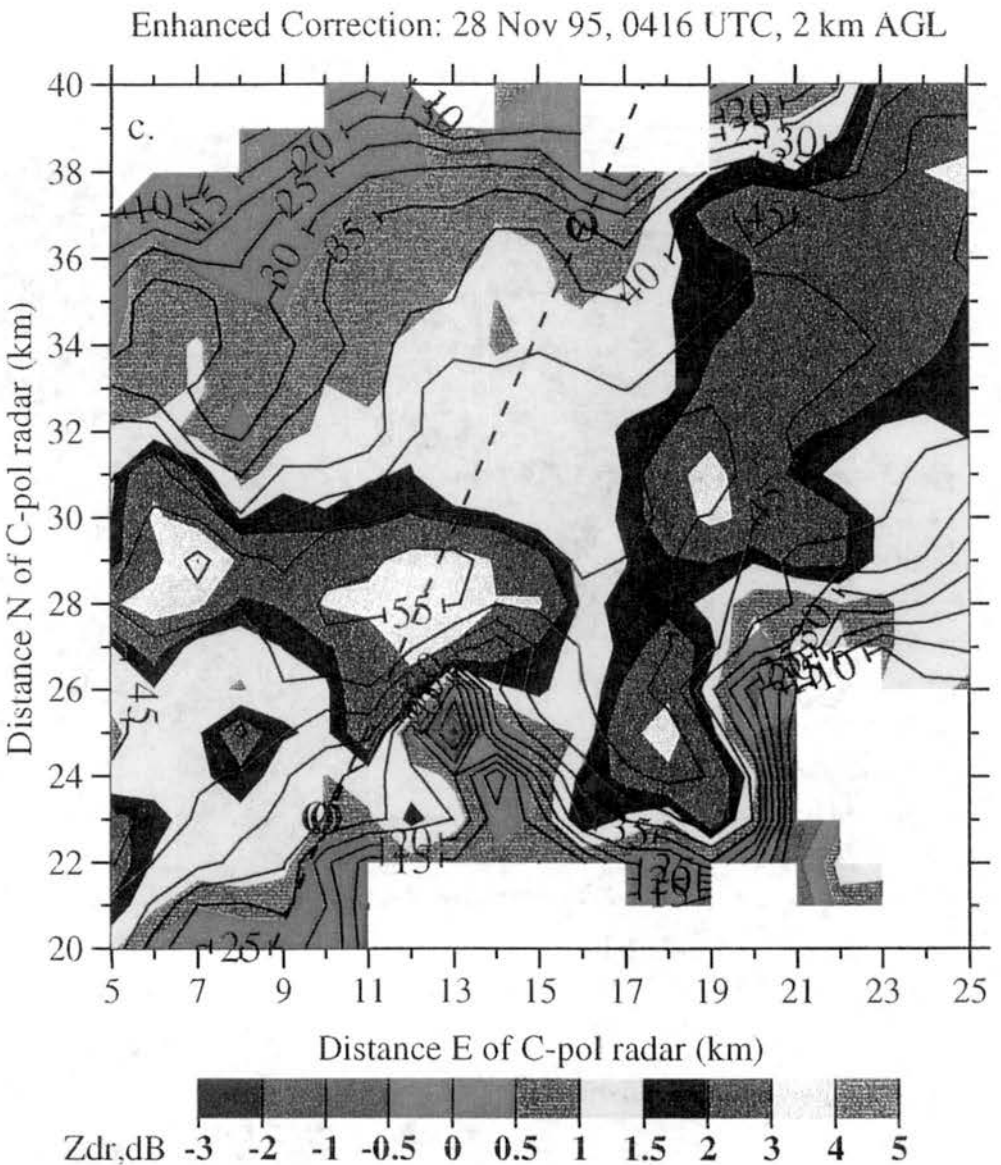

Figure 3.5. (c) as in (a) except after the big drop correction (steps 1 - 6 in Fig. 2.3).

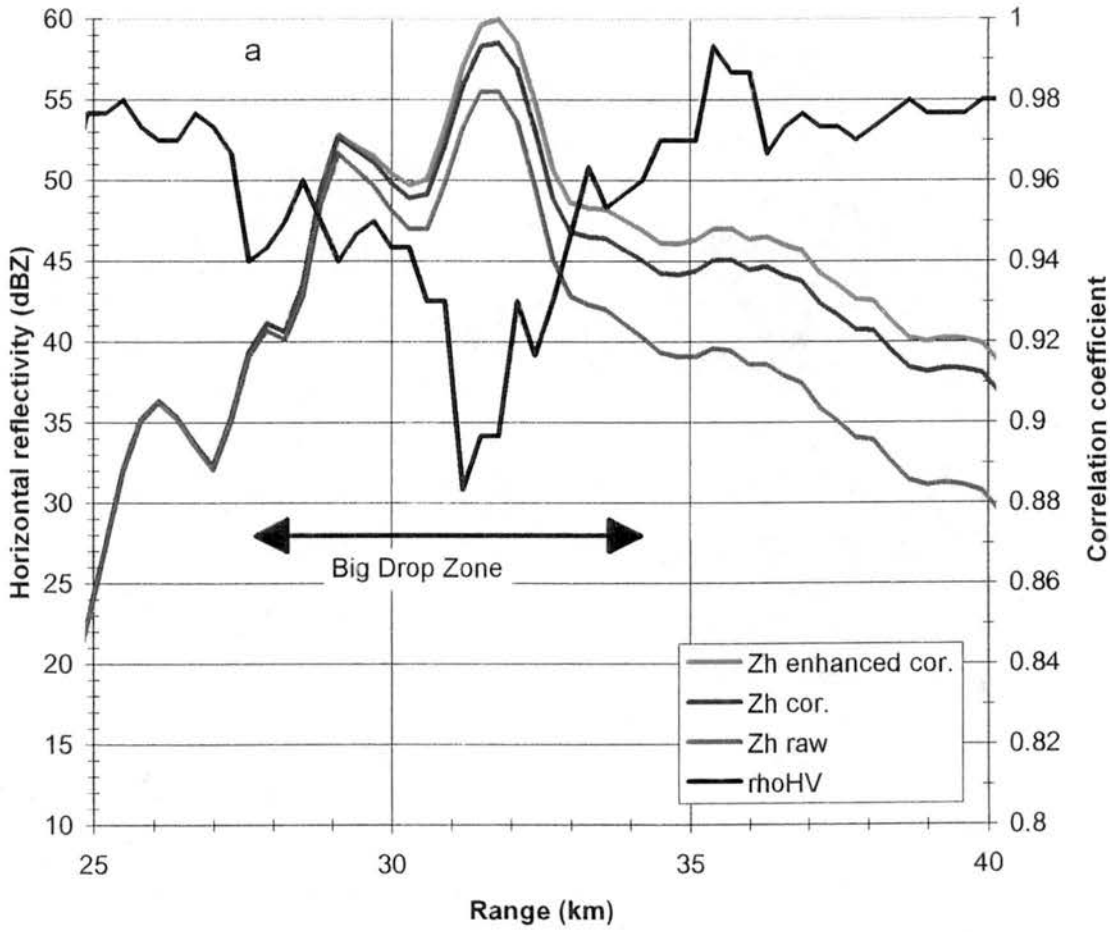

Figure 3.6. Range plots of (a) the correlation coefficient (ρ_{hv}) and the horizontal reflectivity (Z_h, dBZ) before correction (raw), after the mean propagation correction (cor), and after the enhanced correction (enhanced cor.). The range plots display ray # 387 (Azimuth angle = 23.21°, Elevation angle = 3.8°) from R = 25 km to R = 40 km. Range resolution is 0.15 km. The 'big drop zone' as defined in the text is highlighted. Refer to Fig. 2.4b and Figs. 3.5a-c to place this range ray in the context of the entire convective complex.

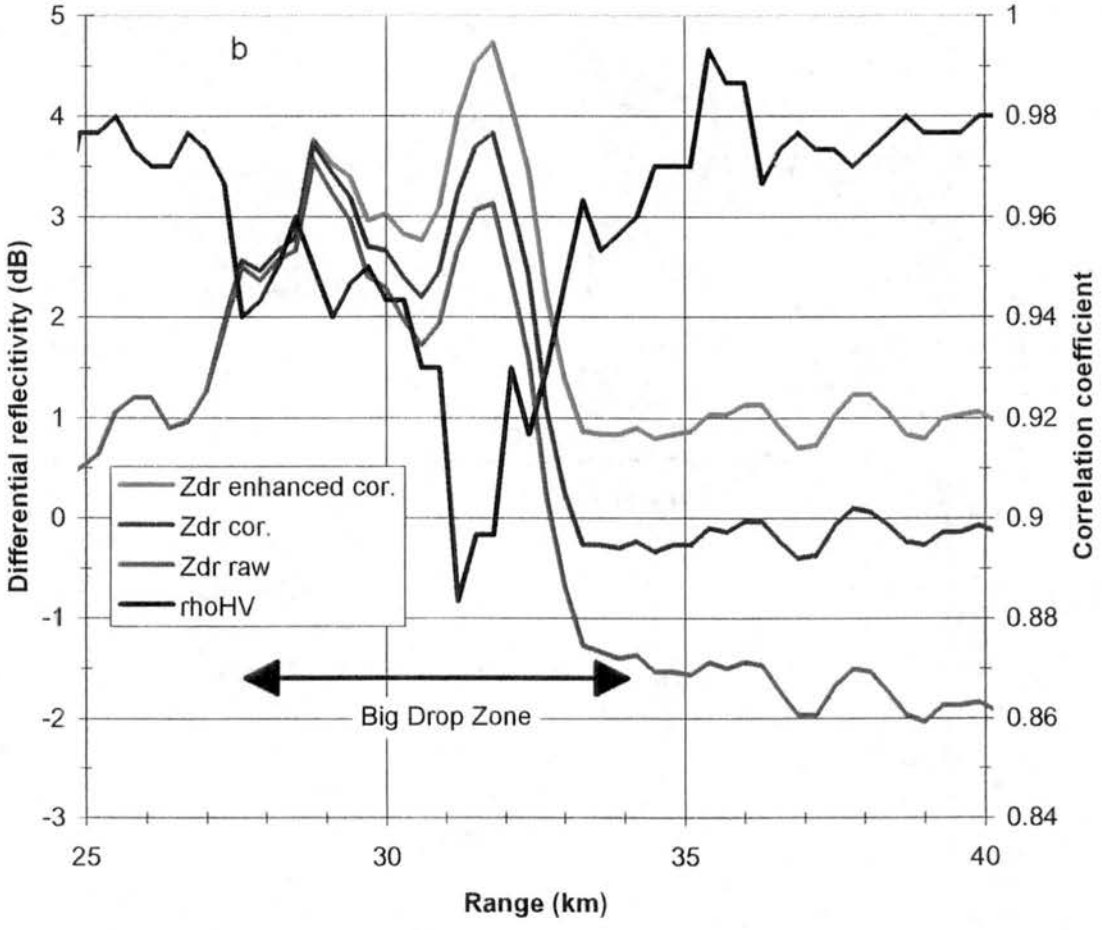

Figure 3.6. (b) as in (a) except the correlation coefficient and differential reflectivity (Z_{dr}, dB) before correction (raw), after the mean propagation correction (cor), and after the enhanced correction (enhanced cor.).

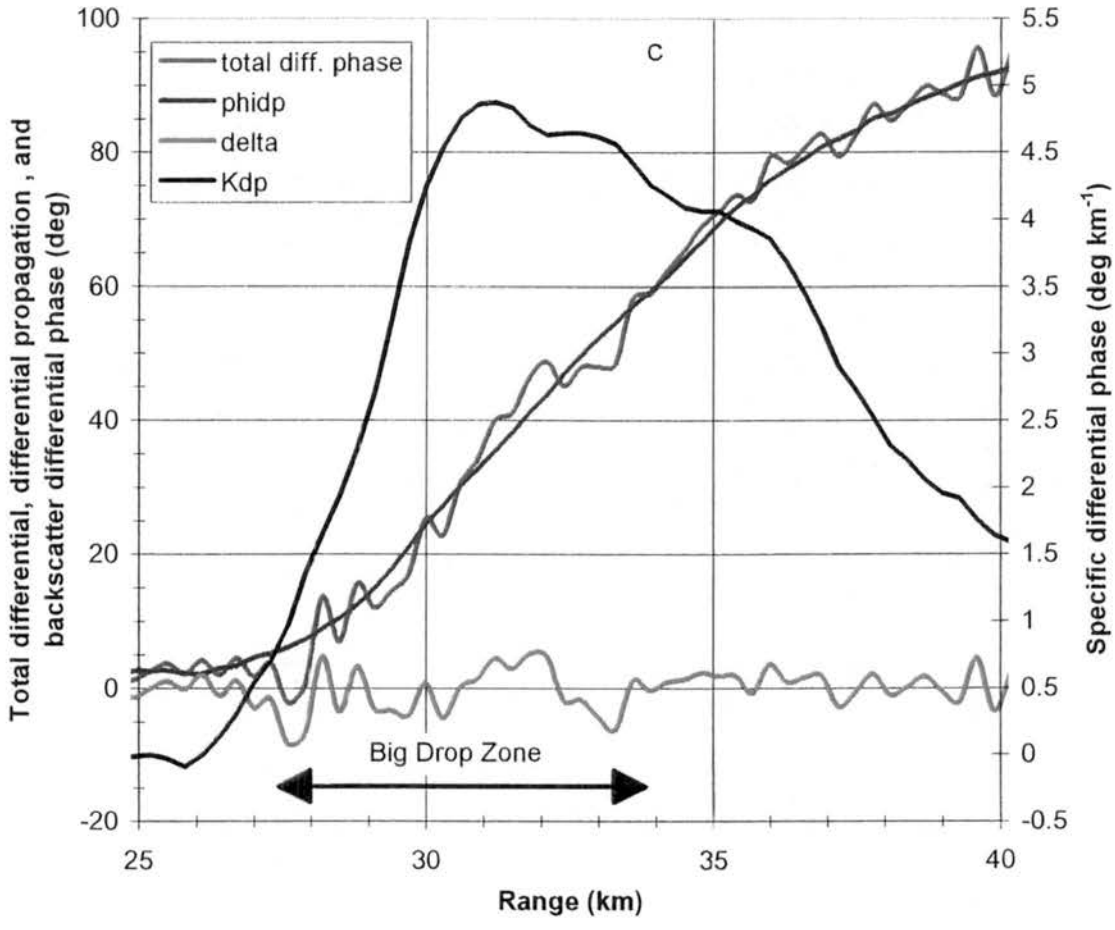

Figure 3.6. (c) as in (a) except the total differential phase (Φ_{dp}, deg), the propagation differential phase (ϕ_{dp}, deg), the backscatter differential phase (δ, deg), and the specific differential phase (K_{dp}, deg km^{-1}).

CHAPTER 4
VALIDATION

4.1. Comparison with rain gauge data

The presence of fourteen tipping bucket rain gauges distributed throughout the Tiwi Islands at ranges of 15 to 88 km from the radar during MCTEX (Keenan et al., 1994) provided an independent data set from which to judge the efficacy of the above propagation correction algorithm. At each gauge site, the time of accumulation of 0.2 mm of rainfall was logged. The accuracy of the gauge rain rates was typically better than 5% for rain rates observed during MCTEX. Quality control of the gauge data included pre- and post-MCTEX rain rate and accumulation calibrations on each gauge.

Our approach was to estimate the cumulative rainfall amount at each gauge while polarimetric data was available (0206 - 0802 UTC) on 28 November 1995. We chose two independent radar rainfall algorithms to compare to the gauges before and after steps 1 - 6 (Fig. 2.3) of the propagation correction algorithm were applied to the C-pol radar data: $R(Z_h)$, and $R(K_{dp}, Z_{dr})$. The equations for these two radar rainfall estimators

$$R(Z_h) = 5.865\times10^{-3}\bullet(Z_h)^{0.862} \tag{4.1}$$

$$R(K_{dp},Z_{dr}) = 25.00\bullet(K_{dp})^{0.988}\bullet(Z_{dr})^{-0.583} \tag{4.2}$$

were derived using a curve fitting procedure on R (mm h^{-1}), Z_h (mm^6 m^{-3}), K_{dp} (° km^{-1}), and Z_{dr} (dB) data from scattering simulations as described in Appendix E. Comparison of the cumulative rainfall amounts over each gauge from $R(Z_h)$ to the associated gauge estimates before and after correction is intended to judge the performance of the attenuation correction method. Since K_{dp} is unaffected by horizontal or differential attenuation (e.g., Zrnic' and Ryzhkov, 1996), the relative comparison of the cumulative $R(K_{dp},Z_{dr})$ rainfall estimates to rain gauge totals before and after correction provides an

opportunity to judge the results of the differential attenuation correction algorithm. Of course, many other physical and engineering factors enter into the absolute comparison of radar and gauge rainfall estimations (e.g., Zawadzki, 1975; 1984). As a result, the use of radar versus gauge rainfall results to substantiate the propagation correction method above is only valid in a *relative* sense. In other words, our only objective was to compare the relative performance of the pre- and post-corrected radar rainfall estimators to the rain gauge totals. A similar approach was taken by Gorgucci et al. (1996). Other studies have focused on the absolute performance of $R(K_{dp},Z_{dr})$ and $R(Z_h)$ versus rain gauges (e.g., Ryzhkov and Zrnic', 1995a; Bolen et al., 1998). More details regarding the procedure for comparing the radar and gauge cumulative rainfall amounts can be found in Appendix E.

Results of the polarization radar versus gauge cumulative rainfall comparison before and after the application of the empirical propagation correction method with large drop adjustment are shown in Figs. 4.1a and 4.1b respectively. The Normalized Bias (NB) and Normalized Standard Error (NSE) as defined in Appendix E for the pre- and post-corrected cumulative $R(Z_h)$ and $R(K_{dp},Z_{dr})$ relative to the gauges are summarized in Tables 4.1 and 4.2 respectively.

Table 4.1. Summary of gauge versus $R(Z_h)$ cumulative rainfall comparison on 28 November 1995 from 0206 - 0802 UTC. The differential propagation phase was utilized to correct attenuation effects in Z_h using various correction coefficients (a) as indicated.

	Mean Cumulative Rainfall (mm)	Normalized Bias (NB)	Normalized Standard Error (NSE)
Gauge	15.36	NA	NA
$R(Z_h)$ no correction	6.76	-56.0 %	74.0 %
$R(Z_h)$ empirical correction[1]	13.67	-11.0 %	45.1 %
$R(Z_h)$ theoretical correction (Gorgucci et al., 1998)[2]	9.69	-36.9 %	59.0 %

[1] Steps 1 - 6 summarized in Fig. 2.3 using a's from Fig. 2.8a and a big drop adjustment ($a^* = 0.130$).

[2] Correction coefficient ($a = 0.0485$) from simulations of Gorgucci et al. (1998) for T = 20° C.

Table 4.2. Summary of gauge versus $R(K_{dp},Z_{dr})$ cumulative rainfall comparison on 28 November 1995 from 0206 - 0802 UTC. The differential propagation phase was utilized to correct differential attenuation effects in Z_{dr} using various correction coefficients (b) as indicated.

	Mean Cumulative Rainfall (mm)	Normalized Bias (NB)	Normalized Standard Error (NSE)
Gauges	15.36	NA	NA
$R(K_{dp},Z_{dr})$ no correction	17.20	+12.0 %	82.6 %
$R(K_{dp},Z_{dr})$ empirical correction[1]	16.31	+6.2 %	15.5 %
$R(K_{dp},Z_{dr})$ theoretical correction (Gorgucci et al., 1998)[2]	23.47	+52.8 %	86.7 %

[1] Steps 1 - 6 summarized in Fig. 2.3 using b's from Fig. 2.8b and a big drop adjustment ($b^* = 0.050$).

[2] Correction coefficient ($b = 0.0110$) from simulations of Gorgucci et al. (1998) for T = 20° C.

Before propagation correction, the scatter between the polarization radar and gauge cumulative rainfall amounts is very large (Fig. 4.1a). This scatter is reflected in very large FSE's of 74% and 83% for pre-corrected $R(Z_h)$ and $R(K_{dp},Z_{dr})$ respectively. As expected, the pre-corrected cumulative $R(Z_h)$ significantly underestimated the rain gauge totals (NB = -56%). Since the differential reflectivity is lowered from its intrinsic value by differential attenuation and $R\left(K_{dp},Z_{dr}\right) \propto Z_{dr}^{-x}$ where $0 < x < 1$ (Jameson, 1991b; Ryzhkov and Zrnic', 1995b; Eqn. 4.2), the overestimation (NB = +12%) of the pre-corrected cumulative $R(K_{dp},Z_{dr})$ is consistent with theoretical expectations.

After the propagation correction algorithm summarized in Fig. 2.3 is applied to Z_h and Z_{dr}, the scatter between the radar and gauge cumulative rainfall totals are significantly reduced (Fig. 4.1b). The FSE for the post-corrected $R(Z_h)$ is reduced to 45%. The FSE for the post-corrected $R(K_{dp},Z_{dr})$ is only 16%, compared to 83% for the pre-corrected estimator. This represents a five-fold reduction in the $R(K_{dp},Z_{dr})$ FSE. The FSE of the post-corrected $R(K_{dp},Z_{dr})$ is nearly a factor of 3 lower than the post-corrected FSE of $R(Z_h)$. These FSE's and the superior performance of $R(K_{dp},Z_{dr})$ compared to $R(Z_h)$ is consistent with theoretical expectations (Jameson, 1991b) and previous experimental results at S-band (Ryzhkov and Zrnic', 1995b; Bolen et al., 1998). The biases in the post-corrected, cumulative radar rainfall estimates are also significantly lower, particularly for

$R(Z_h)$. The NB for post-corrected $R(Z_h)$ is reduced by a factor five to -11.0%. For post-corrected $R(K_{dp},Z_{dr})$, the NB was reduced by a factor of two to 6%. Clearly, the propagation correction algorithm presented above improved the C-band, polarization radar estimation of cumulative rainfall during MCTEX.

For comparison, we corrected Z_h and Z_{dr} using ϕ_{dp} and the coefficients *a* and *b* derived from the simulations of Gorgucci et al. (1998) (see Tables 4.1 and 4.2). Although there was an improvement in the estimation of cumulative rainfall utilizing $R(Z_h)$ compared to uncorrected data, the results using the coefficient *a* from Gorgucci et al. (1998) were not as satisfactory as the empirical algorithm with a large drop adjustment presented in this study. When the Gorgucci et al. (1998) coefficient *b* was utilized to correct Z_{dr}, the $R(K_{dp},Z_{dr})$ cumulative rainfall results were actually worse than those using uncorrected Z_{dr} data. In this instance, the Gorgucci et al. (1998) correction of Z_{dr} actually increased the NB by a factor of 4.4 to 53%. Although somewhat counter-intuitive, inspection of the radar data provided a reasonable explanation of the result. In several instances, correction of Z_{dr} data with the Gorgucci et al. (1998) coefficient *b* resulted in an insufficient increase in Z_{dr} from a negative value to a very small, positive value ($0 < Z_{dr} < 0.2$ dB). When Z_{dr} is negative, the $R(K_{dp},Z_{dr})$ estimator (Eqn. 4.2) is not defined and does not contribute to the cumulative total. On the other hand, an insufficiently corrected positive value of Z_{dr} near zero combined with a significant value of K_{dp} can resulted in a grossly overestimated rain rate using $R(K_{dp},Z_{dr})$. As a result, it is possible for a ϕ_{dp} based propagation correction procedure which utilizes an inappropriately small coefficient *b*, to actually make the $R(K_{dp},Z_{dr})$ estimator significantly worse compared to not correcting Z_{dr} at all. This demonstrates the importance of using appropriate values of the coefficients *a* and *b*. The empirical method for determining unbiased coefficients described in Chapter 2 is superior to choosing coefficients from the published literature, which vary by at least a factor of two (Figs. 2.1a,b), with limited information regarding DSD and drop temperature.

4.2. Comparison with scattering simulations

Another approach used to validate the propagation correction algorithm was the internal consistency among polarimetric radar variables. In this case, we examined the

behavior of pre- and post-corrected Z_h and Z_{dr} versus K_{dp}, which is unaffected by propagation. As shown in Fig. 2.1a, scattering simulations predict very regular behavior for intrinsic $Z_h(K_{dp})$, particularly when DSD's characterized by large D_0 are excluded. There is significantly more scatter in the intrinsic relationship between Z_{dr} and K_{dp} (Fig. 2.1b). When large drops are excluded (i.e., consider solid squares only), the scatter is reduced and there is a generally increasing trend in Z_{dr} with K_{dp}. The scatter in both relationships are further reduced when K_{dp} is limited to values in excess of 2° km^{-1}. Therefore, we chose to compare observations of pre- and post-corrected $Z_h(K_{dp})$ and $Z_{dr}(K_{dp})$ to scattering simulation results for which $2 < K_{dp} < 7°$ km^{-1}, $\rho_{hv} \geq 0.97$, and $|\delta| \leq 1°$ (or 3° for C-pol observations).

Observations of pre- and post-corrected $Z_h(K_{dp})$ and $Z_{dr}(K_{dp})$ at 1 - 2 km from 0344 - 0543 UTC on 28 November 1995 are presented in Figs. 4.2a,b respectively along with curve-fits to the appropriate simulation results (solids squares) shown in Figs. 2.1a,b. As expected, the uncorrected observations of Z_h and Z_{dr} significantly underestimate the theoretical expectation represented by the simulation curves. The bias in the uncorrected Z_h (Z_{dr}) observations for this range of K_{dp} is -4.4 dB (-0.8 dB). In addition, the standard error of the uncorrected observations is considerably larger than the simulation results. For example, the standard error in the uncorrected $Z_h(K_{dp})$ and $Z_{dr}(K_{dp})$ scatterplots is 3.5 dB and 0.7 dB respectively. Note that our scattering simulations do not include the effects of measurement error. Typical standard errors, which are independent of propagation effects, for C-pol observations of Z_h and Z_{dr} are 1 dB and 0.25 dB respectively (Keenan et al., 1998b). A summary of the biases and standard errors resulting from the validation exercise are given in Table 4.3.

The propagation correction procedure nearly removed the significant observational biases in both the $Z_h(K_{dp})$ and $Z_{dr}(K_{dp})$ scatterplots, when compared to theory (Figs. 4.2a,b respectively). After correction, the biases in $Z_h(K_{dp})$ and $Z_{dr}(K_{dp})$ were decreased to 0.34 dB and 0.11 dB respectively. These order of magnitude reductions in the biases represent a substantial improvement over the uncorrected results. In addition, the scatter in both relationships were reduced considerably and are now more consistent with the scattering

simulations (cf Figs. 4.2a,b; Figs. 2.1a,b). For example, the standard errors for both $Z_h(K_{dp})$ and $Z_{dr}(K_{dp})$ were reduced by 35% - 40% to 2 dB and 0.4 dB respectively.

Clearly, the uncorrected Z_h and Z_{dr} observations are ill suited for quantitative use (i.e., rainfall estimation as shown above) or even qualitative use (i.e., hydrometeor identification). As shown in Part III of this study, the relationships between Z_h, Z_{dr}, and K_{dp} are used to differentiate between rainfall and precipitation sized ice and provide a rough estimate of their amounts. In addition to corrupting the estimation of rainfall (Sec. 4.1), these huge biases and standard errors in pre-corrected Z_h and Z_{dr} could result in widespread, incorrect hydrometeor identifications and undefined results. Fortunately, the propagation correction algorithm described in Chapters 2 and 3 substantially reduces both the bias and the standard error in Z_h and Z_{dr} (Table 4.3, Figs. 4.2a,b) relative to theoretical expectations. In Part III of this study, we demonstrate that the propagation corrected Z_h and Z_{dr} are of sufficient quality to differentiate between precipitation sized water drops and ice in the large majority of convective situations.

Table 4.3. Validation of propagation correction method using internal consistency among the polarimetric variables. Comparison of C-pol observations[1] of $Z_h(K_{dp})$ and $Z_{dr}(K_{dp})$ both before and after correction to scattering simulation[2] results.

	Mean	*Bias (Normalized Bias)*	*Standard Error (Normalized Standard Error)*
Z_h			
Scattering simulation	47.02 dBZ	NA	0.78 dB (1.6%)
No attenuation correction	42.63 dBZ	-4.40 dB (-9.4%)	3.46 dB (7.4%)
Attenuation correction	47.36 dBZ	0.34 dB (0.7%)	2.07 dB (4.4%)
Z_{dr}			
Scattering simulation	1.26 dB	NA	0.44 dB (34.9%)
No differential attenuation correction	0.49 dB	-0.77 dB (-61.2%)	0.66 dB (52.4%)
Differential attenuation correction	1.37 dB	0.11 dB (8.7%)	0.43 dB (34.1%)

[1] for $2 < K_{dp} < 7°$ km^{-1} at 1 - 2 km AGL from 0344 - 0543 UTC on 28 Nov 95

[2] assumptions of scattering simulation discussed in Appendix B

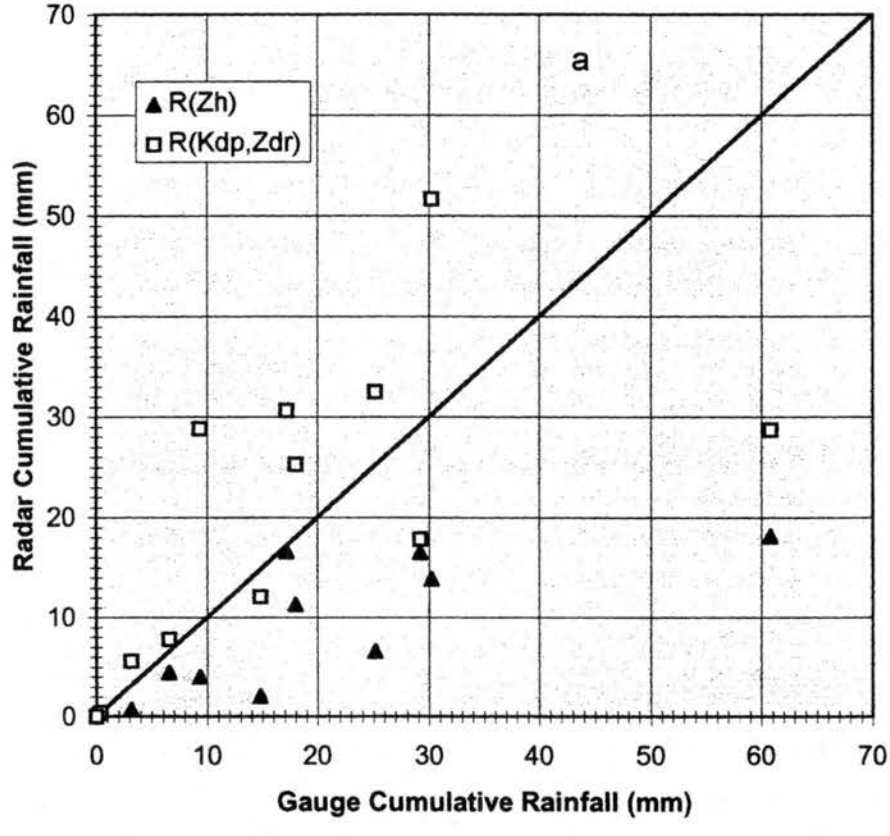

Figure 4.1. Scatterplot of the radar cumulative rainfall (mm) [as determined from both $R(Z_h)$ and $R(K_{dp},Z_{dr})$] versus the gauge cumulative rainfall (mm) for both (a) uncorrected Z_h and Z_{dr} data.

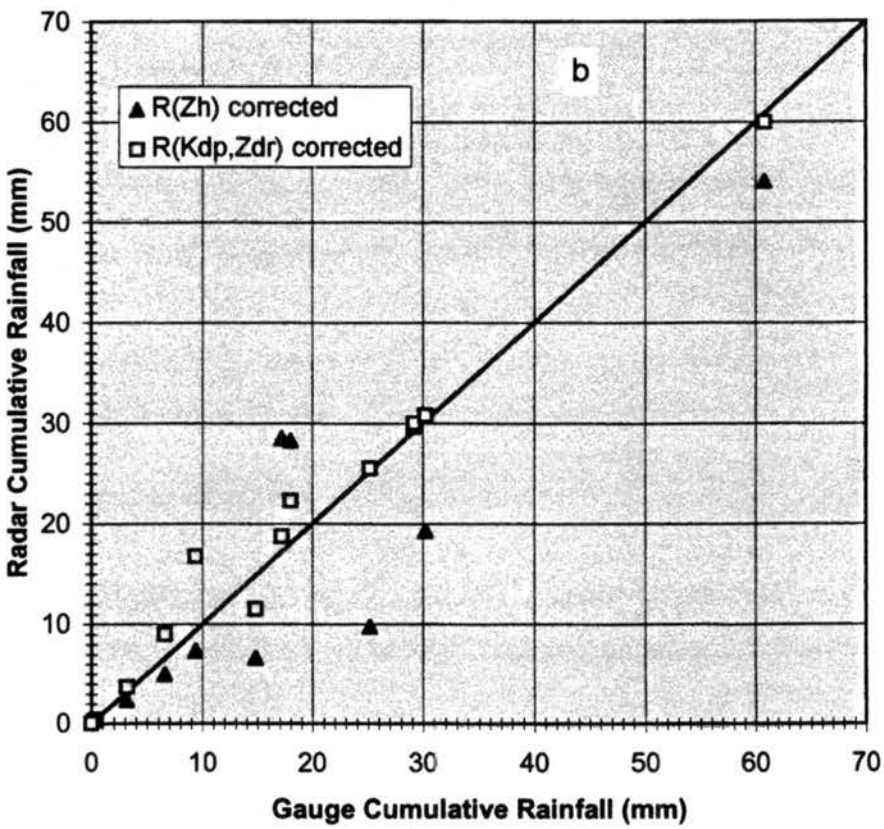

Figure 4.1. (b) as in (a) except propagation corrected (steps 1 - 6 in Fig. 2.3) Z_h and Z_{dr} data.

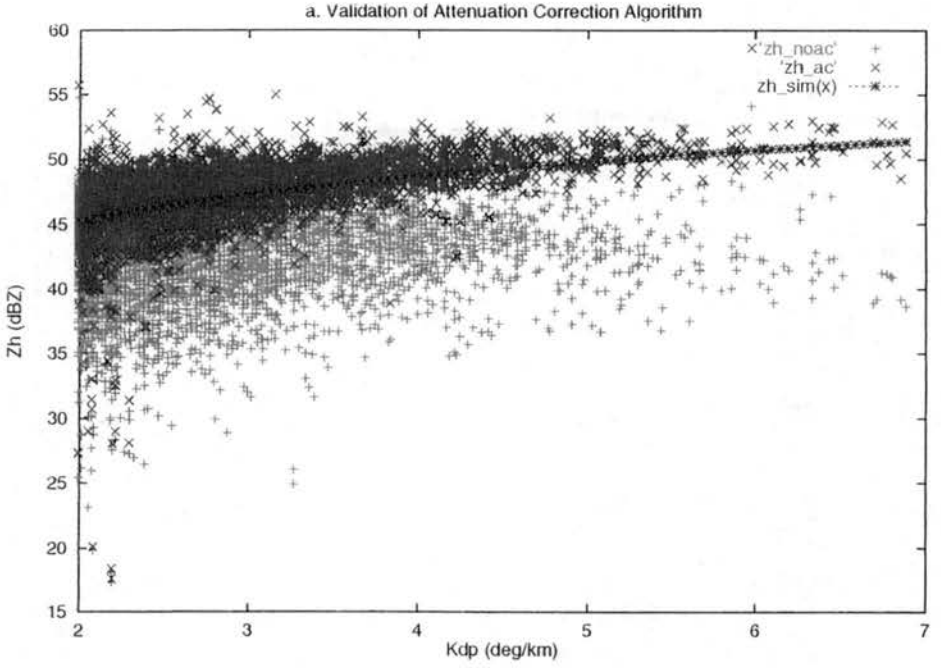

Figure 4.2. Scatterplot of C-pol observed (a) horizontal reflectivity (Z_h, dBZ) versus the specific differential phase (K_{dp}, deg km^{-1}) both before (+) and after (X) the propagation correction algorithm summarized in Fig. 2.3 was implemented. The data is taken from C-pol radar observations at 1 - 2 km AGL from 0344 to 0543 UTC on 28 November 1995.

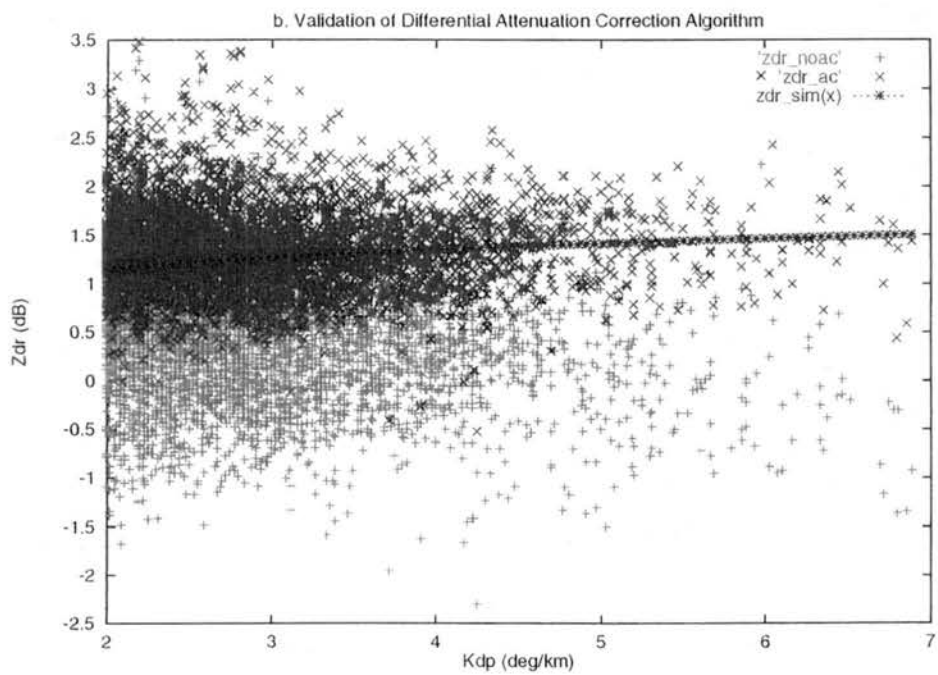

Figure 4.2. (b) as in (a) except differential reflectivity (Z_{dr}, dB) versus the specific differential phase (K_{dp}, deg km^{-1}).

CHAPTER 5
SUMMARY AND CONCLUSIONS

Before meteorological interpretation or analysis of C-band polarimetric radar data can begin, propagation effects must be identified and removed. In particular, the horizontal (differential) reflectivity must be corrected for the deleterious effects of horizontal (differential) attenuation. In this study, we utilize the differential propagation phase to estimate both the horizontal and differential attenuation in C-pol radar observations obtained during MCTEX. This phased-based approach has several advantages over traditional power-based algorithms. The specific differential phase 1) is immune to calibration errors (e.g., Zrnic' and Ryzhkov, 1996), 2) is not adversely affected by attenuation (e.g., Zrnic' and Ryzhkov, 1996), and yet 3) is approximately linearly proportional to both the specific horizontal and differential attenuation (e.g., Bringi et al., 1990).

The relationship between A_h or A_{hv} and K_{dp} is dependent on temperature, DSD, and the drop shape versus size relationship (e.g., Bringi et al., 1990; Jameson, 1991a; 1992; Keenan et al., 1998a). As a result, the calculated values of A_h and A_{hv} for a specific K_{dp} vary by a factor of two or more for relevant precipitation characteristics in published scattering simulations (ref. Figs. 1.1a,b). Without specific information on DSD, temperature, and drop shape throughout each radar echo volume, an unbiased estimate of $a = A_{hv}/K_{dp}$ and $b = A_{hv}/K_{dp}$ cannot be chosen from these published simulations. Therefore, we adapted and modified the empirical approach of Ryzhkov and Zrnic' (1995a) to estimate unbiased correction coefficients a and b for each radar volume.

The coefficients a and b are estimated from the observed decreasing trends of Z_h and Z_{dr} respectively with ϕ_{dp}. A least squares regression technique was applied to observed data to estimate the linear slope of this trend. The theoretical basis for this procedure was

reviewed and the regression method was presented and tested using C-pol radar observations taken during MCTEX. In order to extract the effects of propagation, the intrinsic variations in Z_h and Z_{dr} must be minimized. As in Ryzhkov and Zrnic' (1995a), we utilized a specific range of K_{dp} to mitigate intrinsic differences in Z_h and Z_{dr}. However, we found it also necessary to use ρ_{hv}, δ, and height to restrict the sample from which *a* and *b* were estimated. These polarimetric radar thresholds were chosen using scattering simulation results as a guide. Tropical drop size distributions observed during MCTEX were used as input for these scattering simulations. Statistical procedures to minimize biases in the inferred coefficients *a* and *b* were proposed and demonstrated. A mechanism to test the representativeness of the estimated correction coefficients was presented. Finally, a sensitivity study to investigate the above procedures was conducted.

During the mature phase of a tropical convective system on 28 November 1995, the empirical regression technique reliably produced statistically acceptable correction coefficients. The procedure was not overly sensitive to the choice of polarimetric and height thresholds as long as a sufficiently large sample, characterized by a limited intrinsic range of Z_h and Z_{dr}, was isolated. The range of empirically estimated coefficients was generally consistent with theoretical expectations. However, the coefficients *a* and *b* determined from prior scattering simulations tended to be 10 - 30% lower than the empirical results from MCTEX. When considering appropriate temperatures ($10° < T < 25°$ C) for tropical rainfall at 0.5 to 2 km AGL, the empirically inferred coefficients from MCTEX are 1.5 to 2 times larger than prior scattering simulations. This significant discrepancy between observations and theory at C-band in the tropics is similar to mid-latitude results at S-band by Ryzhkov and Zrnic' (1994, 1995a) and Smyth and Illingworth (1998).

Using scattering simulations, we demonstrated that *a* (A_h/K_{dp}) and *b* (A_{hv}/K_{dp}) are sensitive functions of the drop size if large raindrops are present. For small-to-moderate values of Z_{dr} (0.5 - 2 dB), the coefficients *a* and *b* are relatively insensitive to drop size. For $Z_{dr} > 2$ dB, the coefficients *a* and *b* increase rapidly as a function of Z_{dr}. As a result, the value of *a* (*b*) for large drops (e.g., $Z_{dr} = 4$ dB) is a factor of two (four) times larger than the coefficient for small-to-moderate sized drops. There are two implications for this

large drop sensitivity: 1) As also determined by Ryzhkov and Zrnic (1994, 1995a) and Smyth and Illingworth (1998), the presence of large drops in convection can bias the mean coefficients higher than prior scattering simulations (e.g., Bringi et al., 1990); and 2) the standard error for corrected Z_h and Z_{dr} in precipitation echo down range from large drop cores can be significantly larger than predicted by Bringi et al. (1990) if the mean coefficients are utilized. Since in-situ and radar observations during MCTEX confirmed the presence of large raindrops in tropical convection, these effects were deemed to be significant. The mean empirical method automatically eliminates any bias caused by the presence of large drops since no assumptions regarding DSD are made. Without some extension to this procedure however, the error down range of big drop cores was unacceptably large.

To minimize this error, we proposed the use of enhanced correction coefficients in so-called 'big drop zones.' The enhanced correction coefficients a^* and b^* were determined from scattering simulations of large drops. To locate large drop zones ($D_0 > 2.5$ mm) in the observed C-band data, we searched for dips in ρ_{hv} accompanied by significant perturbations in δ caused by Mie resonance effects. The method was demonstrated on observations of intense MCTEX convection containing a clear-cut example of enhanced propagation effects down range of big drop cores. The "big drop correction" significantly improved the qualitative results of the correction procedure.

To validate the overall propagation correction algorithm utilizing the differential propagation phase, cumulative rain gauge amounts were compared to cumulative radar rainfall estimates using $R(Z_h)$ and $R(K_{dp},Z_{dr})$ before and after correction. The correction procedure significantly reduced both the bias and standard error of both cumulative radar rainfall estimates to within expected ranges given typical measurement errors other than propagation. To further verify the procedure, we compared the behavior of Z_h and Z_{dr} with K_{dp} both before and after correction to theoretical expectations generated with scattering simulations. The uncorrected $Z_h(K_{dp})$ and $Z_{dr}(K_{dp})$ significantly underestimated the simulation results. The correction procedure reduced these negative biases by nearly an order of magnitude and substantially reduced the standard error of the observations relative to scattering simulations.

Given these validation results, we proceeded to qualitatively interpret and quantitatively analyze the propagation corrected Z_h and Z_{dr} with confidence in Part III of this study. The repeated correlation between radar inferred precipitation characteristics and cloud electrification and lightning demonstrated in Part III of this study provide additional indirect support for our propagation correction algorithm.

APPENDICES

Appendix A. Polarimetric radar data processing

Before analyzing any C-pol radar observations, all data were carefully edited using the Research Data Support System (RDSS) software developed at the National Center for Atmospheric Research (NCAR) (Oye and Carbone, 1981). First, all polarimetric radar data (Z_h, Z_{dr}, Φ_{dp}, and ρ_{hv}) at range gates characterized by $\rho_{hv} < 0.7$ were removed. This ρ_{hv} thresholding technique removes range gates in which the returned power is dominated by clear air noise with low signal-to-noise ratio or by ground clutter (Ryzhkov and Zrnic', 1998b). Any remaining ground clutter was manually removed since it has a deleterious effect on the quality of polarimetric radar measurements at low elevation angles. Spurious values of horizontal reflectivity and differential reflectivity caused by three-body scattering effects (Zrnic', 1987; Hubbert and Bringi, 1997) were removed manually. In regions of large reflectivity gradients, antenna pattern induced errors can bias the estimates of Z_{dr}, ρ_{hv}, and to a lesser extent Φ_{dp} (Pointin et al., 1988). In order to remove spurious data, we manually examined all regions of large ∇Z_h (> 20 dBZ km^{-1}) in azimuth and elevation angle and deleted the data if it appeared suspect. During MCTEX, the C-pol differential phase data were recorded between -32° and +32° with folding occurring for values outside of these bounds (Keenan et al., 1998b). A dealiasing algorithm in the RDSS software package was used to unfold the Φ_{dp} data. Next, the horizontal reflectivity data at low elevation angles (< 4°) were corrected for partial beam blocking according to the procedure described in May et al. (1998). We then removed the bias in Z_{dr} of +0.1 dB as determined from a vertically pointing scan in stratiform precipitation on 29 Nov 95 (Keenan et al., 1998b).

Since the differential phase at C-band is a combination of both the backscatter differential phase, which can be significant at C-band (e.g., Bringi et al., 1990; 1991;

Aydin and Giridhar, 1992), and the (forward) propagation differential phase, it was necessary to apply an iterative filtering technique (Hubbert and Bringi, 1995) to the differential phase data. We utilized a 13-point (over 3.9 km) running mean filter. The iterative application of this filter was designed to remove gate-to-gate fluctuations caused by significant δ or system phase noise while preserving the physically meaningful trends caused by ϕ_{dp}. The specific differential phase was then calculated from the filtered differential phase using a finite differencing approximation according to Eqn. 2.4. The accuracy or standard deviation of K_{dp} can be estimated from the expression given by Balakrishnan and Zrnic' (1990)

$$\sigma_{K_{dp}} = \frac{\sqrt{3}\sigma_{dp}}{N^{3/2}\Delta_r} \tag{A.1}$$

where σ_{dp} is the standard deviation of the differential phase, N is the number of range gates in the filter, and Δ_r is the range gate spacing. Given a standard deviation of the differential phase of about 3° - 4° (Keenan et al., 1998b), 13 points in the filter, and a range gate spacing of 0.3 km, the accuracy of K_{dp} is estimated as 0.4 - 0.5° km^{-1}. For the dwell times used in this study, typical standard errors of measurement for the other variables are: 1 dB for Z_h, 0.25 dB for Z_{dr}, and 0.01 for ρ_{hv} (Keenan et al., 1998b).

Some analysis applications in this three part study required gridded Cartesian radar data. Therefore, we interpolated all polarimetric radar variables to a Cartesian grid using the NCAR REORDER software package (Mohr, 1986). The grid was centered on the Tiwi Islands with a horizontal and vertical spacing of 1.0 and 0.5 km respectively. Variable radii of influence consistent with the scanning strategies during MCTEX (Keenan et al., 1994) were utilized in order to maximize the resolution of the data in range from the radar. The radius of influence in the azimuthal (elevational) direction was 1.2° (2°). In range, the radius of influence was equal to the product of the range and the azimuthal radius of influence in radians.

Appendix B. Scattering simulations of C-band polarimetric radar parameters in rain

During MCTEX, a Joss and Waldvogel (1967) disdrometer collected raindrop size distribution information as described in Keenan et al. (1998a). The disdrometer data was fit to gamma drop size distributions according to Ulbrich (1983). As discussed in Keenan et al. (1998a), empirical linear relationships between the gamma DSD parameters were determined. The empirical relations were then used to obtain physically realistic domains for the fitted gamma DSD parameters which were used as input to the T-matrix (Barber and Yeh, 1975) scattering simulations of rainfall at C-band (5.33 cm).

In the T-matrix scattering simulations, raindrops were modeled as oblate spheroids with a shape versus size relationship defined by Green (1975). The dielectric of water was obtained from Ray (1972) using a temperature of 20° C, consistent with typical wet-bulb temperatures near the surface over the Tiwi islands as analyzed from sounding data during MCTEX. Based on in-situ and radar observations of large drops during MCTEX and prior evidence for the presence of large drops in tropical convection (reference summary in Appendix D), the maximum drop diameter, D_{max}, was set at 8 mm and the median volume diameter, D_0, was allowed to vary from 0.8 mm to 5 mm.[4] As discussed above, the other DSD parameters (N_0, μ) of a gamma distribution were varied according to empirical relationships determined by Keenan et al. (1998a).

Using the resulting T-matrices as input to a Mueller-matrix scattering model (e.g., Vivekanandan et al., 1991), C-band backscatter and propagation characteristics as described by various polarimetric radar parameters (Z_h, Z_{dr}, K_{dp}, δ, ρ_{hv}, A_h, and A_{hv}) were simulated. Following Vivekanandan et al. (1991), hydrometeor canting angle and radar elevation angle effects were considered. Rainfall orientation distributions were modeled by a quasi-Gaussian distribution (e.g., Vivekanandan et al., 1991) with a mean of zero and a standard deviation of 5°. For the results in this study, the simulated radar elevation angle was held fixed in a plane 0.5° above the local surface.

[4] In Part III of the dissertation, we investigate the effect of drop size on estimating Z_h(rain) using K_{dp} and Z_{dp}. Therefore, we also ran the simulations assuming D_{max} = 4 mm and $0.8 < D_0 < 4$ mm.

Appendix C. Sensitivity study of the mean empirical correction method

A sensitivity study was conducted to test the effects of varying the regression sample from which the slopes in Eqns. 2.7 and 2.9 were determined, by using various polarimetric radar measurand (K_{dp}, ρ_{hv}, δ) and height thresholds. In essence, we tested the effectiveness of various threshold combinations in mitigating the intrinsic scatter in Z_h and Z_{dr} before regressing the slope of Z_h and Z_{dr} versus ϕ_{dp} (i.e., *a* and *b* respectively) using the least squares method. Many threshold combinations were examined. A summary of sixteen of these tests is given in Tables C.1 - C.3. Table C.1 describes the utilized thresholds and purpose of each test. Each set of thresholds was applied to twelve polarimetric radar volumes from 0344 to 0543 UTC on 28 Nov 95. The mean, median, standard deviation, maximum, and minimum *a* (*b*) regressed from the twelve radar volumes for each test are presented in Table C.2 (C.3). Statistical parameters which describe the "goodness of the fit" including the coefficient of correlation (ρ), the standard error or scatter (S), and the sample size (N), are also provided for each test. We also tallied the percentage of "good retrievals" for each test based on thresholds for ρ, N, S, and ϕ_{dp}(max) given in Sec. 2.2.

The mean and median for *a* and *b* are similar for each test except for test 6 which essentially utilized no polarimetric thresholds. In the mean, the regression procedure was not overly sensitive to variations in the thresholds. However, several of the tests failed to provide reasonable values of *a* and *b* for individual radar volumes. For example, tests 2 and 6 actually produced negative values of *a* for a few radar volumes. A negative correction coefficient implies increasing reflectivity with phase shift, which is not physically meaningful from a propagation perspective. For other tests, retrievals failed for statistical reasons. For example, the sample size was too small; the coefficient of correlation was too low; or the standard error was too high.

For our data set, test 1 contained the best combination of thresholds and was therefore used for analyses in this study, including Part III. We judged test 1 to be superior because 100% of the twelve attempted retrievals were successful. In general, test 1 produced some of the highest coefficients of correlations and lowest standard errors while maintaining a sufficient sample size. Test 1 is an extension of the Ryzhkov and Zrnic'

(1995a) procedure to include ρ_{hv} and δ thresholds and multiple height levels which are well below the melting zone. When we tested the Ryzhkov and Zrnic' (1995a) method, we obtained unsatisfactory results (test 2). The mean standard error was very large compared to test 1 and the coefficient of correlation was lower. The poor statistics for the Ryzhkov and Zrnic' (1995a) method suggest that intrinsic variations in Z_h and Z_{dr} were corrupting the determination of the slope.

Table C.1. Description of sensitivity tests for the mean empirical correction method described in Chapter 2. Thresholds utilized in Step 2 of procedure outlined in Fig. 2.3.

Sensitivity Test	height (km)	K_{dp} (° km^{-1})	ρ_{hv} >	$\lvert\delta\rvert$ < (°)	Comments
Test 1	0.5 - 2.0	1.0 - 2.0	0.95	5	used for analysis in Parts II, III.
Test 2	1.0	1.0 - 2.0	NA	NA	Ryzhkov and Zrnic (1995)
Test 3	0.5 - 2.0	0.5 - 1.0	0.95	5	testing K_{dp}
Test 4	0.5 - 2.0	2.0 - 4.0	0.95	5	testing K_{dp}
Test 5	0.5 - 2.0	0.5 - 1.5	0.95	5	testing K_{dp}
Test 6	0.5 - 2.0	0.25 - 10.0	NA	NA	essentially no radar thresholds
Test 7	0.5 - 2.0	1.0 - 2.0	NA	NA	K_{dp} only; multiple levels
Test 8	0.5 - 2.0	1.0 - 2.0	0.97	5	more restrictive ρ_{hv}
Test 9	0.5 - 2.0	1.0 - 2.0	0.95	2	more restrictive δ
Test 10	0.5 - 2.0	1.0 - 2.0	0.97	2	more restrictive ρ_{hv} and δ
Test 11	0.5 - 1.0	1.0 - 2.0	0.95	5	testing height
Test 12	1.5 - 2.0	1.0 - 2.0	0.95	5	testing height
Test 13	2.5 - 3.0	1.0 - 2.0	0.95	5	testing height
Test 14	3.5 - 4.0	1.0 - 2.0	0.95	5	testing height
Test 15	4.0 - 4.5	1.0 - 2.0	0.95	5	testing height
Test 16	4.5 - 5.0	1.0 - 2.0	0.95	5	testing height

In tests 3 - 5, we applied various ranges of K_{dp}. As discussed in Sec. 2.2, the intrinsic scatter in Z_h or Z_{dr} for a given unit interval of K_{dp} decreases with increasing K_{dp}. As a result, some of the regressions with the best fit as determined by low standard error and high correlation came from samples characterized by $2 < K_{dp} < 4°$ km^{-1} (test 4). However, these high values of K_{dp} are relatively scarce, even during the mature phase of an intense tropical convective system. As a result, test 4 only worked 75% of the time. Lower ranges of K_{dp} were attempted (test 3 and 5) but the regression statistics were inferior to

test 1 because of the increased intrinsic scatter at low K_{dp} (e.g., Figs. 2.1a,b) and often failed to produce an acceptable slope.

Test 6 was a reference test which did not utilize polarimetric measurands to limit the sample. The standard error was a maximum and the correlation a minimum. As a result, an acceptable regression was rarely produced. Test 7 expanded the Ryzhkov and Zrnic' (1995a) K_{dp} threshold to multiple height levels. The increased sample size improved the regression results slightly but test 1 statistics were still far superior. Based on the results of tests 1, 2, 6, and 7, ρ_{hv} and δ thresholds appear to be crucial components in the minimization of the intrinsic scatter. The use of more restrictive ρ_{hv} and δ thresholds (tests 8 - 10) reduced the standard error of the least squares regression. However, the sample size was sometimes too small to get a good regression. Since the standard deviation of the measured differential phase was about 3°, a $|\delta|$ threshold above this value was best. A ρ_{hv} threshold between 0.95 and 0.97 produced fairly similar results. The lower threshold was utilized because it provided the most reliable results.

The effect of varying height on the regression technique was examined (tests 11 - 16). Splitting the sample from test 1 in half for tests 11 and 12 produced nearly identical results. There was a slight advantage to using the larger sample size from test 1. Above about 4 km, there was a rapid decrease in the sample size due to proximity to the environmental freezing level at about 5 km. This adversely affected the results for test 16. Even considering the statistical error in the estimates, there was a slight trend for the correction coefficients *a* and *b* to increase with increasing height of the sample. This is consistent with a generally decreasing temperature of the propagation medium with height (Jameson, 1992).

Finally, we present the temporal evolution of the coefficients *a* and *b* in Figs. C.1a and b respectively for test 1 and the consensus. The consensus estimates of the correction coefficients are an average of all tests which exceeded the statistical thresholds given in Fig. 2.3 or Tables C.2 and C.3. The range of the 95% confidence level for the consensus mean at each time is also presented. Given the varying regression samples for each test, the statistical variability in the consensus means is acceptable. The 95% confidence level

for each consensus mean is less than 10% of the mean value for each radar volume. The coefficients from test 1 and the consensus mean are relatively stable in time.

There is a systematic shift in both coefficients a and b for test 1 and the consensus mean between 0449 and 0514 UTC. The coefficient a increases from 0449 to 0514 UTC (Fig. C.1a) while the coefficient b decreases (Fig. C1.b). The shift in the consensus coefficient b is statistically significant. The shift in the consensus a is less significant given the statistical variability. However, since the temporal variation is systematic for all tests and since the coefficients a and b are relatively stable in time before 0502 UTC and after 0514 UTC, the shift appears to be physically meaningful.

We hypothesize that a systematic shift in the storm wide drop size distribution from the developing-to-mature phase (0344 - 0502) to the late mature phase (0502 - 0543) was responsible for the increase in coefficient a and the nearly simultaneous decrease in coefficient b. More details regarding the life-cycle of this tropical convective system can be found in Part III of this study. If a change in the storm average DSD was responsible for the systematic and yet opposing temporal behavior of the coefficients a and b, Fig. 3.1 suggests that the dominant drop diameter and hence the dominant Z_{dr} of the propagation medium must have decreased. The only portion of the DSD as measured by Z_{dr} for which a increases and b decreases is below about 1 dB to 1.25 dB (Fig. 3.1). To test this hypothesis, we binned the storm integrated K_{dp}, which is proportional to specific attenuation and specific differential attenuation, by Z_{dr} at each range gate below 3 km. To demonstrate the shift in DSD toward smaller drops later in the storm lifecyle, the results for 0433 UTC are compared to 0543 UTC in Fig. C.2. Toward the end of the mature phase (0543 UTC), the fraction of the storm integrated K_{dp} characterized by $Z_{dr} \leq 1.25$ dB is over 81%, compared to only 51% for 0433 UTC. Comparison of Figs. 3.1, C.1a,b, and C.2 provides strong circumstantial evidence for an observed shift in the DSD which resulted in an observed systematic shift in the coefficients a and b according to theory. This consistency between the observational results and theoretical expectations is further proof that the regression technique works.

Table C.2. Summary of sensitivity test results for the estimation of $a = A_h/K_{dp}$ (dB deg^{-1}) using the mean empirical method described in Chapter 2. Tests conducted on twelve radar volumes from 0344 - 0543 UTC on 28 November 1995.

Sensitivity Test	Mean a	Standard Dev. a	Median a	Maximum a	Minimum a	% of good retrievals*	Mean ρ^2	Mean N	Mean S (dB)
Test 1	0.0897	0.0112	0.0901	0.1078	0.0771	100 %	0.61	642	3.7
Test 2	0.0930	0.0382	0.1047	0.1353	-0.0051	58 %	0.56	273	5.4
Test 3	0.0880	0.0342	0.0836	0.1546	0.0185	42 %	0.36	707	5.4
Test 4	0.1012	0.0217	0.0948	0.1524	0.0791	75 %	0.73	389	2.5
Test 5	0.0779	0.0313	0.0817	0.1490	0.0300	50 %	0.34	1088	5.3
Test 6	0.0247	0.0299	0.0329	0.0662	-0.0372	0 %	0.13	3381	7.4
Test 7	0.0950	0.0352	0.1047	0.1289	0.0018	42 %	0.55	1094	5.8
Test 8	0.0770	0.0276	0.0849	0.1277	0.0208	58 %	0.45	231	2.7
Test 9	0.0925	0.0271	0.0917	0.1562	0.0349	75 %	0.43	408	3.6
Test 10	0.0800	0.0396	0.0788	0.1619	0.0016	33 %	0.30	181	2.6
Test 11	0.0888	0.0146	0.0885	0.1104	0.0692	92 %	0.58	313	3.8
Test 12	0.0911	0.0067	0.0916	0.1009	0.0773	92 %	0.60	336	3.9
Test 13	0.0914	0.0136	0.0929	0.1227	0.0705	75 %	0.55	342	4.1
Test 14	0.0993	0.0202	0.1011	0.1291	0.0618	50 %	0.53	310	4.5
Test 15	0.1206	0.0190	0.1166	0.1543	0.0655	42 %	0.58	203	4.9
Test 16	0.1174	0.0592	0.1376	0.2069	0.026	0 %	0.48	85	6.0

* There were a total of 12 retrieval attempts. A "good" retrieval occurs when $\rho^2 \geq 0.25$, $N \geq 200$, $S \leq 5.5$ dB, and $\phi_{dp}(\max) \geq 15°$.

Table C.3. Summary of sensitivity test results for the estimation of $b = A_{hv}/K_{dp}$ (dB deg^{-1}) using the mean empirical method described in Chapter 2. Tests conducted on twelve radar volumes from 0344 - 0543 UTC on 28 November 1995.

Sensitivity Test	Mean *b*	Standard Dev. *b*	Median *b*	Maximum *b*	Minimum *b*	% of good retrievals*	Mean ρ^2	Mean N	Mean S (dB)
Test 1	0.0179	0.0025	0.0172	0.0215	0.0144	100 %	0.76	665	0.42
Test 2	0.0177	0.0054	0.0150	0.0307	0.0130	8 %	0.70	267	0.74
Test 3	0.0173	0.0047	0.0161	0.0284	0.0119	75 %	0.69	734	0.44
Test 4	0.0191	0.0056	0.0172	0.0300	0.0125	75 %	0.79	380	0.39
Test 5	0.0172	0.0044	0.0158	0.0289	0.0133	83 %	0.68	1125	0.45
Test 6	0.0127	0.0020	0.0130	0.0174	0.0096	8 %	0.56	3764	0.74
Test 7	0.0177	0.0045	0.0150	0.0276	0.0146	33 %	0.70	1065	0.72
Test 8	0.0178	0.0046	0.0163	0.0302	0.0133	83 %	0.78	233	0.22
Test 9	0.0181	0.0052	0.0166	0.0296	0.0117	75 %	0.64	411	0.39
Test 10	0.0166	0.0052	0.0158	0.0292	0.0104	25 %	0.69	170	0.20
Test 11	0.0178	0.0024	0.0176	0.0220	0.0144	100 %	0.75	330	0.40
Test 12	0.0183	0.0032	0.0178	0.0233	0.0137	100 %	0.77	342	0.43
Test 13	0.0179	0.0046	0.0170	0.0261	0.0105	75 %	0.77	334	0.43
Test 14	0.0182	0.0051	0.0164	0.0287	0.0115	75 %	0.76	299	0.43
Test 15	0.0190	0.0046	0.0187	0.0268	0.0124	58 %	0.78	210	0.40
Test 16	0.0187	0.0063	0.0199	0.0257	0.0088	8 %	0.76	94	0.38

* There were a total of 12 retrieval attempts. A "good" retrieval occurs when $\rho^2 \geq 0.6$, $N \geq 200$, $S \leq 0.55$ dB, and $\phi_{dp}(max) \geq 15°$.

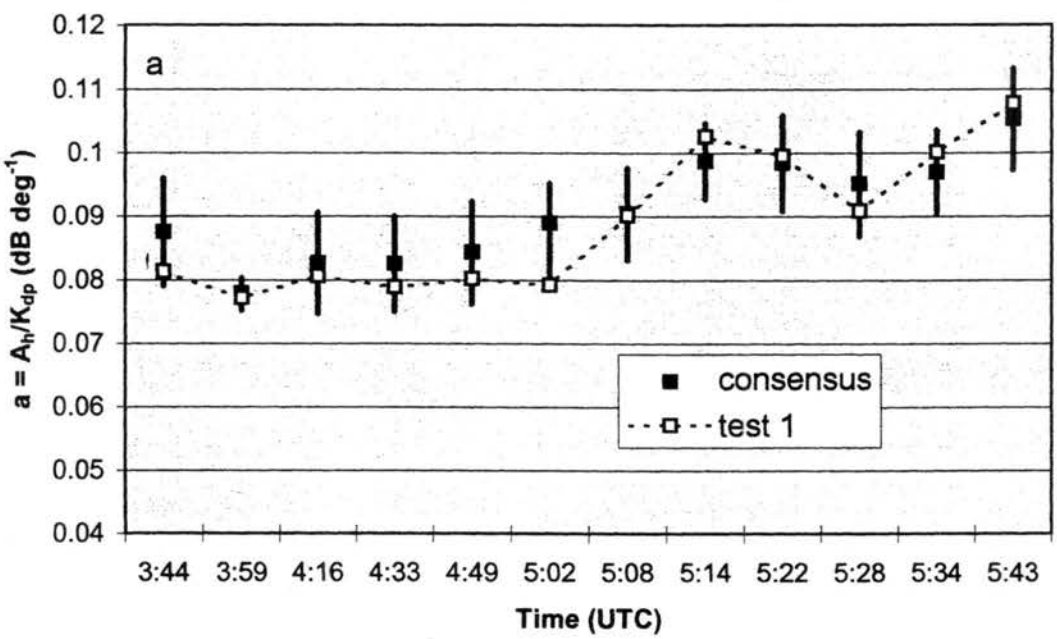

Figure C.1. Temporal evolution of the empirically inferred mean correction coefficient (a) a (dB deg^{-1}) from 0344 to 0543 UTC for both test 1 (cf Tables C.1-C.3) and the consensus mean. The 95% confidence interval for the consensus mean is given.

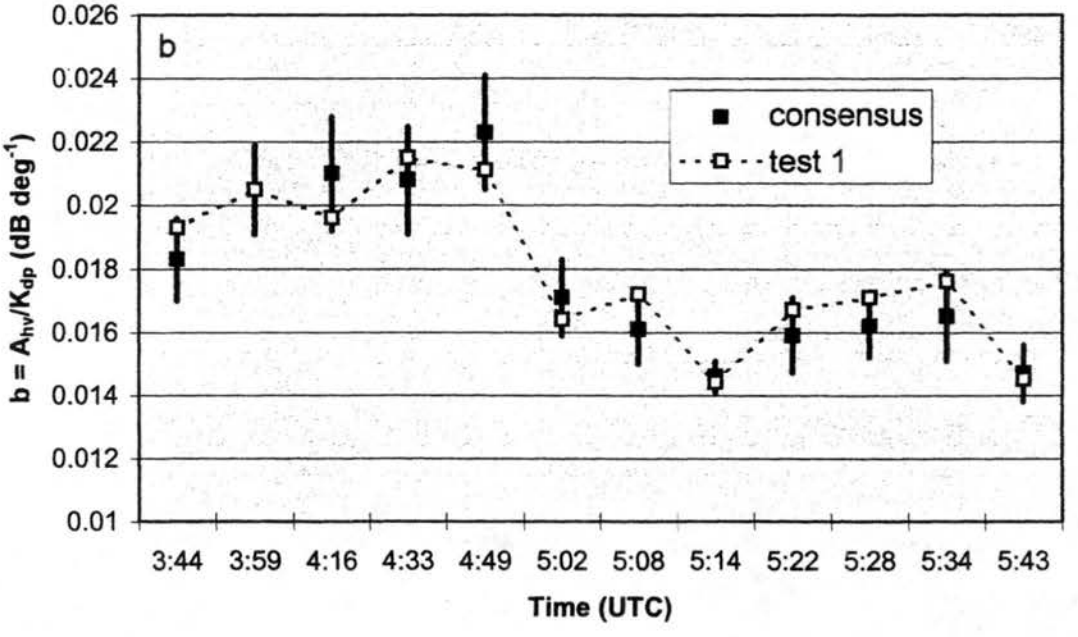

Figure C.1. (b) as in (a) except the mean correction coefficient b (dB deg^{-1}).

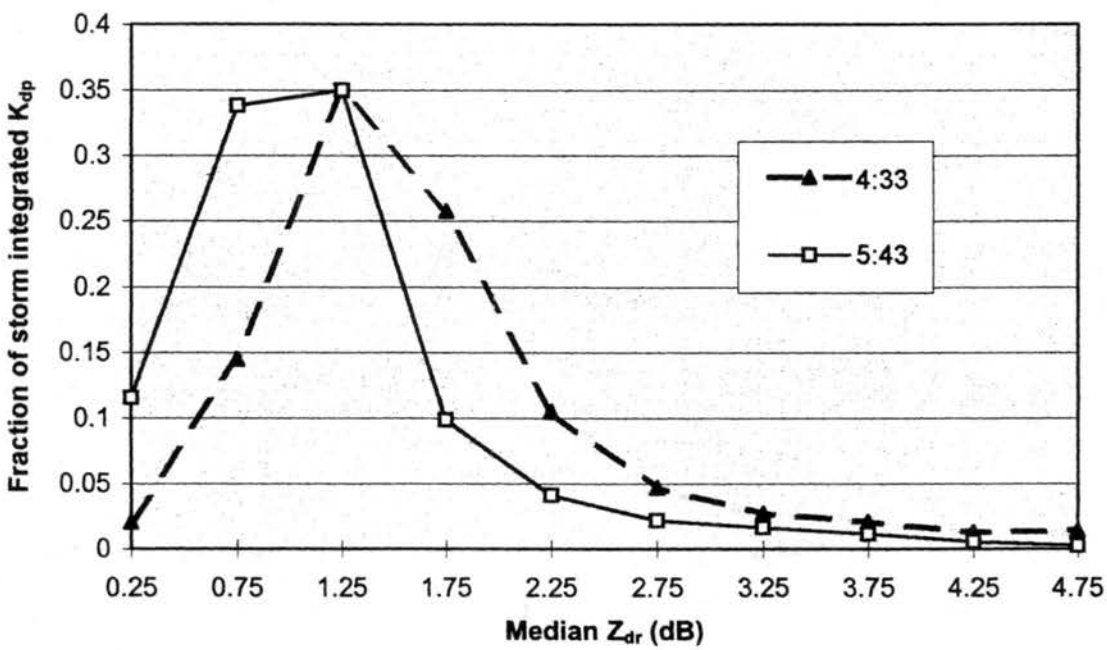

Figure C.2. Histogram of the storm integrated specific differential phase (K_{dp}) versus the median differential reflectivity (Z_{dr}, dB) of each Z_{dr} bin at 0433 and 0543 UTC on 28 November 1995 below 3 km. The storm integrated K_{dp} fraction for each 0.5 dB Z_{dr} bin was calculated by adding the K_{dp} at each range gate below 3 km to the appropriate bin sum and then dividing the bin sum by the storm total K_{dp} sum below 3 km.

Appendix D. In-situ and radar evidence for large drop occurrence during MCTEX

Before offering observational evidence supporting the presence of large (i.e., D > 3 mm) drops in the tropical island convection observed during MCTEX, it is important to review some potential hypotheses for their production. In tropical maritime airmasses, the presence of exceptionally large aerosol particles acting as nuclei for drops near cloud base may allow drops to reach giant size as they accrete smaller drops (e.g., Johnson, 1982; Rauber et al., 1991). Alternatively in the tropics, an active coalesence process in a cloud environment nearly devoid of smaller raindrops, hence limiting collisional break-up, but rich in cloud liquid water can result in large drop production (e.g., Rauber et al., 1991; Szumowski et al., 1998). Although it is beyond the scope of this study to investigate these hypotheses further, it is possible that one or both of these mechanisms were operative over the Tiwi Islands during MCTEX.

Both in-situ and polarimetric radar data collected during MCTEX suggest the presence of large raindrops. A videosonde system described by Takahashi (1990), collected in-situ microphysical data during MCTEX. During six in-cloud ascents in various microphysical conditions, the videosonde observations confirmed the presence of large raindrops in tropical convection. A total of twenty-one (five) drops possessing diameters in excess of 3 mm (5 mm) were observed despite the small sample size of the instrument and a limited number of cloud ascents in microphysical regions typically associated with large drops (personal communication; Takahashi, 1997). The largest rain drop observed by the videosonde system was 8 mm in diameter. In addition, a Joss and Waldvogel (1967) disdrometer collected raindrop information at the surface during MCTEX. Despite a small sample volume, the disdrometer observed twelve drops with diameters in excess of 5 mm (Keenan et al., 1998a). These results are consistent with in-situ aircraft observations of large drops (i.e., 4 - 8 mm in diameter) coincident with high reflectivity cores in tropical rainbands over Hawaii (Beard et al., 1986; Szumowski et al., 1998).

During MCTEX, the C-pol radar observed maximum values of Z_{dr} in excess of 5 dB, suggesting the presence of raindrops possessing $D_0 > 4$ mm and $D_{max} \geq 6$ mm (e.g., Keenan et al., 1998a). At 0416 UTC, there were over twelve distinct precipitation cores

of $Z_{dr} \geq 3$ dB at 2 km AGL (Fig. 2.6b). As shown in Fig. D.1, rain cores characterized by $Z_{dr} \geq 3$ dB (and hence $D_0 > 2.5$ mm) were observed *routinely* by the C-pol radar during the developing-to-mature phase of the 28 Nov 95 tropical convective system. From 0216 to 0626 UTC, these large drop precipitation cores covered from 12 to 74 km^2 of surface area, representing 1 to 6 % of the convective ($Z_h > 25$ dBZ) precipitation echo at 0.5 km AGL.

To demonstrate that these large drops were also a significant component of the propagation medium, we partitioned the storm integrated specific differential phase by differential reflectivity for the developing-to-mature phase (0216 - 0626) of the convection below 3 km (Fig. D.2). Since Z_{dr} is a measure of the reflectivity weighted drop shape (Jameson, 1983) and hence size (e.g., Pruppacher and Beard, 1970) and K_{dp} is proportional to the specific horizontal and differential attenuation (Bringi et al., 1990), the results in Fig. D.2 provide a rough estimate of the role large drops played in propagation effects. As expected, a large majority (74%) of the storm integrated K_{dp} from 0216 - 0626 was caused by drops with small to moderate Z_{dr} ($0.5 < Z_{dr} < 2.0$ dB). However, over 20% of the storm integrated K_{dp} was caused by rainfall characterized by large $Z_{dr} > 2$ dB. During the most intense period of the mature phase (e.g., 0416 UTC as shown in Figs. 2.5, 2.6a,b), 31% of the storm integrated K_{dp} was caused by large drops ($Z_{dr} > 2$ dB). Of course, the juxtaposition of these large drop cores between the radar and the rest of the precipitation echo will also determine how important they are in causing propagation effects. On 28 November 1995, much of the intense convection developed close to the radar with significant echo down range from large drop cores (cf Figs. 2.6a,b). Therefore, large drops did play an important role in the propagation medium over the Tiwi Islands.

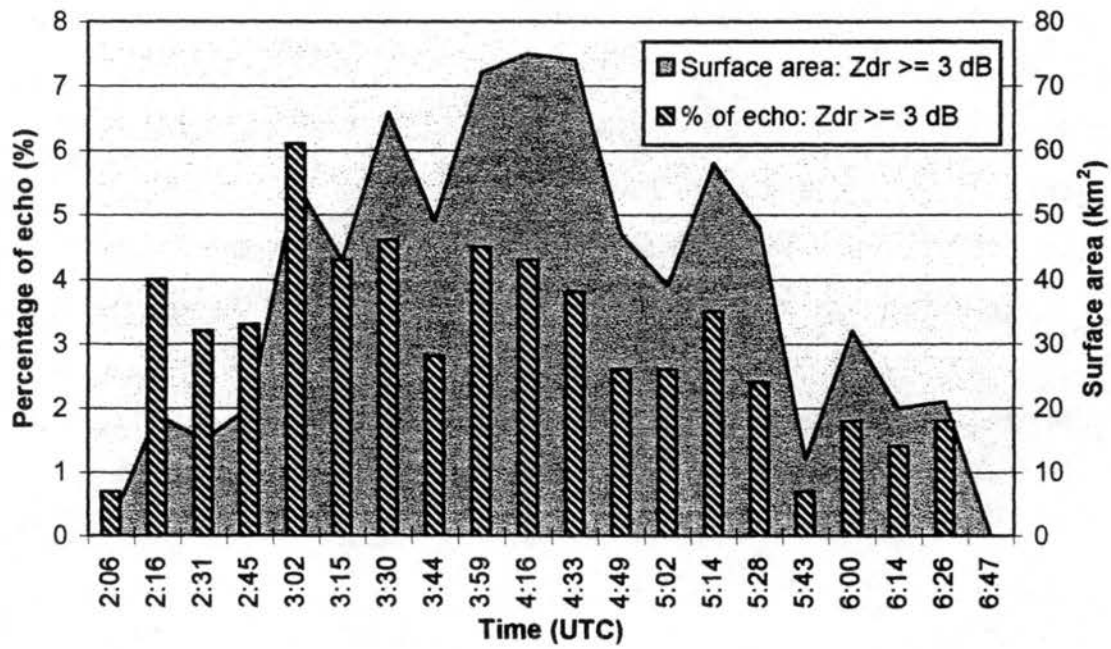

Figure D.1. Plot of the temporal evolution of the surface area (km^2) and percentage of the convective (Z_h > 25 dBZ) precipitation echo at 0.5 km AGL covered by $Z_{dr} \geq 3$ dB during the developing-to-mature phase of the 28 November 1995 tropical convective system.

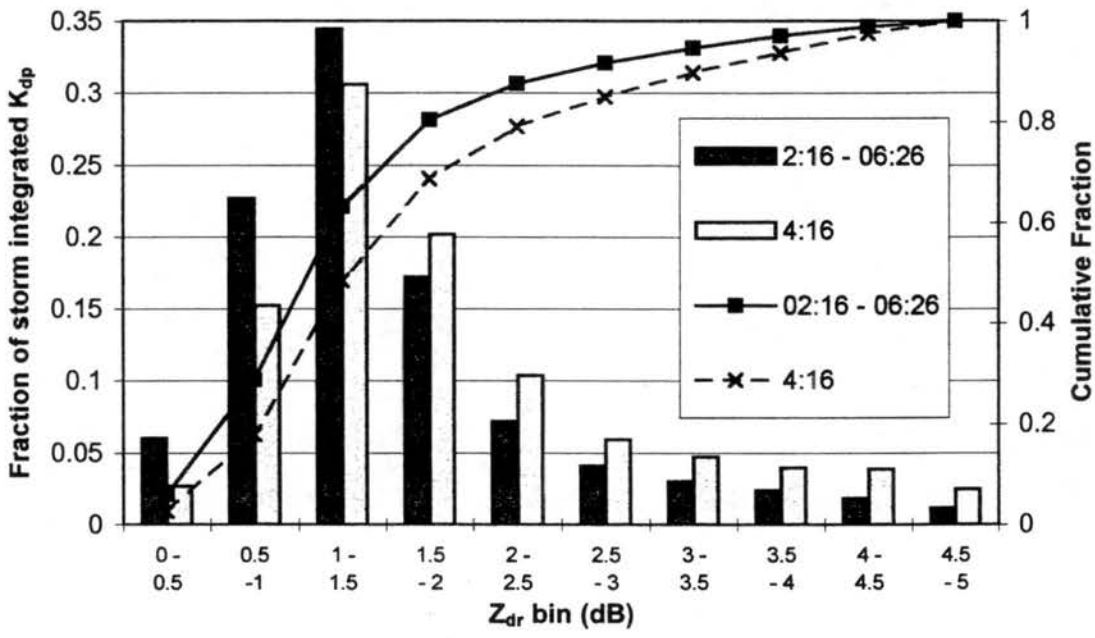

Figure D.2. As in Fig. C.2 except for different times (mean of 0216 - 0626 UTC and 0416 UTC) and cumulative histogram lines are added.

Appendix E. C-band polarimetric radar rain rate equations

Using results of the C-band scattering simulations described in Appendix B, we derived rain rate estimators customized to the DSDs observed during MCTEX based on Z_h, K_{dp}, Z_h/Z_{dr}, and K_{dp}/Z_{dr} using a least-squares curve fitting procedure. The corresponding equations for the four radar rainfall estimators (Eqns. E.1 - E.4) are summarized in Table E.1 along with coefficient of correlations and normalized standard errors of the estimators. The curve fitting samples for the rainfall estimators utilizing either K_{dp} or Z_{dr} were restricted by the standard error of the measurement, which are 0.25 dB for Z_{dr} and 0.4° km^{-1} for K_{dp} as discussed in Appendix A. Note that the statistical errors listed in Table E.1 do not include measurement error.

Table E.1. Regressed Eqns. (E.1 - E.4) for C-band polarimetric radar rain rate estimators and associated coefficients of correlation and normalized standard errors.

Rain rate estimator (R, mm h^{-1})	ρ	Normalized Standard Error (NSE)
E.1. $R(Z_h) = 5.865\text{x}10^{-3} \bullet Z_h^{0.862}$	0.965	193%
E.2. $R(K_{dp}) = 23.37 \bullet K_{dp}^{0.82}$	0.951	41%
E.3. $R(Z_h,Z_{dr}) = 1.783\text{x}10^{-3} \bullet Z_h^{0.983} \bullet Z_{dr}^{-1.24}$	0.999	24%
E.4. $R(K_{dp},Z_{dr}) = 25.00 \bullet K_{dp}^{0.988} \bullet Z_{dr}^{-0.583}$	0.972	8%

Note: Z_h in $mm^6\ m^{-3}$, Z_{dr} in dB, and K_{dp} in deg km^{-1}.

The $R(Z_h)$ and $R(K_{dp},Z_{dr})$ relationships were utilized in the validation of the propagation correction method (Chapter 4, Sec. 4.1). We compared each gauge rainfall total to the radar cumulative rainfall estimates at the closest 1 km × 1 km grid point. Throughout this paper, we utilized the Normalized Bias (NB) and the Normalized Standard Error (NSE) to evaluate the performance of various estimators relative to some reference data or "truth" (e.g., the rain gauges in Sec. 4.1). The normalized bias is defined as

$$NB = \left[\frac{\Sigma(X_e - X_t)}{n}\right] \Big/ \overline{X}_t \qquad \text{(E.5)}$$

and the normalized standard error is defined as

$$NSE = \left[\Sigma\left(X_e - \overline{X}_e - X_t - \overline{X}_t\right)^2 / n\right]^{1/2} \Big/ \overline{X}_t \qquad \text{(E.6)}$$

where X_e is the estimated variable, X_t is the referenced parameter or "truth," the overbar indicates a mean, and n is the number of samples.

A composite rain mass flux algorithm over the Tiwi Islands (kg s^{-1}) which utilized the best available estimator of the four rain rate relationships (E1 - E4) at each point, was applied in Part III of this study after the data was corrected for propagation effects. As shown in Jameson (1991b) and Ryzhkov and Zrnic' (1995b) and confirmed in our study, the standard errors of the polarimetric radar rain estimators decrease significantly from Eqn. E.1 to E.4. In other words, the standard error (SE) of $R(Z_h)$ > SE $R(K_{dp})$ > SE $R(Z_h,Z_{dr})$ > SE $R(K_{dp},Z_{dr})$ as shown in Table E.1. As in Ryzhkov and Zrnic' (1995b), we determined that the statistical error of the $R(K_{dp},Z_{dr})$ estimator is 3 times less than the SE of the $R(Z_h,Z_{dr})$ estimator. Therefore, the composite rain mass flux algorithm first used Eqn. E.4 if possible. The $R(K_{dp},Z_{dr})$ estimator was used at a grid point if $K_{dp} \geq 0.4°$ km^{-1} and $Z_{dr} \geq 0.25$ dB. If $K_{dp} < 0.4°$ km^{-1} (or was missing) and $Z_{dr} \geq 0.25$ dB, then the composite rain mass flux algorithm utilized $R(Z_h,Z_{dr})$ [Eqn. E.3] at the grid point. In the event that $Z_{dr} < 0.25$ dB or was missing and $K_{dp} \geq 0.4°$ km^{-1} at a grid point, the algorithm used the $R(K_{dp})$ estimator [Eqn. E.2]. Finally, if none of the above constraints were met, the mass flux algorithm used $R(Z_h)$ [Eqn. E.1] at the point in question. After applying this selection algorithm to the four rain rate estimators at each point over the entire grid, the selected rain rates (mm h^{-1}) were averaged and then converted from a depth of water over the grid area per unit time to a mass flux (kg s^{-1}) by assuming a density of 1000 kg m^{-3} for water. For a given radar volume, Eqn. E.4 typically accounted for 55% - 70% of the rain mass flux, Eqn. E.3 for 20% - 30%, Eqn. E.2 for 4% - 10%, and Eqn. E.1 for 2% - 5%.

REFERENCES

Atlas, D., and H. C. Banks, 1951: The interpretation of microwave reflections from rainfall. *J. Meteor.*, **8**, 271 - 282.

Aydin, K., Y. Zhao, and T. A. Seliga, 1989: Rain-induced attenuation effects on C-band dual-polarization meteorological radars. *IEEE Trans. Geosci. Remote Sens.*, **27**, 57 - 66.

——, and V. Giridhar, 1992: C-band dual-polarization radar observables in rain. *J. Atmos. Oceanic Technol.*, **9**, 383 - 390.

Balakrishnan, N., and D. S. Zrnic', 1989: Correction of propagation effects at attenuating wavelengths in polarimetric radars. *Preprints, 24th Conf. on Radar Meteorology*, March 27-31, 1989, Tallahassee, Florida, 287 - 291.

——, and ——, 1990: Estimation of rain and hail rates in mixed-phase precipitation. *J. Atmos. Sci.*, **47**, 565 - 583.

Barber, P., and C. Yeh, 1975: Scattering of electromagnetic waves by arbitrarily shaped dielectric bodies. *Appl. Opt.*, **14**, 2864 - 2872.

Beard, K. V., D. B. Johnson, and D. Baumgardner, 1986: Aircraft observations of large raindrops in warm, shallow, convective clouds. *Geophys. Res. Lett.*, **13**, 991 - 994.

Bolen, S., V. N. Bringi, and V. Chandrasekar, 1998: An optimal area approach to intercomparing polarimetric radar rain-rate algorithms with gauge data. *J. Atmos. Oceanic Technol.*, **15**, 605 - 623.

Bringi, V. N., V. Chandrasekar, N. Balakrishnan, and D. S. Zrnic', 1990: An examination of propagation effects in rainfall on radar measurements at microwave frequencies. *J. Atmos. Oceanic Technol.*, **7**, 829 - 840.

——, and A. Hendry, 1990: Technology of polarization diversity radars for meteorology, in *Radar in Meteorology: Battan Memorial and 40th Anniversary Radar Meteorology Conference*, edited by D. Atlas, Amer. Meteor. Soc., Boston, Mass., 153-190.

——, V. Chandrasekar, P. Meischner, J. Hubbert, and Y. Golestani, 1991: Polarimetric radar signatures of precipitation at S- and C-bands. *IEE Proceedings-F*, **138**, 109 - 119.

Carbone, R. E., T. D. Keenan, J. Hacker, and J. W. Wilson, 1999: Tropical island convection in the absence of significant topography, Part I. Sea breezes and early convection. *Preprints, 23rd Conference on Hurricanes and Tropical Meteorology*. Dallas, Texas, 10 - 15 January, 1999.

Doviak, R. J., and D. S. Zrnic', 1993: *Doppler Radar and Weather Observations*, 2nd ed., 562pp., Academic, San Diego, Calif.

Gorgucci, E., G. Scarchilli, and V. Chandrasekar, 1996: Error structure of radar rainfall measurement at C-band frequencies with dual polarization algorithm for attenuation correction. *J. Geophys. Res.*, **101**, 26,461 - 26,472.

——, G. Scarchilli, V. Chandrasekar, P. F. Meischner, and M. Hagen, 1998: Intercomparison of techniques to correct for attenuation of C-band weather radar signals. *J. Appl. Meteor.*, **8**, 845 - 853.

Green, A. W., 1975: An approximation for the shape of large raindrops. *J. Appl. Meteor.*, **14**, 1578 - 1583.

Gunn, K. L. S., and T. W. R. East, 1954: The microwave properties of precipitation particles. *Quart. J. Roy. Meteor. Soc.*, **80**, 522 - 545.

Hildebrand, P. H., 1978: Iterative correction for attenuation of 5 cm radar in rain. *J. Appl. Meteor.*, 17, 508 - 514.

Hitschfeld, W., and J. Bordan, 1954: Errors inherent in the radar measurement of rainfall at attenuating wavelengths. *J. Meteor.*, **11**, 58 - 67.

Holt, A. R., 1988: Extraction of differential propagation phase from data from S-band circularly polarized radars. *Electron. Lett.*, **24**, 1241 - 1242.

Hubbert, J., V. Chandrasekar, V. N. Bringi, P. Meischner, 1993: Processing and interpretation of coherent dual-polarized radar measurements. *J. Atmos. Oceanic Technol.*, **10,** 155-164.

——, and V. N. Bringi, 1995: An iterative filtering technique for the analysis of copolar differential phase and dual-frequency radar measurements. *J. Atmos. Oceanic Technol.*, **12**, 643 - 648.

——, and ——, 1997: The effects of 3-body scattering on differential reflectivity. Preprints, *28th Conf. on Radar Meteorology*, September 7-12, 1997, Austin, Texas, 11 - 12.

Jameson, A. R., and E. A. Mueller, 1985: Estimation of differential phase shift from sequential orthogonal linear polarization radar measurements. *J. Atmos. Oceanic Technol.*, **2**, 133 - 137.

——, and D. B. Johnson, 1990: Cloud microphysics and radar. *Radar in Meteorology: Battan Memorial and 40th Anniversary Radar Meteorology Conference,* edited by D. Atlas, Amer. Meteor. Soc., Boston, Mass., 323-340.

——, 1991a: Polarization radar measurements in rain at 5 and 9 GHz. *J. Appl. Meteor.*, **30**, 1500 - 1513.

——, 1991b: A comparison of microwave techniques for measuring rainfall. *J. Appl. Meteor.*, **30**, 32 - 54.

——, 1992: The effect of temperature on attenuation-correction schemes in rain using polarization propagation differential phase shift. *J. Appl. Meteor.*, **31**, 1106 - 1118.

Johnson, B. C., and E. A. Brandes, 1987: Attenuation of a 5-cm wavelength radar signal in the Lahoma-Orienta storms. *J. Atmos. Oceanic Technol.*, **4**, 512 - 517.

Johnson, D. B., 1982: The role of giant and ultragiant aerosol particles in warm rain initiation. *J. Atmos. Sci.*, **39**, 448 - 460.

Joss, V. J., and A. Waldvogel, 1967: Ein spectograph fur Niederschlagstropher mit automatischer auswertung. *Pure and Appl. Geophys.*, **68**, 240 - 246.

Keenan, T. D, G. Holland, S. Rutledge, J. Simpson, J. McBride, J. Wilson, M. Moncrieff, R. Carbone, W. Frank, B. Sanderson, and J. Hallet, 1994a: Science Plan - Maritime Continent Thunderstorm Experiment, *BMRC Research Report*, **44**, 61 pp.

——, R. Carbone, S. Rutledge, J. Wilson, G. Holland, and P. May, 1996: The Maritime Continent Thunderstorm Experiment (MCTEX): Overview and initial results. *Preprints, Seventh Conference on Mesoscale Processes*, Amer. Meteor. Soc., Reading, UK, Sept. 9-13, 1996., 326-328.

——, L. D. Carey, D. S. Zrnic', P. T. May, and S. A. Rutledge, 1998a: A sensitivity analysis of C-band polarimetric variables in rain. *Meteorol. Atmos. Phys.*, submitted.

——, K. Glasson, F. Cummings, T. S. Bird, J. Keeler, and J. Lutz, 1998b: The BMRC/NCAR C-band polarimetric (C-POL) radar system. *J. Atmos. Oceanic Technol.*, **15**, 871-886.

May, P. T., T. D. Keenan, D. S. Zrnic, L. D. Carey, S. A. Rutledge, 1998: Polarimetric radar measurements of tropical rain at a 5 cm wavelength. *J. Appl. Meteor.*, in press.

Mohr, C. G., 1986: Merger of mesoscale data sets into a common Cartesian format for efficient and systematic analyses. *J. Atmos. Oceanic. Technol.*, **3**, 143-161.

Oguchi, T., 1983: Electromagnetic wave propagation and scattering in rain and other hydrometeors. *IEEE Proc.*, **71**, 1029 - 1078.

Oye, R., Carbone, R. E., 1981: Interactive Doppler editing software. Proc. *20th Conf. Radar Meteorology*, Boston, Amer. Meteor. Soc., 683 - 689.

Pointin, Y. C., C. Ramond, and J. Fournet-Fayard, 1988: Radar differential reflectivity Z_{dr}: A real case evaluation of errors induced by antenna characteristics. *J. Atmos. Oceanic Technol.*, **5**, 416 - 423.

Pruppacher, H. R., and K. V. Beard, 1970: A wind tunnel investigation of the internal circulation and shape of water drops falling at terminal velocity in air. *Quart. J. Roy. Meteor.* Soc., **96**, 247 - 256.

Rauber, R. M., K. V. Beard, and B. M. Andrews, 1991: A mechanism for giant raindrop formation in warm, shallow, convective clouds. *J. Atmos. Sci.*, **48**, 1791 - 1797.

Ray, P. S., 1972: Broad-band complex refractive indices of ice and water. *Appl. Opt.*, **11**, 1836 - 1844.

Ryde, J. W., 1946: The attenuation and radar echoes produced at centimetre wavelengths by various meteorological phenomena. In *Meteorological factors in radio wave propagation*. London, Physical Society, 169 - 189.

Ryzhkov, A. V., and D. S. Zrnic', 1994: Precipitation observed in Oklahoma mesoscale convective systems with a polarimetric radar. *J. Appl. Meteor.*, **33**, 455 - 464.

——, and ——, 1995a: Precipitation and attenuation measurements at a 10-cm wavelength. *J. Appl. Meteor.*, **34**, 2121 - 2134.

——, and ——, 1995b: Comparison of dual-polarization radar estimators of rain. *J. Atmos. and Oceanic Technol.*, **12**, 249 - 256.

——, and ——, 1996a: Rain in shallow and deep convection measured with a polarimetric radar. *J. Atmos. Sci.*, **53**, 2989 - 2995.

——, and ——, 1996b: Assessment of rainfall measurement that uses specific differential phase. *J. Appl. Meteor.*, **35**, 2080 - 2090.

——, ——, and D. Atlas, 1997: Polarimetrically tuned R(Z) relations and comparisons of radar rainfall methods. *J. Appl. Meteor.*, **36**, 340 - 349.

——, and ——, 1998a: Beamwidth effects on the differential phase measurements of rain. *J. Atmos. Oceanic Technol.*, **15**, 624 - 634.

——, and ——, 1998b: Polarimetric rainfall estimation in the presence of anomalous propagation. *J. Atmos. Oceanic Technol.*, in press.

Scarchilli, G., E. Gorgucci, V. Chandrasekar, and T. A. Seliga, 1993: Rainfall estimation using polarimetric techniques at C-band frequencies. *J. Appl. Meteor.*, **32**, 1150 - 1160.

Seliga, T. A., and V. N. Bringi, 1976: Potential use of radar differential reflectivity measurements at orthogonal polarizations for measuring precipitation. *J. Appl. Meteor.*, **15**, 69 - 76.

Shepherd, G. W., J. Searson, A. Pallot, and C. G. Collier, 1995: The performance of a C-band weather radar during a line convection event. *Meteorol. Appl.*, **2**, 65 - 69.

Smyth, T. J., and A. J. Illingworth, 1998: Correction for attenuation of radar reflectivity using polarisation data. *Quart. J. Roy. Meteor.*, in press.

Szumowski, M. J., R. M. Rauber, H. T. Ochs III, and K. V. Beard, 1998: The microphysical structure and evolution of Hawaiian rainband clouds. Part II: Aircraft measurements within rainbands containing high reflectivity cores. *J. Atmos. Sci.*, **55**, 208 - 226.

Takahashi, T., 1990: Near absence of lightning in torrential rainfall producing Micronesian thunderstorms. *Geophys. Res. Lett.*, **17**, 2381 - 2384.

Tan, J., J. W. F. Goddard, and M. Thurai, 1995: Applications of differential propagation phase in polarisation-diversity radars at S-band and C-band. *9th International Conference on Antenna and Propagation*, April 4-7, 1995, Eindhoven, the Netherlands, IEE Conference Publication No 407, 336 - 341.

Torlaschi, E., and A. R. Holt, 1993: Separation of Propagation and backscattering effects in rain for circular polarization diversity S-band radars. *J. Atmos. Oceanic. Technol.*, **10**, 465 - 477.

Ulbrich, C. W., 1983: Natural variations in the analytical form of the raindrop size distribution. *J. Clim. and Appl. Meteor.*, **22**, 1764 - 1775.

Vivekanandan, J., W. M. Adams, and V. N. Bringi, 1991: Rigorous approach to polarimetric radar modeling of hydrometeor orientation distributions. *J. Appl. Meteor.*, **30**, 1053 - 1063.

Wilson, J. W., T. D. Keenan, and R. E. Carbone, 1999: Tropical island convection in the absence of significant topography, Part II. Evolution of mesoscale convective systems. *Preprints, 23rd Conference on Hurricanes and Tropical Meteorology*. Dallas, Texas, 10 - 15 January, 1999.

Yuter, S. E., and R. A. Houze, Jr., 1995: Three dimensional kinematic and microphysical evolution of Florida cumulonimbus. Part II: Frequency distributions of vertical velocity, reflectivity, and differential reflectivity. *Mon. Wea. Rev.*, **123**, 1941 - 1963.

Zawadzki, I., 1975: On radar-rain gage comparison. *J. Appl. Meteor.*, **14**, 1430 - 1436.

——, 1984: Factors affecting the precision of radar measurements of rain. Preprints, *22nd Conf. on Radar Meteorology*, Zurich, Switzerland, Amer. Meteor. Soc., 251 - 256.

Zrnic', D. S., 1987: Three-body scattering produces precipitation signature of special diagnostic value. *Radio Sci.*, **22**, 76 - 86.

——, A. V. Ryzhkov, 1996: Advantages of rain measurements using specific differential phase. *J. Atmos. Oceanic Technol.*, **13**, 465 - 476.

——, and ——, 1997: Polarimetric measurements of rain. In *Weather radar technology for water resources management*. Eds, B. Braga and O. Massambani, UNESCO Press, Montevideo, 77 - 86.

PART III, C-BAND POLARIMETRIC RADAR STUDIES OF TROPICAL ISLAND CONVECTION: ON THE RELATIONSHIP BETWEEN PRECIPITATION AND LIGHTNING

CHAPTER 1
INTRODUCTION AND MOTIVATION

Controversy still exists as to whether tropical convection can become significantly electrified to produce lightning while warm rain processes dominate storm microphysics or whether mixed phase microphysics (involving ice in the presence of supercooled water) is required. Several laboratory studies (e.g., Takahashi, 1978a; Jayaratne et al., 1983; Saunders et al., 1991 among others) of the non-inductive charging (NIC) of graupel particles during rebounding collisions with ice crystals in the presence of supercooled cloud liquid water strongly support the latter argument. In the past, most conventional (not polarized) radar studies of tropical convection (Rutledge et al., 1992; Williams et al., 1992; Zipser and Lutz, 1994; Petersen et al., 1996, 1998) have determined that sufficiently large reflectivities (e.g., $\geq$ 30 dBZ to 40 dBZ) must exist at temperatures below some threshold (e.g., 0° C to -20° C) for a specified period of time (typically on the order of ten minutes) before strong electric fields and hence lightning can occur. These results are an extension of earlier radar and lightning research accomplished at midlatitudes which revealed a strong correlation between the areal distribution (the so-called "Larsen Area") of moderate reflectivity (e.g., $\geq$ 30 - 45 dBZ) at an arbitrary height in the mixed phase zone and lightning (e.g., Larsen and Stansbury, 1974; Stansbury et al., 1978; Marshall and Radhakant, 1978). One possible interpretation of these observations is that graupel particles are a prerequisite for lightning, consistent with the NIC mechanism.

However, the presence of large precipitation sized ice (i.e., D $\geq$ 1 mm) is largely inferred from the temporal evolution of reflectivity at a given environmental temperature and cannot be conclusively determined with conventional radar. Moreover, a few anecdotal observations of warm cloud lightning have been reported (e.g., Foster, 1950; Pietrowski, 1960; Lane-Smith, 1971) and, in one case, investigated in detail with cloud

photography and a 3-cm radar (Moore et al., 1960). More recently, dual-polarimetric radar observations which provide remotely sensed information on the size, shape, orientation, and thermodynamic phase of hydrometeors have been used to differentiate between millimeter sized raindrops and large precipitation sized ice particles (e.g., Jameson, 1985; Bringi and Hendry, 1990; Jameson and Johnson, 1990; Doviak and Zrnic′, 1993) and estimate the radar reflectivity associated with both rain and ice. (e.g., Golestani et al., 1989; Balakrishnan and Zrnic′, 1990; Appendix B).

The microphysical information inferred from polarimetric radar measurements have been correlated to electrical activity in sub-tropical and midlatitude convection. Goodman et al. (1988a) was the first to use reflectivity and differential reflectivity to infer the presence of graupel and hail aloft during a rapid increase in the total lightning flash of an isolated storm in the vicinity of Huntsville, Alabama. Recently, Jameson et al. (1996), Ramachandran et al. (1996), French et al. (1996), and Bringi et al. (1997) employed polarimetric radar data to demonstrate that the onset of significant electrification in small, isolated Florida storms during the Convection and Precipitation/Electrification (CaPE) experiment was coincident with the freezing of supercooled raindrops at -7° C to -10° C and the commencement of mixed phase ice processes. Several multiparameter radar studies of High Plains hailstorms (Carey and Rutledge, 1996; López and Aubagnac, 1997; Carey and Rutledge, 1998) have linked the evolution of cloud-to-ground (CG) and intracloud (IC) lightning flash rates to variations in graupel and hail production aloft.

The purpose of this study is to utilize polarimetric radar observations to further explore the hypothesis that *lightning production in tropical island convection is critically linked to ice processes in the mixed phase region* via the NIC mechanism. During the Maritime Continent Thunderstorm Experiment (MCTEX; Keenan et al., 1994a; 1996), complete life-cycle observations of thunderstorms over the Tiwi Islands (Bathurst and Melville Islands which are centered at about 11.6° S and 130.8° E ; cf. Fig. 1.1) were obtained with the Bureau of Meteorology Research Centre (BMRC) C-band (5.5 cm) dual-polarimetric radar (C-pol) from 13 November to 10 December 1995. The BMRC C-pol observations are the *first comprehensive multiparameter radar observations of tropical convection in general and tropical island convection in particular.*

Consequently, we now have the unique opportunity to remotely explore the precipitation microphysics and lightning behavior of these tropical island thunderstorms characteristic of the climatologically important Maritime Continent region (Ramage, 1968). The deep convection in this region is important in maintaining the Walker and Hadley circulations (e.g., Krishnamurti et al., 1973; Lau and Boyle, 1987). Variations in the convective activity over the Maritime Continent (Horel and Wallace, 1981) are related to the El-Nino-Southern Oscillation (ENSO) phenomena and can also influence the behavior of the sub-tropical jet on a daily basis (Lau et al., 1983). In addition, satellite observations of global lightning distribution (e.g., Orville and Spencer, 1979; Kotaki et al., 1981; Turman and Edgar, 1982; Orville and Henderson, 1986) demonstrate that convection over the Maritime Continent is crucial to the maintenance of the global electrical circuit. Earlier Doppler radar and lightning studies of convection in the vicinity of Darwin, Australia (Rutledge et al., 1992; Williams et al., 1992) confirmed the copious production of lightning in these storms and demonstrated the correlation between vertical reflectivity structure and lightning production in tropical convection.

We extend these results in the present study by correlating the polarimetric radar-inferred production of ice in the mixed phase region to the surface electric field as measured by a shuttered field mill, the total lightning flash rate as estimated from a flat plate antenna, and the cloud-to-ground lightning flash rate and location as measured by a network of Advanced Lightning Direction Finders (ALDFs). With these results, we hope to better understand cloud electrification and the correlation of lightning to the horizontal and vertical precipitation structure of tropical convection.

Part III is the second of a two part series on C-band polarimetric radar studies of tropical island convection. The companion paper (Part II) demonstrates and evaluates a propagation correction technique employing the differential propagation phase, with particular emphasis on new procedures for coping with the presence of large drops in tropical convection. This propagation correction algorithm is crucial to the successful realization of the scientific goals of this study.

In Chapter 2, an overview of radar and lightning data and analysis methods is given. More details regarding the determination of cloud electrical properties, the partitioning of

reflectivity into rain and ice components using polarimetric radar data, and the estimation of rain and ice mass are presented in Appendices A - C. Results from polarimetric radar and electrical observations of tropical island convection which occurred on 28 November 1995 during MCTEX are discussed throughout Chapter 3. First, we characterize the horizontal and vertical storm structure as observed by the C-pol radar (Sec. 3.1). Next, we detail the interrelationship between mixed phase ice microphysics, rainfall, storm electrification, and lightning throughout the six hour evolution of island-wide convection on this day using the ALDF network (Sec. 3.2), the flat plate antenna (Sec. 3.3), and the field mill (Sec. 3.4). In Sec. 3.5, we explore the role of the cumulus merger process (e.g., Simpson et al., 1980; 1993) on the relationship between precipitation and lightning. We then investigate lightning frequency and location as a function of convective versus stratiform rainfall and areal fractions (e.g., Steiner et al., 1995; Rickenbach and Rutledge, 1998) in Sec. 3.6. Throughout Chapter 3, we discuss the implications of these tropical observations on cloud electrification mechanisms and on the potential utility of lightning data for remotely inferring certain microphysical and kinematic properties of tropical convection. Lastly, we summarize the above results in Chapter 4.

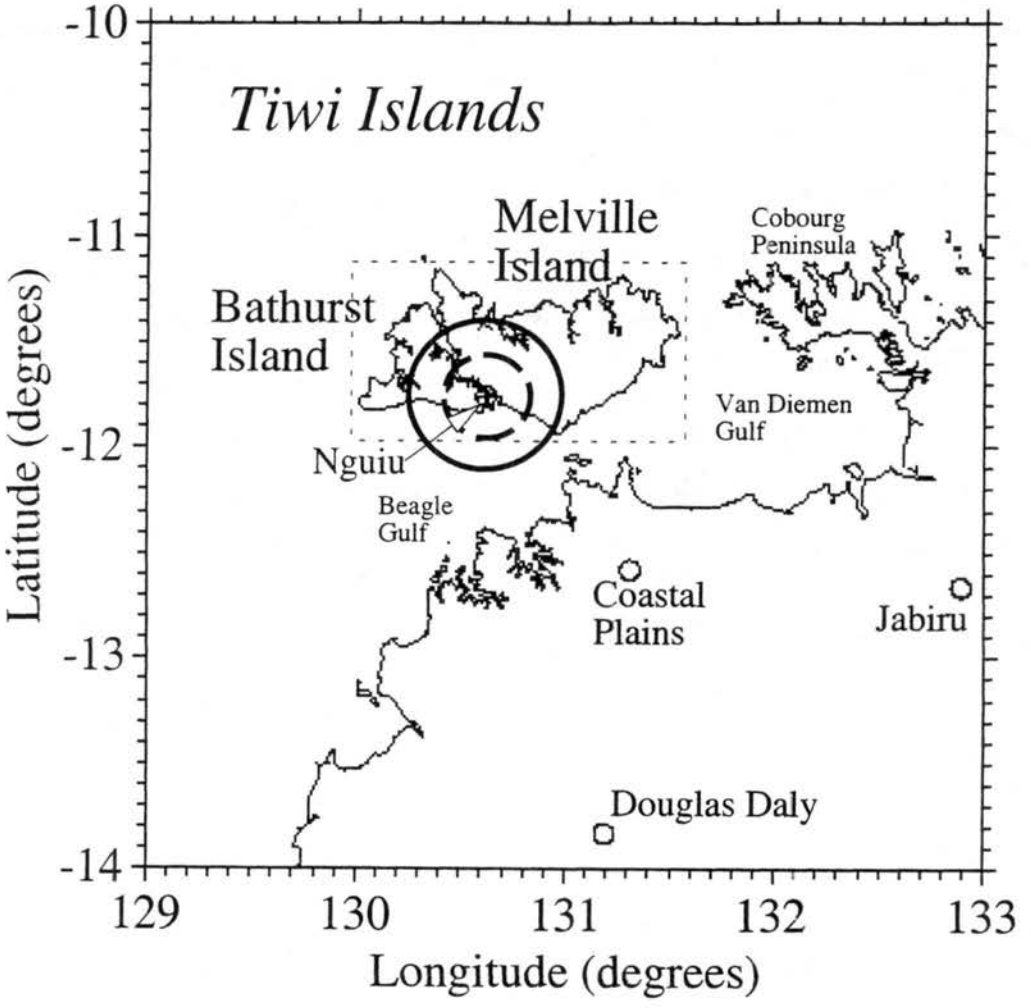

Figure 1.1. A depiction of the radar and electricity/lightning instrumentation network over the Tiwi Islands utilized in this study during the Maritime Continent Thunderstorm Experiment (MCTEX). The BMRC C-pol (5.5 cm, polarized) radar was located near Nguiu on the southeastern tip of Bathurst Island as indicated by the "+" symbol. A flat plate antenna and shuttered field mill were collocated with the radar. The maximum operating range of the flat plate antenna (field mill) was approximately 40 km (20 km) as indicated by the solid (dashed) range ring around the C-pol radar. The ALDF (Advanced Lightning Direction Finder) network was comprised of 4 sensors deployed across the Northern Territories of Australia. One ALDF sensor was collocated with the C-Pol radar at Nguiu. The other three sensor sites were located on the mainland at Coastal Plains, Jabiru, and Douglas Daly.

CHAPTER 2
DATA AND ANALYSIS METHOD

The MCTEX instrumentation network for electrification and lightning studies is depicted in Fig. 1.1. At the center of the network was the BMRC C-band polarimetric radar (C-pol, 5.5 cm; Keenan et al., 1998a) located in the vicinity of Nguiu on Bathurst Island (11.8° S, 130.6° E). Collocated at the radar was a flat plate antenna (e.g., Uman, 1987) for measuring the total lightning flash rate (total = IC + CG) within about 35 to 40 km, a shuttered field mill (Malan and Schonland, 1950) for estimating the surface electric field and total lightning flash rate within about 20 to 25 km, and an Advanced Lightning Direction Finder (ALDF; e.g., Krider et al., 1976) for measuring the azimuth, signal power, polarity, and arrival time of lightning radio sources associated with cloud-to-ground return strokes within 600 km. Three other ALDF stations were positioned in a triangular configuration over the Northern Territory of Australia (at Coastal Plains, Douglas Daly, and Jabiru), completing the ALDF network (cf., Fig. 1.1). Details regarding the determination of cloud electrical properties (e.g., surface E-field, total lightning flash rate, CG lightning flash rate, and ground stroke location) from the above three instruments are presented in Appendix A.

During MCTEX, the C-pol radar collected full volumetric scans of island convection in polarimetric mode every 4 to 15 minutes. Recorded polarimetric variables utilized in this study include horizontal reflectivity (Z_h), differential reflectivity (Z_{dr}), and the total differential phase (Ψ_{dp}). The data were carefully edited and quality controlled to remove any spurious data. Using a 13-sample (3.9 km) running mean, iterative filtering technique (Balakrishnan and Zrnic', 1990; Hubbert and Bringi, 1995), the differential propagation phase (ϕ_{dp}) and the specific differential phase (K_{dp}) were estimated from the total differential phase data. The horizontal reflectivity and the differential reflectivity were

then corrected for propagation effects in rain using ϕ_{dp} (Bringi et al., 1990; Ryzhkov and Zrnic′, 1995). For more details regarding polarimetric radar data editing, processing, and the correction of propagation effects at C-band in tropical convection, the reader is referred to Part II of this study. In addition, the difference reflectivity (Z_{dp}) was calculated from attenuation corrected Z_h and differential attenuation corrected Z_{dr} according to the definition of Golestani et al. (1989). The reader is referred to several review papers and texts for formal definitions of these polarimetric variables and their applications (e.g., Bringi and Hendry, 1990; Jameson and Johnson, 1990; Doviak and Zrnic′, 1993). Finally, all of the processed and corrected polarimetric variables were interpolated to a Cartesian grid with 1 km horizontal and 0.5 km vertical resolution, using the National Center for Atmospheric Research (NCAR) REORDER software package (Mohr, 1986). The horizontal extent of these Cartesian grids covered the entire Tiwi Islands as depicted by the dashed box in Fig. 1.1.

In this study, we compare the lightning and surface electric field data to both polarimetric radar observables and radar derived precipitation characteristics such as the rain mass flux, the mixed phase precipitation ice mass, and the precipitation liquid water content. As discussed in Part II (Appendix E), the rain mass flux (kg s^{-1}) over the Tiwi Islands was calculated from a hybrid polarimetric radar algorithm utilizing propagation corrected Z_h and Z_{dr}, and K_{dp}. As described in Appendix B, a technique for partitioning the measured horizontal reflectivity into Z_h(rain) and Z_h(ice) components using the Z_{dp} method (Golestani et al., 1989) at C-band in tropical convection was developed and evaluated using both C-pol and simulated radar data. As discussed in Appendix C, estimates of rain mass (M_w) and precipitation-sized ice mass (M_i) were then obtained by applying separate Z-M relationships to the partitioned reflectivities.

Another goal of this study was to investigate the role of the cumulus merger process on the production of rainfall, mixed phase graupel mass, and cloud-to-ground lightning in the tropical convective system over the Tiwi Islands (colloquially called Hector), since it has implications for the manner in which tropical island convective systems are parameterized in large scale numerical models (e.g., Simpson et al., 1980; Simpson et al., 1993). For the purposes of comparison with Simpson et al. (1993), we define a merger as

a consolidation of two previously separate echo features at the 25 dBZ reflectivity isopleth (i.e., roughly corresponding to a rain rate of 1 mm h^{-1}). A reflectivity echo feature is defined as a group of horizontally contiguous grid points which exceed the 25 dBZ threshold at the 2 km grid level and which are isolated from other such groups by grid points characterized by reflectivity which does not exceed the threshold. The algorithm of Rickenbach and Rutledge (1998) was utilized to locate 25-dBZ echo features. Mergers between convective features were then identified by manual analysis. The rain mass flux of each feature was determined using the polarimetric rain rate equations in Appendix E of Part II. The number of cloud-to-ground lightning flashes associated with each feature was determined manually using a loop of ground strikes overlaid on the echo features. The mixed phase (5 to 11 km or 0° C to -40° C) graupel mass, calculated using Eqns. C.1 - C.4, was integrated in the vertical at each x-y location in the grid. The Rickenbach and Rutledge (1998) feature identification technique was then applied to the integrated mixed phase graupel mass. The features of mixed phase graupel mass were then manually associated with the 25-dBZ reflectivity features at 2 km. In this manner, we were able to determine the echo area, rainfall, mixed phase graupel mass, and cloud-to-ground lightning associated with every "single echo" and "merged echo" of the 28 November 1995 Hector.

The relative amount of convective versus stratiform precipitation in a tropical convective system provides insight into the dominant microphysical processes responsible for precipitation production and the resultant vertical distribution of latent heating (Houze, 1989). Therefore, an additional objective of this research was to determine the relationship between CG lightning frequency and location and the convective/stratiform rain fraction for the entire lifecyle of the 28 November 1995 Hector. We adapted the radar techniques of Steiner et al. (1995) and Rickenbach and Rutledge (1998) to distinguish convective from stratiform precipitation. In these methods, the magnitude and spatial gradient of radar reflectivity are utilized to isolate regions of more intense, horizontally variable precipitation indicative of convective rain from regions of weaker, widespread precipitation associated with stratiform rain. We refer the interested reader to Rickenbach and Rutledge (1998) for specific details regarding the procedure utilized herein.

CHAPTER 3
RESULTS AND DISCUSSION

3.1. Overview of storm precipitation structure

The Hector on 28 November 1995 was extremely intense from both a radar and lightning perspective. Echo tops (0 dBZ) reached to over 20 km while the 30 dBZ isosurfaces penetrated over 18 km. Maximum rainfall rates estimated by the C-pol radar exceeded 150 mm h^{-1} and observed reflectivities in the most intense cells surpassed 60 dBZ. At peak intensity, the convection spanned across the entire extent of both islands with over 100 km of contiguous radar echo with reflectivities in excess of 30 dBZ along an east-west oriented line (at 2 km; Figs. 3.1c-d). Averaged over one minute periods, the cloud-to-ground and total lightning flash rates peaked at 11 min^{-1} and 60 min^{-1} respectively. Since this Hector is comparable to some of the most intense island thunderstorms observed in the region prior to MCTEX (Keenan et al., 1990; 1994b; Rutledge et al., 1992; Williams et al., 1992), it is considered to be an ideal case for studying the co-evolving precipitation and lightning characteristics of deep island convection.

Precipitating convection lasted for seven hours (0130 - 0830 UTC or 1100 - 1800 local; all times hereafter will be referenced in UTC) over the Tiwi Islands on 28 November 1995. By 0215, initial cumulonimbi were focused along two sea-breeze fronts (Keenan et al., 1994b; Carbone et al., 1999) occurring along the northern and southern coasts of both islands (Fig. 3.1a). Although there was no observed CG lightning over the islands, no lightning (IC or CG) detected by the flat plate antenna within 40 km of the radar, and no significant surface electric fields near the radar at this time, peak reflectivities and rain rates reached up to 55 dBZ and 70 mm h^{-1} respectively. As shown in Fig. 3.2a, most convection was single-celled with typical diameters on the order of 5 - 10 km and echo tops less than 8 km in height. The vertical extent of the 35 dBZ reflectivity and 1 dB

differential reflectivity contours were limited to below the environmental freezing level at 5 km, suggesting that collision-coalescence dominated precipitation processes in most cells across the island. The most organized convection existed in extreme eastern Melville Island (-11.4°, 131.3°) where several cells had merged into a small convective complex on the order of 30 km wide. This merger was the result of the collision of a gust front with existing cumulus convection along the sea-breeze front. This merger process is quite common over the Tiwi Islands (e.g., Keenan et al., 1994b; Wilson et al., 1999).

By 0315 (Fig. 3.1b), several cell mergers had occurred along both sea-breeze fronts. Two of these complexes (-11.8°, 130.8°; -11.45°, 131.1°) were producing cloud-to-ground lightning at this time. The flat plate antenna measured total lightning flash rates of 1 - 2 min^{-1}, probably associated with the CG lightning producing complex to the east-northeast of the radar over southern Melville Island. The largest of the two CG lightning producing mergers, over northeastern Melville Island, had originated the first detected ground flash earlier at 0300. The vertical structure of this complex (Fig. 3.2b) is in stark contrast to that of the earlier single cell which produced no CG lightning (Fig. 3.2a). Echo tops (0 dBZ) in the CG yielding complex exceeded 16 km. The 0.75 dB differential reflectivity contour and the 35 dBZ isopleth extended to 7 km and 8 km respectively. This implies that supercooled raindrops existed in the 0° C to -10° C region and that large precipitation sized ice, most likely in the form of frozen drops and/or graupel, resided above the height of the -10° C isotherm.

As a result of several cell mergers (Simpson et al., 1980; 1993) between 0315 and 0415, widespread deep convection stretched along an east-west line over both islands with the bulk of the activity over Melville Island (Fig. 3.1c). Associated with this explosive development of intense convection, the total lightning flash rate within 40 km of the radar increased from just a few to more than 30 flashes min^{-1}. In addition, the field mill detected the first significant electric field and multiple transients characteristic of lightning during this period. Cloud-to-ground lightning activity increased rapidly over Melville Island and attained a relative maximum of 5 flashes min^{-1} by 0415. Interestingly, despite the widespread nature of significant convection ($Z_h \geq 30$ dBZ) at 2 km, the overwhelming majority of ground discharges were confined to a relatively small region over western

Melville Island near the northern coast (-11.55°. 130.8°). For instance, note the complete absence of CG lightning over Bathurst Island up to and including 0415 (Figs. 3.1a-c).

In order to highlight the microphysical differences between convection which yields CG lightning and convection which does not, we present vertical cross-sections of Z_h, Z_{dr}, and K_{dp} through radar echo over Melville (Fig. 3.3a) and Bathurst (Fig. 3.3b) Islands. First, the storms over Melville Island (18.5 km echo tops) were significantly taller than those above Bathurst Island (13 km tops) at this time. The 35 dBZ echo height extended through the entire depth of the mixed phase region over Melville Island (roughly up to 11 km where T = -40° C) while it did not penetrate the height of the -10° C isotherm over Bathurst Island (only up to 6.5 km). Significant values of differential reflectivity ($\geq$ 1 dBZ) and specific differential phase ($\geq 1°\ km^{-1}$) suggest that supercooled raindrops were being lofted above the -10° C level in both cells (e.g., Caylor and Illingworth, 1987; Illingworth et al., 1987; Tuttle et al., 1989; Goodman et al., 1988a; Meischner et al., 1991; Herzegh and Jameson, 1992; Conway and Zrnic′, 1993; Brandes et al., 1995; Yuter and Houze, 1995; Jameson et al., 1996; French et al., 1996; Ramachandran et al., 1996; Bringi et al., 1996; 1997; Blyth et al., 1997; Hubbert et al., 1998). However, in the convection over Melville Island, there was a large volume of echo characterized by significant reflectivities ($\geq$ 35 dBZ) and near zero values of Z_{dr} and K_{dp} at temperatures colder than -5° C (i.e., heights $\geq$ 5.9 km), which is indicative of the presence of large precipitation sized ice. In contrast, most of the radar echo possessing significant reflectivities over Bathurst Island were also characterized by significant positive values of Z_{dr} and K_{dp}. This indicates that a large fraction of the precipitation mass above the freezing level over Bathurst Island was in liquid form. This is an example where the penetration of some reflectivity threshold (30 - 35 dBZ) above some temperature threshold (-7°to -10° C) does not guarantee the dominance of graupel or frozen drop mass over rain mass.

To explore further the vertical precipitation structure of Hector at 0416, we utilized the methods outlined in the Appendix C to estimate rain (M_w) and graupel mass[1] (M_g)

---

[1]In this context, graupel mass is defined as the ice mass determined by the Z_{dp} method which is characterized by $Z_h \geq 35$ dBZ. The actual ice hydrometeor types could be graupel, frozen drops, and/or large aggregates.

using Z_h and Z_{dp} in these two convective cells characterized by markedly different microphysics and CG lightning properties. Vertical cross-sections of M_w, M_g, and Z_h (Figs. 3.4a,b) are presented in the same planes as Figs. 3.3a,b respectively. The CG producing convective complex (Fig. 3.4a) had significant graupel mass throughout the entire mixed phase region (5 km to 11 km or 0° C to -40° C) with a maximum in the 0° C to -15° C temperature zone. Note that the majority of the ground discharges occurring around 0416 were located beneath and just to the southeast of this peak in the ice mass aloft (cf. Figs. 3.1c and 3.4a). Contours of M_w indicate that supercooled raindrops were lofted to the height of -10° C where they likely froze and thus provided an immediate source of large precipitation ice for riming and charge separation via the NIC mechanism. The location of a maxima in the rain mass (4 km) located just below the peak graupel mass (6.5 km) strongly suggests that the freezing of supercooled raindrops is an important source of precipitation sized ice in tropical convection.

As shown in Fig. 3.4b, the convection over Bathurst Island which had not yielded a single CG lightning flash up to 0416, possessed a very different vertical structure of precipitation mass above 3.5 km ($T < 8°$ C). From the surface to 3.5 km, both cells (Figs. 3.4a,b) had similar values of reflectivity and rain mass. In the Bathurst Island convection (Fig. 3.4b) the rain mass steadily decreased above 3.5 km and the peak in the graupel mass was an order of magnitude less than in the Melville island complex. Indeed, very little graupel mass existed above the height of -10° C. Figs. 3.3b and 3.4b suggest that the Bathurst Island convection possessed sufficient updraft strengths to loft some supercooled drops to temperatures as low as -10° C. However, the lack of significant graupel mass at and above the -10° C level suggests that the updraft was insufficient to levitate precipitation (Atlas, 1966; Lhermitte and Williams, 1985), causing both large supercooled and frozen drops to fall back below the 5 km level. The lack of strong updrafts at and above the height of 0° C has been hypothesized to explain the dearth of lightning in tropical oceanic convection (Zipser and Lutz, 1994; Petersen et al., 1998). In contrast, the Melville Island convection probably had strong enough updrafts (> 6 m s^{-1}; Zipser and

Lutz, 1994) in the 0° to -20° C to loft raindrops, balance frozen drops, and thus provide a source of large ice and supercooled cloud water for the NIC mechanism to be operative.

From 0415 to 0515, Hector moved westward with the most vigorous convection and ground discharge activity now located over Bathurst Island (Fig. 3.1d). The tropical convective complex reached its peak intensity between 0500 and 0515 with maxima in rainfall, ice mass aloft, CG and the total lightning flash rates, and the surface electric field. The merged complex continued to move westward from 0515 to 0615. A short (60 km) leading convective line resided off of the coast of Bathurst Island followed by a narrow (30 km) trailing stratiform region (Fig. 3.1e). Cloud-to-ground lightning activity decreased rapidly during this period as the convective intensity decreased. By 0715, Hector began to take on a stratiform appearance in the horizontal (Fig. 3.1f) and vertical (Fig. 3.5) reflectivity structure (e.g., Steiner et al., 1995), ceased producing cloud-to-ground lightning, and generated less than 0.6 intracloud lightning flashes per minute. The intermittent bright band (Austin and Bemis, 1950) structure in the reflectivity data at and below the melting layer and the peak in the differential reflectivity at and below the bright band (Zrnic´ et al., 1993) support the contention that Hector had taken on stratiform characteristics by 0715 (Fig. 3.5). The storm continued to weaken and move westward for the next two hours. No further electrical activity was detected after 0740.

Using this overview of Hector's horizontal and vertical structure as background, we can now explore the relationship between tropical island precipitation and lightning in detail in the following subsections.

3.2. Relationship between cloud-to-ground lightning and precipitation

As discussed in Sec. 3.1, the first few cloud-to-ground lightning flashes emanated from a convective complex over northeastern Melville Island from 0300 to 0315 (Figs. 3.1b, 3.2b). The microphysical evolution of this complex is revealed in two time-height cross-sections[2] of raw (Fig. 3.6a) and derived (Fig. 3.6b) C-pol radar data.

---

[2]The analysis region for the time-height cross-sections were based on subjectively determined three dimensional boxes encompassing the complex in question. The values of Z_h, Z_{dr}, K_{dp}, M_w, and M_i in Figs. 3.6a,b are averages of values in grid points which possess reflectivities within 3 dBZ of the maximum Z_h.

In Fig. 3.6a, the evolution of Z_h, Z_{dr}, and K_{dp} is depicted from the start of available polarimetric radar data (0215) to the end of the first flurry of CG lightning flashes from Hector (0315) associated with cell merger. First, it is interesting to note that the 30 (35) dBZ reflectivity contour remained at or above the height of the -10° C (-20° C) level during the entire period, regardless of whether the storm was producing CG lightning, in contrast to the behavior of oceanic convection over the western Pacific warm pool (Petersen et al., 1996; 1998). There were two pulses in convective activity. No CG lightning was produced by the first pulse. The second pulse yielded the first 6 ground discharges beneath Hector.

The first convective pulse occurred from 0220 to 0240. Echo tops and the 40 dBZ echo height increased by 2.5 km and 4.5 km respectively during this time period. The 0.5 dB (0.5° km^{-1}) contour for Z_{dr} (K_{dp}) extended to the height of -20° C during the first pulse, suggesting the presence of supercooled raindrops well above the freezing level. The second pulse was sustained for a longer period (0240 - 0315) and was more intense. For example, the second convective surge was characterized by larger values of reflectivity, differential reflectivity, and specific differential phase. Echo tops and the 40 dBZ echo height in the second pulse were higher, reaching up to 16.5 km and 8.5 km respectively. In the second pulse, significant positive values of Z_{dr} and K_{dp}, indicative of raindrops, again extended to 8.5 km (-20° C).

The time-height evolution of the radar inferred rain (M_w) and total ice (M_i) mass for the same time period and convective complex is presented in Fig. 3.6b. Clearly, there was more ice mass above and rain mass below the freezing level in the second, CG producing pulse than in the first surge. The ice mass in the first convective pulse was typically between 0 and 1.5 g kg^{-1} in the 0° C to -20° C region compared to a range of 1.5 to 4 g kg^{-1} for the second surge. Inspection of the first pulse reveals that most of the precipitation mass in the 0° C to -15° C region was actually supercooled water, suggesting that many of the supercooled drops fell back below the 0° C level without freezing. The temporal evolution of Z_h, Z_{dr}, K_{dp}, and M_w contours from 0230 to 0245 implies that much of the supercooled rain mass peak between 0° C and -10° C at the beginning of the pulse rained out near the surface by 0245 without contributing significantly to the ice mass aloft.

Toward the end of the pulse at 0240, a relatively small amount of precipitation ice (M_i < 1.5 g kg^{-1}) was produced via drop freezing. The lack of significant ice mass in the -10° C to -20° C region where the negative charge region typically resides (e.g., Williams, 1989) is consistent with the lack of CG lightning in the complex at this time, if the NIC theory is the primary thunderstorm charging mechanism. More than likely, the updraft was not strong enough to balance the bulk of the rain mass above the height of the -10° C level (Zipser and Lutz, 1994; Petersen et al., 1996; 1998) and/or not of sufficient duration to allow freezing, riming, significant charge separation, and lightning (Solomon and Baker, 1994; Petersen, 1997).

The second convective pulse immediately followed the freezing of the first, weaker pulse of supercooled drops above the 0° C level at 0240. It is possible that the release of latent heat during drop freezing provided enhanced buoyancy to this second, more vigorous updraft. Raindrops were once again lofted into the 0° C to -20° C region. This time, however, the lofted rainmass was significantly larger and the drops immediately began to freeze and produce significant ice mass aloft (Figs. 3.6a,b). The freezing was much more rapid during the second pulse, perhaps as the result of ample residual cloud ice from prior convection initiating contact freezing (Cooper, 1974). Yuter and Houze (1995) also concluded that increased concentrations of ice particles penetrated by new updrafts during the mature phase of a Florida storm observed during CaPE aided in the more rapid freezing of supercooled drops. During this pulse, the updraft was apparently vigorous enough and of sufficient duration to loft supercooled drops above -10° C, balance millimeter-sized precipitation ice there, and allow the riming and electrification of ice via the NIC mechanism.

The first cloud-to-ground lightning flash occurred at 0300, within 5 - 10 minutes of the production of significant ice mass in the -10° C to -20° C region (0250-0255). The occurrence of lightning about ten minutes after the production of significant mixed phase ice mass is consistent with prior studies of mid-latitude and sub-tropical convection (e.g., Workman and Reynolds, 1949; Dye et al., 1986; Goodman et al., 1988a; Williams et al., 1989; Carey and Rutledge, 1996; Jameson et al., 1996; Bringi et al., 1997) and tropical oceanic convection (e.g., Petersen et al., 1996). As seen in Figs. 3.6a-b, the complex

continued to loft supercooled water into the 0° C to -20° C region after the first ground discharge. As a result, the production of ice mass, assumedly via drop freezing, continued to increase and then remained steady after 0305. The complex produced five additional cloud-to-ground lightning flashes before merging with another cell after 0315.

Although empirical and not conclusively causal, the evidence correlating the drop freezing process, large precipitation sized ice production, and subsequent cloud electrification and lightning is fairly strong in this tropical island thunderstorm. In-situ videosonde observations (T. Takahashi, personal communication, 1996) taken in Hector during MCTEX confirm the common presence of supercooled raindrops and frozen drops in the mixed phase region, even at temperatures as cold as -20° to -25° C. These in-situ observations corroborate the importance of drop freezing in Hector's precipitation processes. The importance of drop freezing to the glaciating behavior of warm based clouds has long been known (e.g., Koenig, 1963). The 1-D bulk microphysical cloud modeling studies of Hector by Keenan et al. (1994) and Petersen (1997) reveal the dominance of drop freezing over depositional and aggregational growth in the creation of large ice particles which can continue to grow via riming. In addition, the integrated cloud microphysical and electrical modeling results of Petersen (1997) suggest a critical role for frozen drops in the production of significant electric fields necessary for lightning. The role of drop freezing in subsequent cloud electrification and lightning production also has been demonstrated in the recent radar and/or aircraft studies of Jameson et al. (1996), French et al. (1996), Ramachandran et al. (1996), and Bringi et al. (1997) for sub-tropical convection and by Petersen et al. (1998) for tropical oceanic convection.

With an understanding of how the production of mixed-phase ice mass is correlated to the production of ground discharges beneath a single convective complex, we now present the temporal evolution of the CG lightning flash rate, mixed phase graupel mass, and the rain mass flux over the entire Tiwi Islands for a six hour period (0200 - 0800) during the complete life-cycle of this case (Fig. 3.7). The Hector rain mass flux broadly envelopes the period of significant ice mass and CG production. A non-negligible amount of rain occurred prior to the first CG lightning flash at 0300. As discussed further below, this pre-CG lightning rainfall is associated with primarily warm rain cumulonimbi (see Figs.

3.2a, and 3.8). It is also interesting to note that the overall maximum and gradual decrease in the rain mass flux after 0515 lags the CG lightning flash rate and mixed phase graupel mass by about 20 minutes. This temporal lag is probably associated with the gravitational settling time of the precipitation mass from the assumed position of the negative charge zone during CG lightning (about -10° C; Williams, 1989) to the surface, as will be further demonstrated below.

The general trend of the CG lightning flash rate is well correlated with that of the graupel mass. For example, both parameters undulate in unison in Fig. 3.7; their maxima and minima consistently aligned. Maxima in the mixed phase graupel mass typically preceded or were coincident in time with peaks in the cloud-to-ground lightning flash rate (at the available temporal resolution of 4 - 15 minutes). For example, note the relative maximum in the graupel mass aloft at 0359 which preceded the peak in the ground discharge rate at 0416 associated with the convective complex highlighted in Figs. 3.1c, 3.3a, and 3.4a. Other maxima in the CG lightning flash rate that were preceded by peaks in the graupel mass aloft by 10 to 30 minutes occurred at 0315, 0339, 0522, and 0614. The one-lag correlation coefficient[3] between the graupel mass aloft and the CG lightning flash rate is very high ($\rho = 0.9$). The overall maxima in the CG lightning flash rate of 5.5 min^{-1} which occurred at 0449 was nearly coincident with a relative maxima in the graupel mass. The temporal resolution of the polarimetric radar data surrounding this peak was degraded to about 10 - 15 minutes so it is ambiguous as to whether this marks an actual break from the more typical trend or whether the C-pol radar did not resolve the actual time of the maxima in the graupel mass. * other explanations?

The time-height cross-section of the graupel and rain mass in Fig. 3.8 further elucidate the relationship between lofted drops, large precipitation ice mass, and the CG lightning flash rate. The evolution of the vertical distribution of precipitation mass in Fig. 3.8 clearly demonstrates that Hector was dominated by warm rain microphysical processes prior to 0245 (also see Fig. 3.2a). The absence of CG lightning before 0300 despite

---

[3]The CG lightning flash rate at time = *T* was correlated to the lagged graupel mass at time = (T - τ) where τ = 7 minutes in the mean.

substantial quantities of warm rain is consistent with the requirement for large precipitation sized ice in the charge separation process leading to significant electric fields and lightning (e.g., Takahashi, 1978b; Dye et al., 1986; 1989; Williams, 1989; Willis et al., 1994 among many others). Despite some earlier reports of lightning in warm clouds (e.g., Foster, 1950; Pietrowski, 1960; Moore et al., 1960; Lane-Smith, 1971), the absence of warm rain CG lightning is consistent with many recent radar and in-situ studies of this phenomenon (e.g., Takahashi, 1978b; Chauzy et al., 1985; Selvam et al., 1991; Mikhailovsky et al., 1991; Rutledge et al., 1992; Petersen et al., 1996).

After 0245, the convection became sufficiently vigorous to loft drops, providing a source of precipitation sized ice via drop freezing. As discussed earlier relative to Figs. 3.1b, 3.2b, and 3.6a,c, the first CG flashes occurred at 0300 following the development of significant ice mass in the mixed phase region. As Hector continued to develop and increase in horizontal size and vertical extent (cf. Figs. 3.1a-f; 3.2a,b; 3.3a) via the merger process (Simpson et al., 1993), associated peaks in the graupel mass (Fig. 3.8) between the heights of 0° C and -20° C were associated with rapid increases and maxima in the cloud-to-ground flash rate (e.g., 0315 - 0330, 0345 - 0415, and 0433 - 0500). The effect of the merger process on the production of large ice and CG lightning will be explored further in Sec. 3.5. Note that Hector continued to loft supercooled drops up to the height of the -10° C to -20° C temperature range during the entire CG producing period. The continual presence of supercooled raindrops above the freezing level was likely the result of the continuous development of distinct updrafts within new deep cumulonimbi, resulting from the collision of the westward propagating gust front and existing cumulus convection along the sea-breeze (Keenan et al., 1994b; Wilson et al., 1999).

Each of these new cells in the multi-cell Hector thus provided a new source of lofted drops. The first cells in Hector which penetrated into quiescent air containing no ice particles lofted drops to -20° C and colder as inferred from Z_{dr} and K_{dp} (e.g., Figs. 3.6a, 3.6b, 3.8). Although the supercooled raindrops froze more rapidly when the updrafts carrying them penetrated into existing cloud likely containing ice crystals, there was always at least one new updraft in Hector carrying supercooled drops to -10° C or colder (e.g., Fig. 3.8). This is in contrast to the Florida storm studied by Yuter and Houze

(1995) in which Z_{dr} data indicated that the precipitation at upper levels was nearly glaciated early in the lifecycle of the multicellular convective complex. The difference between the two multicell storms is unclear. We can speculate that more of Hector's nascent updrafts penetrated into cloud-free air because they triggered along the intersection of a horizontally extensive sea-breeze front and a gust front that tended to advect ahead of existing convection (Wilson et al., 1999). Or, the low to mid-level updrafts lofting the supercooled raindrops in Hector may have been more intense than in the Florida storms.

These lofted drops likely froze and quickly rimed, providing a rapid and plentiful source of graupel particles for charge separation via the NIC mechanism. The initial descent of the graupel mass usually triggered pulses in the CG lightning flash rate. This correlation between descending precipitation ice and CG lightning for tropical island convection is similar to prior results for thunderstorms throughout the globe (e.g., Workman and Reynolds, 1949; Goodman et al., 1988a; Williams et al., 1989; Carey and Rutledge, 1996; Petersen et al., 1996; López and Aubagnac, 1997). CG lightning may be initiated by the descent of graupel below the level of main negative charge where the process of charge reversal microphysics causes these ice particles to charge positively (e.g., Jayaratne et al., 1983; Williams et al., 1989; Carey and Rutledge, 1996). This lower positive charge may result in the electrical bias which allows for the transfer of negative charge to ground in CG lightning as first suggested by Clarence and Malan (1957).

As shown in Fig. 3.8, the graupel mass continued its descent below the freezing level where it melted between 3 and 5 km. After sufficient time for gravitational sedimentation (e.g., 15 - 20 minutes, assuming V_t = 5 m s^{-1} and a fall from the 5 to 6.5 km region), a peak in the rain flux (Fig. 3.7) and rain mass (Fig. 3.8) reached near the surface (actually 0.5 km in the gridded data). This tendency for peak rainfall near the surface to lag the maximum cloud-to-ground lightning flash rate by 15 - 20 minutes is also consistent with past studies of sub-tropical and mid-latitude convection (e.g., Goodman et al., 1988a; Carey and Rutledge, 1996).

The freezing of supercooled drops may actually enhance cloud electrification in three ways: 1) provide an instantaneous and abundant source of precipitation sized ice as

discussed above, 2) promote favorable conditions for secondary ice processes via the shattering of freezing drops (e.g., Pruppacher and Klett, 1997) or rime splintering (e.g., Hallet and Mossop, 1974), and 3) increase the buoyancy and hence updraft speed of the air parcel via the latent heat of fusion. As noted in Koenig (1963) and reviewed in Young (1993), most observations of enhanced ice crystal concentrations were obtained in cumulus clouds which contained large supercooled drops. Ice enhancements can be an order of magnitude or more (up to 10^4) for the ice multiplication mechanisms mentioned above (Pruppacher and Klett, 1997). According to the NIC mechanism, an order of magnitude increase in the ice crystal concentration would result in an order of magnitude increase in graupel electrification. The increase in buoyancy associated with drop freezing could be significant. For example, peak mixing ratios of supercooled rain water at -5° C to -10° C in lightning producing cells were typically 3 - 5 g kg^{-1} (cf. Figs. 3.4a, 3.6b) which might have corresponded to 1 - 1.7 degrees of extra buoyancy if all the water froze. Similar suggestions regarding the importance of drop freezing to cloud electrification have been made by other investigators (Carey, 1994; Jameson et al., 1996; Petersen, 1997; López and Aubagnac, 1997).

3.3. Relationship between the total lightning flash rate and precipitation

The presence of a flat plate antenna at the C-pol radar during MCTEX provided us the opportunity to analyze the co-evolution of the radar-inferred precipitation structure and the total lightning flash rate within 40 km of the radar. In Fig. 3.9, we present a temporal evolution of the total lightning flash rate, the total mixed phase (0° to -40° C) ice mass, the integrated mixed phase graupel mass, and the rain mass flux for the entire Hector lifecycle (0200 - 0800) on 28 November 1995. A time-height cross-section of the total slab (kg km^{-1}) ice mass versus the 15-minute total lightning flash rate is shown in Fig. 3.10.

During the dominance of warm rain convection prior to 0225 (cf. Figs 3.1a, 3.2a; 3.9; 3.10), there was no detected lightning activity. The increase in the total ice mass above the height of -5° C was associated with the first lightning flashes from 0230 to 0300. The total lightning flash rate, total ice mass, and graupel mass all dramatically increased from

0315 to 0415 associated with the merger process (cf. Figs. 3.1b,c; 3.9; 3.10). The role of the merger process in the production of mixed phase ice mass, rainfall, and lightning will be investigated further in Sec. 3.5. As shown in Fig. 3.9, the total lightning flash rate and total mixed phase ice mass are well correlated ($\rho = 0.93$). The three primary peaks in the total lightning flash rate (0416, 0502, 0522) were either preceded by or coincident with maxima in the total ice mass (0416, 0502, 0514; Fig 3.9). As presented in Fig. 3.10, these peaks in the total lightning flash rate were also accompanied by upward perturbations in the height of the slab ice mass and large temporal gradients of the slab ice mass in the 0° to -40° C region. The overall maxima in the mean[4] total lightning flash rate of 55 min^{-1} at 0502 was coincident with the absolute peak in the total ice mass and graupel mass (Figs. 3.9 and 3.10). As Hector weakened from 0515 to 0615 within 40 km of the radar (cf. Figs. 3.1d,e; 3.9; 3.10), the total lightning flash rate dropped precipitously along with the total ice and graupel masses. This decrease in ice mass was most dramatic in the mixed phase zone and was also accompanied by downward perturbations in the height of the ice mass (Fig. 3.10).

The correlation between total ice mass and the total lightning flash rate documented here is similar to previous observations of sub-tropical and mid-latitude thunderstorms (e.g., Larsen and Stansbury, 1974; Stansbury et al., 1978; Marshall and Radhakant, 1978; Goodman et al., 1988a; Carey and Rutledge, 1996) and is consistent with a charging mechanism which relies on ice-ice collisions in the presence of supercooled cloud water for particle scale charge separation (e.g., Takahashi, 1978a; Jayaratne et al., 1983; Saunders et al., 1991 among others).

Interestingly, the total ice mass tracked the total flash rate from first lightning until about 0600 when Hector began to dissipate near the radar and visually glaciate, and the total lightning flash rate decreased to < 10 min^{-1}. As seen in Figs. 3.9 and 3.10, the total ice mass began to increase after 0600 in the -15° to -30° C region and experienced a secondary maxima at 0645 while the total flash rate continued to decrease. We speculate

---

[4]The total lightning flash rate was averaged over the temporal resolution of the radar data (4 - 15 minutes). The maximum one-minute average was 60 min^{-1}, occurring at 0454 and 0458.

that this sudden disconnect between the total ice mass and the total lightning flash rate is related to the transition from vigorous updraft (i.e., convective) to weak updraft or downdraft (i.e., stratiform), the subsequent loss of cloud water, and the fallout of large precipitation sized ice. Indeed, graupel and frozen drops were non-existent in Hector after about 0555 within 40 km of the radar (Fig. 3.9). The lack of large ice and possibly cloud water, both necessary ingredients in the NIC mechanism, could have rendered the electrical generator ineffective despite the presence of smaller, precipitation-sized ice. The relationship between convective/stratiform rain fraction and lightning frequency will be explored further in Sec. 3.6.

The fine scale temporal evolution of the rain mass flux shown in Fig. 3.9 does not match some of the undulations (i.e., relative minima and maxima) seen in the total lightning flash rate and mixed phase total ice mass (Fig. 3.9). However, the rain flux does envelope the total lightning flash rate. Indeed, the two quantities are very well correlated ($\rho = 0.94$). As a matter of fact, comparison with Sec. 3.2 suggests that the integrated rain flux is actually better correlated with the total lightning flash rate than with the CG lightning flash rate.

3.4. Relationship between the surface electric field and precipitation

In this section, we compare the polarimetric radar inferred precipitation structure of a portion of Hector which passed within 20 km of the radar (cf. Figs. 3.1a-e), to field mill observations of the surface electric field and total lightning flash rate from 0200 to 0630. In addition, the ALDF network was used to isolate the ground discharges associated with this convection. The results are synthesized in Fig. 3.11 which depicts the temporal evolution of the total ice and rain masses in the vertical, the surface electric field, the total lightning flash rate, and time of occurrence of each CG lightning flash.

The early, pre-merger stage of Hector (0200-0245) was dominated by warm rain processes as can seen by the lack of significant ice-mass and supercooled water above 0° C (Fig. 3.11). This slab water mass is associated with a warm rain cell which was located to the east-northeast of the radar (Fig. 3.1a) and characterized by reflectivities up to 50 dBZ. During this entire time, the field mill indicated a fair weather electric field (e.g.,

Uman, 1987) of 60 - 80 V m^{-1} and no lightning transients. From 0245 to 0345, distant convection (at ranges of 20 - 30 km) caused an enhancement in the fair weather field up to 200 V m^{-1}. This enhanced fair field was probably caused by a reversal of the sign of the surface electric field associated with a distant thunderstorm dipole (i.e., the so-called "field reversal distance," Uman, 1987). Distant lightning was registered by the field mill from 0325 to 0345 while the E-field was still fair and there was little in the way of convection within 20 km of the radar (e.g., Fig. 3.1b).

From 0345 to 0415, new cells developed to the north of the radar and field mill at ranges less than 20 km, along a gust front on the southern side of Hector (Fig. 3.1c). Aided by convergence along the gust front, these vigorous new cells lofted drops above the freezing level and began the production of precipitation sized ice (Fig. 3.11). Within 10 to 15 minutes of precipitation ice production above -10° C, the surface electric field began to increase rapidly toward foul (i.e., positive) values and the first lightning transient was recorded by the field mill at 0415. The first couple of ground discharges occurred 5 - 10 minutes later. The positive slope of the surface electric field corresponds well with the increase in the amount and height of the ice mass from 0415 to 0430. The presence of supercooled drops colder than -10° C during this time suggests that drop freezing was a major source of precipitation sized ice for subsequent riming and cloud electrification via the NIC mechanism.

Between 0430 and 0445, a weak excursion in the electric field from a foul field to a near zero and slightly negative (i.e., fair) E-field was followed by a maximum in the rain mass near the surface (Fig. 3.11). The field excursion associated with precipitation (FEAWP; Moore and Vonnegut, 1977; Krehbiel, 1986) began (peaked) about fifteen (seven) minutes prior to the maximum rainfall near the surface at 0445. The E-field recovered to pre-FEAWP values just after the peak in precipitation near the surface.

There are several competing theories advanced to explain the FEAWP. Theories include the Wilson capture of positive corona ions by descending precipitation in the sub-cloud air (Malan, 1952; Rust and Moore, 1974), the deposition of positive charge on precipitation by lightning in the lower portion of the cloud (Holden et al., 1980; Marshall and Winn, 1982), the lateral displacement of negative charge aloft (Moore and Vonnegut,

1977), and the positive charging of descending graupel particles at higher temperatures via the NIC mechanism (T > -10° C; Takahashi, 1978a) as proposed by Takahashi (1983), Williams (1990), and Carey and Rutledge (1996). More recently, Soula and Chauzy (1997) hypothesized that the FEAWP is caused by the fallout of negatively charged precipitation to the ground, revealing a narrow, positive space charge layer just above the surface.

Since the rainfall maximum near the ground lagged the FEAWP in Fig. 3.11, the hypothesis of Soula and Chauzy (1997) does not appear to apply in our case. We suspect that the Wilson capture of positive space charge was ineffective since most space charge associated with point discharge exists in the lowest several hundred meters above ground (e.g., Standler and Winn, 1979; Soula and Chauzy, 1991) while most of the rainfall was still several km or more above ground during the FEAWP. Inspection of the radar data reveal that there was little horizontal displacement of the echo during the FEAWP, eliminating the theory of Moore and Vonnegut (1977). Although there was an increase in the total lightning flash rate during this time (Fig. 3.11), the deposition of positive charge by lightning is an unlikely explanation in our case since the E-field excursion to near zero and negative values occurred gradually over a seven minute period rather than instantaneously during one or more lightning flashes. As in Carey and Rutledge (1996), the FEAWP in Fig. 3.11 appears to be associated with the descent of frozen precipitation in the 0° to -10° C region. As shown in Fig. 3.11, ample precipitation ice existed at temperatures warmer than -10° C prior to the FEAWP where it could have charged positively according to Takahashi (1978a). The descent of this ice and its subsequent melting after 0430 is most closely correlated with the FEAWP.

As seen in Fig. 3.11, the surface electric field increased from 100 V m^{-1} at 0440 to 1000 - 1500 V m^{-1} by 0500. During the same time, isosurfaces of total ice mass extended vertically (cf. E-field trace to the 1×10^7 kg km^{-1} isosurface in Fig. 3.11) and the amount of integrated mixed phase (e.g., 5 to 11 km) ice mass increased. Supercooled drops were continually lofted above the height of -10° C as depicted in the contours of slab rain mass in Fig. 3.11. The freezing of these drops undoubtedly provided a source of large

precipitation sized ice as the cell developed and became more electrified as will be shown below.

A horizontal cross-section of Z_h, Z_{dr}, and M_i at 6.5 km (-10° C) for the cell which likely caused the peak in the surface E-field and total lightning at 0500 is presented in Fig. 3.12. A polarimetric radar signature of lofted supercooled drops is the "Z_{dr} column" (e.g. Illingworth et al., 1987). A good example of this feature was located at x = -15 km and y = 10 km (Fig. 3.12). Peak values of Z_{dr} in the column were just above 2 dB and were collocated with reflectivities between 50 and 55 dBZ. Inspection of M_i inferred from Z_h and Z_{dp} reveals that the column was probably a mixture of rain and ice. Note the high reflectivities collocated with low values of Z_{dr} just to the southeast of the Z_{dr} column. This combination results in a peak in the ice mass over 12 g kg^{-1}. Due to the close proximity between the Z_{dr} column and the peak ice mass, we suggest that the source of large ice in this example was drop freezing. We also believe that it is these frozen drops at this level and higher which subsequently rimed and participated in the charging process via the NIC mechanism, eventually leading to the peak E-field and total lightning flash rate measured by the field mill as shown in Fig. 3.11.

The maximum E-field for this case reached only 1.5 kV. This is a factor of 2 to 5 less than typically reported beneath electrically active midlatitude thunderstorms (e.g., Dye et al., 1988). It is well known that space charge limits the magnitude of the electric field measured at the surface and that the surface E-field is typically less than the actual in-cloud field (Standler and Winn, 1979; Soula and Chauzy, 1991). However, this cannot explain the differences between various surface measurements. We suspect that the relatively small maximum E-field in Fig. 3.11 is primarily the result of the large horizontal distance to the cell (R = 15 - 20 km, Fig. 3.12). It is also possible that the elevated height of the mixed phase zone in tropical convection relative to midlatitude convection could account for some of the observed differences. Sensitivity tests with the equations for an electrical tripole (e.g., Uman, 1987) are consistent with both of these explanations. Measured total lightning flash rates of up to one per second (Fig. 3.10) strongly suggest that the electric fields in vigorous tropical island storms are comparable to mid-latitude storms.

As the cell depicted in Fig. 3.12 began to dissipate after 0530, the lofting of supercooled drops stopped and the production of large precipitation ice was ended (Fig. 3.11). As the remaining large precipitation sized ice fell out of the storm from 0530 to 0545, the field switched from positive to negative polarity (i.e., from predominately negative to positive charge aloft). The onset of this so-called end of storm oscillation (EOSO; Moore and Vonnegut, 1977) in the surface E-field following the fallout of large precipitation sized ice suggests that the large precipitation sized ice carried the negative charge to the ground (Fig. 3.11). The advection of this storm further away from the field mill, past the so-called "field reversal distance" (e.g., Uman, 1987) may have also contributed to the reduction and eventual switch in polarity of the surface E-field. After 0545, the E-field remained fair, CG lightning ceased, and the total lightning flash rate continued to decrease toward zero. The remaining ice mass between -20° C and -40° C during this time was likely associated with ice crystals in the rear anvil. The implication in Fig. 3.11 is that the large precipitation sized ice particles were the predominate negative charge carriers while ice crystals in the anvil at 10 km and higher were the predominate positive charge carriers, consistent with the NIC theory. Combining this inference with the discussion of the FEAWP above, we find the observations summarized in Fig. 3.11 to be consistent with the classical thunderstorm tripole reviewed in Williams (1989). In addition, the correlation between ice production and the surface electric field demonstrated above for tropical island thunderstorms is similar to behavior in mid-latitude (Dye et al., 1988; 1989), sub-tropical (Jameson et al., 1996), and tropical oceanic (Takahashi, 1978b; 1983; Petersen et al., 1996) convection.

3.5. Role of the merger process

In their investigation of the cumulus merger process over the Tiwi Islands, Simpson et al. (1993) determined that 90% of the rainfall beneath a typical Hector comes from merged systems as defined in Chapter 2. Using C-pol radar and ALDF data, we extend the Simpson et al. (1993) results to include the role of the merger process in the production of *mixed phase graupel mass* and *cloud-to-ground lightning* in addition to rainfall and echo area.

The results are summarized in Table 3.1. Merged convective features in this Hector accounted for 93% of the echo area, 97% of the rainfall, 97% of the mixed phase graupel mass, and *100% of the cloud-to-ground lightning production* over the Tiwi Islands despite representing the minority of convective features (45%). On 28 Nov 95, there were typically more single cell than merged features despite the fact that merged features accounted for over an order of magnitude more instantaneous echo area in the mean. The average merged convective feature produced approximately 30 times more rainfall and mixed phase ice mass than the mean single cell feature. These tendencies are consistent with past merger results in subtropical (Simpson and Woodley, 1971; Simpson et al., 1980), tropical oceanic (Houze and Cheng, 1977; Demott and Rutledge, 1998), midlatitude (Changnon, 1976), and tropical island (Keenan et al., 1990; Simpson et al., 1993) convection. In summary, these studies found that merged systems are larger, taller, more intense, and produce more rainfall than single cell convection. We extend these results with the additional finding that merged convective complexes also produce significantly more mixed phase ice mass and cloud-to-ground lightning than single cells.

Table 3.1. Average properties of instantaneously occurring features for the 28 November 1995 case.

Average Feature Property	**Single-cell features**	**Merged features**
Number	10.1 (55%)	8.1 (45%)
Echo area (km^2)	86.3 (7%)	1155.9 (93%)
Rain flux (10^6 kg s^{-1})	0.28 (3%)	8.62 (97%)
CG lightning flash rate (min^{-1})	0.0 (0%)	2.0 (100%)
Mixed phase graupel mass (10^7 kg)	1.26 (3%)	35.18 (97%)

It is quite remarkable that single-cell convective features produced *no* detectable CG lightning despite the continual presence of 5 - 20 isolated cells over the Tiwi Islands throughout Hector's lifecycle on this day. Analysis of C-pol radar data suggest that most of these features were either entirely contained below the 0° C isotherm or were otherwise dominated by warm rain microphysics (e.g., Fig. 3.2a). The simultaneous lack of mixed

phase graupel mass and CG lightning is consistent with the crucial role of graupel particles in the NIC mechanism. Since our electric field and total lightning flash measurements were limited to within about 20 km and 40 km respectively of the radar, it is quite possible that some of these single cell features were electrified to the point of producing intracloud lightning. However, all of the single cell features within 20 - 40 km of the radar produced little mixed phase ice mass and generated no significant E-fields or intracloud lightning (cf. Figs. 3.1a, 3.9, 3.10, and 3.11 from 0200 - 0245).

On two occasions (around 0345 and 0430), single cell features produced a significant amount ($> 5 \times 10^7$ kg) of graupel mass in the mixed phase region. Both of these isolated cells originated along a gust front, explosively developed, and quickly merged with the parent complex before producing any CG lightning. The role of these daughter cells in lightning production cannot be underestimated however because their mergers with the parent complex were closely followed by two of the primary peaks in graupel mass and CG lightning production in Hector (cf. Fig 3.7, 0345 - 0415 and 0430 - 0500). This process was captured by the field mill as depicted in Fig. 3.11. An earlier single cell along the southern coast sea-breeze produced no measurable electric fields or lightning from 0200 - 0245. In contrast, an intense cell along a gust front produced significant ice mass and electric fields before merging with the parent echo after 0400.

These results provide some circumstantial support for one of the earliest merger hypotheses developed from observations (Simpson and Woodley, 1971; Simpson, 1980) and tested by numerical models (Tao and Simpson, 1984; 1989) which suggests the critical role of the downdraft and gust front outflows in cumulus merging. It is interesting to speculate on the differences between those single cells which developed vertically into the mixed phase zone and produced significant ice mass and electric fields and those which did not. The one-dimensional cloud and electricity modeling study of Hector by Petersen (1997) provides insight into this question. Model results revealed great sensitivity of cloud vertical development and subsequent electrification to the strength and duration of low-level forcing applied in the model. Therefore, it is likely that there was insufficient low-level forcing along the Tiwi Islands' sea-breeze fronts on 28 November 1995 to produce vertically developed and CG lightning producing single cell convection. On the

other hand, forcing along certain gust fronts appears to have been more than sufficient to cause explosive convective development before merging with the parent cell. In order to definitively determine the role of gust front forcing on ice production and cloud electrification over the Tiwi Islands, more observational research is required with the MCTEX data set (e.g., Doppler radar, wind profiler, aircraft, and aerosonde).

3.6. Convective versus stratiform precipitation and lightning

Keenan et al. (1990; 1994b) reported that stratiform decks are commonly found during the mature to dissipating phase of Hector. Precipitation over the Tiwi Islands on 28 November 1995 was no exception (e.g., Figs. 3.1f and 3.5). We found a convective (stratiform) rain fraction of 92% (8%) and a convective (stratiform) area fraction of 22% (78%). This convective rain fraction is considerably higher than typical values, which range from 50% to 70%, reported for tropical oceanic and continental (e.g., Houze, 1977; Cheng and Houze, 1979; Leary, 1984; Houze and Rappaport, 1984; Churchill and Houze, 1984; Chong and Hauser, 1989; Gage et al., 1994; Rickenbach and Rutledge, 1998), sub-tropical (e.g., Steiner et al., 1995), and midlatitude (e.g., McAnelly and Cotton, 1989) convective systems. However, these results are very consistent with the 92% convective rainfall fraction found by Simpson et al. (1993) for three monsoon-break Hectors and with the 84% convective rainfall fraction determined by Rosenfeld et al. (1995) for the Darwin area. The consistency with our results is striking since all three studies employed different convective/stratiform partitioning techniques. Simpson et al. (1993) hypothesized that the typically drier moisture profile over the Tiwi Islands during the monsoon break is a major factor in reducing the stratiform rainfall fraction. This is consistent with our visual and radar observations during MCTEX which suggest that Hector stratiform anvils often sublimated rapidly after the convective portion dissipated as it exited the western coast of Bathurst Island (e.g. Figs. 3.1e,f).

The stratiform rain and area fractions along with the CG lightning flash rate for the 28 November 1995 Hector life-cycle are presented in Fig. 3.13. The stratiform rain and area fractions increased during the mature to dissipating stage of this Hector (0515 - 0800), as they do in most tropical convection (e.g., Houze, 1989). By 0800, the stratiform rain and

area fractions reached nearly 100%. Interestingly, there is a significant anti-correlation between the cloud-to-ground lightning flash rate and the stratiform rain and area fractions in Fig. 3.13, particularly after 0500 when ρ_{rain} = -0.7 and ρ_{area} = -0.9 respectively. Both stratiform fractions increased dramatically while Hector's CG lightning flash rate decreased by an order of magnitude (from 5 flashes min^{-1} at 0500 to 0.5 flashes min^{-1} by 0600). A similar result was found by Rutledge and MacGorman (1988) for a midlatitude Mesoscale Convective System (MCS). During the active phase of cloud-to-ground lightning in Hector (0330 - 0530), the stratiform rain and area fractions were at a minimum of less than 6% and 70% respectively. As shown in Fig. 3.13, the stratiform area and rain fractions experienced a relative maximum during the initial phases of Hector when there was little or no CG lightning (0200 - 0300). However, analyses presented above in Secs. 3.1-3.5 clearly demonstrate that Hector was dominated primarily by small, isolated, warm rain cumulonimbi and not stratiform precipitation at this time. Therefore, it is likely that the radar algorithm based on reflectivity and reflectivity gradient thresholds (Steiner et al., 1995; Rickenbach and Rutledge, 1998) overestimated the amount of stratiform precipitation during the initial, warm-rain phase of Hector. More research is necessary to confirm this speculation.

As expected from the results presented in Secs. 3.1 and 3.2, inspection of the ground strike locations and processed radar data reveal that CG lightning and convective rainfall characterized by active mixed phase ice-processes aloft are spatially correlated. For example, most of the lightning during the mature phase around 0514 clustered around one large, convective rainfall feature over Bathurst Island (cf. Figs. 3.1d and 3.14). In this Hector, most cloud-to-ground lightning tended to avoid radar echo identified as stratiform precipitation, as demonstrated in Fig. 3.14. Of course, cloud-to-ground lightning can occur in the stratiform region of precipitating systems. However, the CG lightning flash density in the convective region is typically an order of magnitude or more than that of the stratiform region (e.g., Rutledge and MacGorman, 1988; Rutledge et al., 1990; Petersen and Rutledge, 1992), as it was for this tropical island convective system.

As discussed in Secs. 3.1, 3.2, and 3.4 cloud-to-ground lightning was also absent from those precipitation regions which were dominated by warm rain processes as deduced

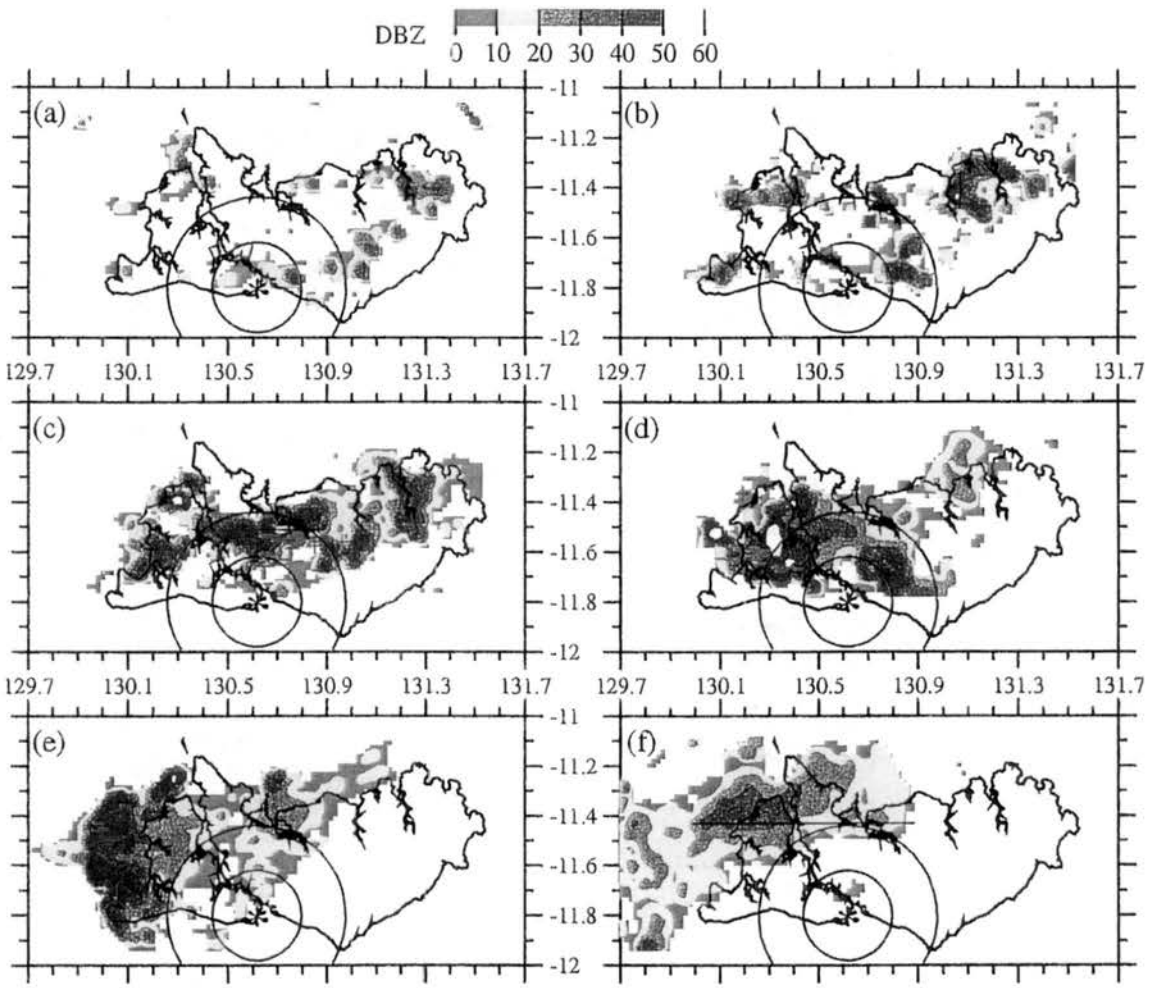

Figure 3.1. Evolution of the horizontal reflectivity (dBZ) at 2 km altitude over the Tiwi Islands on 28 November 1995 at (a) 0216, (b) 0315, (c) 0416, (d) 0514, (e) 0614, and (f) 0715 UTC. The reflectivity is color shaded as shown. The radar location is indicated by a "*" symbol and the flat plate (field mill) operating range ring at 40 km (20 km) is shown. The cloud-to-ground lightning flash locations during a ten minute period centered on the radar time are depicted. The blue "-" ("+") symbol indicates a negative (positive) polarity ground flash. The solid lines in Figs. 3.1a,b,c,f depict the planes of the vertical cross-sections in Figs. 3.2 - 3.5.

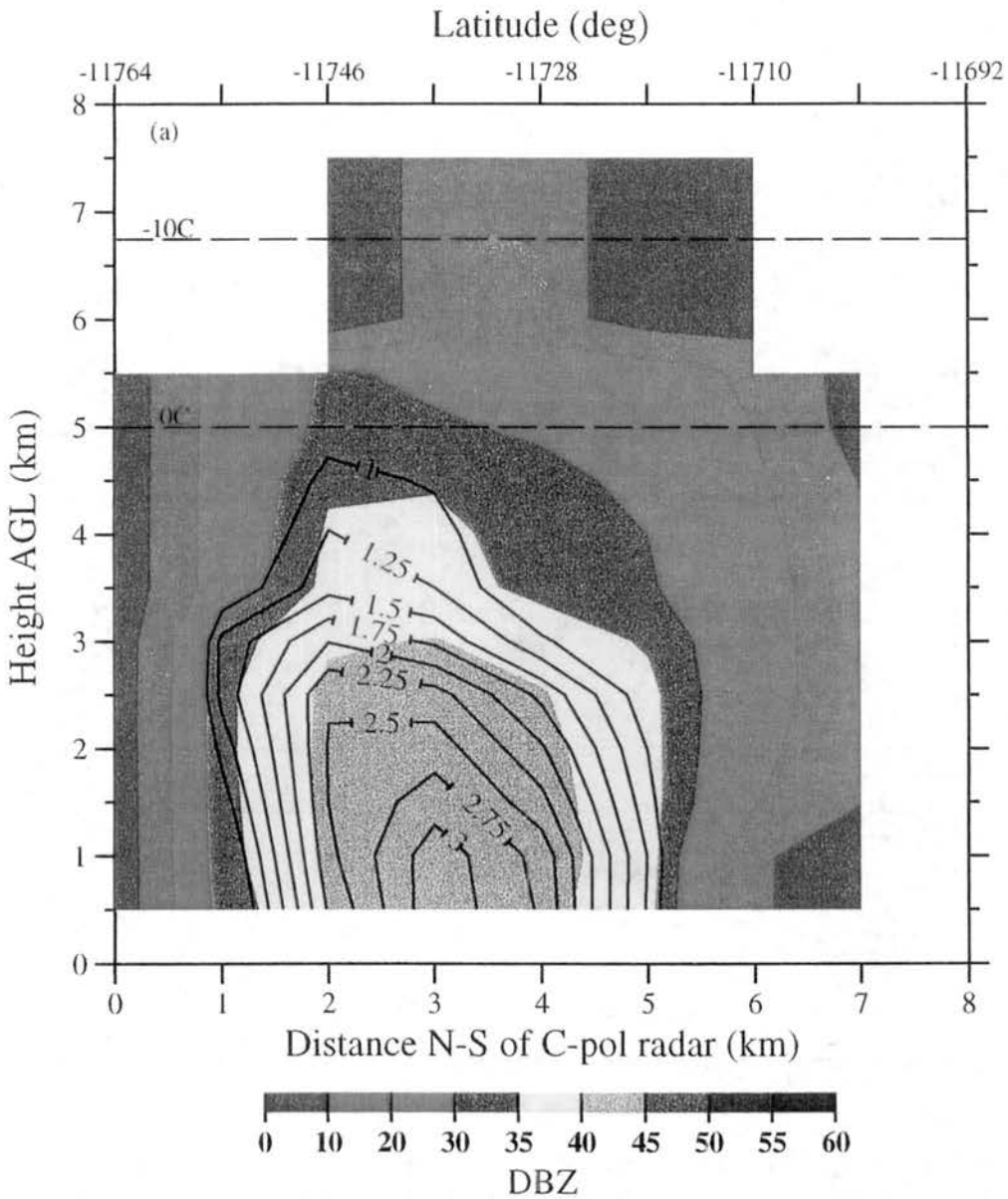

Figure 3.2. North-south vertical cross-section of Z_h (dBZ, color shaded) and Z_{dr} (dB, contoured) through a (a) non-CG lightning producing cell at 0216 UTC over southern Melville Island as depicted by the solid line in Fig. 3.1a. Environmental temperature levels deduced from sounding data are given.

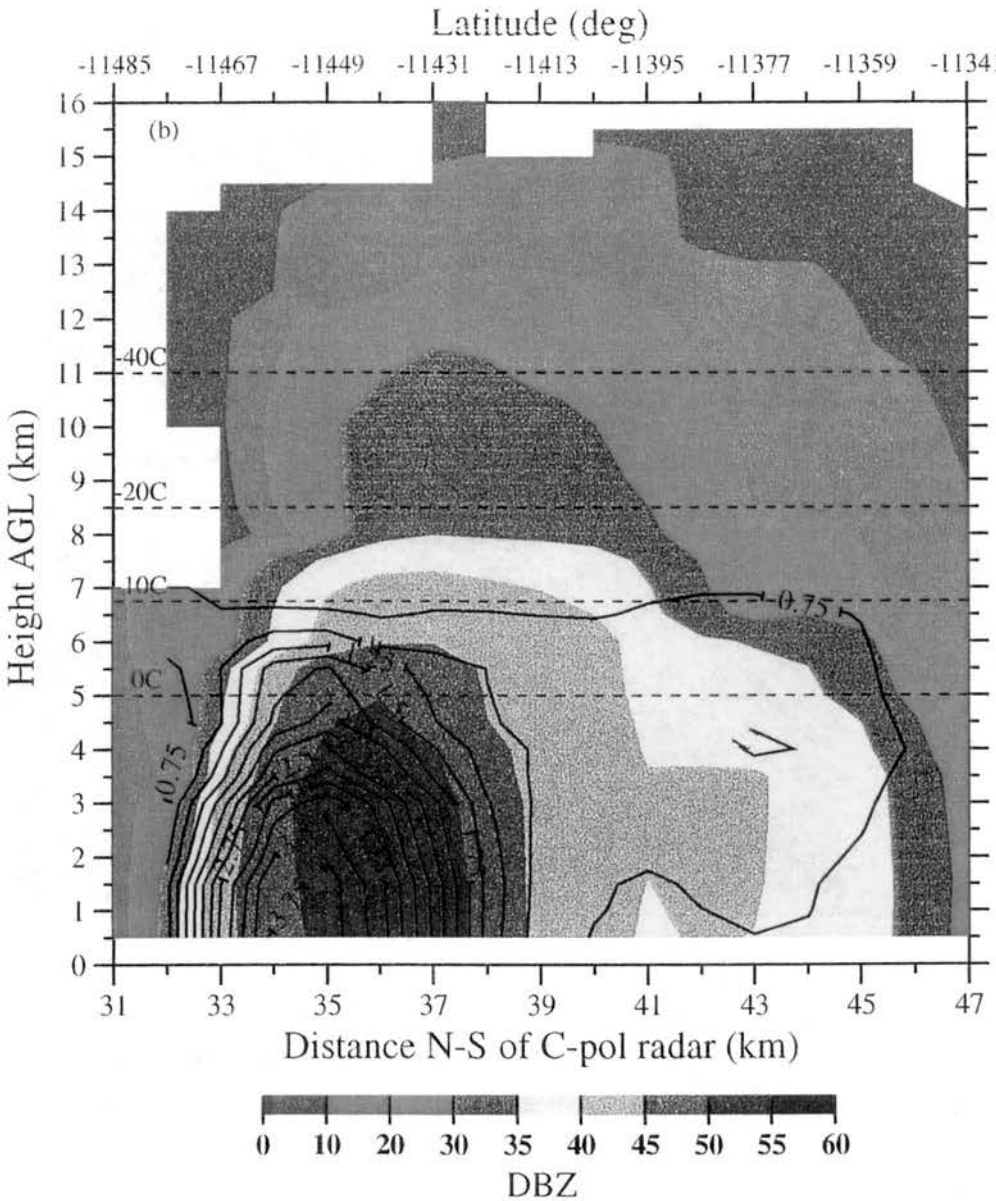

Figure 3.2. (b) as in (a) except a CG lightning producing convective complex at 0315 UTC over northern Melville Island as depicted by the solid line in Fig. 3.1b.

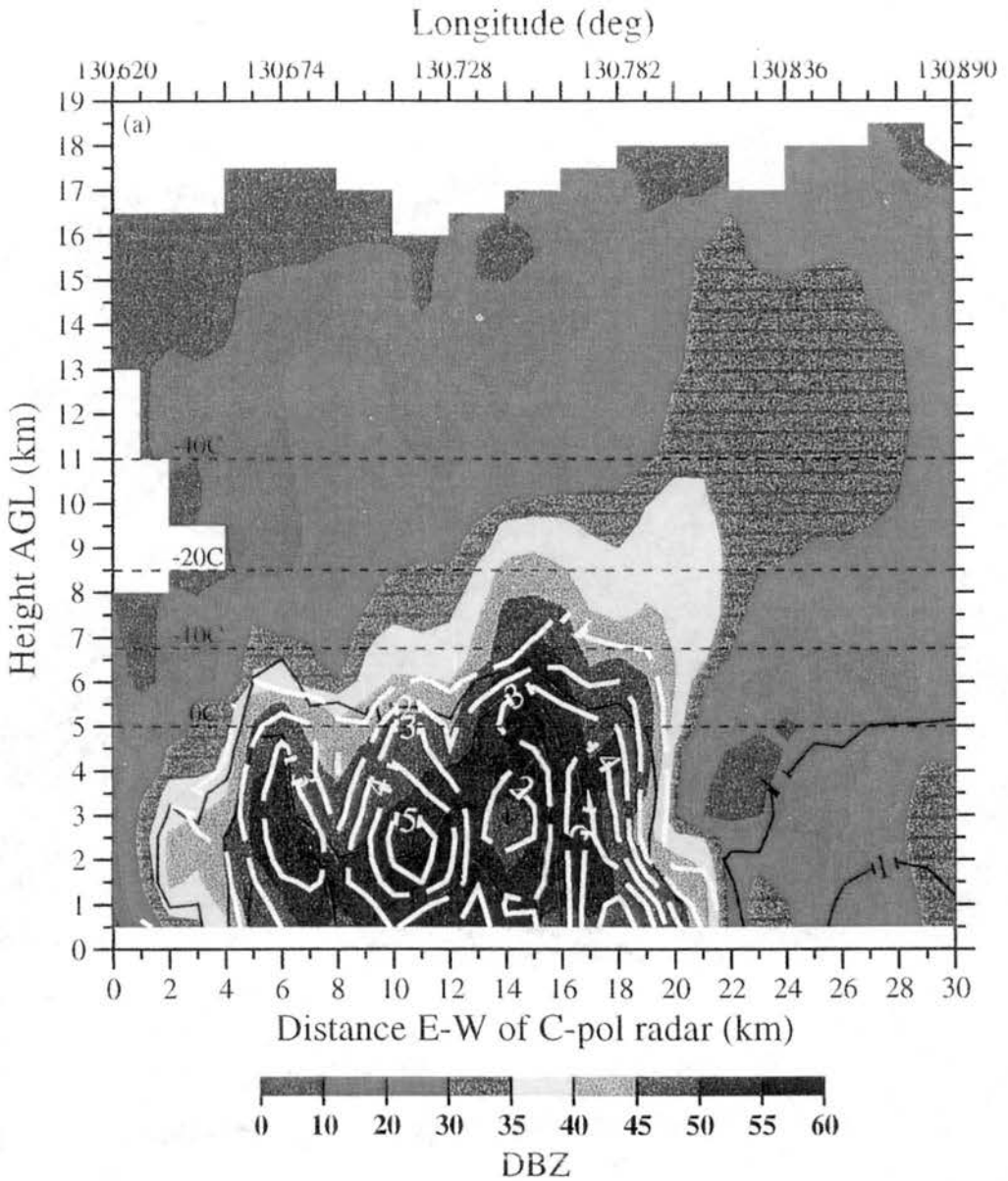

Figure 3.3. East-west vertical cross-section of Z_h (dBZ, color shaded as shown), Z_{dr} (dB, solid black contours), and K_{dp} (° km^{-1}, dashed white contours) through a (a) CG lightning producing convective complex over Melville Island at 0416 UTC as depicted by the solid line (latitude = -11.51° or y = 28 km north of the C-pol radar) in Fig. 3.1c.

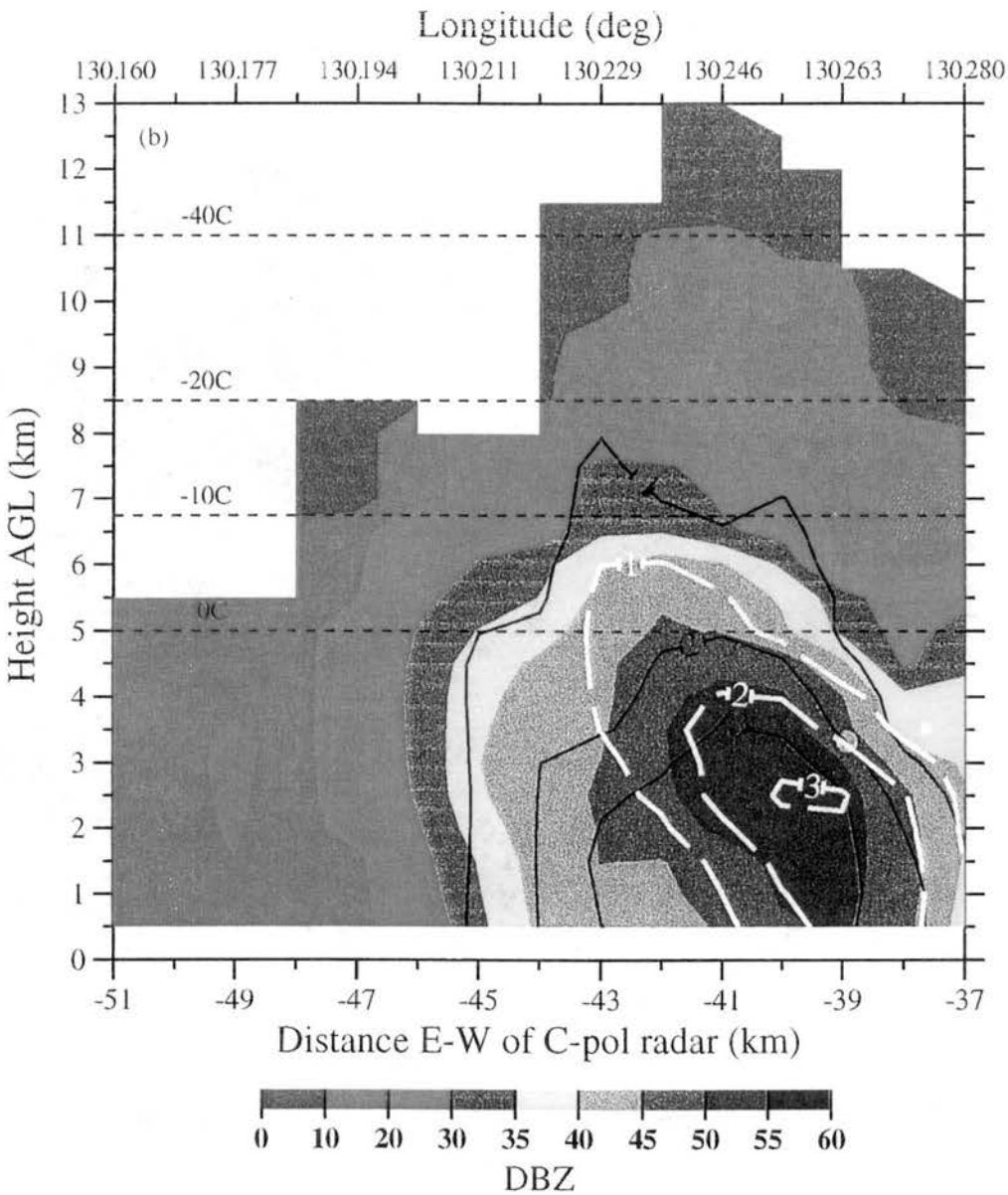

Figure 3.3. (b) as in (a) except non-CG lightning producing cell over Bathurst Island at 0416 UTC as depicted by the solid line (latitude = -11.59° or y = 19 km north of the C-pol radar) in Fig. 3.1c.

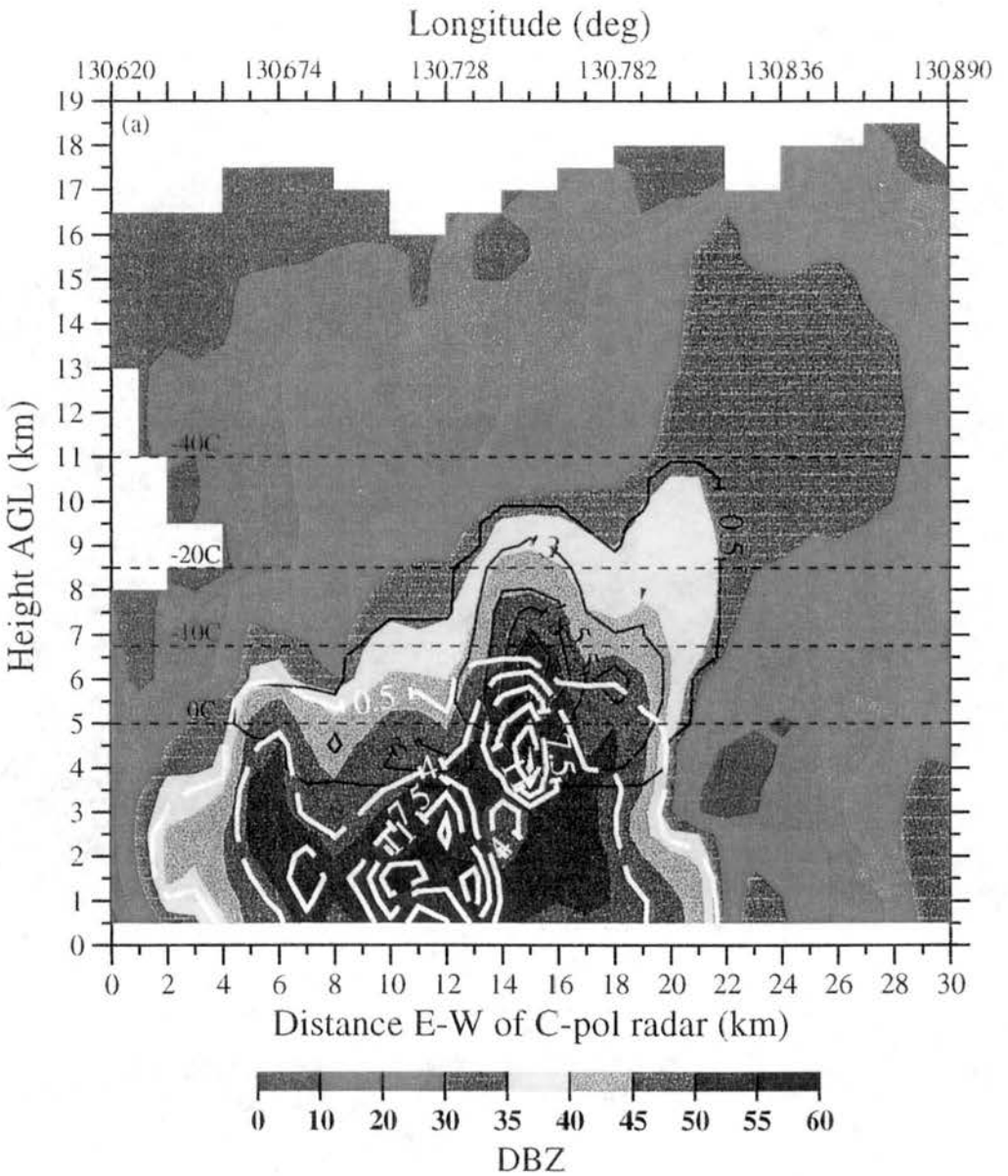

Figure 3.4. (a) As in Fig. 3.3a except of the polarimetric radar inferred graupel mass (M_g, solid black contours every 2.5 g kg^{-1} starting at 0.5 g kg^{-1}) and the rain mass (M_w, dashed white contours every 3.5 g kg^{-1} starting at 0.5 g kg^{-1}).

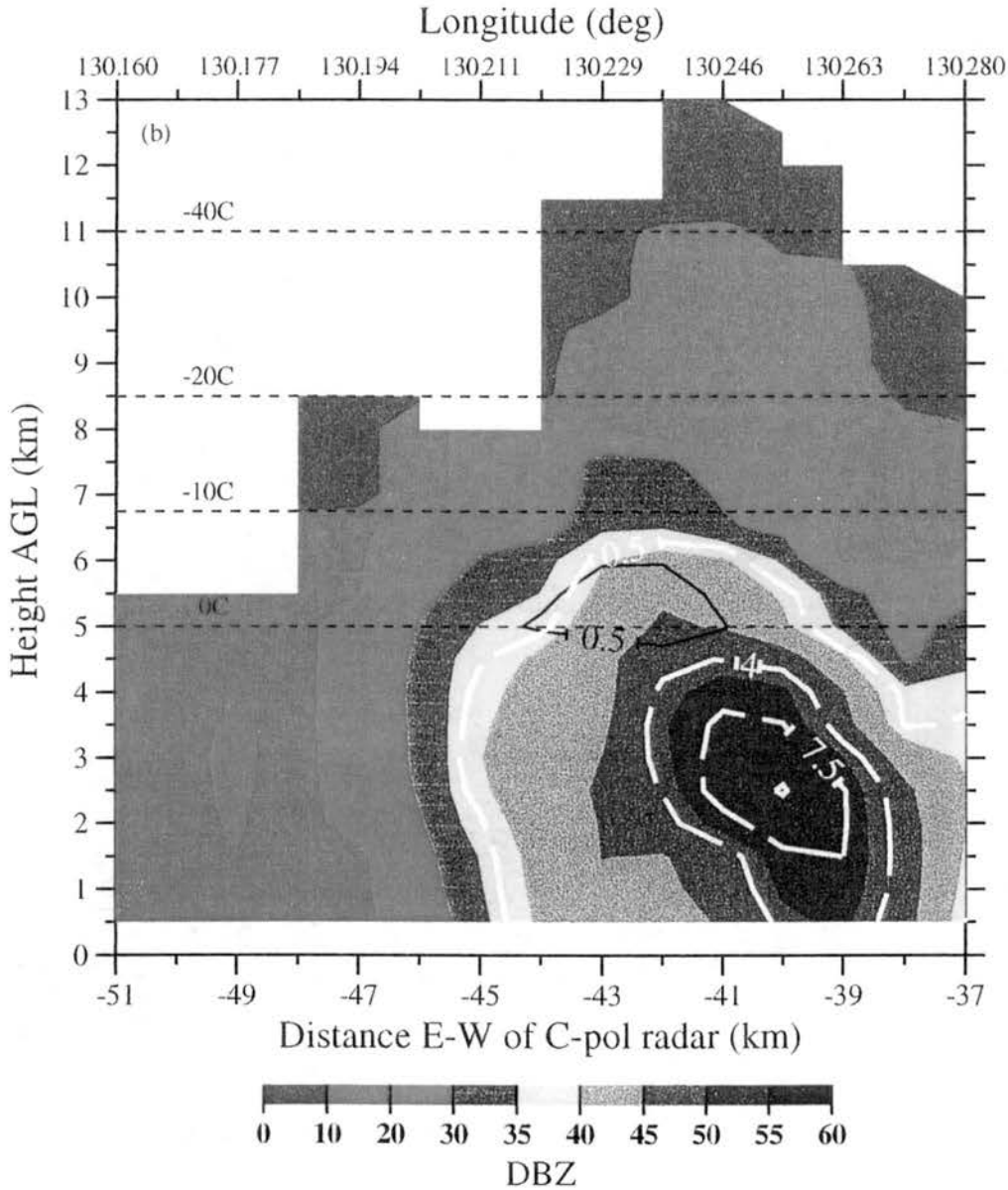

Figure 3.4. (b) As in Fig. 3.3b except of the polarimetric radar inferred graupel mass (M_g, solid black contours every 2.5 g kg^{-1} starting at 0.5 g kg^{-1}) and the rain mass (M_w, dashed white contours every 3.5 g kg^{-1} starting at 0.5 g kg^{-1}).

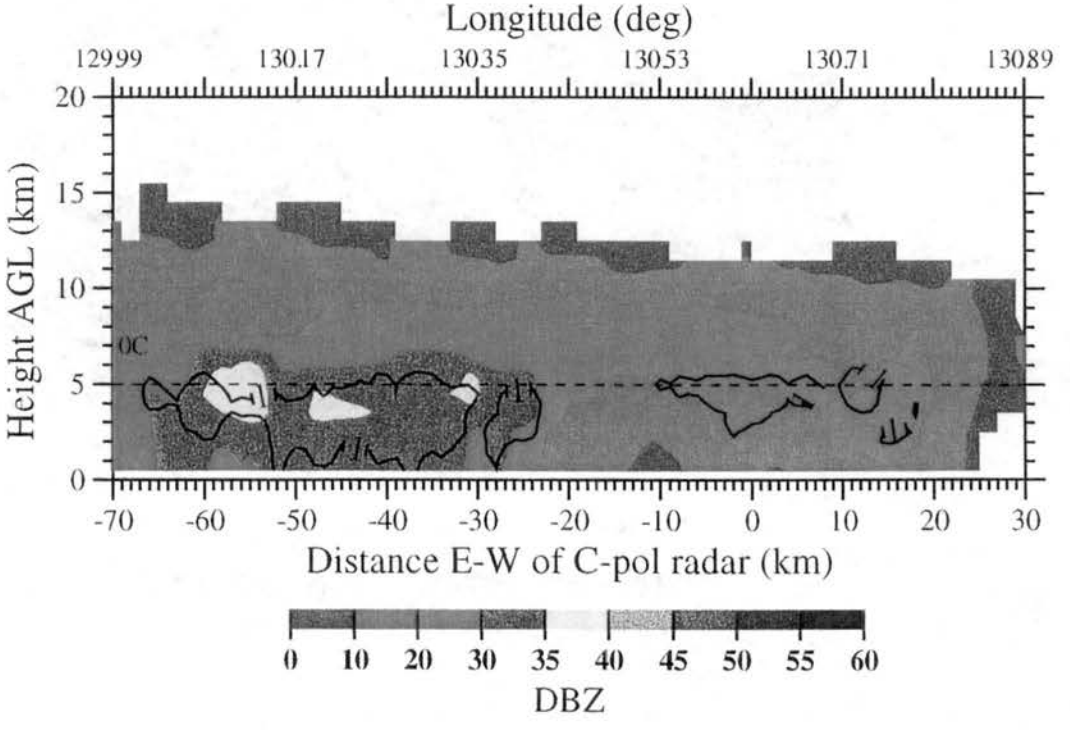

Figure 3.5. East-west vertical cross-section of Z_h (dBZ, color shaded) and the 1 dB Z_{dr} contour through stratiform precipitation at 0715 UTC as depicted by the solid line in Fig. 3.1f.

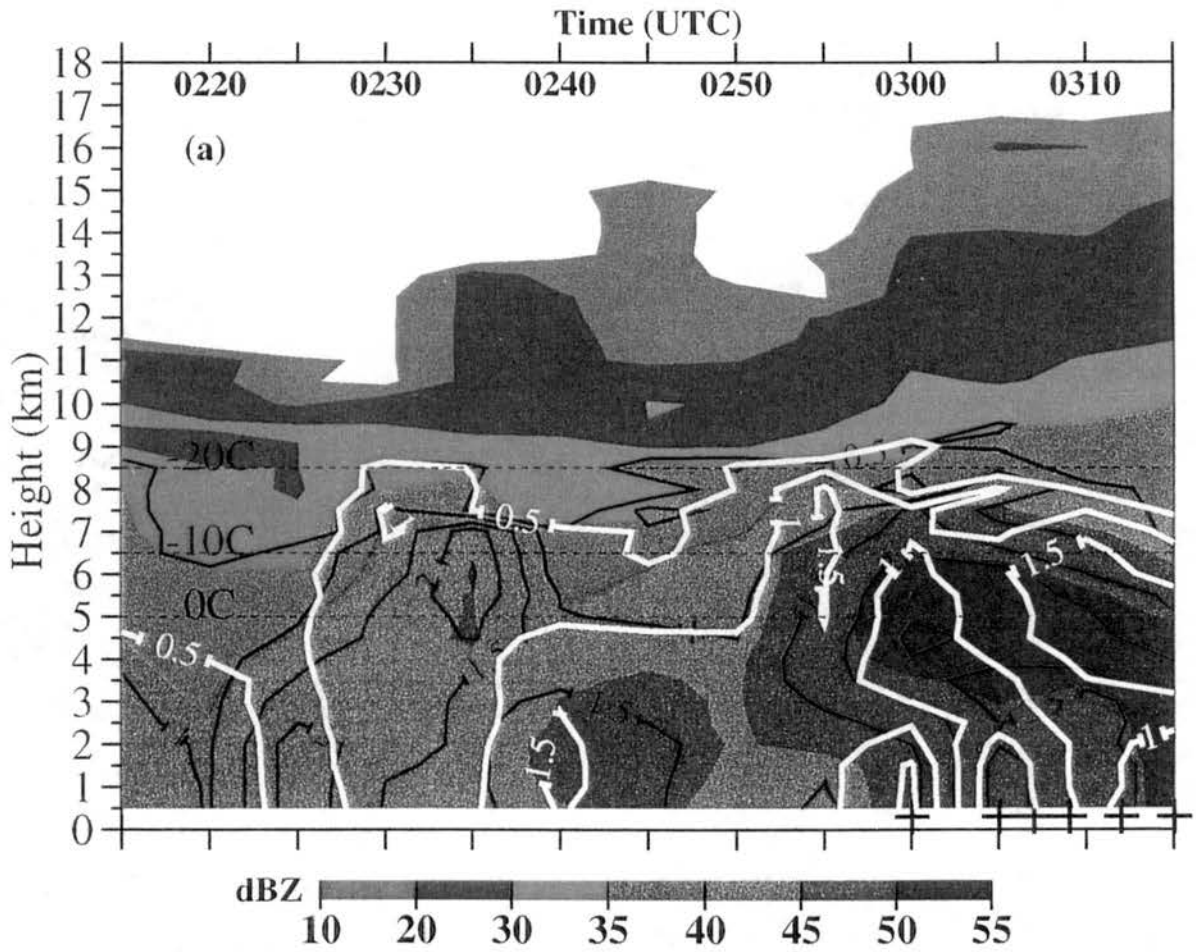

Figure 3.6. Time-height cross section of the mean (a) Z_h (dBZ, color shaded), Z_{dr} (dB, black contour), and K_{dp} (° km^{-1}, white contour) through the convective complex over northeastern Melville Island, as depicted in Figs. 3.1b and 3.2b, which produced the first cloud-to-ground lightning flashes over the Tiwi Islands from 0300 to 0315 UTC. The time of each CG lightning flash is depicted by a "+" symbol along the bottom of the figure.

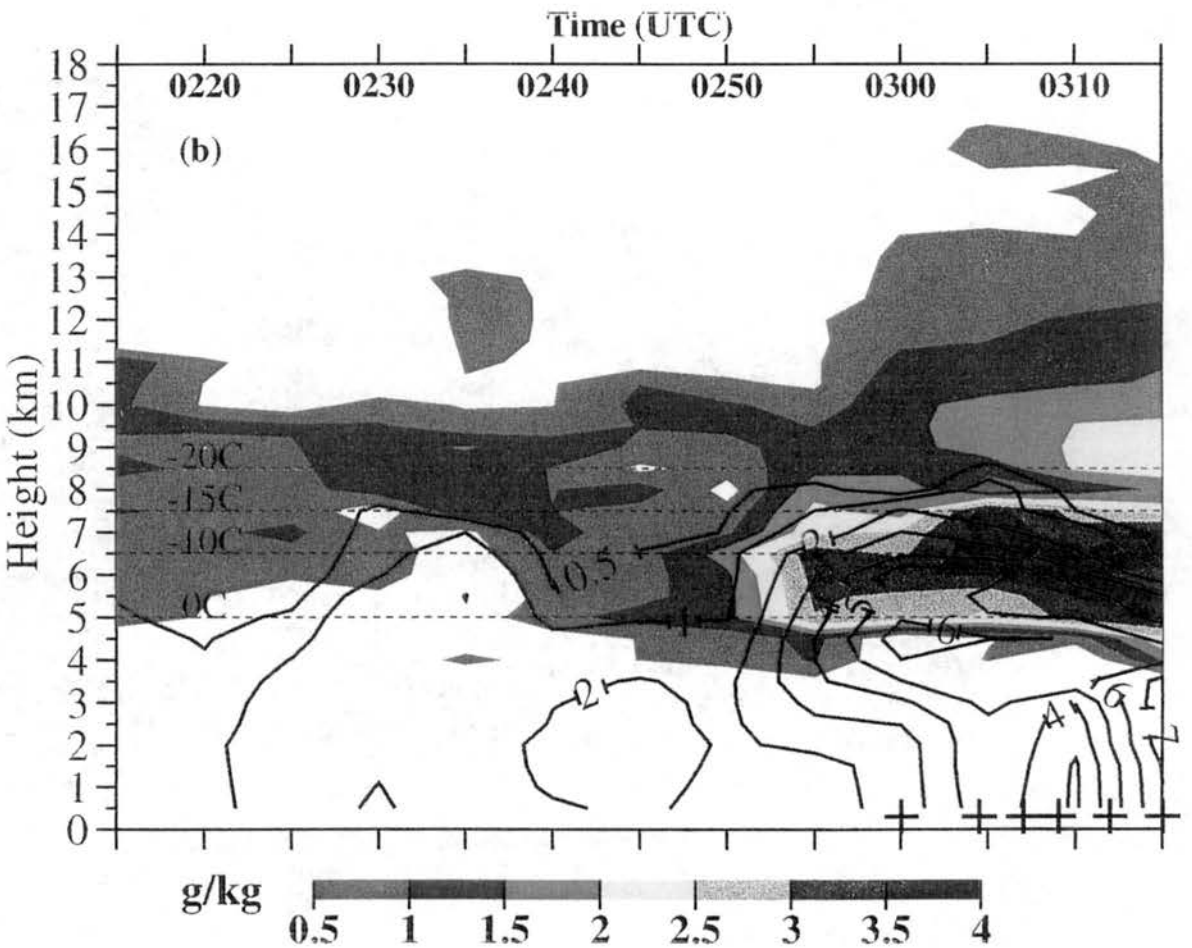

Figure 3.6. (b) as in (a) except radar derived M_w (g kg^{-1}, black contour) and M_i (g kg^{-1}, color shaded).

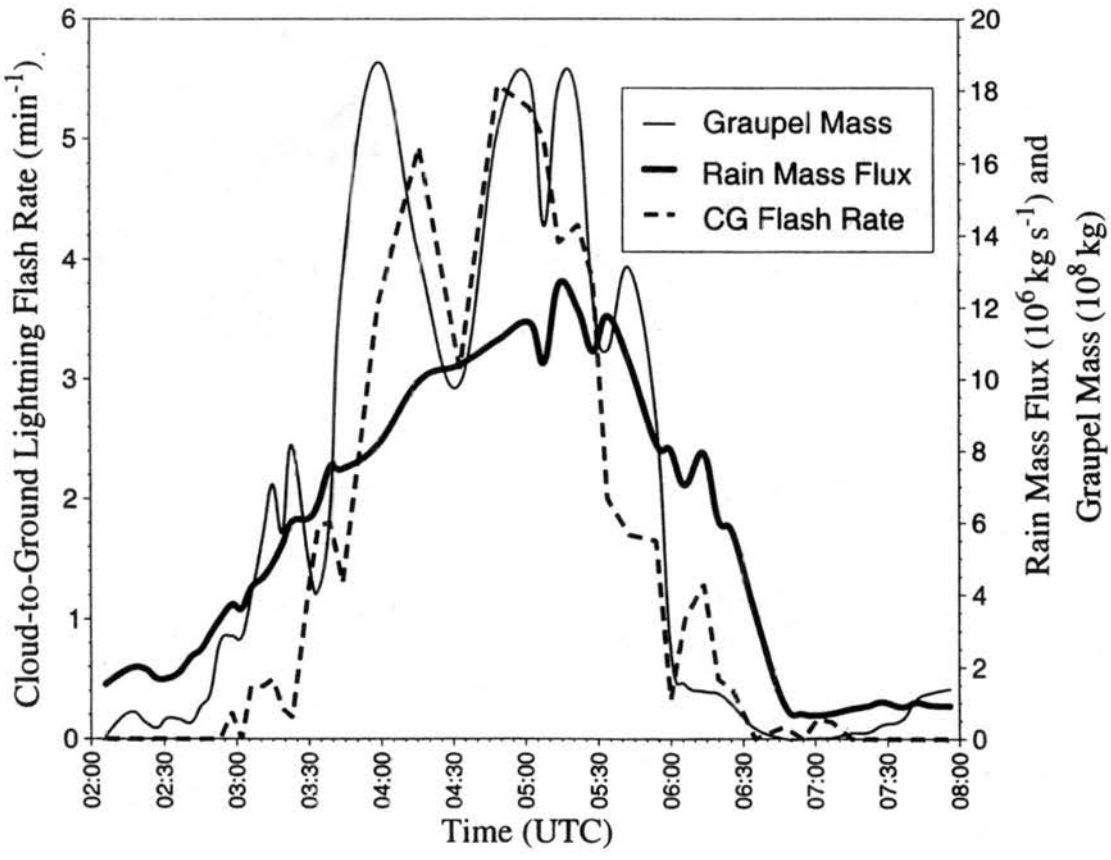

Figure 3.7. Evolution of Hector's cloud-to-ground lightning flash rate (min^{-1}), rain mass flux (10^6 kg s^{-1}), and mixed phase graupel mass (M_g, 10^8 kg) over the Tiwi Islands from 0200 to 0800 UTC.

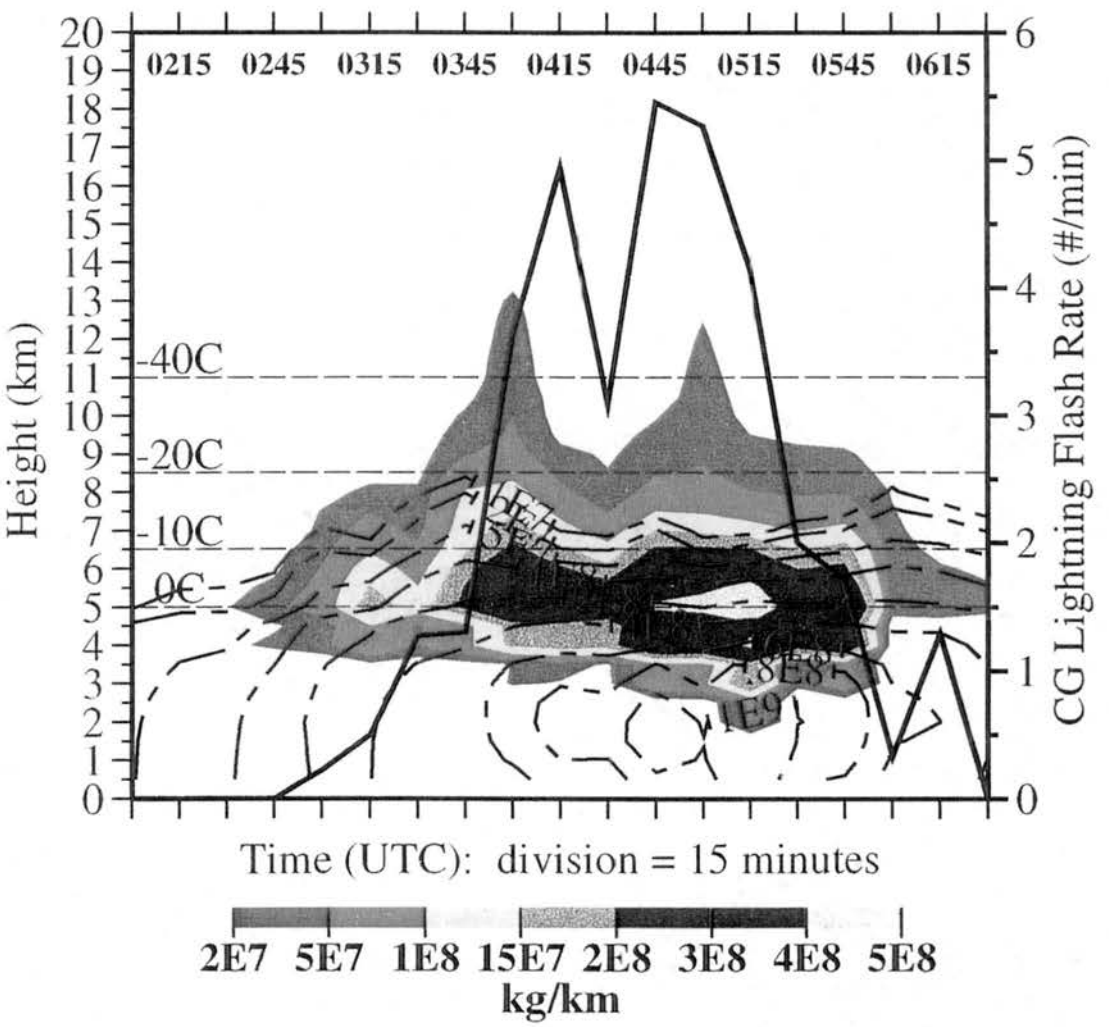

Figure 3.8. Time-height cross-section of Hector's slab total graupel ice mass (kg km^{-1}, color shaded) and rain mass (kg km^{-1}, dashed contour) over the Tiwi Islands from 0200 to 0630 UTC. The slab graupel ice mass is calculated by adding the graupel ice mass at each vertical level in a Cartesian grid over the Tiwi Islands. The cloud-to-ground lightning flash rate (min^{-1}, solid line) during this period is repeated for direct comparison.

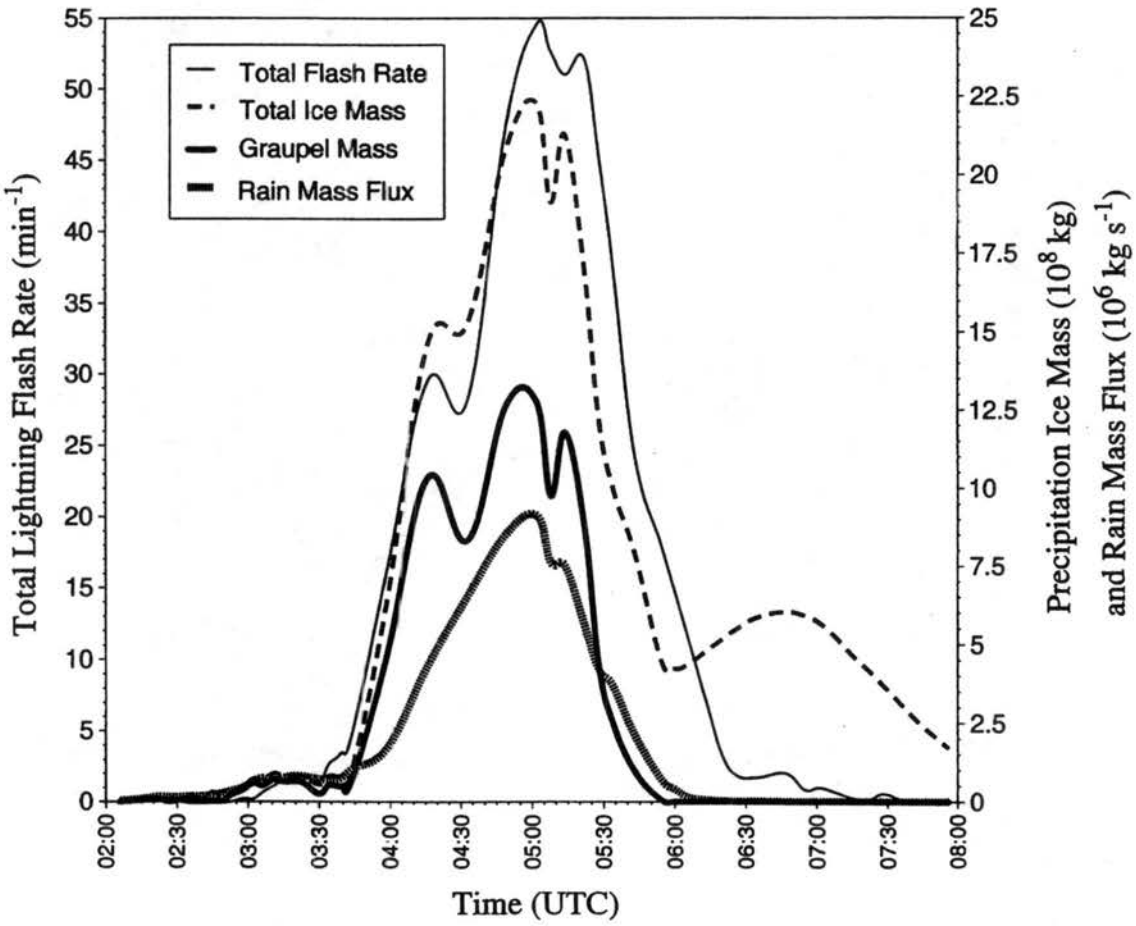

Figure 3.9. Evolution of Hector's total lightning flash rate (min^{-1}), total precipitation sized ice mass (10^8 kg), graupel ice mass (10^8 kg), and rain mass flux (10^6 kg s^{-1}) within 40 km of the flat plate antenna which was collocated with the C-pol radar.

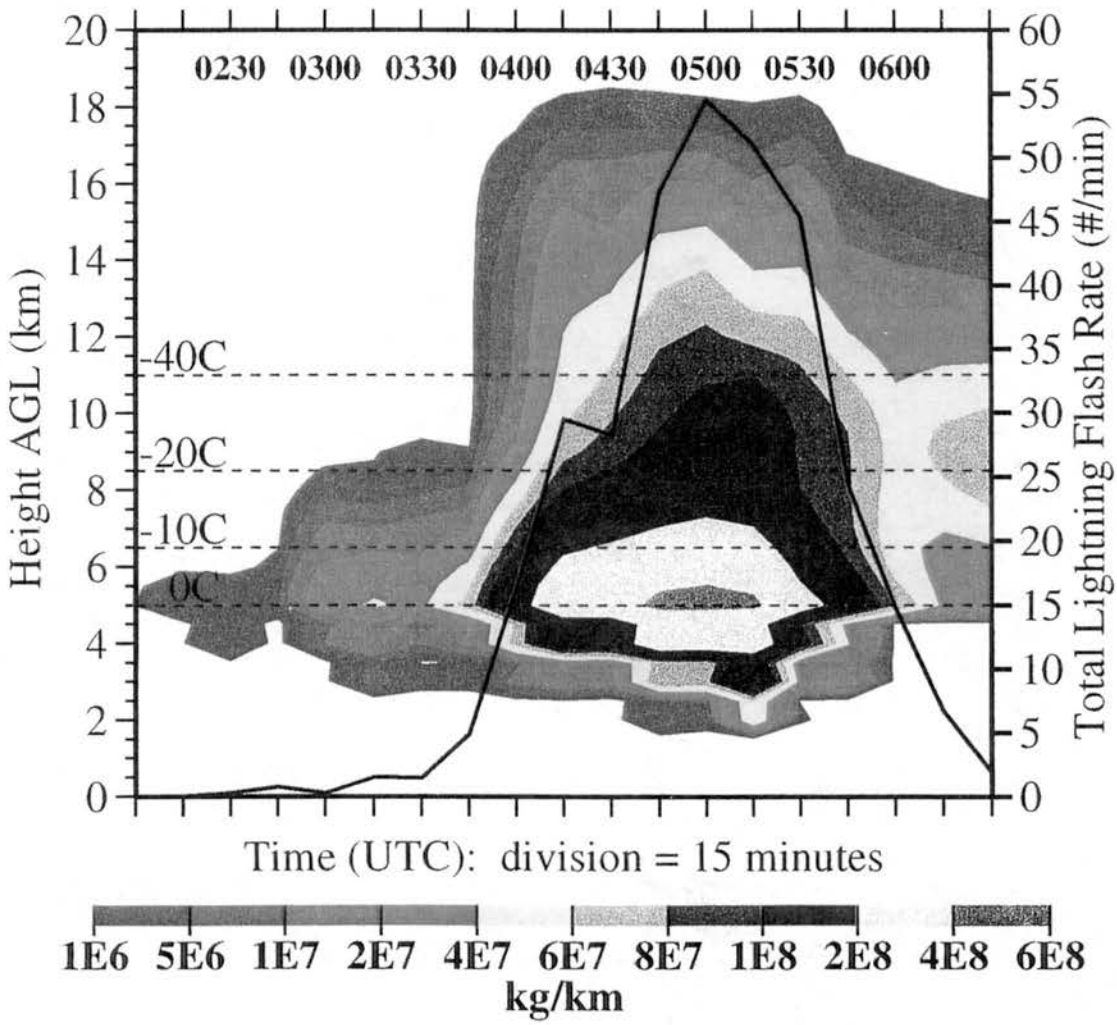

Figure 3.10. Time-height cross-section of Hector's slab total precipitation sized ice mass (kg km^{-1}, color shaded) within 40 km of the C-pol radar from 0200 to 0630 UTC. The slab precipitation sized ice mass is calculated by adding the precipitation ice mass at each vertical level in a Cartesian grid over the Tiwi Islands. The total lightning flash rate (min^{-1}, solid line) during this period is repeated for direct comparison.

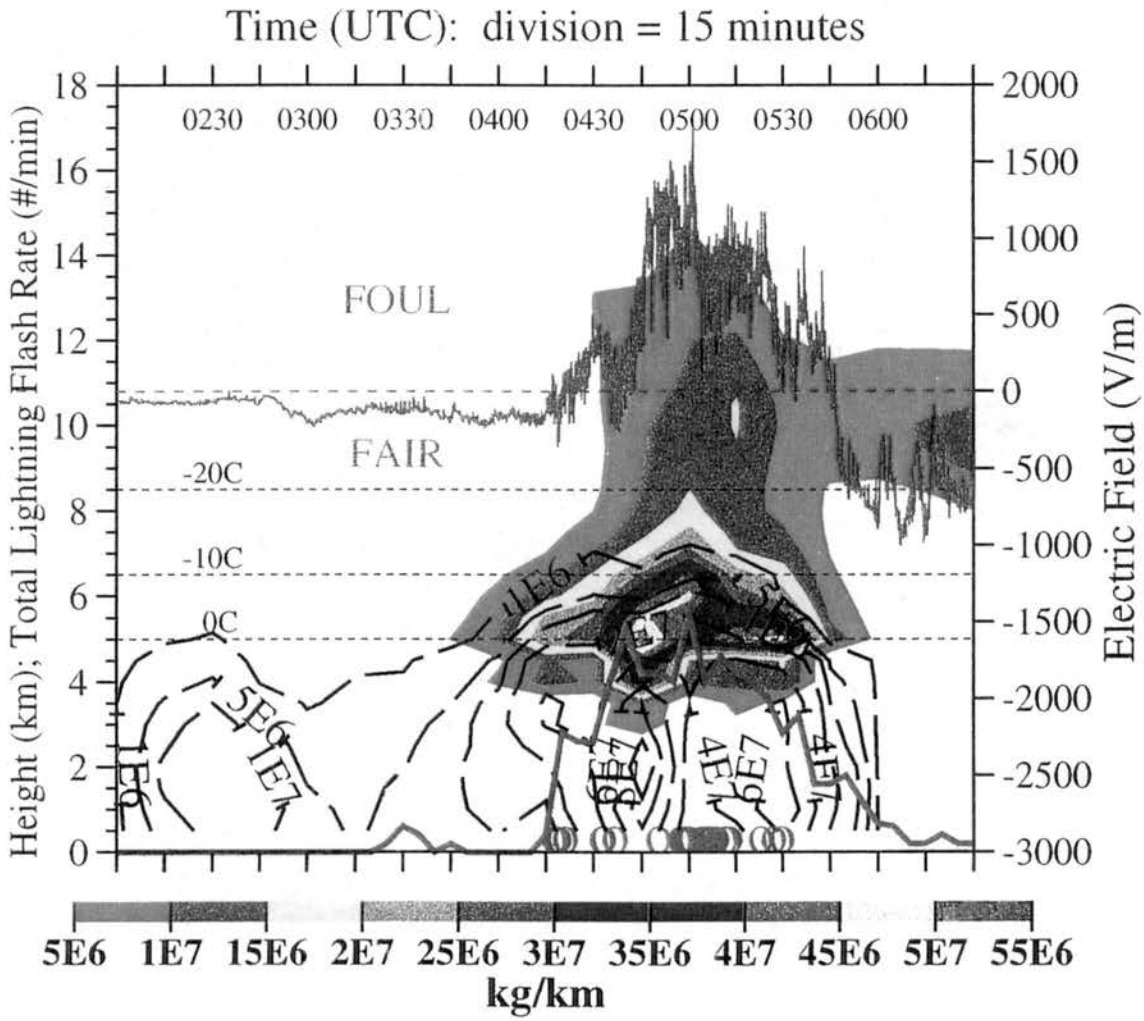

Figure 3.11. Evolution of the slab total precipitation sized ice mass (kg km^{-1}, color shaded), slab rain mass (kg km^{-1}, black dashed contours), surface electric field (V m^{-1}, pink line), total lightning flash rate derived from the field mill (min^{-1}, thick solid blue line), and the time of occurrence for cloud-to-ground lightning as depicted by the symbol "**O**" within 20 km of the C-pol radar from 0200 to 0630 UTC. Slab mass refers to the summation of all mass at each vertical level in a Cartesian grid over the Tiwi Islands.

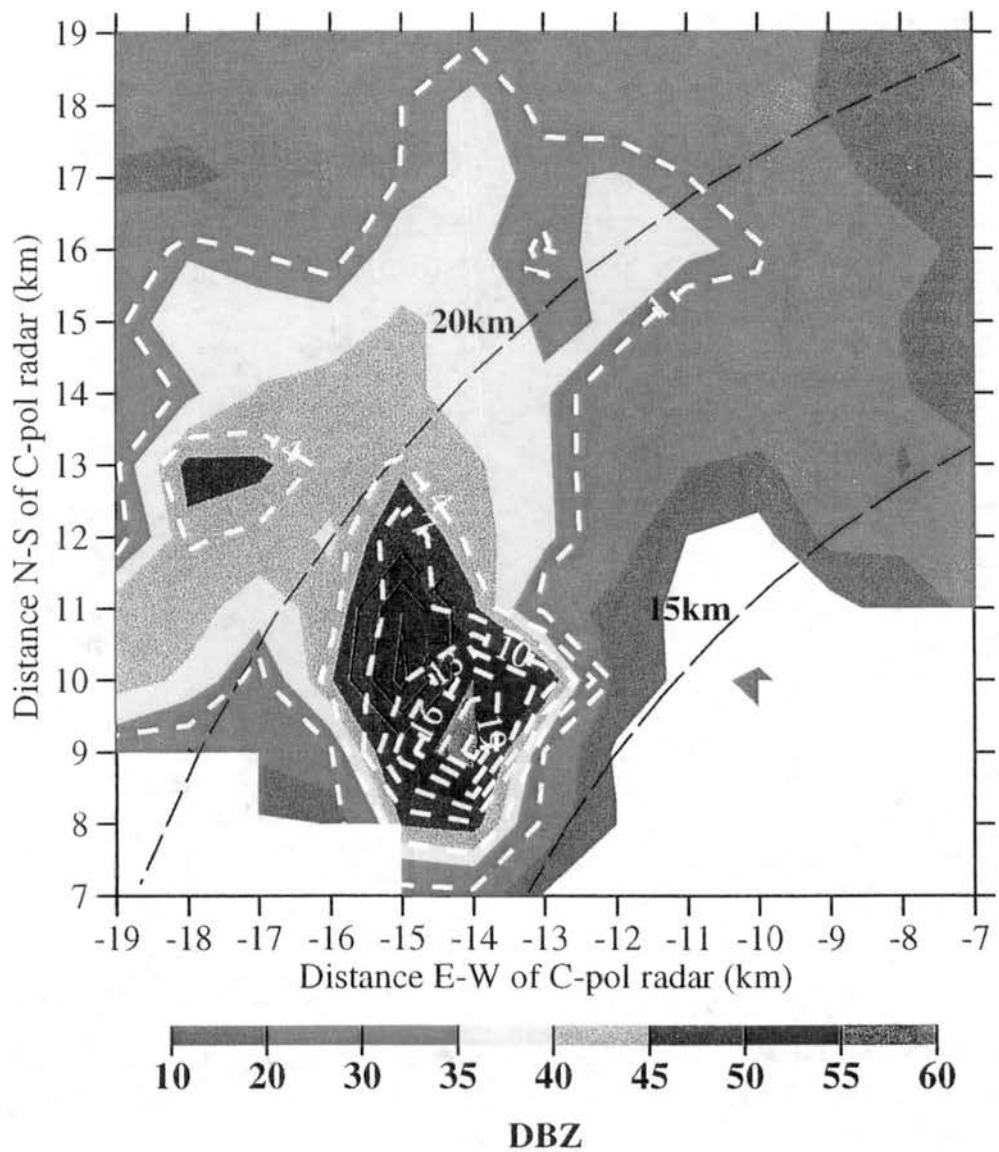

Figure 3.12. Horizontal cross-section of Z_h (dBZ, color shaded as shown), Z_{dr} (solid black contour every 0.5 dB starting at 1 dB), and M_i (dashed white contour every 3 g kg^{-1} starting at 1 g kg^{-1}) through the 6.5 km (-10° C) level at 0502 UTC for the cell which likely produced the peak electric field shown in Fig. 3.11. Range rings at 15 km and 20 km are depicted.

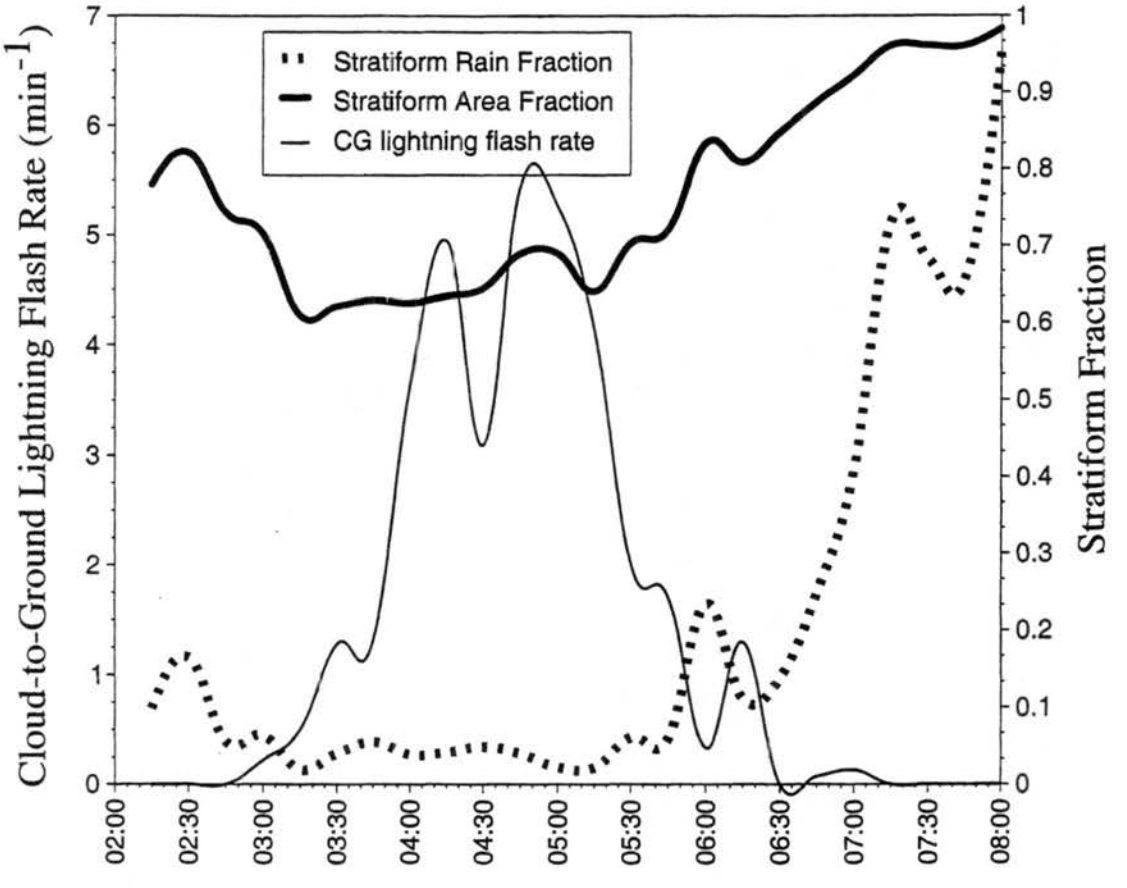

Figure 3.13. Evolution of Hector's stratiform rain and area fractions and the cloud-to-ground lightning flash rate (min^{-1}) over the Tiwi Islands from 0200 to 0800 UTC.

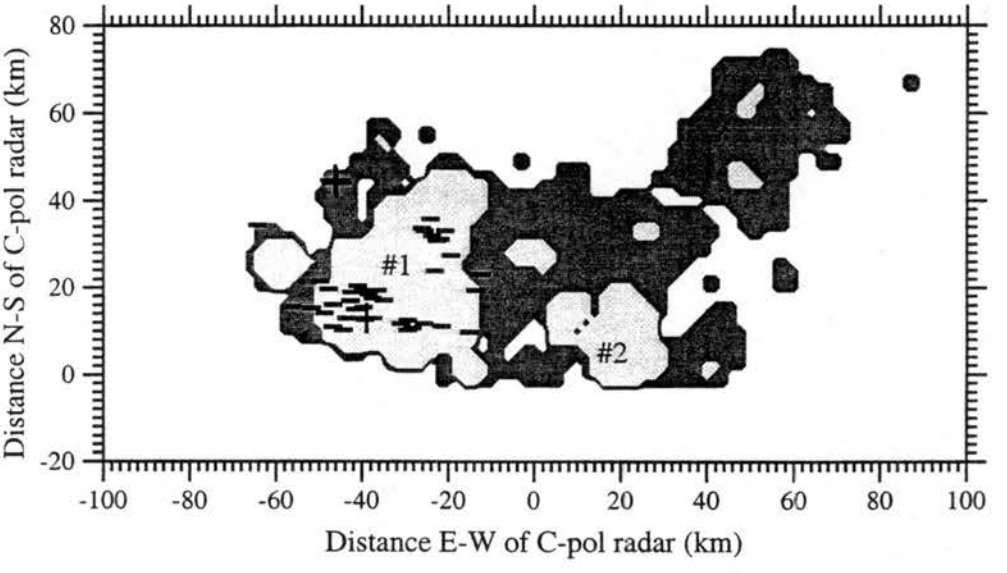

Figure 3.14. Cloud-to-ground lightning (0509 - 0519 UTC) overlaid on the convective (light gray shade) or stratiform (dark gray shade) precipitation classification for Hector at 0514 UTC. Reference Fig. 3.1d for the horizontal reflectivity structure at 2 km.

CHAPTER 4
SUMMARY AND CONCLUSIONS

As recently stated in MacGorman and Rust (1998), "the available data [on tropical lightning] are sparse so our understanding should be considered embryonic." Indeed, one of the primary objectives of the Maritime Continent Thunderstorm Experiment (MCTEX; Keenan et al., 1994a) was to "study cloud electrification mechanisms, especially couplings between ice phase precipitation and the occurrence of strong electric fields and lightning." MCTEX provided a unique data set with which to accomplish this objective.

Using observations from the first C-band polarimetric radar (BMRC C-pol) deployed beneath tropical convection, a network of ALDFs, a flat plate antenna, and a field mill, we have attempted to demonstrate that lightning production in tropical island convection is critically linked to ice processes in the mixed phase region. Although a direct causal relationship cannot be established from remote measurements, we have demonstrated a clear correlation between mixed phase ice mass and lightning in an intense tropical island thunderstorm.

This was accomplished by refining earlier techniques aimed at correlating the surface area of an arbitrary radar reflectivity threshold at some height above the freezing level (the so-called Larsen Area; Larsen and Stansbury, 1974) to the occurrence of lightning. As in other recent studies (e.g., Bringi et al., 1997; López and Aubagnac, 1997), we partitioned the reflectivity into rain and ice components using a polarimetric radar. The reflectivity associated with ice was then converted into an estimate of ice mass through application of an appropriate Z-M equation. We then integrated the radar inferred ice mass throughout the entire mixed phase zone for comparison with the surface electric field measured by a field mill, the total lightning flash rate as estimated by a flat plate antenna, and the cloud-

to-ground lightning flash rate and location observed by a network of Advanced Lightning Direction Finders.

An equally important goal of this study was to determine the connection between cloud-to-ground lightning and overall storm morphology. For example, we explored the role of the cumulus merger process on the relationship between precipitation and CG lightning. In addition, we investigated the correlation between convective versus stratiform precipitation and CG lightning. The results presented herein suggest robust relationships between the merger process, convective rainfall, mixed phase ice mass, and lightning in tropical island thunderstorms.

Specific scientific findings from the study are:

1. The 28 Nov 95 storm was intense and electrically active. Total lightning flash rates easily exceeded one per second and island wide CG lightning flash rates reached up to 11 per minute. Echo tops penetrated 20 km. The 30 dBZ contour reached up to 18 km in height. Maximum observed reflectivities and rainfall rates exceeded 60 dBZ and 150 mm h^{-1} respectively.

2. No significant surface electric fields or lightning of any kind were associated with convection dominated by warm rain microphysical processes despite substantial reflectivities and rainfall rates.

3. The surface electric field, the total lightning flash rate, and cloud-to-ground lightning were all highly correlated to the radar inferred mixed phase ice mass in time and space. The results were consistent with prior findings from investigations of midlatitude, sub-tropical, and tropical oceanic convection.

a. The integrated observations are consistent with the non-inductive charging (NIC) theory which relies on collisions between large precipitation sized ice and smaller ice crystals in the presence of supercooled water.

b. Cloud-to-ground lightning was associated with the production and subsequent descent of large precipitation sized ice (graupel and frozen drops) from the -10° C to -20° C region. Peaks in the CG lightning flash rate typically lagged peaks in the graupel mass aloft.

c. Ground stroke locations clustered beneath maxima in radar inferred mixed phase ice mass.

d. Rainfall was correlated to both the CG and total lightning flash rates.

e. The total lightning flash rate and the total ice mass were highly correlated.

f. The lack of large precipitation sized ice and possibly supercooled cloud water during the final dissipative stages rendered the electrical generator ineffective, thus short circuiting the relationship between total ice mass and the total lightning flash rate.

g. The radar and field mill measurements were generally consistent with the classical tripole model.

h. A field excursion associated with precipitation (FEAWP) was observed by the field mill as ice descended from the -10° C level, subsequently melted, and finally caused a peak in the surface rain flux about 15 minutes after the start of the E-field excursion. We attribute the FEAWP to the positive charging of descending graupel particles at warm temperatures in the mixed phase zone (≥ -10° C).

4. Supercooled raindrops were common in the 0° C to -20° C region of this tropical island convection. Due to the multicell nature of Hector, a continual supply of supercooled rain water was available in the mixed phase zone throughout the developing and mature phases. This is in contrast to Yuter and Houze (1995) who found that selected multicell storms in Florida almost completely glaciate early in the storm's life-cycle. We speculate that the updrafts in Hector were either more intense and/or tended to ascend in cloud (and hence ice) free air more frequently.

5. The freezing of supercooled raindrops likely provided a) an instantaneous and plentiful supply of large precipitation sized ice, b) a potential source of secondary ice, and c) an enhancement in the updraft via the latent heat of freezing. Frozen drops appear to have played a crucial role in storm kinematics, microphysics, and electrification of Hector.

6. Single cell cumulonimbi did not produce a single detectable CG lightning flash. Merged cells produced 97% of the rainfall and mixed phase ice mass and 100% of the CG lightning. We speculate that strong gust front forcing, likely responsible for the merger process, also results in sufficient mixed phase ice mass for CG production. The two primary peaks in the mixed phase graupel mass and CG lightning were both preceded by

the explosive development of a daughter cell along a gust front and subsequent merger with the parent cell.

7. The stratiform rain and area fractions were highly *anti*-correlated with the cloud-to-ground lightning frequency. The general lack of lightning during the dissipative phase of Hector followed the fallout of large precipitation sized ice as inferred from C-pol radar and the likely diminution of cloud liquid water as updrafts weakened aloft. This behavior is consistent with the NIC theory which stipulates that particle scale charge separation requires collisions between large precipitation ice and ice crystals in the presence of cloud liquid water. A rapid decrease in the CG lightning flash rate appears to be a useful indicator for the onset of primarily stratiform precipitation.

APPENDICES

Appendix A. Overview of procedures for determining cloud electrical properties

The flat plate derived total lightning flash rate was computed using a signal-to-noise amplitude ratio technique described in Carey and Rutledge (1996) and is typically compared to radar echo characteristics within 40 km of the instrument. Return strokes were handled by requiring 500 ms to pass before the next signal could be considered a separate flash.

An independent estimate of the total lightning flash rate within about 20 km of the radar was obtained by applying a filtered derivative algorithm (Basseville and Nikiforov, 1993) on the 50-Hz surface field mill data. The field mill data was passed through a 5-point running mean filter. The temporal derivative of the electric field data was accomplished using a simple finite differencing scheme. If |dE/dt| was greater than 400 V m^{-1} s^{-1} for at least 0.1 s, then a lightning flash was tabulated. As in the flat plate algorithm, a gap of 0.5 s between E-field perturbations was required before the next distinct lightning flash was recorded by the field mill.

This |dE/dt| threshold is well above the instrument noise level determined from inspection of 141 hours of lightning free field mill data (i.e., no radar echo within 50 km). During the thunderstorm free periods, over 99.9% of the |dE/dt| was less than 40 V m^{-1} s^{-1}. In an independent test, the automated algorithm compared favorably to a subjective, visual determination of lightning flash rate.

The field mill estimate of the surface electric field is calibrated and accurate to within 4 V m^{-1}. The effective range for detecting the surface electric field and associated lightning transients is approximately 20 km (Uman, 1987). Occasionally, transients from a particularly vigorous lightning flash can be detected in the surface electric field at ranges

as distant as 25 km. In this study, we adapt the convention that a positive surface electric field corresponds to an upward directed electric field vector (the so-called "foul field" characterized by net negative charge aloft).

A linear analytic inversion algorithm (Koshak et al., 1998) was utilized on CG data from the network of four ALDFs to retrieve estimates of return stroke location and time of occurrence. Over the Tiwi Islands, Koshak et al. (1998) estimate lightning location retrieval errors of about 0.1 to 1 km for a four station solution and 5 to 10 km for a three station solution. For the purpose of this study, the location accuracy is sufficient to assign a particular ground stroke to a given convective cell. The retrieved CG return *strokes* were combined into cloud-to-ground lightning *flashes* using a temporal and spatial clustering algorithm similar to that described in Cummins et al. (1998).

Appendix B. Estimation of the reflectivity associated with rain in mixed phase precipitation in the presence of large raindrops

As reviewed in Doviak and Zrnic (1993), there are two methods by which the horizontal reflectivity associated with rain can be estimated in mixed phase precipitation (i.e., a mixture of rain and ice): a power-based method utilizing the difference reflectivity, $Z_{dp} = 10 \bullet \log(Z_h - Z_v)$ (Golestani et al., 1989), and a phase-based method utilizing the specific differential phase, K_{dp} (Balakrishnan and Zrnic', 1990). Both methods rely on the known behavior of equilibrium rain drop shape with size (e.g., Pruppacher and Beard, 1970). Scattering simulations have demonstrated that the horizontal reflectivity associated with rain is linearly proportional to Z_{dp} (Golestani et al., 1989) and the natural logarithm of K_{dp} (Balakrishnan and Zrnic', 1990).

These methods assume that precipitation sized ice particles (i.e., graupel, hail, and frozen drops) tend to be more spherically symmetrical or tumble (e.g., Pruppacher and Klett, 1997). Deviations from the assumption of sphericity are mitigated by the significantly lower dielectric constant of ice (e.g., Seliga and Bringi, 1976; Herzegh and Jameson, 1992). As a result, ice particles contribute to the horizontal reflectivity and vertical reflectivity equally ($Z_h \approx Z_v$) such that Z_{dp} would be due solely to the presence of rain. Similarly, the specific differential phase of ice is approximately zero such that K_{dp} is

also only sensitive to the rain in the radar resolution volume (Balakrishnan and Zrnic', 1990). Therefore, the rain reflectivity in mixed phase precipitation can be estimated directly from either Z_{dp} or K_{dp} without being significantly biased by the presence of ice. As discussed in Appendix C, the horizontal reflectivity associated with ice in mixed phase precipitation can then be estimated as a residual difference of the observed Z_h and estimated Z_h(rain).

The Z_{dp}-method has been utilized to estimate latent heating rates associated with precipitation (Chandrasekar et al., 1991; Tong et al., 1998), to investigate microphysical processes within isolated convection (Takahashi et al., 1996) and hailstorms (Meischner et al., 1991; Conway and Zrnic', 1993), and to explore the relationship between precipitation and cloud electrification (Carey and Rutledge, 1996; Bringi et al, 1997). Similarly, Carey and Rutledge (1996, 1998) and López and Aubagnac (1997) have used the K_{dp}-method to investigate hail microphysics and the relationship between precipitation and lightning. With the exception of Meischner et al. (1991), all of the above studies utilized S-band radar observations. This study is the first to employ these methods with C-band observations of tropical convection. In addition, there has been little critical intercomparison of the Z_{dp} and K_{dp} methods. Therefore, we explored the relative performance of each procedure to estimate the horizontal reflectivity associated with rain in tropical convection at C-band using both scattering simulations and C-pol observations taken during MCTEX.

Using disdrometer observations of tropical rainfall collected during MCTEX as input to a scattering model (see Appendix B, Part II of this study for details), we calculated the $Z_h(Z_{dp})$ and $Z_h(K_{dp})$ relationships (Table B.1) in rain using a least squares regression procedure. As discussed in Appendix D, Part II of this study, large drops were observed in both the videosonde and disdrometer observations. C-pol radar measurements during MCTEX often indicated the presence of large drops via Z_{dr} measurements (e.g., $Z_{dr} \geq 3$ dB). In order to investigate the effect of large drops on these relationships and their accuracy, the scattering simulations were conducted assuming both D_{max} = 4 mm and 8 mm. The resulting Z_h(rain) versus Z_{dp} and LN(K_{dp}) scatterplots as a function of maximum drop size are presented in Figs. B.1a,b respectively. The standard error for both $Z_h(Z_{dp})$

and $Z_h(K_{dp})$ are about 0.9 dB for D_{max} = 4 mm. When the maximum drop size is increased to 8 mm, the scatter for the $Z_h(K_{dp})$ relationship increases significantly (Fig. B.1a) while the $Z_h(Z_{dp})$ scatter remains about the same (Fig. B.1b). This is reflected in a factor of two increase of the standard error of the $Z_h(K_{dp})$ estimator when D_{max} is increased from 4 to 8 mm (Table B.1). In the presence of large drops, the difference reflectivity is clearly superior to the specific differential phase in estimating the horizontal reflectivity associated with rain.

Table B.1. Equations for estimating the horizontal reflectivity associated with rain as derived from scattering simulations.

Equation	Standard Error (dBZ)	ρ^2
D_{max} = 4 mm		
$Z_h(Z_{dp}) = 0.822 \bullet Z_{dp} + 13.09$	0.93	0.966
$Z_h(K_{dp}) = 4.817 \bullet LN(K_{dp}) + 42.11$	0.93	0.965
D_{max} = 8 mm		
$Z_h(Z_{dp}) = 0.776 \bullet Z_{dp} + 14.59$	1.07	0.969
$Z_h(K_{dp}) = 5.314 \bullet LN(K_{dp}) + 42.57$	1.96	0.892

The above simulations did not include the effects of measurement error. As demonstrated in Fig. B.1a and Table B.1 and prior studies (e.g., Tong et al., 1998), Z_h is highly correlated to Z_{dp} in rainfall. Hence, the scatter between Z_h and Z_{dp} was not significantly perturbed by the addition of simulated measurement error. In contrast, the addition of 0.4° km^{-1} of standard measurement error to K_{dp} in the above scattering simulation increases the standard error of the $Z_h(K_{dp})$ estimator to 2.3 dBZ (3 dBZ) for Dmax = 4 mm (8 mm). Clearly, $Z_h(Z_{dp})$ is more immune to measurement error than $Z_h(K_{dp})$.

To support these simulation results and also to derive unbiased relationships for rain reflectivity in MCTEX convection, we utilized C-pol radar data at 1 km AGL from 0344 to 0433 UTC on 28 November 1995 to derive empirical $Z_h(Z_{dp})$ and $Z_h(K_{dp})$ relationships in rainfall using least squares regression. All grid points which satisfied $Z_h \geq 35$ dBZ, $Z_{dr} >$ 0.25 dB, and $K_{dp} > 0.4°$ km^{-1} were included in the regression sample. The resulting $Z_h(Z_{dp})$ and $Z_h(K_{dp})$ scatterplots and regression results are given in Figs. B.2a,b respectively. As expected, Z_h is highly correlated to Z_{dp} in rain (e.g., 94 % of the variance explained). In

contrast, only 41% of the variance in Z_h is explained by $LN(K_{dp})$ in C-pol observations of rainfall. The standard error (SE) of the empirically derived $Z_h(K_{dp})$ estimator is a factor of three higher than the SE of $Z_h(Z_{dp})$ (Figs. B.2a,b). The empirically derived $Z_h(Z_{dp})$ relationship appears to be superior to $Z_h(K_{dp})$.

To evaluate the stability of these empirically derived Z_h estimators in rain at different altitudes, times, and days, three independent test samples were compiled from C-pol radar observations during MCTEX and compared to the regression equations in Figs. B.2a,b. The bias and standard error in dBZ for $Z_h(Z_{dp})$ and $Z_h(K_{dp})$ were calculated for each complete test sample ($Z_h \geq 35$ dBZ) and for four separate sub-samples every 5 dBZ for each test data set (Tables B.2 and B.3 respectively). The results are consistent among the three different test samples. The standard error for $Z_h(Z_{dp})$ is consistently around 1 dBZ, compared to 2 - 3 dBZ for $Z_h(K_{dp})$. The overall sample bias for both estimators was small (< 0.5 dBZ) in all three tests. However, the bias for $Z_h(K_{dp})$ in individual sub-samples was often very large (2 - 6 dBZ). Comparatively, biases in the $Z_h(Z_{dp})$ sub-samples were typically very small (0.2 - 0.9 dBZ).

Table B.2. Evaluation of the empirical $Z_h(Z_{dp})$ equation using observed data from other days, times, and altitudes during MCTEX.

$Z_h(Z_{dp})$ (dBZ)	**Test 1[1]**			**Test 2[2]**			**Test 3[3]**		
	N	*Bias (dBZ)*	*SE (dBZ)*	*N*	*Bias (dBZ)*	*SE (dBZ)*	*N*[4]	*Bias (dBZ)*	*SE (dBZ)*
All Z_h	3744	-0.29	1.05	6624	-0.27	0.95	5432	+0.29	1.03
$35 \leq Z_h < 40$	901	+0.28	1.05	1471	+0.23	1.01	1721	+0.93	1.01
$40 \leq Z_h < 45$	1469	-0.20	0.92	2646	-0.20	0.84	2401	+0.17	0.84
$45 \leq Z_h < 50$	1168	-0.76	1.01	2026	-0.63	0.92	1276	-0.33	0.93
$50 \leq Z_h < 55$	192	-0.76	0.71	446	-0.66	0.67	34	+0.31	0.37

[1] Test 1: 28 Nov 95, 1 km, 0330, 0334, 0339, 0449, 0502, 0508 UTC

[2] Test 2: 28 Nov 95, 2.5 km, 0330, 0334, 0339, 0449, 0502, 0508 UTC

[3] Test 3: 23 Nov 95, 1 km, 0640 - 0645 UTC

[4] For N < 100, the SE as defined in Part II of this study was multiplied by $\sqrt{N/N-3}$

Table B.3.. Evaluation of the empirical $Z_h(K_{dp})$ equation using observed data from other days, times, and altitudes during MCTEX.

$Z_h(K_{dp})$ (dBZ)	Test 1[1]			Test 2[2]			Test 3[3]		
	N	*Bias (dBZ)*	*SE (dBZ)*	*N*	*Bias (dBZ)*	*SE (dBZ)*	*N*[4]	*Bias (dBZ)*	*SE (dBZ)*
All Z_h	3744	-0.48	2.88	6624	-1.18	3.11	5432	+0.35	2.69
$35 \le Z_h < 40$	901	+2.59	2.19	1471	+2.37	2.24	1721	+2.58	2.55
$40 \le Z_h < 45$	1469	-0.56	1.97	2646	-1.06	1.92	2401	-0.19	1.89
$45 \le Z_h < 50$	1168	-2.00	1.92	2026	-2.83	2.12	1276	-1.44	1.87
$50 \le Z_h < 55$	192	-4.34	2.67	446	-5.34	2.83	34	-6.41	2.06

[1] Test 1: 28 Nov 95, 1 km, 0330, 0334, 0339, 0449, 0502, 0508 UTC

[2] Test 2: 28 Nov 95, 2.5 km, 0330, 0334, 0339, 0449, 0502, 0508 UTC

[3] Test 3: 23 Nov 95, 1 km, 0640 - 0645 UTC

[4] For N < 100, the SE as defined in Part II of this study was multiplied by $\sqrt{N/N-3}$

Based on the empirical and simulation results above, we have chosen to use Z_{dp} over K_{dp} to estimate the reflectivity associated with rain in mixed phase precipitation since the $Z_h(Z_{dp})$ estimator 1) is less affected by the presence of large drops and measurement error, 2) has a significantly smaller standard error and bias, and 3) provides stable results in rainfall at different heights, times, and days.

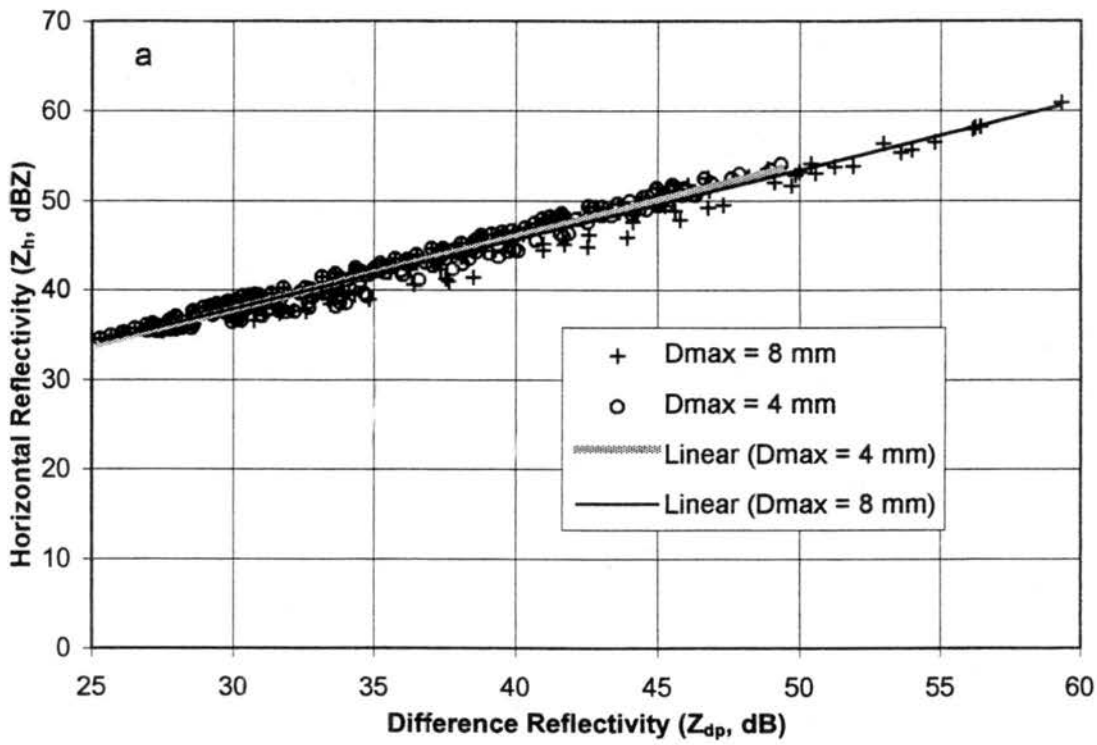

Figure B.1. Scatterplots of the horizontal reflectivity (Z_h, dBZ) versus (a) the difference reflectivity (Z_{dp}, dB) in rainfall as derived from scattering simulations described in Appendix B of Part II of this study using D_{max} = 4 mm (O) and 8 mm (+). A least squares regression line for each simulation run is plotted (4 mm: thick/light line; 8 mm: narrow/dark line). The associated regression equation, coefficient of correlation, and standard error for each regression line is given in Table B.1.

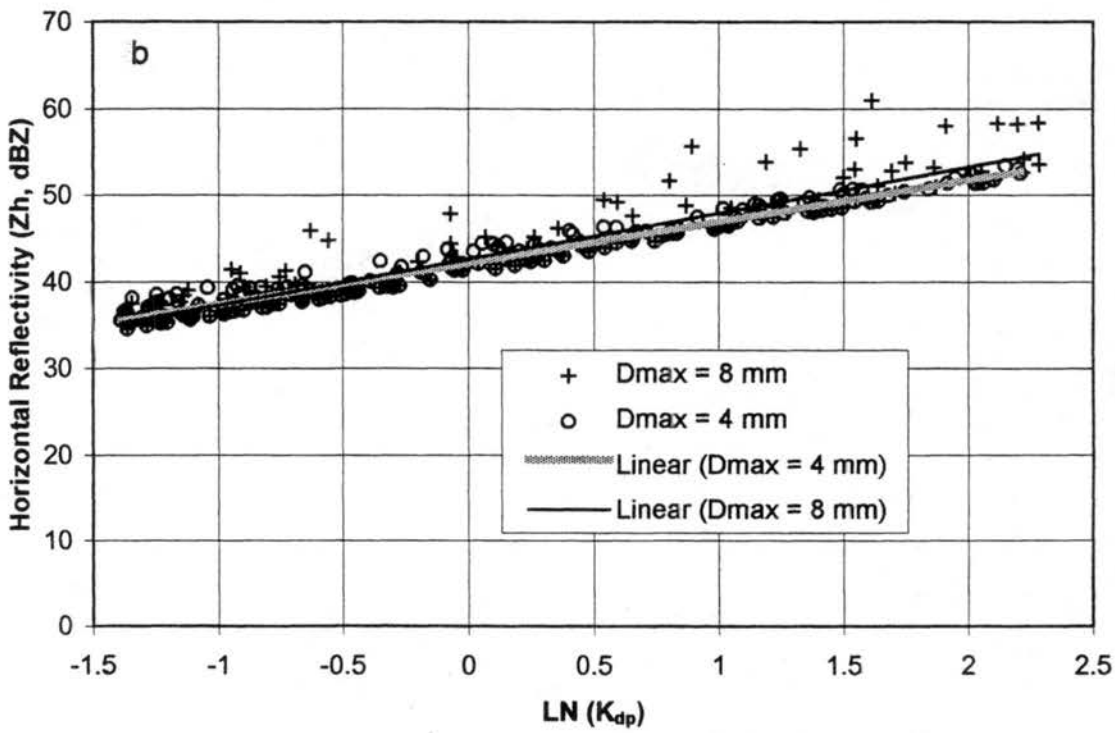

Figure B.1. (b) as in (a) except scatterplot of the horizontal reflectivity (Z_h, dBZ) versus the natural logarithm of the specific differential phase (K_{dp}, ° km^{-1}).

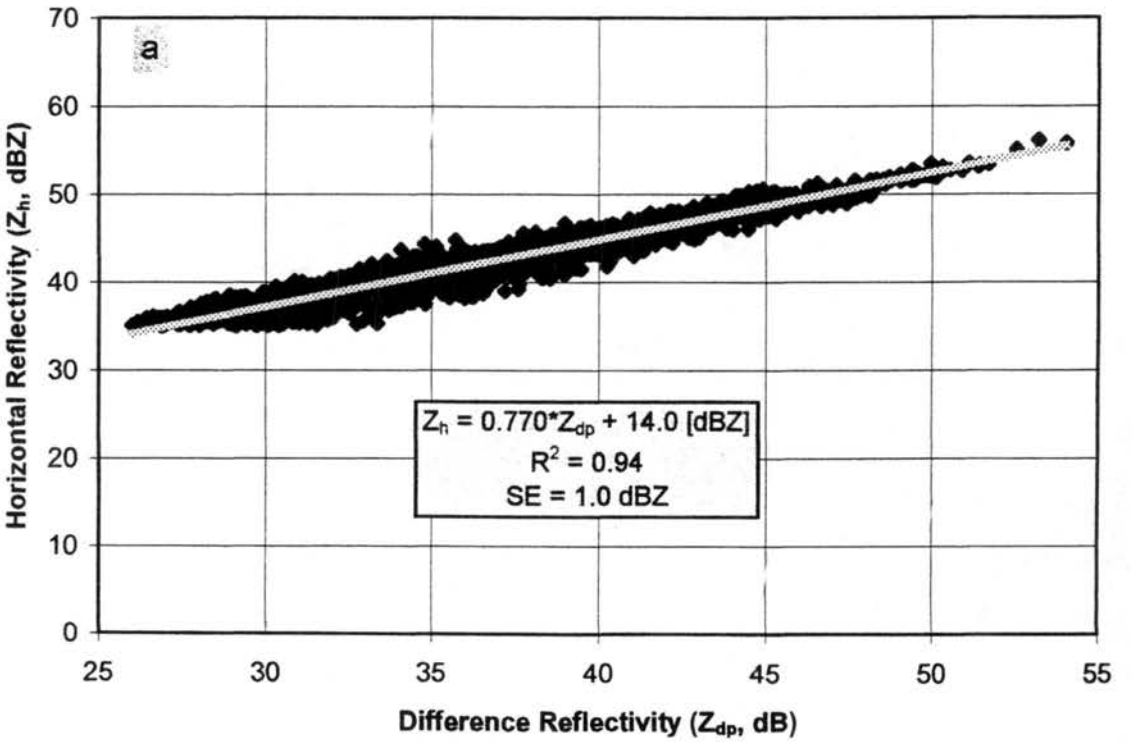

Figure B.2. Scatterplot of the horizontal reflectivity (Z_h, dBZ) versus (a) the difference reflectivity (Z_{dp}, dB) obtained from C-pol radar observations of tropical rainfall at 1 km AGL on 28 November 1995 from 0344 - 0433 UTC. A least squares regression line for each empirical data set is shown along with the associated equation, coefficient of correlation, and the standard error.

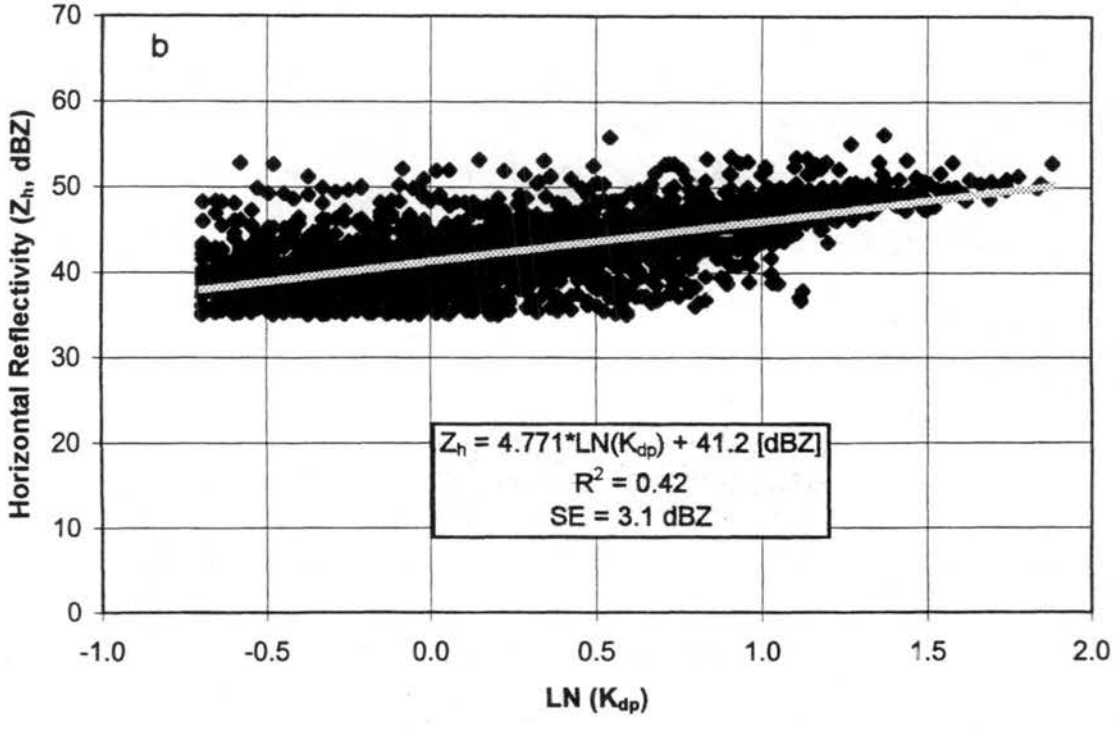

Figure B.2. (b) as in (a) except scatterplot of the horizontal reflectivity (Z_h, dBZ) versus the natural logarithm of the specific differential phase (K_{dp}, ° km^{-1}).

Appendix C. Equations for estimating the rain and ice mass

In this section, we review a method of inverting rain and ice mass from observed C-band polarimetric radar quantities. As derived and evaluated in Appendix B above, the difference reflectivity (Z_{dp}, dB) (Golestani et al., 1989) is first used to estimate directly the contribution of rain to the horizontal reflectivity (Z_h,dBZ).

$$Z_h^{rain} = 0.77 \bullet Z_{dp} + 14.0 \quad [\text{dBZ}] \tag{C.1}$$

An estimate of the rain mass (M_w) is then obtained from the following Z-M relationship,

$$M_w = 3.01 \times 10^{-4} \bullet \left(Z_H^{rain} \right)^{0.846} \quad [\text{g kg}^{-1}] \tag{C.2}$$

where the units of Z_H(rain) are in mm^6 m^{-3}. Equation C2 above was developed using a curve fitting procedure on simulated radar data of rain over the Tiwi Islands. In order to create the simulated rainfall data, observations of drop size distributions taken during MCTEX with a disdrometer (Keenan et al., 1998b) were used as input to the T-matrix scattering model (Barber and Yeh, 1975), assuming C-band (5.5 cm), T = 20°C, a maximum drop diameter of 8 mm, and an equilibrium drop shape versus size relationship (Green, 1975).

The contribution of ice to the horizontal reflectivity can then be calculated as a residual from

$$Z_H^{ice} = Z_H - Z_H^{rain} \quad [\text{mm}^6\ \text{m}^{-3}] \tag{C.3}$$

where Z_H is the observed horizontal reflectivity. With this estimate of Z_H(ice), we then calculate the precipitation-sized ice mass (M_{ice}) using a relationship based on the Rayleigh approximation,

$$M_{ice} = 1000\pi \left(\frac{\rho_i}{\rho_a} \right) N_o^{3/7} \left(\frac{5.28 \times 10^{-18}\, Z_H^{ice}}{720} \right)^{4/7} \quad [\text{g kg}^{-1}] \tag{C.4}$$

where Z_H(ice) is in mm^6 m^{-3}, ρ_i is the ice density (kg m^{-3}), ρ_a is the air density (kg m^{-3}), and N_o (m^{-4}) is the intercept parameter of an assumed inverse exponential distribution for ice. In this study, we utilize an optimized intercept parameter ($N_{oi} = 4 \times 10^6$ m^{-4}) from a bulk-microphysical cloud modeling study of Tiwi Island convection by Petersen (1997).

The standard error of the rain reflectivity estimate using the Z_{dp} method (Eqn. C.1) is approximately 1 dB (see Appendix B). As a result, we require that Z_h - Z_h(rain) > 1 dB below the melting level in order to accurately estimate the residual Z_h(ice). Otherwise, we set Z_H(rain) = Z_H and Z_H(ice) = 0 mm^6 m^{-3}. Similarly, if Z_h - Z_h(ice) < 1 dB above the freezing level, then Z_H(ice) = Z_H and Z_H(rain) = 0 mm^6 m^{-3}.

It is important to note that Z_{dp} can be used to differentiate between rain and ice only if Z_h is sufficiently large (i.e., diameter ≥ 1 mm) such that rain is characterized by significant oblateness (e.g., Green, 1975). Based on the scattering properties of typical drop size distributions for convection over the Tiwi Islands (Keenan et al., 1998b) and an equilibrium drop shape versus size relationship (Green, 1975), we have utilized the Z_{dp} rain-ice partitioning method (Eqns. C.1 - C.4) if Z_h ≥ 35 dBZ. In this case, Eqn. C.4 would yield the ice mass, M_g, associated primarily with large precipitation sized ice (e.g., graupel, frozen drops, and large aggregates). If Z_h < 35 dBZ above the -10° C level, we then assume that Z_H(ice) = Z_H in Eqn. C.4 which would now be associated primarily with ice crystals and small aggregates, since horizontal reflectivity is proportional to D^6. In this study, we will consider both the ice mass associated with large ice (Z_h > 35 dBZ, M_g) and the total ice mass (M_i) which includes echoes of all reflectivities. Below the 0° C level, we assume that reflectivity echoes characterized by Z_h < 35 dBZ are dominated by rain.

REFERENCES

Atlas, D. A., 1966: The balance level in convective storms. *J. Atmos. Sci.*, **23**, 635-651.

Austin, P. M., and A. C. Bemis, 1950: A quantitative study of the "bright band" in radar precipitation echoes. *J. Meteor.*, **7**, 145-151.

Balakrishnan, N., and D. S. Zrnic´, 1990: Estimation of rain and hail rates in mixed-phase precipitation. *J. Atmos. Sci.*, **47**, 565-583.

Barber, P. and C. Yeh, 1975: Scattering of electromagnetic waves by arbitrarily shaped dielectric bodies. *Applied Opt.*, **14**, 2864-2872.

Basseville, M., and I. V. Nikiforov, 1993: *Detection of Abrupt Changes: Theory and Application.* 528 pp., Prentice Hall, Englewood Cliffs, New Jersey.

Blyth, A. M., R. E. Benestad, P. R. Krehbiel, and J. Latham, 1997: Observations of supercooled raindrops in New Mexico summertime cumuli. *J. Atmos. Sci.*, **54**, 569-575.

Brandes, E. A., J. Vivekanandan, J. D. Tuttle, and C. J. Kessinger, 1995: A study of thunderstorm microphysics with multiparameter radar and aircraft observations. *Mon. Wea. Rev.*, **123**, 3129-3143.

Bringi, V. N., and A. Hendry, 1990: Technology of polarization diversity radars for meteorology, in *Radar in Meteorology: Battan Memorial and 40th Anniversary Radar Meteorology Conference*, edited by D. Atlas, Amer. Meteor. Soc., Boston, Mass., 153-190.

——, V. Chandrasekar, N. Balakrishnan, and D. S. Zrnic´, 1990: An examination of propagation effects on radar measurements at microwave frequencies. *J. Atmos. Oceanic. Technol.*, **7**, 829-840.

——, L. Liu, P. C. Kennedy, V. Chandrasekar, and S. A. Rutledge, 1996: Dual multiparameter radar observations of intense convective storms: The 24 June 1992 case study. *Meteorol. Atmos. Phys.*, **59**, 3-31.

——, K. Knupp, A. Detwiler, L. Liu, I. J. Caylor, and R. A. Black, 1997: Evolution of a Florida thunderstorm during the Convection and Precipitation/Electrification Experiment: The case of 9 August 1991. *Mon. Wea. Rev.*, **125**, 2131-2160.

Carbone, R. E., T. D. Keenan, J. Hacker, and J. W. Wilson, 1999: Tropical island convection in the absence of significant topography, Part I. Sea breezes and early convection. *Preprints, 23rd Conference on Hurricanes and Tropical Meteorology*. Dallas, Texas, 10 - 15 January, 1999.

Carey, L. D., 1994: Multiparameter radar case studies of the microphysical and kinematic evolution of lightning producing storms. MS Thesis, Colorado State University Paper No. 567., 228 pp.

——, and S. A. Rutledge, 1996: A multiparameter radar case study of the microphysical and kinematic evolution of a lightning producing storm, *Meteorol. Atmos. Phys.*, **59**, 33-64.

—— and ——, 1998: Electrical and multiparameter radar observations of a severe hailstorm. *J. Geophys. Res.*, **103**, 13979-14000.

Caylor, I. C., and A. J. Illingworth, 1987: Radar observations and modeling of warm rain initiation. *Q. J. R. Meteorol. Soc.*, **113**, 1171-1191.

Chandrasekar, V., C. A. Atwater, and T. H. Von de Haar, 1991: Convective latent heating estimates from radar data. In Preprints, 25th Int. Conf. on Radar Meteorology, Paris, France, Amer. Meteor. Soc., 155 - 158.

Changnon, S. A., Jr., 1976: Effects of urban areas and echo merging on radar echo behavior. *J. Appl. Meteor.*, **15**, 561-570.

Chauzy, S., M. Chong, A. Delannoy, and S. Despiau, 1985: The June 22 tropical squall line observed during COPT 81 experiment: Electrical signatures associated with dynamical structure and precipitation. *J. Geophys. Res.*, **90**, 6091-6098.

Cheng, C-P., and R. A. Houze, Jr., 1979: The distribution of convective and mesoscale precipitation in GATE radar echo patterns. *Mon. Wea. Rev.*, **107**, 1370-1381.

Chong, M., and D. Hauser, 1989: A tropical squall line observed during the COPT 81 experiment in West Africa. Part II: Water budget. *Mon. Wea. Rev.*, **117**, 728-744.

Churchill, D. D., and R. A. Houze, Jr., 1984: Development and structure of winter monsoon cloud clusters on 10 December 1978. *J. Atmos. Sci.*, **41**, 933-960.

Clarence, N. D., and D. J. Malan, 1957: Preliminary discharge processes in lightning flashes to ground. *Quart. J. Roy. Meteor. Soc.*, **83**, 161-172.

Conway, J. W., and D. S. Zrnic′, 1993: A study of embryo production and hail growth using dual-Doppler and multiparameter radars. *Mon. Wea. Rev.*, **121**, 2511-2528.

Cummins, K. L., M. J. Murphy, E. A. Bardo, W. L. Hiscox, R. B. Pyle, and A. E. Pifer, 1998: A combined TOA/MDF technology upgrade of the U.S. National Lightning Detection Network. *J. Geophys. Res.*, **103**, 9035-9044.

DeMott, C. A., and S. A. Rutledge, 1998: The vertical structure of TOGA COARE convection. Part I: Radar echo distributions. *J. Atmos. Sci.*, **55**, 2730-2747.

Doviak, R. J., and D. S. Zrnic′, 1993: *Doppler Radar and Weather Observations*, 2nd ed., 562 pp., Academic, San Diego, Calif.

Dye, J. E., J. J. Jones, W. P. Winn, T. A. Cerni, B. Gardiner, D. Lamb, R. L. Pitter, J. Hallett, and C. P. R. Saunders, 1986: Early electrification and precipitation development in a small, isolated Montana cumulonimbus. *J. Geophys. Res.*, **91**, 1231-1247.

——, J. J. Jones, A. J. Weinheimer, and W. P. Winn, 1988: Observations within two regions of charge during initial thunderstorm electrification. *Q. J. R. Meteorol. Soc.*, **114**, 1271-1290.

——, W. P. Winn, J. J. Jones, and D. W. Breed, 1989: The electrification of New Mexico Thunderstorms 1. Relationship between precipitation development and the onset of electrification. *J. Geophys. Res.*, **94**, 8643-8656.

Foster, H., 1950: An unusual observation of lightning. *Bull. Amer. Meteor. Soc.*, **31**, 140-141.

French, J. R., J. H. Helsdon, A. G. Detwiler, and P. L. Smith, 1996: Microphysical and electrical evolution of a Florida thunderstorm, 1, observations, *J. Geophys. Res.*, **101**, 18961-18978.

Gage, K. S., C. R. Williams, and W. L. Ecklund, 1994: UHF wind profilers: A new tool for diagnosing tropical convective cloud systems. *Bull. Amer. Meteor. Soc.*, **75**, 2289-2294.

Golestani, Y., V. Chandrasekar, and V. N. Bringi, 1989: Intercomparison of multiparameter radar measurements, in *Proceedings of the 24th Conference on Radar Meteorology*, Amer. Meteor. Soc., Boston, Mass., 309-314.

Goodman, S. J., D. E. Buechler, P. D. Wright, and W. D. Rust, 1988a: Lightning and precipitation history of a microburst-producing storm. *Geophys. Res. Let.*, **15**, 1185-1188.

Green, A. W., 1975: An approximation for the shape of large raindrops. *J. Appl. Meteor.*, **14**, 1578-1583.

Hallett, J., and S. C. Mossop, 1974: Production of secondary ice crystals during the riming process. *Nature*, **249**, 26-28.

Herzegh, P. H., and A. R. Jameson, 1992: Observing Precipitation through dual-polarization radar measurements. *Bull. Amer. Meteor. Soc.*, **73**, 1365-1374.

Holden, D. N., C. R. Holmes, C. B. Moore, W. P. Winn, J. W. Cobb, J. E. Griswold, and D. M. Lytle, 1980. Local charge concentrations in thunderclouds, in *Proceedings of Sixth International Conference on Atmospheric Electricity*, Session XII-15, pp. 1-5, Univ. of Manchester Press, Manchester, England, 28 July - 1 August, 1980.

Horel, J. D., Wallace, J. M., 1981: Planetary scale atmospheric phenomena associated with the southern oscillation. *Mon. Wea. Rev.*, **109**, 813-829.

Houze, R. A., Jr., 1977: Structure and dynamics of a tropical squall-line system. *Mon. Wea. Rev.*, **105**, 1540-1567.

——, C-P Cheng, 1977: Radar characteristics of tropical convection observed during GATE: Mean properties and trends over the summer season. *Mon. Wea. Rev.*, **105**, 964-980.

——, E. N. Rappaport, 1984: Air motions and precipitation structure of an early summer squall line over the eastern tropical Atlantic. *J. Atmos. Sci.*, **41**, 553-574.

——, 1989: Observed structure of mesoscale convective systems and implications for large-scale heating. *Q. J. R. Meteorol. Soc.*, **115**, 425-461.

Hubbert, J., and V. N. Bringi, 1995: An iterative filtering technique for the analysis of copolar differential phase and dual-frequency radar measurements. *J. Atmos. Oceanic Technol.*, **12**, 643 - 648.

——, V. N. Bringi, L. D. Carey, and S. Bolen, 1998: CSU-CHILL polarimetric radar measurements from a severe hailstorm in eastern Colorado. *J. Appl. Meteor.*, **37**, 749-775.

Illingworth, A. J., J. W. Goddard, and S. M. Cherry, 1987: Polarization radar studies of precipitation development in convective storms. *Q. J. R. Meteorol. Soc.*, **113**, 469-489.

Jameson, A. R., 1985: Deducing the microphysical character of precipitation from multiple-parameter radar polarization measurements. *J. Clim. Appl. Meteor.*, **24**, 1037-1047.

——, and D. B. Johnson, 1990: Cloud microphysics and radar. *Radar in Meteorology: Battan Memorial and 40th Anniversary Radar Meteorology Conference,* edited by D. Atlas, Amer. Meteor. Soc., Boston, Mass., 323-340.

——, M. J. Murphy, and E. P. Krider, 1996: Multiple-parameter radar observations of isolated Florida thunderstorms during the onset of electrification, *J. Appl. Meteor.*, **35**, 343-354.

Jayaratne, E. R., C. P. R. Saunders, and J. Hallet, 1983: Laboratory studies of the charging of soft hail during ice crystal interactions. *Q. J. R. Meteorol. Soc.*, **109**, 609-630.

Keenan, T. D., B. R. Morton, Xu Shu Zhang, and K. Nyguen, 1990: Some characteristics of thunderstorms over Bathurst and Melville Islands near Darwin, Australia. *Q. J. R. Meteorol. Soc.*, **116**, 1153-1172.

——, G. Holland, S. Rutledge, J. Simpson, J. McBride, J. Wilson, M. Moncrieff, R. Carbone, W. Frank, B. Sanderson, and J. Hallet, 1994a: Science Plan - Maritime Continent Thunderstorm Experiment, *BMRC Research Report*, **44**, 61 pp.

——, B. Ferrier, and J. Simpson, 1994b: Development and structure of a maritime continent thunderstorm. *Meteorol. Atmos. Phys.*, **53**, 185-222.

——, R. Carbone, S. Rutledge, J. Wilson, G. Holland, and P. May, 1996: The Maritime Continent Thunderstorm Experiment (MCTEX): Overview and initial results. Preprints, Seventh Conference on Mesoscale Processes, Amer. Meteor. Soc., Reading, UK, Sept. 9-13, 1996., 326-328.

——, K. Glasson, F. Cummings, T. S. Bird, J. Keeler, and J. Lutz, 1998a: The BMRC/NCAR C-band polarimetric (C-POL) radar system. *J. Atmos. Oceanic Technol.*, **15**, 871-886.

——, L. D. Carey, D. S. Zrnic', P. T. May, and S. A. Rutledge, 1998b: A sensitivity analysis of C-band polarimetric variables in rain. *J. Appl. Meteor.*, submitted.

Koenig, L. R., 1963: The glaciating behavior of small cumulonimbus clouds. *J. Atmos. Sci.*, **20**, 29-47.

Koshak, W. J., R. J. Blakeslee, and J. C. Bailey, 1998: Lightning radio source retrieval using Advanced Lightning Direction Finder (ALDF) networks. *J. Geophys. Res.*, submitted.

Kotaki, M. I. Kurika, C. Kotoh, and H. Sugiuchi: Global distributions of thunderstorm activity observed with ISS-b. *J. Radio Res. Lab. Tokyo*, **28**, 49-71.

Krider, E. P., R. C. Noggle, and M. A. Uman, 1976: A gated wideband magnetic direction finder for lightning return strokes. *J. Appl. Meteor.*, **15**, 301-306.

Krishnamurti, T. N., Kanamitsu, M., Koss, W. J., Lee, J. D., 1973: Tropical east-west circulations during the northern winter. *J. Atmos. Sci.*, **30**, 780-787.

Lane-Smith, D. R., 1971: A warm thunderstorm. *Q. J. R. Meteorol. Soc.*, 97, 577-578.

Larsen, H. R., and E. J. Stansbury, 1974: Association of lightning flashes with precipitation cores extending to height 7 km. *J. Atmos. Terr. Phys.*, **36**, 1547-1553.

Lau, K. M., Chang, C. P., Chan, P. H., 1983: Short-term planetary-scale interactions over the tropics and midlatitudes. Part II: Winter-MONEX period. *Mon. Wea. Rev.*, **111**, 1372-1388.

——, and J. S. Boyle, 1987: Tropical and extratropical forcing of the large-scale circulation: a diagnostic study. *Mon. Wea. Rev.*, **115**, 400-428.

Leary, C. A., 1984: Precipitation structure of the cloud clusters in a tropical easterly wave. *Mon. Wea. Rev.*, **112**, 313-325.

Lhermitte, R., and. E. Williams, 1985: Thunderstorm electrification: A case study. *J. Geophys. Res.*, **90**, 6071-6078.

López, R. E., and J-P Aubagnac, 1997: The lightning activity of a hailstorm as a function of changes in its microphysical characteristics inferred from polarimetric radar observations. *J. Geophys. Res.*, **102**, 16799-16813.

MacGorman, D. R., and W. D. Rust, 1998: *The Electrical Nature of Storms*. 422 pp., Oxford University Press, New York.

Malan, D. J., and B. F. J. Schonland, 1950: An electrostatic fluxmeter of short response-time for use in studies of transient field-changes. *Proc. Phys. Soc. London Ser. B*, **63**, 402-408.

——, 1952: Les décharges dans l'air et la charge inférieure positive d'un nuage orageux. *Ann. Geophys.*, **8**, 385-401.

Marshall, J. S., and S. Radhakant, 1978: Radar precipitation maps as lightning indicators. *J. Appl. Meteor.*, **17**, 206-212.

Marshall, T. C., and W. P. Winn, 1982: Measurements of charged precipitation in a New Mexico thunderstorm: Lower positive charge centers. *J. Geophys. Res.*, **87**, 7141-7157.

McAnelly, R. L., and W. R. Cotton, 1989: The precipitation life cycle of mesoscale convective complexes over the central United States. *Mon. Wea. Rev.*, **106**, 101-113.

Meischner, P. F., V. N. Bringi, D. Heimann, and H. Höller, 1991: A squall line in southern Germany: Kinematics and precipitation formation as deduced by advanced polarimetric and Doppler radar measurements. Mon. Wea. Rev., **119**, 678-701.

Mikhailovsky, Y., Y. Agapov, B. Koloskov, 1992: Electrification of the tropical clouds. *Proceedings, 9th Inter. Conf. on Atmos. Electricity*, June 15-19, 1992, St. Petersburg, Russia, 176-178.

Mohr, C. G., 1986: Merger of mesoscale data sets into a common Cartesian format for efficient and systematic analyses. *J. Atmos. Oceanic. Technol.*, **3**, 143-161.

Moore, C. B., B. Vonnegut, B. A. Stein, and H. J. Survillas, 1960: Observations of electrification and lightning in warm clouds. *J. Geophys. Res.*, **65**, 1907-1910.

——, and B. Vonnegut, 1977: The thundercloud, in *Lightning, Vol. 1*, R. H. Golde, ed., Academic Press, New York, 51-98.

Orville, R. E., and D. W. Spencer, 1979: Global lightning flash frequency. *Mon. Wea. Rev.*, **107**, 934-943.

——, and R. W. Henderson, 1986: Global distributions of midnight lightning: September 1977 to August 1978. *Mon. Wea. Rev.*, **114**, 2640-2653.

Petersen, W. A., and S. A. Rutledge, 1992: Some characteristics of cloud-to-ground lightning in tropical northern Australia. *J. Geophys. Res.*, **97**, 11553-11560.

——, S. A. Rutledge, R. E. Orville: 1996: Cloud-to-ground lightning observations from TOGA COARE: Selected results and lightning location algorithms. *Mon. Wea. Rev.*, **124**, 602-620.

——, 1997: Multi-scale process studies in the tropics: Results from lightning observations. Ph.D. Dissertation. Colorado State University Paper No. 632, 354 pp.

——, R. C. Cifelli, S. A. Rutledge, B. S. Ferrier, and B. F. Smull, 1998: Shipborne dual-Doppler operations during TOGA COARE: Integrated observations of storm kinematics and electrification. *Bull. Amer. Meteor. Soc.*, in press.

Pietrowski, E. L., 1960: An observation of lightning in warm clouds. *J. Meteor.*, **17**, 562-563.

Pruppacher, H. R., and K. V. Beard, 1970: A wind tunnel investigation of the internal circulation and shape of water drops falling at terminal velocity in air. *Quart. J. Roy. Meteor.* Soc., **96**, 247 - 256.

——, and J. D. Klett, 1997: *Microphysics of Clouds and Precipitation.* 2nd ed., 954 pp., Kluwer Academic, Boston, Mass.

Ramachandran, R. A. Detwiler, J. Helsdon Jr., P. L. Smith, and V. N. Bringi, 1996: Precipitation development and electrification in Florida thunderstorm cells during Convection and Precipitation/Electrification Project, *J. Geophys. Res.*, **101**, 1599-1620.

Ramage, C. S., 1968: Role of a tropical "maritime continent" in the atmospheric circulation. *Mon. Wea. Rev.*, **96**, 365-370.

Rickenbach, T. M., and S. A. Rutledge, 1998: Convection in TOGA COARE: Horizontal scale, morphology, and rainfall production. *J. Atmos. Sci.*, **55**, 2715 - 2729.

Rosenfeld, D., E. Amitai, and D. B. Wolf, 1995: Classification of rain regimes by the three-dimensional properties of reflectivity fields. *J. Appl. Meteor.*, **34**, 198-211.

Rutledge, S. A., and D. R. MacGorman, 1988: Cloud-to-ground lightning activity in the 10-11 June 1985 Mesoscale Convective System observed during the Oklahoma-Kansas PRE-STORM Project. *Mon. Wea. Rev.*, **116**, 1393-1408.

——, C. Lu, and D. R. MacGorman, 1990: Positive cloud-to-ground lightning in mesoscale convective systems. *J. Atmos. Sci.*, **47**, 2085-2100.

——, E. R. Williams, and T. D. Keenan, 1992: The Down Under Doppler and Electricity Experiment (DUNDEE): Overview and preliminary results. *Bull. Amer. Meteor. Soc.*, **73**, 3-16.

Rust, W. D., and C. B. Moore, 1974: Electrical conditions near the bases of thunderclouds over New Mexico. *Q. J. R. Meteorol. Soc.*, **100**, 450-468.

Ryzhkov, A., and D. S. Zrnic', 1995: Precipitation and attenuation measurements at a 10-cm wavelength, *J. Appl. Meteor.*, **34**, 2121-2134.

Saunders, C. P. R., W. D. Keith, and R. P. Mitzeva, 1991: The effect of liquid water content on thunderstorm charging. *J. Geophys. Res.*, **96**, 11007-11017.

Seliga, T. A., and V. N. Bringi, 1976: Potential use of radar differential reflectivity measurements at orthogonal polarizations for measuring precipitation. *J. Appl. Meteor.*, **15**, 69 - 76.

Selvam, A. M., R. Vijayakumar, G. K. Manohar, and A. S. R. Murty, 1991: Electrical, microphysical, and dynamical observations in summer monsoon clouds. *Atmos. Res.*, **26**, 19-32.

Simpson, J., and W. L. Woodley, 1971: Seeding cumulus in Florida: New 1970 results. *Science*, **176**, 117-126.

——, N. E. Westcott, R. J. Clerman, R. A. Pielke, 1980: On cumulus mergers. *Arch. Met. Geoph. Biocl., Ser. A*, **29**, 1-40.

——, T. D. Keenan, B. Ferrier, R. H. Simpson, and G. J. Holland, 1993: Cumulus Mergers in the Maritime Continent Region. *Meteorol. Atmos. Phys.*, **51**, 73-99.

Solomon, R., and M. Baker, 1994: Electrification of New Mexico thunderstorms. *Mon. Wea. Rev.*, **122**, 1878-1886.

Soula, S., and S. Chauzy, 1991: Multilevel measurement of the electric field underneath a thundercloud. 2: Dynamical evolution of a ground space charge layer. *J. Geophys. Res.*, **96**, 22327-22336.

——, and ——, 1997: Charge transfer by precipitation between thundercloud and ground. *J. Geophys. Res.*, **102**, 11061-11069.

Standler, R. B. and W. P. Winn, 1979: Effects of corona on electric fields beneath thunderstorms. *Q. J. R. Meteorol. Soc.*, **105**, 285-302.

Stansbury, E. J., and J. S. Marshall, 1978: Sferics at two stations compared with radar-observed precipitation. *Atmosphere-Ocean*, **16**, 281-292.

Steiner, M., R. A. Houze, Jr., S. E. Yuter, 1995: Climatological characterization of three-dimensional storm structure from operational radar and rain gauge data. *J. Appl. Meteor.*, **34**, 1978-2007.

Takahashi, T., 1978a: Riming electrification as a charge generation mechanism in thunderstorms. *J. Atmos. Sci.*, **35**, 1536-1548.

——, 1978b: Electrical properties of oceanic tropical clouds at Ponape, Micronesia. *Mon. Wea. Rev.*, **106**, 1598-1612.

——, 1983: Electric structure of oceanic tropical clouds and charge separation processes. *J. Meteor. Soc. Japan*, **61**, 656-669.

Takahashi, N., H. Uyeda, and K. Kikuchi, 1996: Evolution process and precipitation particles of an isolated echo observed with dual-polarization Doppler radar near Sapporo on July 9, 1992. *Jour. Fac. Sci. Hokkaido Univ., Ser. VII (Geophysics)*, **10**, 135-153.

Tao, W-K., J. Simpson, 1984: Cloud interactions and merging: numerical simulations. *J. Atmos. Sci.*, **41**, 2901-2917.

——, and ——, 1989: A further study of cumulus interactions and mergers: Three-dimensional simulation with trajectory analyses. *J. Atmos. Sci.*, **46**, 2974-3004.

Tong, H., V. Chandrasekar, K. R. Knupp, and J. Stalker, 1998: Multiparameter radar observations of time evolution of convective storms: Evaluation of water budgets and latent heating rates. *J. Atmos. Oceanic Technol.*, **15**, 1097 - 1109.

Turman, B. N., and B. C. Edgar, 1982: Global lightning distributions at dawn and dusk. *J. Geophys. Res.*, **87**, 1191-1206.

Tuttle, J. D., V. N. Bringi, H. D. Orville, and F. J. Kopp, 1989: Multiparameter radar study of a microburst: Comparison with model results. *J. Atmos. Sci.*, **46**, 601-620.

Uman, M. A., 1987: *The lightning discharge*, 377 pp., Academic, San Diego, Calif. Williams, E. R., 1989: The tripole structure of thunderstorms. *J. Geophys. Res.*, **94**, 13151-13167.

Williams, E. R., 1989: The tripole structure of thunderstorms. *J. Geophys. Res.*, **94**, 13151-13167.

——, M. E. Weber, and R. E. Orville, 1989: The relationship between lightning type and convective state of thunderclouds. *J. Geophys. Res.*, **94**, 13213-13220.

——, 1990: Lightning and microbursts in convective clouds. *Conf. on Atmos. Electricity*, Kananaskis Park, Alta., Canada, Amer. Meteor. Soc., 738-743.

——, S. A. Rutledge, S. C. Geotis, N. Renno, E. Rasmussen, and T. Rickenbach, 1992: A radar and electrical study of tropical hot towers. *J. Atmos. Sci.*, **49**, 1386-1395.

Willis, P. T., J. Hallett, R. A. Black, and W. Hendricks, 1994: An aircraft study of rapid precipitation development and electrification in a growing convective cloud. *Atmos. Res.*, **33**, 1-24.

Wilson, J. W., T. D. Keenan, and R. E. Carbone, 1999: Tropical island convection in the absence of significant topography, Part II. Evolution of mesoscale convective systems. *Preprints, 23rd Conference on Hurricanes and Tropical Meteorology*. Dallas, Texas, 10 - 15 January, 1999.

Workman, E. J., and S. E. Reynolds, 1949: Electrical activity as related to thunderstorm cell growth. *Bull. Amer. Meteor. Soc.*, **30**, 142-149.

Young, K. C., 1993: *Microphysical Processes in Clouds*. 427 pp., Oxford University Press, New York.

Yuter, S. E., and R. A. Houze Jr., 1995: Three-dimensional kinematic and microphysical evolution of Florida Cumulonimbus. Part II: Frequency distributions of vertical velocity, reflectivity, and differential reflectivity. *Mon. Wea. Rev.*, **123**, 1941-1963.

Zipser, E. J., and K. R. Lutz, 1994: The vertical profile of radar reflectivity of convective cells: A strong indicator of storm intensity and lightning probability? *Mon. Wea. Rev.*, **122**, 1751-1759.

Zrnic', D. S., and N. Balakrishnan, C. L. Ziegler, V. N. Bringi, K. Aydin, T. Matejka, 1993: Polarimetric signatures in the stratiform region of a mesoscale convective system. *J. Appl. Meteor.*, **32**, 678-693.